

DISSERTATION

Reconstruction of Exclusive B Decays into J/ψ Using Data from the DELPHI Experiment and Implications to Future CP Violation Measurements at the LHC

ausgeführt zum Zwecke der Erlangung des akademischen Grades
eines Doktors der technischen Wissenschaften

eingereicht an der Technischen Universität Wien
Technisch-Naturwissenschaftliche Fakultät

von

Dipl.-Ing. Norbert Neumeister

Mucelle
F-01630 Challex

Matr. Nr.: 8625516



Genf, im Juli 1996

.....

*To my father
and in memory of my mother*

Contents

Kurzfassung	v
Preface	vii
Acknowledgements	ix
1 Introduction	1
1.1 Beauty Quark Physics	3
1.2 Exclusive B Hadron Decays	5
1.3 CP Violation	5
1.4 Outline	6
2 Theory	9
2.1 The Standard Model	9
2.1.1 The Electroweak Interaction	11
2.1.2 The Higgs Mechanism	14
2.1.3 Quantum Chromodynamics	15
2.1.4 Parameters of the Standard Model	16
2.2 Physics of e^+e^- annihilation	18
2.2.1 Quark-Pair Production at LEP	21
2.2.2 Heavy Quark Fragmentation	23
2.3 Beauty Quark Physics	24
2.3.1 Beauty Hadron Production at LEP	25
2.3.2 Beauty Hadron Decays	26
2.3.3 Weak Decays of B Hadrons	27
2.3.4 Semileptonic B Hadron Decays	29
2.3.5 Hadronic B Decays	30
2.3.6 B Hadron Decays into J/ψ	32
3 CP Violation in the B System	35
3.1 Introduction	35

3.2	The Cabibbo-Kobayashi-Maskawa Matrix	36
3.2.1	Parametrization of the CKM Matrix	38
3.2.2	The Elements of the CKM Matrix	40
3.3	Unitarity Triangles	41
3.4	Mixing of Neutral B Mesons	44
3.5	CP Violation in B Decays	47
3.6	How to Measure CP Violation	49
4	The DELPHI Experiment	53
4.1	The LEP Collider	53
4.2	The DELPHI Detector	55
4.2.1	General Layout	55
4.2.2	Tracking	56
4.2.2.1	The Time Projection Chamber	58
4.2.2.2	The Inner Detector	58
4.2.2.3	The Outer Detector	59
4.2.2.4	The Vertex Detector	59
4.2.2.5	Forward Chamber A	61
4.2.2.6	Forward Chamber B	61
4.2.2.7	Overall Tracking Performance	61
4.2.3	Calorimetry	64
4.2.3.1	The High Density Projection Chamber	65
4.2.3.2	The Forward Electromagnetic Calorimeter	67
4.2.3.3	The Hadron Calorimeter	67
4.2.4	The Scintillation Counters	68
4.2.4.1	The Time of Flight Detector	68
4.2.4.2	The Forward Hodoscope	68
4.2.5	The Luminosity Detectors	68
4.2.5.1	The Small Angle Tagger	69
4.2.5.2	The Small Angle Tile Calorimeter	69
4.2.5.3	The Very Small Angle Tagger	69
4.2.6	The Muon Chambers	69
4.2.6.1	The Barrel Muon Chambers	69
4.2.6.2	The Forward Muon Chambers	70
4.2.7	The Ring Imaging Cherenkov Detectors	70
4.2.7.1	The Barrel Ring Imaging Cherenkov Detector	70
4.2.7.2	The Forward Ring Imaging Cherenkov Detector	71
4.2.8	The Trigger System	71
4.2.9	The Data Acquisition System	72
4.3	Particle Identification	73
4.3.1	Hadron Identification	73

4.3.1.1	Specific Ionization in the TPC	73
4.3.1.2	Ring Imaging Cherenkov Detectors	75
4.3.2	Lepton Identification	77
4.3.2.1	Muon Identification	77
4.3.2.2	Electron Identification	78
5	Analysis	79
5.1	Introduction	79
5.2	Event Selection	81
5.3	Kinematical Study	83
5.4	J/ψ Reconstruction	83
5.4.1	Muon Selection	85
5.4.2	Electron Selection	86
5.4.3	Secondary vertex fit	86
5.5	Background and Efficiency	90
5.6	Inclusive Branching Ratios	92
5.7	Exclusive B Meson Reconstruction	93
5.7.1	Monte Carlo Study	95
5.7.2	Reconstruction of the Individual Decay Channels	95
5.7.2.1	$B^\pm \rightarrow J/\psi K^\pm$	97
5.7.2.2	$B_d^0 \rightarrow J/\psi K_S^0$	97
5.7.2.3	$B_d^0 \rightarrow J/\psi K^{*0}$	98
5.7.2.4	$B^\pm \rightarrow J/\psi K^{*\pm}$	98
5.7.2.5	$B_d^0 \rightarrow J/\psi K^+ \pi^-$	99
5.7.2.6	$B^\pm \rightarrow J/\psi K_S^0 \pi^\pm$	99
5.7.2.7	$B^\pm \rightarrow J/\psi K^\pm \pi^- \pi^+$	99
5.7.3	Background and Efficiency	99
5.8	Results and Discussion	105
6	Future Search for CP Violation	113
6.1	Introduction	113
6.2	e^+e^- B Factories	115
6.3	Fixed Target Experiments	116
6.4	Hadron Colliders	117
6.5	LHC	118
6.5.1	LHC Experiments	119
7	Simulation	123
7.1	Introduction	123
7.2	B Production at the LHC	124
7.3	The CMS Detector	127

7.3.1	Muon System	127
7.3.2	Tracker	128
7.3.3	Trigger	129
7.4	Measuring $\sin 2\beta$	130
7.5	Simulation of the $B_d^0 \rightarrow J/\psi K_S^0$ Channel	131
7.5.1	Kinematics	132
7.5.2	Trigger and Event Selection	133
7.5.3	K_S^0 Reconstruction	136
7.6	Tagging and Dilution	137
7.7	Background	141
7.8	Expected Sensitivity	141
7.9	Results and Discussion	143
8	Summary and Conclusions	145
	List of Figures	148
	List of Tables	151
	Bibliography	160

Kurzfassung

Der Large Electron Positron Collider (LEP) am Europäischen Laboratorium für Teilchenphysik, CERN, bietet durch die hohe Rate an erzeugten b Quarks die Möglichkeit, Zerfälle von B Mesonen zu studieren. Es wurde eine Untersuchung der seltenen, farbladungsunterdrückten B Meson Zerfällen in J/ψ Mesonen durchgeführt. Von besonderem Interesse dabei ist der Zerfall $B_d^0 \rightarrow J/\psi K_S^0$, der bei genügend hoher Statistik zur Messung von CP Verletzungseffekten im System neutraler B Mesonen verwendet werden kann. J/ψ Mesonen werden bei LEP hauptsächlich durch den Zerfall von B Hadronen erzeugt und eignen sich daher als Ausgangspunkt für die Untersuchung von exklusiven B Meson Zerfällen. Experimentell kann das J/ψ Meson durch seine Zerfälle in Leptonpaare ($\mu^+\mu^-$, e^+e^-) mit großer Effizienz identifiziert werden. Der DELPHI Detektor verfügt über einen Vertexdetektor zur genauen Rekonstruktion von Zerfallsvertices und einen "Ring Imaging Cherenkov" Detektor (RICH) zur Teilchenidentifikation und eignet sich daher ausgezeichnet zur Rekonstruktion von B Meson Zerfällen. Zur Analyse wurden die 1991 bis 1994 beim DELPHI Experiment am LEP gesammelten Daten von hadronischen Z^0 Zerfällen verwendet.

Wegen der zu kleinen Statistik ist es jedoch bei LEP nicht möglich genügend exklusive B Zerfälle zu rekonstruieren um CP Verletzung zu messen. Daher wurde im zweiten Teil dieser Arbeit untersucht, ob eine solche Messung am geplanten Large Hadron Collider (LHC) möglich ist. Der LHC bietet durch die enorme Anzahl an erzeugten $b\bar{b}$ Ereignissen die Möglichkeit auch B Zerfallskanäle mit kleiner Zerfallswahrscheinlichkeit mit hoher Statistik zu untersuchen. Daher scheint er für die Messung von CP Verletzungseffekten im $B_d^0 - \bar{B}_d^0$ System geeignet zu sein. Bisher wurde CP Verletzung nur im System neutraler Kaonen gefunden, eine zufriedenstellende Erklärung dieses Phänomens konnte bis heute nicht gegeben werden. Im System neutraler B Mesonen wird jedoch ein starker CP Verletzungseffekt erwartet. Am vielversprechendsten scheint dabei der Zerfall $B_d^0 \rightarrow J/\psi K_S^0$ zu sein, der durch seine deutliche Signatur auch bei Hadron Collidern gefunden und rekonstruiert werden kann. Am Beispiel des CMS Detektors wurde die Möglichkeit solche Zerfälle zu rekonstruieren studiert. Mit Hilfe von Monte Carlo Simulationen wurde die Messung von CP Verletzung im Zerfallskanal $B_d^0 \rightarrow J/\psi K_S^0$ im Detail untersucht und der zu erwartende Fehler auf die Messung berechnet.

Preface

Since the discovery of the beauty quark in 1977, the physics of particles containing beauty quarks has played a dominant role in high energy physics research. Studying the properties of B decays can help to determine some of the fundamental parameters of the Standard Model and offers the possibility to better understand the mechanism of weak decays of the b quark. Particles containing a b quark have a lifetime of the order of 1 ps and if produced at high enough energies they will fly several millimeters before decaying. That makes it possible to identify B hadrons by reconstructing their separated decay vertices. Decays of B particles into charmonium states are of special interest for exclusive reconstructions. Charmonium states can be easily identified through their decay into lepton pairs and reconstructed with good efficiency and relatively low background. The decay channel of the neutral B meson into $J/\psi K_S^0$ is of particular interest for the search for CP violation in the B system.

The importance of CP violation in physics is in no doubt. Within the Standard Model, there is only one CP-violating parameter: the phase of the CKM matrix. This is an important parameter and, as such, has the importance within the model of the mass of the Z^0 or that of the top quark. Although CP violation has been observed in the neutral kaon system, strong-interaction uncertainties render the measurements rather inadequate as a means of determining the phase. Therefore, the CKM phase remains one of the poorest-determined parameters of the Standard Model. The system of neutral B mesons seems to be an excellent environment to measure CP violation and specially the decay $B_d^0 \rightarrow J/\psi K_S^0$ is a good candidate.

The Large Electron Positron collider, LEP, at the European Laboratory for High Energy Physics, CERN, is an excellent machine for the study of beauty hadrons, since a substantial fraction of all Z^0 decay modes consist of decays into beauty quarks. In order to reconstruct these B decays a detector with a vertex detector, which permits a high track extrapolation resolution to the collision point is required. Furthermore hadron identification and a good lepton reconstruction efficiency is needed.

The DELPHI experiment is performed by a large international collaboration. One of its members is the Institute for High Energy Physics of the Austrian Academy of Sciences. I had the privilege to join the institute and to work at CERN for the DELPHI experiment. As a member of the Austrian group I was involved in the maintenance

and operation of the Forward Chamber A, where I worked mainly on online-monitoring and calibration.

The following analysis on reconstruction of exclusive B meson decays is based on data recorded at the DELPHI experiment. The DELPHI detector is well suited for studying fully reconstructed B decays, since the vertex detector provides a high track extrapolation resolution and the Ring Imaging Cherenkov detectors enable particle identification over a wide momentum range. Since decays of the type $B \rightarrow J/\psi X$ have small branching ratios the main limitation in the search for fully reconstructed B events at LEP is statistics, and even under the most optimistic circumstances a measurement of CP violation in the neutral B system is not possible. Therefore I was studying the possibilities of future experiments in the search for CP violation, with special emphasis on the planned experiments at the LHC.

Since the early design phase I was involved in the CMS collaboration, where I was working in the physics group and performed a study on CP violation measurements at the LHC. This led to a couple of publications and conference reports and showed that even with a general purpose detector like CMS it will be possible to measure CP violation in the B system with very high precision.

My thesis is summarizing the analyses I performed at DELPHI and CMS.

Acknowledgements

Many people have been of great, even essential, help in the production of this thesis. I would like to thank all members of the DELPHI Collaboration. It has been a privilege to work with the team. In addition, there are a few individuals I would like to mention.

My advisor, *Univ. Doz. Dr. Manfred Markytan*, has been a source of encouragement and experience. I greatly appreciate the independence he allowed me and the support he provided.

I am very grateful to *Univ. Prof. Dr. W. Majerotto*, director of the Institute for High Energy Physics in Vienna for his constant support and for providing me a position at the institute.

Furthermore I have to thank *Dr. Gerhard Leder*, the group leader of the DELPHI project at the institute, for his kind support. I am indebted to many colleagues from the Institute of High Energy Physics for many discussions, help and explanations. I consider it a privilege to have worked with so many gifted people.

Very important for my work was the interest and the encouragement by *Daniel Denegri*. He provided me with many good ideas and taught me much of what I now know of B physics. In addition I enjoyed the help of a large number of colleagues from the CMS physics group, who supported this work by their direct help and their constructive criticism.

Last, but not least, I want to thank my friends who let me enjoy the life outside CERN. They have been the source of all my hope.

Chapter 1

Introduction

*Before I came here I was confused about this subject.
Having listened to your lecture, I am still confused,
but on a higher level.*

— ENRICO FERMI, 1938 Nobel Laureate in physics

Over the past several decades, tremendous theoretical and experimental advances have been made in elementary particle physics. A renormalizable quantum field theory of strong and electroweak interactions based on an underlying local $SU(3) \otimes SU(2) \otimes U(1)$ gauge invariance has emerged. It beautifully describes all known particles and their observed interaction properties while incorporating the proven symmetries and successes of the quark model, quantum electrodynamics, and the old four-fermion vector-axial vector theory. It even correctly predicted weak neutral currents, as well as the existence and properties of gluons, W^\pm and Z^0 bosons and the top quark. Those impressive successes have earned this theory its title as the Standard Model. It is supported by a large number of fundamental experiments in the past decades, and at the present time there are no solid experimental results that cannot be accounted for by the Standard Model.

According to the Standard Model quarks and leptons interact by exchanging gauge bosons. Eight massless gluons couple to the colour charge of quarks and mediate strong interactions, while the W^\pm , Z^0 and γ are responsible for weak and electromagnetic interactions.

One crucial event on the way towards understanding the interactions of matter was the discovery of the intermediate vector bosons W^\pm and Z^0 in 1983 at the European Laboratory for High Energy Physics, CERN, by the UA1 and UA2 collaborations [1–4] at the Sp \bar{p} S collider. This was the pinnacle achievement toward the establishment of the Standard Model as it confirmed the existence of heavy gauge bosons at their

predicted mass values.

In order to investigate the properties of the electroweak gauge bosons Z^0 and W^\pm the Large Electron Positron collider (LEP) at CERN has been built. In the years 1989 - 1995 the collider provided high energy e^+e^- collisions with a center-of-mass energy of about 91 GeV, corresponding to the mass of the Z^0 boson. Approximately 17 million hadronic Z^0 decays have been produced during that time. Four experiments - ALEPH, DELPHI, L3 and OPAL - collected the data.

The LEP collider has provided an unbiased almost background-free environment for the production of the Z^0 boson. The Z^0 is unique in its coupling to all known elementary fermions, and therefore LEP as a Z^0 factory is a rich source of a wide variety of particles. The Z^0 has been extensively studied and very high accuracy has been reached in the measurements of the electroweak parameters. Experimental data have been found to be in excellent agreement with its predictions and these results highly constrain possible extensions of the Standard Model. Up to now no evidence for physics beyond the present theory has been discovered and the Standard Model has proven to be very successful.

In a second stage of LEP starting in 1996 the collider is upgraded to an energy twice the W^\pm mass, in order to produce W^\pm pairs. In this way the charged electroweak gauge bosons can be investigated. This second stage of LEP is called LEP200.

In 1993 the CDF [5,6] collaboration at FNAL has reported experimental evidence for the top quark, one of the last undiscovered particles in the Standard Model. The mass of the top quark was measured to be $m_t = 174 \pm 16 \text{ GeV}/c^2$ and the measurement provided even further support for the Standard Model.

However, in spite of all the success of the Standard Model, the opinion among many physicists is that, because it still leaves many questions unanswered and leads to some contradictions when its predictions are extrapolated to higher energies, it is probably far from being an ultimate theory of nature.

There are two aspects of the Standard Model which have not yet been confirmed. The origin of CP violation, which is connected to the number of fundamental families of fermions, and the understanding of the spontaneous symmetry breaking mechanism remain the main experimental goals for the next decade.

In the Standard Model the mechanism of spontaneous symmetry breaking is linked to the existence of a scalar field, the Higgs boson H^0 which becomes responsible for the generation of masses via the Higgs mechanism. Its interaction with particles generates the masses dynamically. It is possible that the Higgs sector is more complicated than in its minimal version. Various extensions of the Standard Model allow for more than one Higgs boson, but suffer from the same lack of experimental evidence.

Experimentally, there has been no direct evidence for the existence of the Higgs boson. At present the four LEP experiments have ruled out the existence of a Higgs boson up to a mass of $m_{H^0} \geq 63.9 \text{ GeV}/c^2$. The value of the Higgs mass is not predicted by the Standard Model. On the other hand the Higgs cannot be too heavy, otherwise

the perturbative regime breaks down, and this leads to an upper bound of the Higgs mass at about 1 TeV [7]. It is clear that a complete success of the Standard Model can only be achieved if the Higgs mechanism is demonstrated experimentally by a direct discovery of the Higgs boson.

Therefore it is planned to install the Large Hadron Collider (LHC) in the existing LEP tunnel. This new machine will provide proton-proton collisions at a center-of-mass energy of 14 TeV with a design luminosity of $10^{34} \text{ cm}^{-2}\text{s}^{-1}$ and should start in 2005. The energy spectrum of the proton constituents makes these high energy proton-proton collisions an ideal tool to explore a new energy domain and to look for new phenomena. Two general purpose detectors, ATLAS and CMS, are planned to search for the Higgs boson and look for new physics beyond the Standard Model.

1.1 Beauty Quark Physics

The beauty quark was introduced in 1973, as the 5th quark in a 6 quark model, by Kobayashi and Maskawa in order to describe the observed CP violation in the decay of neutral K mesons. Experimentally it was first observed in 1977 by the Columbia-Fermilab-Stony Brook collaboration (CFS) at Fermilab in proton collisions with a beryllium target [8]. They observed a narrow resonance in the invariant mass spectrum of muon pairs at $9.46 \text{ GeV}/c^2$ in the reaction $p + \text{Be} \rightarrow \mu^+\mu^- + X$. This resonance was interpreted as the $1S$ state of the $b\bar{b}$ bound system and was named Υ . More data and an improved mass resolution led to the discovery of a second resonance at about $10 \text{ GeV}/c^2$, the $\Upsilon(2S)$, and possibly a third one, the $\Upsilon(3S)$ at about $10.4 \text{ GeV}/c^2$. In order to confirm the discovery of the Υ resonances, the e^+e^- storage ring DORIS at DESY was upgraded in energy to reach the Υ region. In the spring of 1978 the PLUTO [9] and DASP [10] collaborations at DESY confirmed the existence of the Υ resonance and somewhat later also the $\Upsilon(2S)$ was confirmed. Early in 1980 the full set of three resonances was confirmed by the CLEO [11] and CUSB [12] collaborations at the Cornell Electron Storage Ring (CESR).

The resonances $\Upsilon(1S)$, $\Upsilon(2S)$ and $\Upsilon(3S)$ provided a determination of the electric charge of the b quark. The assignment of other quantum numbers, like the weak isospin and the hypercharge, required the production of B mesons, which are bound state of a b quark and a \bar{u} , \bar{d} , \bar{s} or \bar{c} quark with spin parity $J^P = 0^-$, and their subsequent decays.

In a number of models it has been estimated that the $\Upsilon(4S)$ should lie above the $B\bar{B}$ threshold. In contrast to the other three Υ resonances the $\Upsilon(4S)$ should be a broad resonance with significantly different final-state topologies. Indeed, the $\Upsilon(4S)$ was found by the CLEO and CUSB collaborations in 1980 and since then the major features of the b quark have been studied extensively at e^+e^- colliders running at the $\Upsilon(4S)$ [13]. As the mass of the $\Upsilon(4S)$ is $10.580 \text{ GeV}/c^2$, only B^0 and B^\pm mesons are

produced. A pair of B mesons has a combined mass of $10.557 \text{ GeV}/c^2$, so the B mesons are produced practically at rest with no other additional particles. At the $\Upsilon(4S)$ one finds a large cross-section for $b\bar{b}$ production, $\sigma_{b\bar{b}} \sim 1.1 \text{ nb}$, sitting on a continuum background of 3.3 nb . The signal-to-background ratio is therefore $1 : 3$.

Today e^+e^- colliders running at the $\Upsilon(4S)$ are still providing a lot of information about B meson production and their decays, but beauty quark physics has become an important topic for many machines and experiments [13].

Also e^+e^- colliders operating at higher energies, in the continuum region, like PEP, PETRA and TRISTAN, are used to study B-physics. The drawback of e^+e^- machines working in the continuum is the much smaller hadronic cross-section, which falls as $1/s$, and results in a smaller amount of produced b quarks. At PEP ($\sqrt{s} = 29 \text{ GeV}$) the $b\bar{b}$ cross-section is 35 pb and at TRISTAN ($\sqrt{s} = 55.2 \text{ GeV}$) only 13 pb . The signal-to-noise ratio in hadronic events is only of the order of $1:10$. Due to the higher energy the produced b quarks hadronize separately and all kinds of B hadron species can be produced. About 75% of the B hadrons produced are B_d^0 and B^\pm mesons, 15% B_s^0 mesons and about 10% B baryons. The big advantage of continuum machines compared to e^+e^- colliders running at the $\Upsilon(4S)$ is the boost received by the B hadrons, which allows a better separation of the decay vertices. Already at 29 GeV , the B hadrons decay after a flight distance of about 1 mm . Therefore the B hadron lifetime which could not be measured at $\Upsilon(4S)$ machines, was first measured at PEP and PETRA.

The LEP collider, operating at the center-of-mass energy of the Z^0 mass, allows to study the electroweak properties of the b quark with high precision [14]. Due to resonant production at the Z^0 pole a much higher event rate is obtained than at continuum machines. As the Z^0 boson couples to all fermions, the LEP collider provides a rich source of a wide variety of particles. About 15% of all produced Z^0 bosons decay into $b\bar{b}$ pairs. The full spectrum of B hadrons, including B_s^0 mesons and B baryons, are produced. The cross-section for b quark production is about $\sigma_{b\bar{b}} = 7 \text{ nb}$. The high boost at LEP leads to a decay length of B hadrons of about 2.7 mm compared to $27 \mu\text{m}$ at $\Upsilon(4S)$ machines. This permitted the first measurement of time-dependent $B_d^0-\bar{B}_d^0$ mixing. The large number of produced B hadrons allows also to study B decay modes with low branching ratios.

Hadron colliders are a copious source of B hadrons, because of the large $b\bar{b}$ cross-section and the high luminosity. The main disadvantage is that the signal-to-background ratio is very small which makes event reconstruction and triggering difficult. The pioneering exploration of B-physics in a hadron collider environment was performed by the UA1 experiment at the CERN Sp \bar{p} S collider. They were the first to observe $B_d^0-\bar{B}_d^0$ [15] and found first evidence for a B baryon, the Λ_b [16]. Since σ_{tot} is several orders of magnitude higher than $\sigma_{b\bar{b}}$, special triggers are needed to extract the interesting events. In order to identify B events either high transverse momentum leptons from semileptonic B hadron decays or the decays of J/ψ mesons into two leptons are

used. The CDF experiment at the Tevatron ($\sqrt{s} = 1.8$ TeV) demonstrated that silicon vertex detectors mounted close to the interaction region can not only be used in e^+e^- experiments but also in a high luminosity hadron collider environment. Recently they showed an impressive large number of fully reconstructed B decays including the decay of a J/ψ .

1.2 Exclusive B Hadron Decays

Since the discovery of the beauty quark, B-physics has played a dominant role in high energy research. A real breakthrough in this field occurred through the successful introduction of silicon vertex detectors which provide very high spatial resolution. These detectors make it possible to select B hadrons with high purity and to reconstruct their decay vertices with high precision.

In order to study B decay modes with low branching ratios a large number of produced B hadrons is needed. Since a substantial fraction of all Z^0 decay modes consists of decays into bottom quarks ($\sim 15\%$), the LEP collider provides a large number of produced B hadrons and allows precision measurements in the heavy quark sector. Ever since the existence of heavy quarks was established, there has been a considerable interest in the study of heavy quarkonia ($c\bar{c}$ and $b\bar{b}$ mesons) because the leptonic decay channels of these resonances provide the cleanest signals of heavy quarks. At LEP, the primary source of J/ψ mesons is the decay of beauty hadrons. Hence, the reconstruction of J/ψ mesons provides a clean tag for b hadrons.

The first fully reconstructed B mesons were reported in 1983 by the CLEO I collaboration [17]. The exclusive reconstruction of B decays gives the possibility to better understand the mechanism of weak decays of the b quark. Of particular interest is the study of the contribution of non-spectator processes.

The DELPHI detector at LEP, with a silicon vertex detector and a Ring Imaging Cherenkov detector for particle identification, makes it possible to reconstruct exclusive B decays. The presented analysis is performed using approximately 3.2 million multi-hadronic Z^0 events recorded by the DELPHI detector in the years 1991–1994.

1.3 CP Violation

Understanding the CP violation mechanism is one of the most important issues in particle physics. It is needed in cosmology to generate the observed matter-antimatter asymmetry in the universe (Sakharov 1967). In the Standard Model CP violation has its origin through the mass generation mechanism, therefore it could allow to explore this mechanism. Its comprehensive study allows one to test the consistency of the Standard Model and possibly explore physics beyond it.

CP violation is one of the least understood aspects of the Standard Model. The discovery of CP violation in the neutral kaon system was a remarkable breakthrough in elementary particle physics. Despite its fundamental importance, after more than 30 years from its discovery, CP violation appears to be a phenomenon not well understood from the theoretical point of view and not well documented experimentally. Up to now it has only been observed in kaon systems. The observed flavour oscillation in the $B^0-\bar{B}^0$ system confirmed that mixing is not unique to the $K^0-\bar{K}^0$ system.

B-physics offers the possibility to study CP violation in a different context and therefore promises to provide a clue for a better understanding of this phenomenon. Indeed its observation in B decays would allow one to test the Standard Model picture of CP violation through the Cabibbo-Kobayashi-Maskawa matrix mechanism of the weak mixing and maybe to discover new physics beyond the Standard Model. Particularly promising are CP asymmetries in neutral B meson decays into CP eigenstates which are subject to clean theoretical interpretation and seem to be experimentally most accessible.

One of the most promising channels to study CP violation is the decay $B_d^0 \rightarrow J/\psi K_S^0$, because it has a clean signature and a reasonably low background. Through the leptonic decay of the J/ψ , this channel makes the study of CP violation also possible at hadron colliders.

High energy hadron colliders, such as the planned LHC, are particularly suitable to perform these investigations, because of the copious production of B hadrons that is expected.

1.4 Outline

The thesis is structured in 8 chapters. After this introduction chapter 2 summarizes the theoretical inputs that motivated the measurements described in this thesis. The basic ideas of the Standard Model are described and the framework for precision measurements at the Large Electron Positron collider (LEP) is explained. It contains a description of the relevant heavy flavour phenomenology and a summary of the different decay models of B mesons.

In chapter 3 the phenomenon of CP violation is discussed. Starting from the discussion of the CKM matrix, $B^0-\bar{B}^0$ mixing and CP violation is described. Emphasis is given to the phenomenological description of CP violation in the B system and how it can be measured.

Chapter 4 contains a description of the LEP collider and the DELPHI detector, with which the data for this thesis was collected. DELPHI has a number of detector components, which can be classified according to their functions in detectors for charged particle reconstruction, particle energy reconstruction and particle identification. After a description of the geometrical setup of the detector the most important detector

components and their performance are presented. Special emphasis is given to the sub-detectors used in the analysis.

Chapter 5 describes in detail the analysis I have performed. Starting with a description of the J/ψ selection in hadronic Z^0 events the measurement of the inclusive branching fractions $Z^0 \rightarrow J/\psi + X$ and $b \rightarrow J/\psi + X$ is presented. The measurement of the total J/ψ production is followed by a search for exclusive B meson decays into charmonium states. Finally, the obtained results are discussed. The data used in this analysis was obtained during the running periods 1991 to 1994 of the DELPHI detector.

Chapter 6 gives an outlook to future measurements of CP violation in the B system. The different existing and proposed experiments at e^+e^- and hadron colliders are described and the capabilities in measuring CP violation are discussed.

In chapter 7 a study in order to investigate whether a CP violation measurement with a general purpose detector at the LHC will be possible is presented. First the different production mechanisms of $b\bar{b}$ events in proton-proton collisions are discussed and a short overview of the assumed detector configuration is given. This is followed by a description of the detector simulation and a detailed discussion of the simulation of the decay channel $B_d^0 \rightarrow J/\psi K_S^0$. The performed time-integrated decay-asymmetry measurement based on Monte Carlo events is presented and the expected error on the measurement of the angle β of the unitarity triangle is calculated.

Finally, chapter 8 summarizes all results obtained in this thesis and discusses their implications and prospects.

Chapter 2

Theory

There is a theory which states that if ever anyone discovers exactly what the universe is for and why it is here, it will instantly disappear and be replaced by something even more bizarre and inexplicable. There is another which states that this has already happened.

— DOUGLAS ADAMS, The Restaurant at the End of the Universe

The annihilation of an e^+e^- pair into a Z^0 and its subsequent decay into fermion pairs can be precisely calculated within the Standard Model. A substantial fraction of Z^0 decays into a pair of $b\bar{b}$ quarks. The produced b quarks then hadronize and build up B hadrons. Hadrons containing a b quark have only a limited lifetime and will decay after a short time. In this chapter a short overview of the Standard Model and e^+e^- physics at LEP, with special emphasis on B-physics, is presented. After a brief discussion of B hadron production, various decay modes and some phenomenological approaches to describe these B hadron decays are discussed.

2.1 The Standard Model

The Standard Model of particle physics is the most successful achievement of modern day particle physics. It is a gauge theory which describes the unification of the electromagnetic, the weak and the strong forces and incorporates the electroweak theory postulated by Glashow, Weinberg and Salam [18–21] and the theory of Quantum Chromodynamics (QCD) [22–26].

The Standard Model is based on the principle of local gauge symmetry under the gauge group

$$G_{\text{SM}} = \text{SU}(3)_{\text{colour}} \otimes \text{SU}(2)_L \otimes \text{U}(1)_Y \quad (2.1)$$

and on spontaneous breakdown of the $SU(2)_L \otimes U(1)_Y$ symmetry to the $U(1)_Q$ symmetry of QED via the Higgs mechanism.

It integrates in a single framework the spectrum of all known particles and their observed interactions and is able to explain a remarkable variety of observed phenomena. It has survived a recent set of precision tests at the Large Electron Positron collider (LEP) and at the Stanford Linear Collider (SLAC), and to date no experimental phenomena have been observed which are inconsistent with the Standard Model. The Higgs boson, required to exist by the Standard Model, has not yet been observed but neither it has been ruled out at all masses.

Matter is known to be composed of two classes of spin- $\frac{1}{2}$ particles: *leptons* and *quarks*. The distinction between these classes of particles is that while quarks carry colour charge and feel the strong force, leptons do not. In the Standard Model, particles are grouped according to their weak isospin properties in left handed doublets and right handed singlets:

$$\begin{aligned} \text{Leptons :} & \quad \begin{pmatrix} \nu_e \\ e \end{pmatrix}_L, \begin{pmatrix} \nu_\mu \\ \mu \end{pmatrix}_L, \begin{pmatrix} \nu_\tau \\ \tau \end{pmatrix}_L ; e_R, \mu_R, \tau_R \\ \text{Quarks :} & \quad \begin{pmatrix} u \\ d \end{pmatrix}_L, \begin{pmatrix} c \\ s \end{pmatrix}_L, \begin{pmatrix} t \\ b \end{pmatrix}_L ; u_R, d_R, c_R, s_R, b_R, t_R \end{aligned}$$

As far as we can tell, quarks and leptons are fundamental point particles with no substructure. Experiments are consistent with massless neutrinos as required by the *Minimal Standard Model* (i.e. with no right-handed neutrinos and only one Higgs doublet).

The fundamental fermions are organized into three generations (or *families*) of leptons and quarks, where the quantum numbers of the leptons and quarks are identical from one generation to the next, with only the mass differing.

Some of the properties of quarks are listed in table 2.1. Quarks have never been observed as isolated objects and are apparently always confined within hadrons, so the masses of the quarks are not precisely known. While it is conventional to refer to quarks

<i>Name</i>	<i>Abbreviation</i>	<i>Electric charge</i>	<i>Mass</i>
down	d	$-1/3 e$	$9.9 \pm 1.1 \text{ MeV}/c^2$
up	u	$+2/3 e$	$5.6 \pm 1.1 \text{ MeV}/c^2$
strange	s	$-1/3 e$	$199 \pm 33 \text{ MeV}/c^2$
charm	c	$+2/3 e$	$1.35 \pm 0.05 \text{ GeV}/c^2$
bottom	b	$-1/3 e$	$\sim 4.5 \text{ GeV}/c^2$
top	t	$+2/3 e$	$180 \pm 12 \text{ GeV}/c^2$

Table 2.1: *The properties of quarks [27].*

only by their type, or *flavour*, each quark listed in table 2.1 actually represents three different quarks which are identical except that each has a different colour quantum number (red, green, blue). Likewise, antiquarks have one of 3 anticolours, and gluons one of the 8 colour-octet combinations of a colour and an anticolour.

As far as we know, there are two ways of forming colour-neutral hadrons from quarks. *Mesons* are made of a quark and an antiquark of the same colour, while *baryons* are a colour-singlet combination of 3 quarks, each of which has a different colour.

The forces between fermions are mediated by spin-1 particles, the *gauge bosons*. The massless photon, γ , is associated with the electromagnetic force. The weak force has as its mediators three massive intermediate vector bosons W^\pm and Z^0 , and the strong force is mediated by eight massless vector particles called gluons, g .

In addition there is a spin-0 particle, the Higgs boson, H^0 , which is needed to give mass to the W^\pm and Z^0 bosons and to the fermions due to its coupling to these particles.

2.1.1 The Electroweak Interaction

The theory of electroweak interactions introduced by Glashow [18], Weinberg [19] and Salam [20,21] in the 1960s is the product of successful unification of quantum electrodynamics (QED) with a theory of weak interactions. It has been experimentally verified with increasing precision since the discovery of the predicted W^\pm and Z^0 bosons [1,3,2,4]. In 1972 the renormalizability of the theory was shown by 't Hooft and Veltman [28].

The underlying symmetry of electroweak theory is $SU(2)_L \otimes U(1)_Y$. This symmetry group has four generators, the *weak isospin* I_1, I_2, I_3 , and the *weak hypercharge* Y . Local gauge symmetry invariance requires that each of these generalized charges is associated with a vector field. The non-abelian weak isospin group $SU(2)_L$ introduces three fields W_μ^i ($i = 1, 2, 3$) which can be associated with three massless vector bosons. These vector bosons couple with strength g to all left-handed fermions. The abelian group $U(1)_Y$ introduces one gauge field with an associated massless vector boson B_μ . This boson couples with strength g' to all particles with a weak hypercharge Y .

The left-handed components of weakly interacting particles are arranged in $I = \frac{1}{2}$ doublets, and the right-handed components of particles are singlet states of the weak isospin with $I = 0$.

In the electroweak theory quarks and leptons can be characterized by the quantum numbers I, I_3 , and Y , which determine the charge of the particle through the Gell-Mann-Nishijima relation

$$Q = I_3 + \frac{1}{2}Y \quad (2.2)$$

The values of the hypercharge are not predicted by the Standard Model but must be put in by hand in order to get the electric charges to come out correctly.

<i>Fundamental fermion families</i>			<i>Electroweak quantum numbers</i>			
1st	2nd	3rd	I	I_3	Y	Q
$\begin{pmatrix} \nu_e \\ e \end{pmatrix}_L$	$\begin{pmatrix} \nu_\mu \\ \mu \end{pmatrix}_L$	$\begin{pmatrix} \nu_\tau \\ \tau \end{pmatrix}_L$	$\frac{1}{2}$	$+\frac{1}{2}$ $-\frac{1}{2}$	-1 -1	0 -1
e_R	μ_R	τ_R	0	0	-2	-1
$\begin{pmatrix} u \\ d \end{pmatrix}_L$	$\begin{pmatrix} c \\ s \end{pmatrix}_L$	$\begin{pmatrix} t \\ b \end{pmatrix}_L$	$\frac{1}{2}$	$+\frac{1}{2}$ $-\frac{1}{2}$	$+\frac{1}{3}$ $+\frac{1}{3}$	$+\frac{2}{3}$ $-\frac{1}{3}$
u_R	c_R	t_R	0	0	$+\frac{4}{3}$	$+\frac{2}{3}$
d_R	s_R	b_R	0	0	$-\frac{2}{3}$	$-\frac{1}{3}$

Table 2.2: Electroweak SU(2) and U(1) quantum numbers of the fundamental left-handed (L) fermion doublets and the right-handed (R) singlets.

The four massless fields, introduced by the invariance under the gauge group $SU(2)_L \otimes U(1)_Y$, can be associated with “physical” fields through the following relations:

$$A_\mu = \sin \theta_W W_\mu^3 + \cos \theta_W B_\mu \quad (\gamma) \quad (2.3a)$$

$$Z_\mu = \cos \theta_W W_\mu^3 - \sin \theta_W B_\mu \quad (Z^0) \quad (2.3b)$$

$$W_\mu^\pm = \frac{1}{\sqrt{2}}(W_\mu^1 \mp iW_\mu^2) \quad (W^\pm) \quad (2.3c)$$

where θ_W is the weak mixing angle (*Weinberg angle*). It can be seen in the above relations, that the field A_μ represents the neutral photon field γ , the W_μ^\pm fields represent the charged W^\pm boson fields, and the field Z_μ represents the neutral Z^0 boson field.

All the above bosons, along with the Higgs boson and the leptons and quarks, are the fundamental constituents of the electroweak theory. The quantum number assignments in terms of electric charge (Q), the weak hypercharge (Y), the weak isospin (I) and its third component (I_3) are shown in table 2.2 and table 2.3.

The *Weinberg angle* is a free parameter in the theory and connects the weak and

<i>Bosons</i>	<i>Electroweak quantum numbers</i>			
	I	I_3	Y	Q
γ	0	0	0	0
W^+	+1	+1	0	+1
Z^0	+1	0	0	0
W^-	+1	-1	0	-1
H	$\frac{1}{2}$	$-\frac{1}{2}$	1	0

Table 2.3: *Electroweak quantum numbers of the Standard Model bosons.*

the electromagnetic coupling constants through

$$e = g \sin \theta_W = g' \cos \theta_W = \sqrt{g^2 + g'^2} \sin \theta_W \cos \theta_W \quad (2.4)$$

where g denotes the non-abelian SU(2) gauge coupling constant and g' the abelian U(1) coupling.

The interaction Lagrangian density of the electroweak theory can be written as

$$\mathcal{L}_I = -e A_\mu J_{\text{EM}}^\mu - \frac{g}{2\sqrt{2}} (W_\mu^+ J_+^\mu + W_\mu^- J_-^\mu) - \frac{g}{\cos \theta_W} Z_\mu J_{\text{NC}}^\mu \quad (2.5)$$

where the terms in order describe the coupling of the *electromagnetic current*, the weak *charged current* and the weak *neutral current* to the respective gauge fields. The currents are given by

$$J_{\text{EM}}^\mu = \bar{\psi}_f Q_f \gamma^\mu \psi_f \quad (2.6a)$$

$$J_\pm^\mu = \bar{\psi}_f \frac{1 - \gamma_5}{2} I_\pm \gamma^\mu \psi_f \quad (2.6b)$$

$$J_{\text{NC}}^\mu = \bar{\psi}_f \left[I_3 \frac{1 - \gamma_5}{2} - Q_f \sin^2 \theta_W \right] \gamma^\mu \psi_f \quad (2.6c)$$

where ψ_f are the fermion fields, $I_\pm = (I_1 \pm iI_2)$ and Q_f is the charge of the fermions. It can be seen that the W^\pm boson coupling is of pure $V-A$ (vector – axial-vector) nature, while the electromagnetic interaction mediated by the γ is of pure vector type. The weak neutral current is a combination of the third component of the weak isospin current and the electromagnetic current. It is a mixture of a vector and an axial-vector coupling.

For a comparison between theory and experiment three independent experimental input data are required. The most natural choice for Z^0 physics is given by the electromagnetic fine structure constant α , the Fermi constant G_F , and the mass of the Z^0 boson, which has meanwhile been measured with high accuracy.

2.1.2 The Higgs Mechanism

In the electroweak theory, as it is described in the previous section, the boson fields W_μ^i and B_μ and the fermion fields ψ_f correspond to massless particles. In order to give mass to these particles, the local gauge symmetry has to be *spontaneously broken* through a process known as the *Higgs mechanism* [29–31]. After spontaneous symmetry breaking $SU(2)_L \otimes U(1)_Y \rightarrow U(1)_Q$, leaving the electromagnetic gauge group $U(1)_Q$ unbroken, the W^\pm and Z^0 bosons and the fermions acquire masses while the photon remains massless.

The Higgs mechanism must not only generate the masses of all the elementary particles but also lead to a renormalizable theory. This is a theory in which the observables can be calculated to any order of perturbation theory in terms of a finite number of input parameters. This can be achieved by the introduction of a doublet of complex scalar fields with hypercharge $Y = 1$ and weak isospin $I = \frac{1}{2}$

$$\Phi = \sqrt{\frac{1}{2}} \begin{pmatrix} \phi_1 + i\phi_2 \\ \phi_3 + i\phi_4 \end{pmatrix} \quad (2.7)$$

which couples to the gauge fields. The self interaction of this Higgs field

$$V(\Phi) = \mu^2 |\Phi|^2 + \lambda |\Phi|^4 \quad (2.8)$$

is constructed in a way that for $\mu^2 < 0$ and $\lambda > 0$ it has a minimum at $\Phi \neq 0$. The ground state of the field Φ , its vacuum expectation value, can be expressed after a suitable choice of gauge as

$$\Phi_0 = \sqrt{\frac{1}{2}} \begin{pmatrix} 0 \\ v \end{pmatrix} \quad (2.9)$$

where $v = \sqrt{\frac{-\mu^2}{\lambda}}$. The potential $V(\Phi)$ is invariant under gauge transformation, but the symmetry is explicitly broken when the field is expanded along a particular minimum. Using the unitary gauge the Higgs doublet can then be written as

$$\Phi(x) = \sqrt{\frac{1}{2}} \begin{pmatrix} 0 \\ v + H(x) \end{pmatrix} \quad (2.10)$$

Of the four degrees of freedom in the Higgs field Φ , three seem to have disappeared through the proper choice of gauge (actually they have turned into additional longitudinal degrees of freedom for the massive vector bosons), and the fourth is that of a scalar particle, the Higgs, whose mass is given by $M_H^2 = -2\mu^2$. The Higgs mechanism not only generates the masses of the gauge bosons, but also makes a prediction for the ratio of the masses of the charged and neutral gauge bosons in terms of the weak

mixing angle. The masses of the fermions are generated by Yukawa couplings of the Higgs field to the fermions.

The Higgs field couples to the fermions, as well as to the bosons, with a strength that is proportional to their masses. The Higgs boson will therefore predominantly decay into the heaviest particle-antiparticle pair kinematically allowed, which at LEP is a $b\bar{b}$ pair. At higher energies the Higgs can also decay into $t\bar{t}$ or W^+W^- pairs.

Up to now the Higgs boson predicted by the Standard Model has not been observed. Its long-awaited discovery would put the Standard Model on even stronger footing.

2.1.3 Quantum Chromodynamics

The theory of strong interactions, Quantum Chromodynamics or QCD for short, describes the interaction between quarks and gluons. The concept of quarks was introduced independently by Gell-Mann [22], who also proposed the name, and Zweig [24] in 1964. The idea of *colour* was introduced soon thereafter [25] to account for the apparent breaking of the spin-statistics theorem by members of the $J^P = \frac{3}{2}^+$ baryon decuplet. For example the Δ^{++} is the ground state of a system of three u quarks and has a symmetric wavefunction, something clearly forbidden for fermions. An additional degree of freedom has been introduced, so that each quark flavour is assumed to come in three different colours.

The characteristics of the strong interaction are largely determined by the non-abelian nature of the underlying symmetry group $SU(3)_{\text{colour}}$. The mediators of the strong interaction, the 8 massless gluons, themselves carry a colour charge and thus interact strongly with each other. The theory has one free parameter, the dimensionless coupling constant α_s .

At high energies and short distances quarks behave essentially as if they were free and perturbative calculations can be done in this regime. This phenomenon is known as *asymptotic freedom*. An example of perturbative QCD is the gluon radiation in e^+e^- collisions. At large distances, as in the transition phase from coloured quarks and gluons to colourless hadrons, the interaction strength increases, and the perturbative approach fails.

The self-interactions among gluons create a colour screening effect which introduces a dependence of the coupling constant on the energy scale. The coupling constant $\alpha_s(Q^2)$ decreases, unlike the coupling constant in QED, with increasing momentum transfer Q^2 . This so-called running of the strong coupling constant α_s can be written in second-order perturbative QCD as:

$$\alpha_s(\mu^2) = \frac{12\pi}{(33 - 2N_f) \ln(\mu^2/\Lambda_{\overline{\text{MS}}}^2)} \left\{ 1 - 6 \frac{153 - 19N_f}{(33 - 2N_f)^2} \frac{\ln(\ln(\mu^2/\Lambda_{\overline{\text{MS}}}^2))}{\ln(\mu^2/\Lambda_{\overline{\text{MS}}}^2)} \right\} \quad (2.11)$$

where N_f is the number of quark flavours (five at LEP), μ is the “typical” energy of

the reaction at which the theory is renormalized and Λ is the QCD scale parameter. The coupling constant α_s and the QCD scale parameter Λ , however, are dependent on the renormalization scheme being used. The most popular scheme is the *modified-minimal-subtraction scheme* $\overline{\text{MS}}$ [32].

A recent measurement has found the strong coupling constant at $\mu^2 = M_Z^2$ to be [33]

$$\alpha_s(M_Z^2) = 0.123 \pm 0.006 \quad (2.12)$$

2.1.4 Parameters of the Standard Model

The Standard Model contains a number of free parameters whose values are not given by the theory but must be determined by experiments. Besides the strong coupling constant from QCD, the fermion masses, the Higgs mass and four CKM parameters (see section 3.2), the three basic parameters of the model are the two gauge group coupling constants g and g' and the vacuum expectation value of the Higgs field v (introduced in equation 2.9). However, none of these can be measured directly by experimental techniques and they are therefore usually replaced by observable quantities that can be measured most accurately. The specific choice of input parameters defines the renormalization scheme. A natural choice for the electroweak parameters is to use the *on-shell renormalization scheme* [34], which replaces the original parameters g , g' , λ , μ^2 and m_f by an equivalent set of more physical parameters: α , M_Z , M_W , M_H , m_f , where each of them can (in principle) directly be measured in a suitable experiment. They are related to the original parameters through

$$\alpha = \frac{1}{4\pi} \frac{g^2 g'^2}{g^2 + g'^2} = \frac{e^2}{4\pi} \quad (2.13a)$$

$$M_Z = \frac{1}{2} v \sqrt{g^2 + g'^2} \quad (2.13b)$$

$$M_W = \frac{1}{2} v g \quad (2.13c)$$

$$M_H = \sqrt{2\lambda} v = \sqrt{-2\mu^2} \quad (2.13d)$$

where g and g' represent the coupling constants and μ and λ are the coefficients of the Higgs potential (see equation 2.8). The parameters M_Z and M_W are defined at the pole position of their corresponding propagators. Instead of M_W , which is poorly known, one often uses the Fermi constant

$$\frac{G_F}{\sqrt{2}} = \frac{g^2}{8M_W^2} \quad (2.14)$$

which has been determined with high precision from the measurement of the muon lifetime. The fine structure constant α is defined at $q^2 = 0$ (Thomson limit). At higher

energies, such as $q^2 = M_Z^2$, the running nature of the coupling constant raises the value to $\alpha(M_Z^2) = 1/128$.

Since in the on-shell renormalization scheme there is no room for the mixing angle θ_W as a free parameter, one can use the simple definition proposed by Sirlin [35] to define $\sin \theta_W$ in terms of the physical W^\pm and Z^0 masses:

$$\sin^2 \theta_W = 1 - \frac{M_W^2}{M_Z^2} \quad (2.15)$$

This definition is independent of a specific physical process and valid to all orders of perturbation theory.

The Minimal Standard Model (MSM), assuming all neutrinos to be massless, can thus be specified by 18 parameters:

- the six quark masses: $m_u, m_d, m_c, m_s, m_t, m_b$
- the three lepton masses: m_e, m_μ, m_τ
- the Higgs mass: M_H
- three gauge couplings: G_F, α, α_s
- the weak mixing angle: $\sin^2 \theta_W$
- four parameters to describe the CKM matrix, e.g. $\theta_1, \theta_2, \theta_3, \delta$ (see section 3.2)

At lowest order, the W^\pm and Z^0 masses are predicted in the Standard Model as functions of the parameters, α, G_F and $\sin^2 \theta_W$:

$$M_{W^\pm}^2 = \frac{\pi\alpha}{\sqrt{2} G_F \sin^2 \theta_W} \quad (2.16)$$

$$M_{Z^0}^2 = \frac{M_W^2}{\cos^2 \theta_W} = \frac{\pi\alpha}{\sqrt{2} G_F \sin^2 \theta_W \cos^2 \theta_W} \quad (2.17)$$

where

- $\alpha = e^2/4\pi = 1/137.035989$ [27] is the fine structure constant measured in the low energy classical limit of Thomson scattering.
- $G_F = 1.16639 \times 10^{-5} \text{ GeV}^{-2}$ [27] is the Fermi coupling constant determined from precise measurement of the muon lifetime.
- $\sin^2 \theta_W = 0.2325 \pm 0.0016$ [36] is the electroweak mixing angle determined from the measurement of the forward-backward asymmetry at LEP.

At LEP I the obvious candidates for precise measurements are the Z^0 resonance parameters: the mass M_Z and the width Γ_Z . Table 2.4 shows the measured values of M_Z and Γ_Z , and the result of a fit to current electroweak data from LEP to m_t and $\alpha_s(M_Z^2)$.

Parameter	Central value and error
M_Z [GeV/ c^2]	91.1884 ± 0.0027
Γ_Z [GeV/ c^2]	2.4963 ± 0.0038
m_t [GeV/ c^2]	170 ± 10
$\alpha_s(M_Z^2)$	0.125 ± 0.004

Table 2.4: *Standard Model parameters: The values of M_Z and Γ_Z are from recent LEP measurements and the values of m_t and $\alpha_s(M_Z^2)$ are obtained by a fit to current electroweak data from LEP [36].*

2.2 Physics of e^+e^- annihilation

At LEP energies, the process which dominates e^+e^- collisions is the annihilation of the electron positron via a photon or a Z^0 into a fermion pair $f\bar{f}$. The fermion f may be a charged lepton e, μ, τ , a neutrino ν_e, ν_μ, ν_τ , or one of the five quark flavours u, d, s, c, b (the top quark is too heavy to be produced at LEP). Figure 2.1 shows the lowest order Feynman diagrams for the production of a fermion pair, through the exchange of a γ or a Z^0 . The annihilation through a Standard Model Higgs boson H^0 is negligible since the coupling to e^+e^- is $\sim \frac{m_e}{M_W}$. The very small electron mass also ensures helicity conservation at the e^+e^- vertex: only $e_L^-e_R^+$ and $e_R^-e_L^+$ contribute. Exchange terms

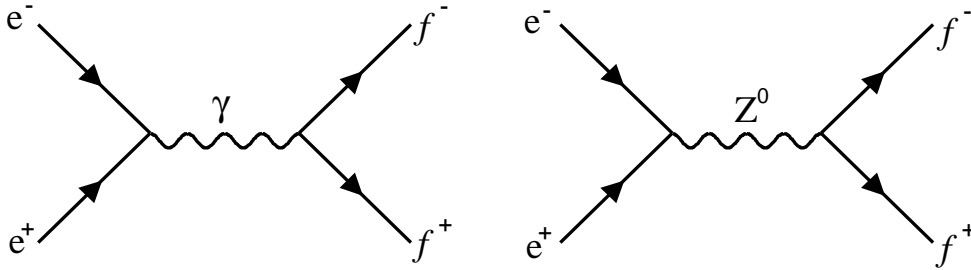


Figure 2.1: *Lowest order Feynman diagrams for electron positron annihilation into a fermion pair via a γ or Z^0 boson.*

in the t-channel can be important for $e^+e^- \rightarrow e^+e^-$ and two photon production, but are not considered here.

The differential cross-section is directly proportional to $|\mathcal{M}|^2$, where \mathcal{M} is the scattering amplitude, which for the process $e^+e^- \rightarrow f^+f^-$ becomes:

$$|\mathcal{M}|^2 = |\mathcal{M}_\gamma|^2 + |\mathcal{M}_{Z^0}|^2 + (\mathcal{M}_\gamma^* \mathcal{M}_{Z^0} + \mathcal{M}_\gamma \mathcal{M}_{Z^0}^*) \quad (2.18)$$

There are terms with pure Z^0 exchange, pure γ exchange, and Z^0 - γ interference.

At low energies, far below the Z^0 mass, taking only the photon exchange into account, the differential cross-section into a fermion-antifermion pair is:

$$\frac{d\sigma_\gamma}{d\Omega} = \frac{\alpha^2}{4s} \beta_f Q_f^2 [1 + \cos^2 \theta + \frac{4m_f^2}{s} \sin^2 \theta] \quad (2.19)$$

and integrating over the solid angle, the corresponding total cross-section becomes

$$\sigma_\gamma = \frac{4\pi\alpha^2}{3s} \beta_f \left(\frac{3 - \beta_f^2}{2} \right) Q_f^2 \quad (2.20)$$

which gives, if the fermion mass m_f is neglected, the *point cross-section* $\sigma_{\text{tot}} = \frac{4\pi\alpha^2}{3s} = \frac{86.8 \text{ nb}}{s [\text{GeV}^2]}$. θ is the polar angle between the outgoing fermion and the electron, α the fine structure constant, s the center-of-mass energy squared, Q_f the electric charge of the fermion, and β_f the velocity of the fermion defined as

$$\beta_f = \sqrt{1 - 4\mu_f} \quad \text{with} \quad \mu_f = \frac{m_f^2}{s} \quad (2.21)$$

Taking into account all terms in equation 2.18, the differential cross-section for $e^+e^- \rightarrow f\bar{f}$ in Born approximation can be written as:

$$\frac{d\sigma}{d\Omega} = \frac{\alpha^2}{4s} N_c^f \beta_f \{ G_1(s)(1 + \cos^2 \theta) + G_2(s)4\mu_f \sin^2 \theta + G_3(s)2\beta_f \cos \theta \} \quad (2.22)$$

where the functions G_i are given by

$$G_1(s) = Q_f^2 - 2v_e v_f Q_f \text{Re}(\chi_0(s)) + (v_e^2 + a_e^2)(v_f^2 + a_f^2 - 4\mu_f a_f^2) |\chi_0(s)|^2 \quad (2.23a)$$

$$G_2(s) = Q_f^2 - 2v_e v_f Q_f \text{Re}(\chi_0(s)) + (v_e^2 + a_e^2)v_f^2 |\chi_0(s)|^2 \quad (2.23b)$$

$$G_3(s) = -2a_e a_f Q_f \text{Re}(\chi_0(s)) + 4v_e a_e v_f a_f |\chi_0(s)|^2 \quad (2.23c)$$

and $\chi_0(s)$ is the Z^0 propagator in the lowest order Breit-Wigner approximation:

$$\chi_0(s) = \frac{s}{s - M_Z^2 + iM_Z \Gamma_Z^0} \quad (2.24)$$

with the total width of the Z^0

$$\Gamma_Z^0 = \sum_f \frac{\alpha M_Z}{3} N_c^f \beta_f (v_f^2(1 + 2\mu_f) + a_f^2(1 - 4\mu_f)) \quad (2.25)$$

The weak vector and axial-vector coupling constants v_f and a_f are defined as

$$v_f = \frac{I_3^f - 2Q_f \sin^2 \theta_W}{2 \sin \theta_W \cos \theta_W}, \quad a_f = \frac{I_3^f}{2 \sin \theta_W \cos \theta_W} \quad (2.26)$$

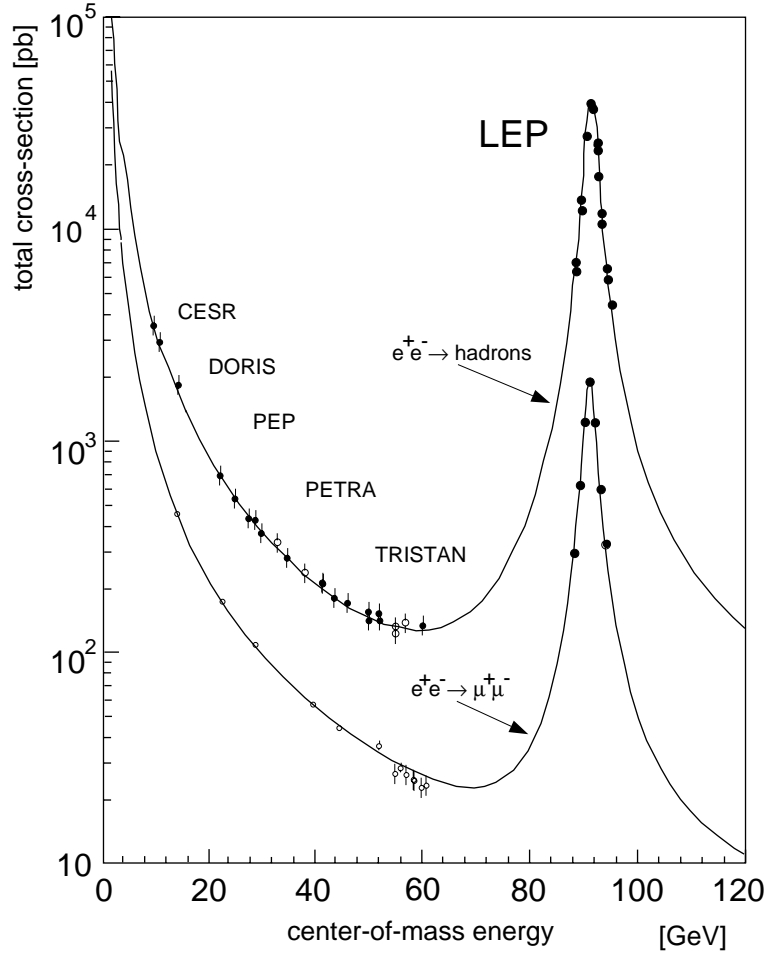


Figure 2.2: Total e^+e^- cross-section as a function of the center-of-mass energy.

In the above formulas I_3^f is the third component of the weak isospin and N_c^f is the colour factor: 3 for quarks and 1 for leptons.

Terms in (2.22) with $|\chi_0(s)|^2$ are due to Z^0 exchange, terms independent of $\chi_0(s)$ are due to γ exchange, and the ones with $\text{Re}(\chi_0(s))$ are due to Z^0 - γ interference. The cross-section at and near the peak is dominated by the Z^0 exchange. The Born approximation cross-section (2.22), when integrated over the solid angle near the Z^0 pole, has a Breit-Wigner form for spin-1 exchange:

$$\sigma(e^+e^- \rightarrow f\bar{f}) = \frac{12\pi}{M_Z^2} \frac{\Gamma_e \Gamma_f}{\Gamma_Z^2} \frac{s \Gamma_Z^2}{|s - M_Z^2 + i M_Z \Gamma_Z|^2} \quad (2.27)$$

where Γ_e , Γ_f are the partial decay widths of the Z^0 to the electron and fermion final-state respectively and s is the square of the center-of-mass energy. The contributions

of small terms due to photon exchange and Z^0 - γ interference are not included in equation 2.27. The Born approximation of the cross-section (2.22) is not adequate for the analysis at LEP. It is essential to include corrections due to *initial-state radiation* (ISR) and other higher order radiative effects [37]. The largest correction is due to initial-state radiation. It is $\sim 40\%$ on the Z^0 peak. The other corrections are small and calculable in the Standard Model.

Figure 2.2 shows the total e^+e^- cross-section as a function of the center-of-mass energy. The Z^0 branching fractions are approximately 3.4% into a pair of leptons, 6.6% into a pair of neutrinos, 12.5% into a pair of up quarks, and 15% into a pair of down quarks. At the top of the Z^0 resonance the visible cross-section is about 4000 times the *point cross-section*. This will be somewhat reduced by initial state radiation.

2.2.1 Quark-Pair Production at LEP

In the first step of the process $e^+e^- \rightarrow q\bar{q} \rightarrow \text{hadrons}$, an electron positron pair annihilates into a virtual photon or a Z^0 , followed by a decay into a quark antiquark final state. This is a purely electroweak process and the cross-section for this reaction has been calculated in the previous section. At LEP the process is dominated by the exchange of a Z^0 boson which decays into a quark antiquark pair with a probability of about 70%. The produced quarks and antiquarks are coloured objects and can radiate gluons, just as electric charges radiate photons. The radiation of gluons and quarks for large momentum transfer processes can be calculated with perturbative QCD.

Since only colourless hadrons are seen, a hadronization or fragmentation process must occur to convert the coloured quarks and gluons to hadrons. As the momentum transfer decreases during the evolution of a hadronic event, α_s increases until it becomes of order 1 and perturbative QCD fails. This is the regime of the binding of quarks and gluons into hadronic systems. It is characterized by an energy scale of about 1 GeV. Unfortunately, no calculational procedure exists for this low momentum transfer regime, so a common procedure is to use phenomenological models to describe the hadronization process.

Figure 2.3 shows the sequence of separate phases in the formation of a hadronic e^+e^- event:

- I) Production of a primary quark pair: This is a purely **electroweak** process, involving the exchange of a photon or a Z^0 . Real photons can be radiated both from the initial e^+e^- state and from the final $q\bar{q}$ state. These bremsstrahlung effects are covered by QED.
- II) Radiation of hard gluons and quarks: This phase is governed by **perturbative QCD** which means that it can be calculated numerically beyond lowest order α_s . Two approaches have been used for making predictions with perturbative QCD.

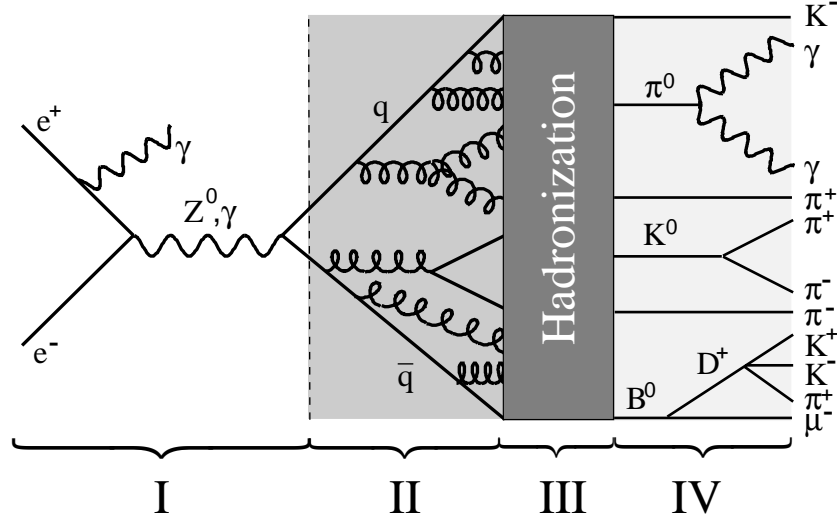


Figure 2.3: Schematic view of the evolution at a hadronic e^+e^- annihilation with some examples of possible final state particles.

In the *parton shower* (PS) model, the leading and next-to-leading logarithmic terms from all orders in the perturbation series are summed and used to propagate a shower of quarks and gluons down to some cutoff value in the virtual parton mass. At LEP energies, typically 10 final state partons are generated for a cutoff value of 1 GeV. An alternative approach is to compute the complete QCD matrix element. These so-called ME model calculations are available up to second order α_s , i.e. it can be used for final states with up to four partons.

III) Hadronization: This phase is **non-perturbative** which means it cannot be calculated with QCD, but must be described by various phenomenological models. These models can be grouped into three classes: independent fragmentation, string fragmentation, and cluster fragmentation (see section 2.2.2).

IV) The decay of unstable particles created in the fragmentation.

The result from this chain is the formation of two or more *jets* of hadrons. Experimental evidence for jets in e^+e^- collisions was found first by the SPEAR collaboration at SLAC [38] and their existence was confirmed at the DORIS collider, where due to the higher energy also gluon jets were found [39–42].

2.2.2 Heavy Quark Fragmentation

Since the fragmentation process is not exactly calculable, various models have been developed to provide a phenomenological description of this phase.

Historically, one of the first fragmentation models was the *independent fragmentation* model of Feynman and Field [43]. In this model the original quark and antiquark transform into a jet of hadrons, independently of each other. A quark gets an antiquark partner from the vacuum to produce a meson, leaving another quark which reproduces the process, with a definite rule for sharing the longitudinal momentum and choosing the quark flavour. This process repeats itself until the remaining quark has too little energy to form a meson.

Another, more physical model of fragmentation is *string fragmentation* [44]. In this model, the colour field between a quark and an antiquark is a massless colour flux tube, or string, that is uniform along its length. As the quark and antiquark separate, energy goes into the string and eventually it is energetically advantageous to break the string with the creation of quark antiquark pairs. These pairs terminate the flux line and thus break the string. The string will break a number of times until there is not enough energy to create new quark antiquark pairs, at which point the fragmentation of the system is complete and each quark antiquark pair forms a meson. The popular implementation of the model is the *Lund model*.

The probability, at each step in the fragmentation chain, that a fraction z of the energy and the longitudinal momentum of the quark goes into the formed hadron is given by the fragmentation function $f(z)$, where $z = (E + p_l)_{\text{hadron}} / (E + p_l)_{\text{quark}}$. An important feature of the Lund model is the requirement that, on average, the fragmentation starting from one end of the string is the same as the fragmentation starting from the other end of the string. This determines the form of the *Lund symmetric function*:

$$f(z) \propto \frac{(1-z)^a}{z} \exp\left(\frac{-bm_T^2}{z}\right) \quad (2.28)$$

The two parameters a and b have to be adjusted to the data.

Heavy quarks fragmentation is experimentally accessible by the transverse momentum spectrum of leptons in hadronic events. While the value of z cannot be measured directly, the resulting average energy taken by the hadrons, $\langle x_q \rangle$, can be determined for c and b quark events.

It has been found that heavy flavours need a harder fragmentation function than provided by the Lund symmetric function. The best known function has been given by Peterson *et al.*,

$$f(z) \propto \frac{1}{z(1 - \frac{1}{z} - \frac{\epsilon_q}{1-z})^2}, \quad (2.29)$$

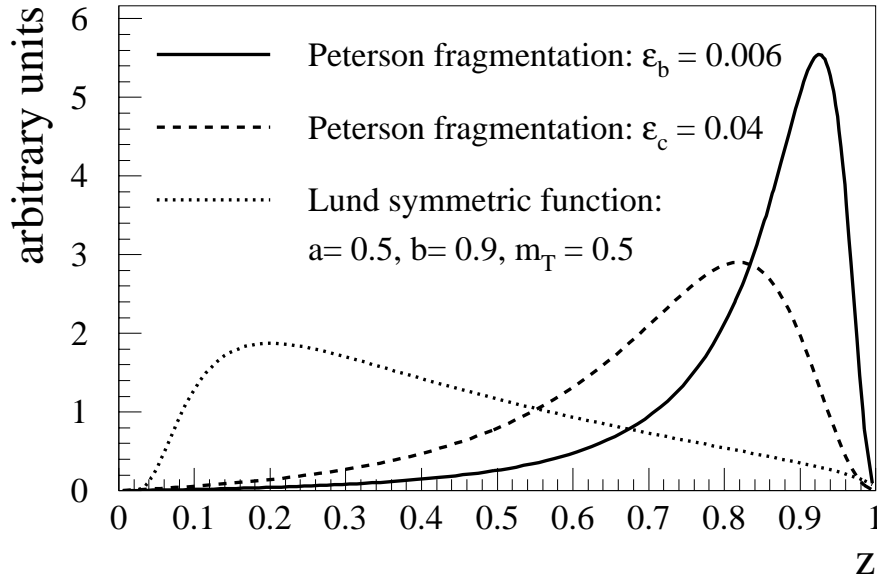


Figure 2.4: Peterson fragmentation function for b and c quark compared with the fragmentation function of a light quark.

where ε_q is a free parameter which has to be adjusted for c and b events separately and scales between flavours like $\varepsilon_q \propto 1/m_q$. Figure 2.4 shows the Peterson fragmentation function for b and c quarks, compared to the Lund symmetric function for light quarks.

Another approach is the *cluster fragmentation* model, in which a quark finds in the nearby phase space a neighbour with the proper colour to produce a hadron, which is then decaying according to phase space. The cluster fragmentation model has no fragmentation function.

In practise the models are incorporated in Monte Carlo programs. The Lund model is implemented in JETSET [45] and cluster fragmentation is used by HERWIG [46]. At LEP the most popular Monte Carlo program is JETSET, which successfully reproduces a wide class of experimental data, but has many free parameters which must be determined from the data. HERWIG tries to rely on a minimum of adjustable parameters, but cannot be used to describe heavy flavour fragmentation.

2.3 Beauty Quark Physics

The first experimental evidence for the existence of the b quark came in 1977 from an experiment at Fermilab [8], studying muon pair production in $p + \text{Be}$ reactions. A broad resonance at $\sim 9.5 \text{ GeV}/c^2$ in the invariant mass spectrum of the two muons

was observed, which was interpreted as the three lowest lying quark anti-quark bound states of a new quark flavour, the b quark. The $b\bar{b}$ bound states were called Υ , Υ' and Υ'' . Their discovery was confirmed at the e^+e^- colliders DORIS and CESR, where the three states could be resolved and at the latter also a fourth state, the $\Upsilon(4S)$, was discovered at 10.58 GeV/ c^2 . The total width of $\Upsilon(4S)$ is about 24 MeV, which is 3 orders of magnitude larger than the width of the 3 precedent Υ resonances, which lie below the $B\bar{B}$ threshold. Therefore the $\Upsilon(4S)$ decays only into $B\bar{B}$ pairs.

From the beginning of the 1980s the properties of the b quark have been studied intensively by the experiments CLEO, CUSB and ARGUS with electron positron colliders working at the $\Upsilon(4S)$, whose mass is above the production threshold of the lightest beauty mesons, B^\pm and B_d^0 . The B mesons are practically created at rest, permitting the measurement of the lifetime and spectroscopy.

LEP is an excellent machine for the study of beauty hadrons, since a substantial fraction of the Z^0 produced decays into $b\bar{b}$ pairs. Approximately 3×10^5 beauty hadrons are produced in a sample of 10^6 Z^0 decays. The big advantage of LEP compared to e^+e^- colliders running at the $\Upsilon(4S)$ resonance is that the B's are produced with a substantial boost. The average momentum of B hadrons at LEP is about 30 GeV/ c allowing them to fly several mm before decaying. B hadrons have a lifetime of the order of 1 ps and at LEP the average decay distance in space is $\langle d_B \rangle = 2.7$ mm. That makes it possible to identify B events by reconstructing their separated decay vertices.

Contrary to the experiments working at the $\Upsilon(4S)$ resonance at LEP all 4 possible B mesons can be produced:

$$B^+ = (\bar{b}u), B_d^0 = (\bar{b}d), B_s^0 = (\bar{b}s), \text{ and } B_c^+ = (\bar{b}c)$$

Only the B_c^\pm has not been observed yet. Each ground state meson is expected to have a vector state corresponding to the parallel spin alignment of its constituent quark spins. This vector partner of the pseudoscalar B is called B^* . The B mesons are produced either in their ground state or in excited states as B^* and B^{**} .

Moreover, baryons containing a b quark can be formed, such as the $\Lambda_b^0 = (udb)$, the $\Sigma_b^0 = (udb)$, the $\Sigma_b^- = (ddb)$ or the $\Xi_b^+ = (usb)$. Up to now only the lightest B baryon, the Λ_b^0 , has been observed [16], but at LEP there is now some evidence for the production of Ξ_b , Σ_b and Σ_b^* [47].

2.3.1 Beauty Hadron Production at LEP

The hadronic cross-section at the Z^0 pole is $\sigma_{\text{had}}^0 = 41.488 \pm 0.078$ nb [36], compared with a cross-section of 1.5 nb at the $\Upsilon(4S)$. In the Born approximation the partial Z^0 decay width to heavy quarks is:

$$\Gamma_{\text{Born}}(Z^0 \rightarrow q\bar{q}) = \Gamma_{\text{Born}}^V + \Gamma_{\text{Born}}^A = \frac{G_F M_Z^3}{8\sqrt{2}\pi} \left(v_q^2 \frac{3 - \beta_q^2}{2} \beta_q + a_q^2 \beta_q^3 \right) \quad (2.30)$$

where G_F is the Fermi coupling constant, $v_q = I_3 - 2Q_q \sin^2 \theta$ and $a_q = I_3$ are the electroweak vector and axial-vector couplings to a quark q , and β_q is the velocity of the quark (2.21). For beauty quarks (2.30) gives:

$$\Gamma_{\text{Born}}(Z^0 \rightarrow b\bar{b}) \approx 360 \text{ MeV} \implies Br(Z^0 \rightarrow b\bar{b}) \approx 15\%$$

For practical applications electroweak and QCD corrections have to be taken into account [14]. Of particular interest are electroweak vertex corrections, which involve the exchange of a virtual top quark. A recent LEP measurement of the ratio $\Gamma_{b\bar{b}}/\Gamma_{\text{had}}$ gives $R_b = \Gamma_{b\bar{b}}/\Gamma_{\text{had}} = 0.2219 \pm 0.0022$ [36].

The decay process $Z^0 \rightarrow b\bar{b}$ is completed after a time of the order of $m_{Z^0}^{-1} \sim 10^{-3} \text{ fm}$. The produced b quarks fragment into B hadrons, in about 90% by picking up an antiquark from the vacuum to form a primary B meson, and in about 10% by picking up a diquark to form a B baryon. The mean energy carried by the primary hadron in b -jets is found to be 70% of the b quark energy, more than in charm jets and much more than in light quark jets. The fractional momentum distribution can approximately be described by a Peterson fragmentation function (see section 2.2.2). About 30% of the B mesons formed are orbitally excited ($L = 1$) (generally called B^{**}) and 70% are in the ground state (without orbital angular momentum). All B^{**} states decay strongly into ground state B mesons. The latter are the pseudoscalar B meson and the vector meson B^* , which is just $46 \text{ MeV}/c^2$ heavier and can only decay via photon emission. The ratio of primary B^* to primary B mesons production is $3 : 1$, in accordance with the naive spin counting picture. About 12% of the B hadrons produced are B_s^0 mesons. Most of the B baryons created will finally decay into the weakly decaying Λ_b^0 .

The relative production ratio for B hadrons at the Z^0 peak is:

$$B^\pm : B_d^0 : B_s^0 : \Lambda_b^0 = 0.4 : 0.4 : 0.12 : 0.08$$

2.3.2 Beauty Hadron Decays

In order to decay, the b quark must undergo a flavour transition which can only happen in a weak decay, since the strong and electromagnetic interactions conserve quark flavours. The neutral weak current also conserves flavour, and it is only due to the charged weak current interaction that the b quark can decay. From this it follows that the decay of the b quark is unfavoured, which results in a long lifetime. However, the large mass of the b quark authorizes many decay channels and thus decreases its lifetime. The relatively long lifetime of the b quark has important phenomenological consequences as, for example, the possibility to measure B_d^0 - \bar{B}_d^0 mixing.

In a simple minded picture the decay of a B meson (ignoring the light quark) looks like a muon decay. Since the weak eigenstates are not flavour eigenstates one has to include the appropriate Cabibbo-Kobayashi-Maskawa (CKM) matrix element (see section 3.2) at the W^\pm vertex to convert between flavours. In addition there will be

form-factors that describe how to turn free quarks into hadrons, and the decay rates of B hadrons will also depend on the available phase space.

B hadron decays offer the most direct way to determine the elements V_{cb} and V_{ub} of the CKM matrix. Since b quarks don't exist as free states, the confinement due to QCD must be modelled to get access to these fundamental parameters. Actually several models exist describing the decay of heavy mesons. The study of B decays also helps to get a better understanding of non-perturbative QCD confinement.

2.3.3 Weak Decays of B Hadrons

The weak decay of a free particle by a charged weak current is well described by the muon decay. The width is proportional to the fifth power of the mass. In the decay of a hadron containing a b quark, the dominant process comes from the heavy quark. The light quark plays a passive role and is neglected in the *spectator model*. The b quark couples either to a c or an u quark by the charged weak current, which is mediated by a W^\pm . The off-shell W then decays either into a lepton-antineutrino pair or a quark-antiquark pair. The weak transition between the quarks are governed by the elements of the CKM matrix. As $V_{ub} \ll V_{cb}$ the $b \rightarrow c$ transition dominates. The simplest processes are those involving a minimum number of hadrons, i.e. a semileptonic decay with a single hadron in the final state, or a nonleptonic decay with two hadrons in the final state.

The weak decays of B mesons can be classified in four diagrams, shown in figure 2.5: **External spectator diagram:** This diagram is similar to the decay of a free quark. It is the dominant contribution to the partial width in most decay channels. The quarks created by the W hadronize separately.

Internal spectator diagram: This diagram is equivalent to the external spectator diagram, except that one of the quarks coming from the W^\pm is recombined with the spectator quark. When a B decays through an internal spectator diagram, the colour of the quarks from the virtual W^\pm must match those in the original B meson in order to produce a final state particle which is a colour singlet. This leads to a *colour suppression* of $1/N_c = 1/3$ due to the necessary adjustment in order to form a colour singlet. The suppression is not exactly $1/N_c$ as the exchange of soft gluons reduces the colour factor. To date, the only colour suppressed B meson decay modes that have been observed are final states which contain charmonium mesons e.g. $B \rightarrow \psi K$ and $B \rightarrow \psi K^*$.

Exchange diagram: It only contributes to neutral B mesons decays and is unfavoured by helicity conservation.

Annihilation diagram: This diagram only contributes to charged B mesons decays and is unfavoured by the CKM matrix elements and by helicity conservation.

All B meson decays that do not occur through the $b \rightarrow c$ transition are known as rare B decays. Since the contribution of the spectator diagram to rare B decays is

suppressed by V_{ub} , it is expected that additional diagrams will make a large contribution to some decay modes. The most significant of these diagrams is the so-called *penguin diagram* with a fermion-boson-loop, radiating either a photon or a gluon (see figure 2.6). The order of suppression of these channels is interesting for the observation of deviations from the Standard Model, which forbids flavour changing neutral currents (FCNC) at tree level. Penguin diagrams are much more significant in B decays than in D decays because the $b \rightarrow s$ loop contains the heavy top quark with large couplings V_{tb} and V_{ts} . In addition there are *box diagrams* responsible for the mixing of neutral B mesons, which will be discussed in section 3.4.

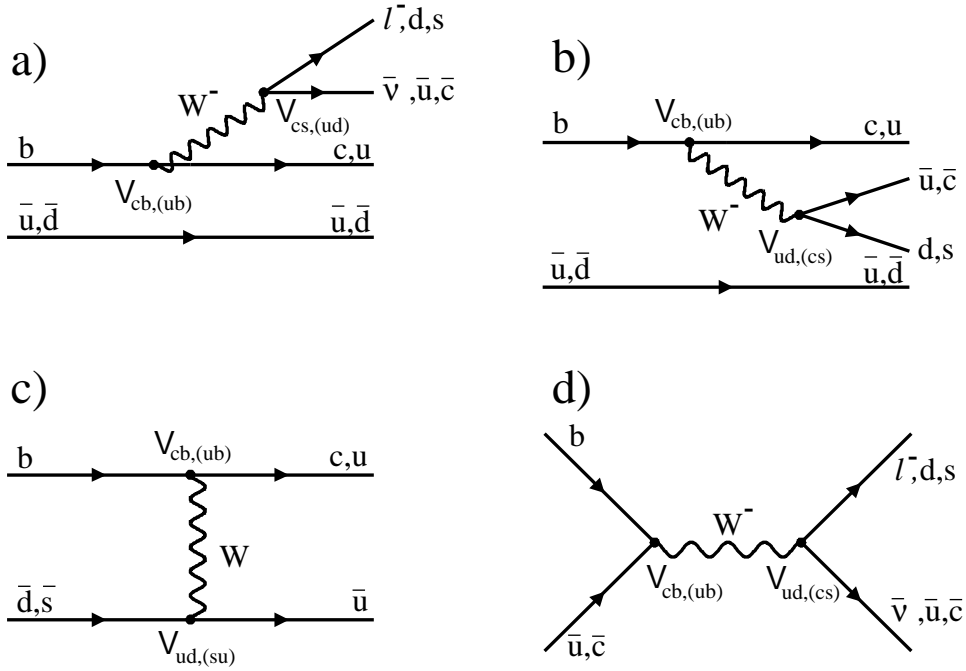


Figure 2.5: Lowest order Feynman diagrams for weak decays of B mesons. a) external spectator, b) internal spectator, c) W exchange, d) annihilation.

All experimental results are based on decays of hadrons, i.e. on bound states of quarks. Since we deal with heavy mesons, its decay can to a first approximation be described by the spectator model in which the dynamics is governed by the heavy quark decay while the light quark is regarded as a spectator. In order to improve this approximation, models are employed, which additionally try to respect the bound state nature of the particles by introducing form-factors. These form-factors are different for each decay mode. In the last few years various models have been developed to describe the decay of heavy mesons and to calculate the form-factors.

The decay model of *Altarelli et al.* (ACM) [48] uses an inclusive approach to describe the decay of B mesons at the parton level. This model treats the spectator quark as a real particle while the heavy quark enters as a virtual particle. In addition QCD corrections and bound state corrections from soft gluons are taken into account. The momentum distribution (Fermi motion) of the b quark inside the B hadron is described by a Gaussian distribution. Unfortunately, this QCD improved spectator model seems to have problems describing the endpoint region of the lepton spectrum of semileptonic decays.

The *Isgur, Scora, Grinstein, Wise* (ISGW) model [49] is based on a constituent quark model and replaces the inclusive approach of the ACM model with explicit summation over all exclusive channels. The confinement is modelled by introducing form-factors for the hadrons, which are calculated in a nonrelativistic limit. Furthermore, it is assumed that the sum over all hadronic final states will be saturated by the ordinary quark model resonances. The model is better suited to describe low-lying resonances that contribute to the endpoint of the lepton spectrum of semileptonic decays and the extracted value for $|V_{ub}|/|V_{cb}|$ is larger than in the ACM model.

The relativistic quark model approach of *Bauer, Stech and Wirbel* (BSW) [50,51] formulates the form-factors for the hadronic currents in terms of relativistic bound state wave functions in contrast to the nonrelativistic limit used in the ISGW model. This avoids several problems present in the ISGW model. The BSW model assumes monopolar form-factors, whereas the ISGW model prefers exponential form-factors. A similar approach has been developed by *Körner and Schuler* (KS) [52].

More recently, the *Heavy Quark Effective Theory* (HQET) [53] seems to provide a more universal description of heavy meson decays. The essential idea is that in the limit $m_Q \rightarrow \infty$ new symmetries appear and mesons containing a heavy quark ($Q\bar{q}$) can be described by the total angular momentum of the light quark q . In this approximation the hadron can be treated analogously to the hydrogen atom. The properties of the heavy hadrons will only depend on the light quark and the soft gluons. In the infinite quark mass limit, the corresponding hadronic form-factors can all be expressed in terms of a single universal function $\xi(v \cdot v')$, the Isgur-Wise function. It only depends on the four-velocities of the heavy particles. The Isgur-Wise function is not explicitly known, but several parametrizations exist.

2.3.4 Semileptonic B Hadron Decays

Semileptonic decays play an important role in heavy quark physics. They are theoretically well understood and have a clean signature due to the presence of a high momentum lepton in an environment of hadrons. The charge of the lepton indicates the flavour of the B hadron at the time of its decay. The only diagram which contributes to semileptonic decays is the external spectator shown in figure 2.5a. Theoretical models must account only for strong interaction effects among three primary quarks (b, \bar{q}

and c or u) rather than five in the more complicated case of hadronic decays. The aim of the models is to predict shape and normalization of measured lepton spectra for inclusive as well as for exclusive decays. Very important is the endpoint region of the lepton spectrum where the contribution from $b \rightarrow u$ transitions enters.

Taking into account $b \rightarrow c$ and $b \rightarrow u$, the semileptonic decay width can be written as:

$$\Gamma_{\text{sl}}(b \rightarrow \ell \bar{\nu} q) = \frac{G_F^2 m_b^5}{192\pi^3} \left[|V_{cb}|^2 \eta^{\text{QCD}}\left(\frac{m_c}{m_b}\right) f\left(\frac{m_c}{m_b}\right) + |V_{ub}|^2 \eta^{\text{QCD}}\left(\frac{m_u}{m_b}\right) f\left(\frac{m_u}{m_b}\right) \right] \quad (2.31)$$

where $f(x)$ is the phase space factor and η^{QCD} is the QCD correction term. This estimate needs to be corrected for hadronic effects due to the exchange of gluons between quarks lines.

Semileptonic decays are used to measure the values of the CKM matrix elements V_{ub} and V_{cb} . By studying the prompt lepton spectrum it has been established, that the b quark couples dominantly to the c quark [54,55] and that $V_{ub} \ll V_{cb}$. Near the kinematical limit of $b \rightarrow c \ell \bar{\nu}$, the ratio $|V_{ub}|/|V_{cb}|$ can be determined.

In the spectator model it is assumed that the light quark has no influence on the decay. Therefore the decay widths should be the same for all B hadrons. Consequently, the lifetimes $\tau_b = \frac{1}{\Gamma_{\text{tot}}} = \frac{Br_{\text{sl}}}{\Gamma_{\text{sl}}}$ of all B hadrons would be degenerate. However, the semileptonic branching ratio depends on the total width $\Gamma_{\text{tot}} = \Gamma_{\text{sl}} + \Gamma_{\text{had}}$, with the hadronic part being different for each B hadron. For instance in the hadronic decay of a B^\pm , the u quark accompanying the b quark can interfere, due to the Pauli principle, with the u quark created by the W, if they are near in phase space. This effect increases the lifetime of the B^\pm compared to the B_d^0 and therefore the hadronic partial width and the lifetimes will be different for each kind of B hadron. The following hierarchy in the lifetimes of B hadrons is predicted: $\tau_{\Lambda_b^0} < \tau_{B_s^0} < \tau_{B_d^0} < \tau_{B^\pm}$.

2.3.5 Hadronic B Decays

Hadronic B meson decays occur primarily through the external spectator diagram with the Cabibbo favoured $b \rightarrow c$ transition where the virtual W^\pm decays into either a $\bar{u}d$ or a $\bar{c}s$ pair. This pair becomes one of the final state hadrons while the c quark pairs with the spectator antiquark to form the other hadron. For two-body decays, if strong effects are ignored and the approximation $V_{ud} = V_{cs} = 1$ is made, the Hamiltonian which describes this process at the quark level is

$$\mathcal{H} = \frac{G_F}{\sqrt{2}} V_{cb} \{ [(\bar{d}u) + (\bar{s}c)] (\bar{c}b) \} \quad (2.32)$$

where G_F is the Fermi coupling constant, V_{cb} is the CKM matrix element, and $(\bar{q}_i q_j)$ is the weak-current $(\bar{q}_i q_j) = \bar{q}_i \gamma_\mu (1 - \gamma_5) q_j$. A similar Hamiltonian describes the transition $b \rightarrow u$.

However, the quarks involved in the decay may radiate gluons, which in turn will produce additional hadrons. This leads to QCD corrections and the result is an effective Hamiltonian which contains the original terms multiplied by a factor c_1 and an additional term multiplied by c_2 :

$$\mathcal{H}_{\text{eff}} = \frac{G_F}{\sqrt{2}} V_{cb} \left\{ c_1(\mu) [(\bar{d}u) + (\bar{s}c)] (\bar{c}b) + c_2(\mu) [(\bar{c}u)(\bar{d}b) + (\bar{c}c)(\bar{s}b)] \right\} \quad (2.33)$$

where c_1 and c_2 are the Wilson coefficients evaluated at the appropriate QCD mass scale μ . The additional term in (2.33) corresponds to the *colour suppressed* internal spectator diagram. The coefficients c_1 and c_2 give the relative contributions of the external and internal spectator diagram, respectively. Although the Wilson coefficients can be calculated in the framework of perturbative QCD, the predictions for decay rates are uncertain because it is unclear exactly what mass scale should be used. The usual approach is to assume $\mu \simeq m_b$. Defining

$$c_{\pm}(\mu) = c_1(\mu) \pm c_2(\mu) \quad (2.34)$$

the leading-log approximation gives:

$$c_{\pm}(\mu) = \left(\frac{\alpha_s(M_W^2)}{\alpha_s(\mu)} \right)^{\frac{-6\gamma_{\pm}}{(33-2N_f)}} \quad (2.35)$$

where $\gamma_- = -2\gamma_+ = 2$ and N_f is the number of active flavours. Numerically, including next-to-leading log corrections, one obtains: $c_1(m_b) \simeq 1.13$ and $c_2(m_b) \simeq -0.29$ [56].

An important class of hadronic B decays are two-body decays. Two body decays can be described similarly to inclusive decays and decay models taking bound states of quarks into consideration have been developed at the price of some parameters to be determined.

Most phenomenological models assume that the W^{\pm} fragmentation products are moving sufficiently fast that they do not interact with the other quarks in the decay. This allows the decay amplitude to be expressed as a product of two independent hadronic currents, one describing the decay of the W^{\pm} and the other the formation of the charmed meson. This is known as the *factorization* hypothesis. For the reaction $B \rightarrow M_1 M_2$ the amplitude is factorized as:

$$\langle M_1 M_2 | J_{\mu}^1 J_{\mu}^2 | B \rangle \simeq \langle M_1 | J_{\mu}^1 | B \rangle \cdot \langle M_2 | J_{\mu}^2 | 0 \rangle \quad (2.36)$$

If M_1 is a pseudoscalar particle $\langle M_1 | J_{\mu} | 0 \rangle = i f_P p_{\mu}$ and if it is a vector particle $\langle M_1 | J_{\mu} | 0 \rangle = i f_V m_V \varepsilon_{\mu}$, where p_{μ} is the four-momentum vector, ε_{μ} is the polarization vector and $f_{V,P}$ are the decay constants.

Although the effective Hamiltonian accounts for perturbative hard gluons, it is difficult to predict the effects that non-perturbative soft gluons may have. The BSW

model assumes factorization and replaces the Wilson coefficients with two new coefficients a_1 and a_2 . In the framework of perturbative QCD, these are related to the Wilson coefficients by:

$$a_1 \sim c_1 + \xi c_2 \quad \text{and} \quad a_2 \sim c_2 + \xi c_1 \quad (2.37)$$

where $\xi = 1/N_{\text{colour}}$ and $N_{\text{colour}} = 3$. However, because they are introduced to absorb the unknown effects of soft gluons, they are intended to be extracted from experimental results. The BSW model, which leaves ξ as a free parameter, can be used to predict many two-body branching fractions as a function of a_1 and a_2 . The dominant term a_1 is not very sensitive to variations of ξ , contrary to a_2 . The branching fractions of B meson decays to charmonium states depend only on a_2 .

2.3.6 B Hadron Decays into J/ψ

In B decays to charmonium the c quark from the decay of the b combines with a \bar{c} quark from the virtual W^- to form a charmonium state. This process is described by the colour suppressed internal spectator diagram shown in figure 2.6a. Other production modes exist at higher orders due to penguin diagrams. These processes are highly suppressed and can be neglected. Figure 2.6 shows the tree level and penguin diagrams responsible for the decay of a B meson into J/ψ . By comparing B meson decays to different final states with charmonium mesons the dynamics of this decay mechanism can be investigated.

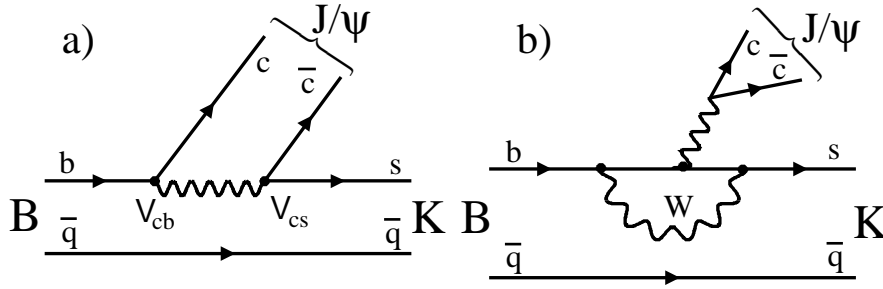


Figure 2.6: Tree level and penguin diagram responsible for the decay of B mesons into J/ψ .

The J/ψ is generally accompanied by a K meson. The production of a $\bar{c}d$ quark pair is suppressed by the Cabibbo angle. That is why the non-strange decay of B mesons into J/ψ at the first order are suppressed by a factor $|V_{cd}|^2/|V_{cs}|^2$ compared to strange decays. Theoretical calculations based on the spectator model predict an inclusive branching ratio of: $Br(B \rightarrow J/\psi X) = 1.0 \pm 0.24\%$.

B decays to charmonium are important because they allow us to evaluate a_2 , and therefore the degree of “colour-suppression” present in B decays. The predictions of

branching ratios for exclusive decay channels by an improved BSW model [57] and by a model based on HQET [58] are given in table 2.5. It can be seen that there is a large fraction of two-body decays compared to the inclusive ratio, and that the decay into K^* is favoured compared to K .

<i>Channel</i>	<i>Neubert et al. [57]</i>		<i>Deandrea et al. [58]</i>	
$B^\pm \rightarrow J/\psi K^\pm$	$1.819a_2^2$	$0.12 \pm 0.02\%$	$1.634a_2^2$	$0.11 \pm 0.06\%$
$B^\pm \rightarrow \psi(2S)K^\pm$	$1.068a_2^2$	$0.07 \pm 0.01\%$	$0.552a_2^2$	$0.04 \pm 0.02\%$
$B^\pm \rightarrow J/\psi K^{*\pm}$	$2.932a_2^2$	$0.20 \pm 0.04\%$	$2.393a_2^2$	$0.16 \pm 0.05\%$
$B^\pm \rightarrow \psi(2S)K^{*\pm}$	$1.971a_2^2$	$0.13 \pm 0.03\%$	$1.104a_2^2$	$0.07 \pm 0.02\%$
$B_d^0 \rightarrow J/\psi K^0$	$1.817a_2^2$	$0.12 \pm 0.02\%$	$1.634a_2^2$	$0.11 \pm 0.06\%$
$B_d^0 \rightarrow \psi(2S)K^0$	$1.065a_2^2$	$0.07 \pm 0.01\%$	$0.552a_2^2$	$0.04 \pm 0.02\%$
$B_d^0 \rightarrow J/\psi K^{*0}$	$2.927a_2^2$	$0.20 \pm 0.03\%$	$2.393a_2^2$	$0.16 \pm 0.05\%$
$B_d^0 \rightarrow \psi(2S)K^{*0}$	$1.965a_2^2$	$0.13 \pm 0.04\%$	$1.104a_2^2$	$0.07 \pm 0.02\%$

Table 2.5: *Branching ratios for exclusive B decay channels expressed in terms of a_2 and evaluated using a value of $a_2 = 0.26$. The quoted errors come from the uncertainties on the form-factors.*

The decay modes $B_d^0 \rightarrow J/\psi K_S^0$ and $B_d^0 \rightarrow \psi' K_S^0$ are of special interest since the final states are CP eigenstates. These decays are of great importance for the measurement of one of the three CP violating angles accessible to study in B decays. It is also possible to use the decay $B_d^0 \rightarrow J/\psi K^{*0} \rightarrow J/\psi K\pi$ which has a somewhat higher branching ratio, but this final state consists of a mixture of CP eigenstates. A detailed discussion of CP violation in B decays is given in the next chapter.

At hadron colliders a measurement of the inclusive production rate for $B \rightarrow J/\psi X$ allows to derive a value for $\sigma_{b\bar{b}}$.

Chapter 3

CP Violation in the B System

“It seems very pretty,” she said when she had finished it, “but it’s rather hard to understand! Somehow it seems to fill my head with ideas – only I don’t exactly know what they are!”

— LEWIS CARROLL, *Through the Looking Glass*

3.1 Introduction

Symmetries play a very important role in physics, since they describe the invariance of physical phenomena with respect to fundamental transformations. Their incorporation into a theory greatly simplifies the mathematical description, and in many instances introduces a clarity of formulation which is apparent without detailed calculation.

In the world of classical physics, space-time symmetry is inherent and the laws of physics are invariant under parity inversion (P), or reflection of the system in a mirror, time-reversal (T) and charge conjugation (C). Charge conjugation symmetry, relates particle and antiparticle, parity relates a left-handed particle to a similar right-handed one, and time-reversal invariance relates a process or state to the time-reversed process or state.

In all local quantum field theories the product of these three symmetry operations, CPT, is an exact symmetry of the equation of motion, with the consequence that within such a theory, the masses and lifetimes of particles and their antiparticles are identical. Parity and charge conjugation symmetries are individually violated by the weak interaction, although conserved in strong and electromagnetic interactions. In contrast, their product CP was thought to be conserved until in 1964 Christenson, Cronin, Fitch and Turlay discovered the decay $K_L^0 \rightarrow \pi^+\pi^-$ [59]. CP violation was unambiguously demonstrated by this decay and it was found that the CP-violating

amplitude in the weak decay of a neutral kaon is very small ($\sim 2 \times 10^{-3}$) compared with the CP-conserving amplitude.

This CP asymmetry provides an *absolute* definition of charge and plays an important role in models describing the large scale homogeneity of the expanding universe and the observed small ratio of baryons to photons. CP violation is one of Sakharov's conditions for explaining the observed baryon asymmetry in the universe [60].

It is of the utmost importance to understand the origin of CP violation, and to know whether it arises accidentally in the K^0 system, as described by the superweak model [61], or it is a natural feature of the three-generation Standard Model. Up to now CP violation has only been observed in the neutral kaon system.

In the Standard Model CP violation occurs because there is a single phase that remains in the Cabibbo-Kobayashi-Maskawa matrix after all possible field redefinitions that can remove such phases have been made. Extensions beyond the minimal Standard Model, such as theories with additional Higgs multiplets, give further ways to introduce CP violation into the theory. Hence it is of great interest to study whether the pattern of CP-violating effects that can be observed in B decays follows the predictions of the Standard Model, or instead requires the introduction of new effects beyond the Standard Model. This makes the investigation of CP violation in the B meson system extremely interesting. It will allow us to measure some of the remaining parameters of the Standard Model which are as fundamental as the quark masses themselves. If the results are inconsistent with Standard Model predictions they may provide some clues about physics beyond the Standard Model [62].

3.2 The Cabibbo-Kobayashi-Maskawa Matrix

Both leptons and quarks are subject to charge-changing weak interactions. But while the lepton couples only to the corresponding neutrino, quarks have a rich pattern of mixing between the families. The quark mass eigenstates are not the same as the weak eigenstates. The charged current interaction Lagrangian, before electroweak symmetry breaking, is given by

$$\mathcal{L}_{\text{int}} = -\frac{g}{\sqrt{2}} \left[(\bar{u}', \bar{c}', \bar{t}')_L \gamma^\mu \begin{pmatrix} d' \\ s' \\ b' \end{pmatrix}_L W_\mu^+ + \text{h.c.} \right] \quad (3.1)$$

where u', d', c', s', t', b' are the *weak quark eigenstates*, and g is the weak coupling constant. Quark masses arise through terms in the Lagrangian which in general are permitted to connect weak eigenstates with one another.

$$\mathcal{L}_{\text{mass}} = - \left[(\bar{u}', \bar{c}', \bar{t}')_R M_U \begin{pmatrix} u' \\ c' \\ t' \end{pmatrix}_L + (\bar{d}', \bar{s}', \bar{b}')_R M_D \begin{pmatrix} d' \\ s' \\ b' \end{pmatrix}_L + \text{h.c.} \right] \quad (3.2)$$

The mass matrices for up- and down-type quarks M_U and M_D are not simultaneously diagonal in this basis. However, any 3×3 matrix can be diagonalized via a bi-unitary transformation. Thus

$$V_{dL}^\dagger M_D V_{dR} = M_D^{\text{diag}} \quad V_{uL}^\dagger M_U V_{uR} = M_U^{\text{diag}} \quad (3.3)$$

where the M_Q^{diag} matrices are real and diagonal. The matrices V_{qL} and V_{qR} define the transformation from the *weak eigenstates* to the *quark mass eigenstates*. For three generations of quarks, this transformation is given by a unitary 3×3 matrix $V_{\text{CKM}} = V_{uL}^\dagger V_{dL}$, where by convention the up-type quarks are left unmixed:

$$\begin{pmatrix} d' \\ s' \\ b' \end{pmatrix} = V_{\text{CKM}} \cdot \begin{pmatrix} d \\ s \\ b \end{pmatrix} = \begin{pmatrix} V_{ud} & V_{us} & V_{ub} \\ V_{cd} & V_{cs} & V_{cb} \\ V_{td} & V_{ts} & V_{tb} \end{pmatrix} \cdot \begin{pmatrix} d \\ s \\ b \end{pmatrix} \quad (3.4)$$

Thus the interaction of equation 3.1 can be rewritten in the mass eigenbasis:

$$\mathcal{L}_{\text{int}} = -\frac{g}{\sqrt{2}} \left[(\bar{u}, \bar{c}, \bar{t})_L \gamma^\mu V_{\text{CKM}} \begin{pmatrix} d \\ s \\ b \end{pmatrix}_L W_\mu^+ + \text{h.c.} \right] \quad (3.5)$$

The matrix V_{CKM} is the so-called Cabibbo-Kobayashi-Maskawa (CKM) matrix. For three generations it was introduced in 1973 by Kobayashi and Maskawa [63], even before the discovery of the charm quark [64,65] and the τ lepton [66], in order to provide the required degrees of freedom to allow CP violation, as observed in the neutral K system, within the Standard Model. It is a generalization of the 2×2 matrix, used in a four-quark theory, which was introduced by Cabibbo in the 1960's [67], when only the three lightest quarks were known. To explain the absence of strangeness-changing neutral currents, this hypothesis was extended with the prediction of a fourth quark flavour by Glashow, Iliopoulos, and Maiani [68] (GIM mechanism). For a two-family theory the quark mixing matrix could be parametrized by introducing one mixing angle, the so-called Cabibbo angle θ_C [67]. The discovery of the third family was leading from the Cabibbo angle to the quark mixing matrix, the Cabibbo-Kobayashi-Maskawa matrix, V_{CKM} . Each element in this 3×3 matrix relates a transition between a quark of charge $2/3$ with one of charge $-1/3$. The transition itself is proportional to the $|V_{qq'}|^2$ participating in the decay process.

In the leptonic sector the analogous mixing matrix is a unit matrix due to the masslessness of neutrinos in the Minimal Standard Model. The fact that the CKM matrix is unitary $V_{\text{CKM}}^\dagger V_{\text{CKM}} = 1$ assures the absence of elementary flavour-changing neutral currents (FCNC). In the Standard Model flavour-changing neutral currents can only proceed by penguin or box diagrams. On the other hand, the fact that the elements of the CKM matrix can a priori be complex numbers allows the introduction of

CP violation in the Standard Model. In contrast the original 2×2 Cabibbo matrix [67] was real and had only one single parameter, therefore CP violation is not possible in a two-family theory. The precise determination of the elements of the CKM matrix is one of the primary goals of heavy flavour physics.

3.2.1 Parametrization of the CKM Matrix

A general 3×3 unitary matrix can be parametrized by nine parameters: three real Euler-like rotational angles plus six complex phases. However not all complex phases have physical meaning, as some of them can be removed by a redefinition of quark fields. To count the uneliminable, or physical, phases is essential, since any such phase entering the Lagrangian of a local quantum field theory is a necessary and sufficient condition for CP violation. To this purpose, we have to remember that the CKM matrix enters into the charged current, $J_\mu^- = \bar{u}_{Li}(V_{CKM})_{ij}\gamma_\mu d_{Lj}$, which involves $2n$ independent fields. Their phase redefinitions allow to multiply the elements $(V_{CKM})_{ij}$ by $(2n-1)$ independent phases, which do not show up anywhere else in the Lagrangian. They would actually do in the fermion masses or in the Higgs interactions, but they can be compensated by a redefinition of the fields u_i , d_i , which do not appear in the charged current interactions. For 3 generations five of the nine initial parameters can be removed by a suitable choice of relative phases of the quark fields, leaving four non-trivial independent parameters: three angles and one physical phase, which is just enough to describe CP violation.

It is important to fix a parametrization for V_{CKM} in terms of a minimum number of physical parameters. Let us discuss such a parametrization, having in mind the possibility of n generations, rather than 3.

A complex $n \times n$ matrix has $2n^2$ arbitrary real parameters, which are reduced to n^2 when the unitarity condition ($V^\dagger V = 1$) is imposed. An $n \times n$ orthogonal matrix i.e. a unitary $n \times n$ matrix with real coefficients, depends on $\frac{1}{2}n(n-1)$ parameters¹. Therefore a unitary $n \times n$ matrix has $\frac{1}{2}n(n-1)$ angles (the parameters of the orthogonal matrix, i.e. the number of independent rotations in n dimensions) and $\frac{1}{2}n(n+1)$ phases. We can remove $2n-1$ of these phases by appropriate redefinitions of the quark fields. The number of remaining physical phases is then $[n^2 - \frac{1}{2}n(n-1) - (2n-1)] = \frac{1}{2}(n-1)(n-2)$.

To summarize, a $n \times n$ quark mixing matrix is described by $(n-1)^2$ parameters. $\frac{1}{2}n(n-1)$ of these parameters can be represented by Cabibbo-type angles and $\frac{1}{2}(n-1)(n-2)$ as complex phases. Whereas the original 2×2 Cabibbo matrix was real and had only one angle and no phase, the 3×3 matrix of the Standard Model is complex and can in general be parametrized by four quantities, what usually is done

¹A real orthogonal matrix O ($O^T O = 1$) can be written in the form $O = e^A$, where A is a real antisymmetric matrix ($A^T = -A$). Evidently $A_{ii} = 0$, $A_{jk} = -A_{kj}$, $j \neq k$. Hence, the matrix A is specified by $n(n-1)/2$ real parameters.

by three angles and one phase. This phase (the imaginary part of the mixing matrix) is necessary to describe CP violation and therefore there is a strong relation between the mixing matrix and CP violation. The three-generation Standard Model predicts CP violation unless this phase δ is 0.

There are several parametrizations of the Cabibbo-Kobayashi-Maskawa matrix. A standard parametrization is proposed by the Particle Data Group (PDG) [27] in terms of three angles, θ_{ij} , $ij = 12, 13, 23$, and a phase factor, δ_{13} . The mixing matrix is then given by

$$\begin{aligned} V_{\text{CKM}} &= \begin{pmatrix} 1 & 0 & 0 \\ 0 & c_{23} & s_{23} \\ 0 & -s_{23} & c_{23} \end{pmatrix} \begin{pmatrix} c_{13} & 0 & s_{13}e^{-i\delta} \\ 0 & 1 & 0 \\ -s_{13}e^{i\delta} & 0 & c_{13} \end{pmatrix} \begin{pmatrix} c_{12} & s_{12} & 0 \\ -s_{12} & c_{12} & 0 \\ 0 & 0 & 1 \end{pmatrix} \\ &= \begin{pmatrix} c_{12}c_{13} & s_{12}c_{13} & s_{13}e^{-i\delta_{13}} \\ -s_{12}c_{23} - c_{12}s_{23}s_{13}e^{i\delta_{13}} & c_{12}c_{23} - s_{12}s_{23}s_{13}e^{i\delta_{13}} & s_{23}c_{13} \\ s_{12}s_{23} - c_{12}c_{23}s_{13}e^{i\delta_{13}} & -c_{12}s_{23} - s_{12}c_{23}s_{13}e^{i\delta_{13}} & c_{23}c_{13} \end{pmatrix} \quad (3.6) \end{aligned}$$

where $s_{ij} = \sin \theta_{ij}$ and $c_{ij} = \cos \theta_{ij}$ and i, j label the generations. In the limit $\theta_{13} = \theta_{23} = 0$ the third generation decouples, and θ_{12} can be identified with the Cabibbo angle, θ_C .

An approximate form for V_{CKM} was given by Wolfenstein [69], based on the observation of the following pattern in the data:

$$\begin{aligned} |V_{ii}| &\simeq 1, i = 1, 2, 3 \\ |V_{12}| &\simeq |V_{21}| \approx \lambda \\ |V_{23}| &\simeq |V_{32}| \approx \lambda^2 \\ |V_{13}| &\simeq |V_{31}| \approx \lambda^3 \end{aligned}$$

with $\lambda \equiv \sin \theta_C$. Using only three additional parameters, A, ρ and η , the mixing matrix can be written as

$$V_{\text{CKM}} = \begin{pmatrix} 1 - \frac{\lambda^2}{2} & \lambda & A\lambda^3(\rho - i\eta) \\ -\lambda & 1 - \frac{\lambda^2}{2} & A\lambda^2 \\ A\lambda^3(1 - \rho - i\eta) & -A\lambda^2 & 1 \end{pmatrix} + \mathcal{O}(\lambda^4). \quad (3.7)$$

A and ρ are numbers of the order of 1, λ is given by $\sin \theta_C$ and η is related to the weak CP violation phase. The Wolfenstein parametrization is an expansion in the small parameter λ and is a very convenient parametrization of the CKM matrix.

In this approach only the elements V_{ub} and V_{td} are complex. By studying the features of B decays, one also uses the following crude approximation for the mixing matrix:

$$V = \begin{pmatrix} \sim 1 & \lambda & \sim \lambda^3 \\ -\lambda & \sim 1 & \sim \lambda^2 \\ \sim \lambda^3 & \sim -\lambda^2 & 1 \end{pmatrix} \quad (3.8)$$

thus depending only on the parameter λ . This expansion shows clearly that the transitions within one generation are dominant ($V_{tb} \sim V_{cs} \sim V_{ud} \sim 1$) and jumps between the first and the third generation are highly suppressed.

The following formulas relate the parameters of the Wolfenstein parametrization (3.7) to the parameters of the standard parametrization (3.6):

$$\lambda = s_{12}c_{13} \quad (3.9a)$$

$$A = \frac{s_{23}}{s_{12}^2 c_{13}} \quad (3.9b)$$

$$\rho = \frac{s_{13}^2 + 2s_{12}s_{23}s_{13}c_{12}c_{23}\cos\delta - c_{12}^2c_{23}^2s_{13}^2}{2s_{12}^2s_{23}^2} \quad (3.9c)$$

$$\eta = \frac{s_{13}}{s_{12}s_{23}}\sin\delta \quad (3.9d)$$

3.2.2 The Elements of the CKM Matrix

The elements of the CKM matrix are fundamental parameters of the Standard Model and it is a prime task of experimentalists to measure them. Our present knowledge of the matrix elements comes from the following sources [70]:

V_{ud} : The most precise determination of $|V_{ud}|$ comes from comparing nuclear beta decay with muon decay. An alternative way to determine $|V_{ud}|$ is by measuring both the neutron lifetime, τ_n , and g_A (from neutron decay correlations) or by measuring the pion decay rate $\Gamma(\pi^+ \rightarrow \pi^0 e^+ \nu_e)$, which has a relatively small uncertainty in its radiative corrections.

V_{us} : This element is determined from averaging the rates of K_{e3} decays and of a number of semileptonic hyperon decays. The notation K_{e3}^+ and K_{e3}^0 refers to $K^+ \rightarrow \pi^0 e^+ \nu_e$ and $K_L^0 \rightarrow \pi^\pm e^\mp \nu_e$ respectively.

V_{cd} : There are two main sources of information on the $c \leftrightarrow d$ transition: deep inelastic neutrino excitation of charm via reactions such as $\nu_\mu d \rightarrow \mu^- c$ and $\bar{\nu}_\mu \bar{d} \rightarrow \mu^+ \bar{c}$ and semileptonic decays of charmed mesons to non-strange final states.

V_{cs} : This matrix element is obtained from dimuon production in ν_μ scattering and from $D \rightarrow \bar{K} e^+ \nu_e$ decays.

V_{cb} : The semileptonic decay rate of the b quark is proportional to $\alpha|V_{cb}|^2 + \beta|V_{ub}|^2$, where α and β are phase-space factors. $|V_{cb}|$ is obtained from a measurement of the average b lifetime τ_b and the semileptonic decay rate, $\Gamma(b \rightarrow c \ell \nu)$.

V_{ub} : From the semileptonic decay of B mesons, by measuring the lepton energy spectrum above the endpoint region, the ratio $|V_{ub}|/|V_{cb}| = 0.08 \pm 0.02$ can be obtained.

Further information, particularly on CKM matrix elements involving the top quark, can be obtained from flavour-changing processes that occur at the one-loop level.

The present experimental status of the elements of this matrix is shown in table 3.1.

<i>Element</i>	<i>Experimental value</i>	<i>Method</i>
$ V_{ud} $	0.9736 ± 0.0010	Nuclear β decay
$ V_{us} $	0.2205 ± 0.0018	K_{e3}^+ , K_{e3}^0 and hyperon decays
$ V_{cd} $	0.224 ± 0.016	Neutrino dilepton production
$ V_{cs} $	1.01 ± 0.18	$D \rightarrow K e \nu$
$ V_{cb} $	0.041 ± 0.003	Beauty particle decay
$ V_{ub} $	0.00328 ± 0.002	Charmless beauty decay

Table 3.1: *Experimental values of the elements of the CKM matrix.*

3.3 Unitarity Triangles

The unitarity of the CKM matrix

$$V^\dagger V = V V^\dagger = 1 \quad (3.10)$$

implies that any pair of rows, or any pair of columns are orthogonal: $\sum_i V_{ij}^* V_{ik} = \delta_{jk}$ and $\sum_j V_{ij}^* V_{kj} = \delta_{ik}$. This leads to six unitarity relations. Explicitly written these six unitarity equations are:

$$\mathbf{db} : V_{ud} V_{ub}^* + V_{cd} V_{cb}^* + V_{td} V_{tb}^* = 0 \quad (3.11a)$$

$$\mathbf{ds} : V_{ud} V_{us}^* + V_{cd} V_{cs}^* + V_{td} V_{ts}^* = 0 \quad (3.11b)$$

$$\mathbf{sb} : V_{us} V_{ub}^* + V_{cs} V_{cb}^* + V_{ts} V_{tb}^* = 0 \quad (3.11c)$$

$$\mathbf{uc} : V_{ud} V_{cd}^* + V_{us} V_{cs}^* + V_{ub} V_{cb}^* = 0 \quad (3.11d)$$

$$\mathbf{ct} : V_{cd} V_{td}^* + V_{cs} V_{ts}^* + V_{cb} V_{tb}^* = 0 \quad (3.11e)$$

$$\mathbf{ut} : V_{ud} V_{td}^* + V_{us} V_{ts}^* + V_{ub} V_{tb}^* = 0 \quad (3.11f)$$

An important feature arising from the unitarity of V is the geometrical interpretation of these relations: Each of the six relations (3.11a–f) can be represented by a triangle in the complex plane, the so-called *unitarity triangles*, where each side of a triangle is given by $V_{ij} V_{jk}^*$. This is shown in figure 3.1, in which each triangle is marked by the pair of quarks, representing the pair of columns, or of rows, whose orthogonality is represented by this triangle. The triangle labelled (ds) represents the unitarity constraints on the transition $s \rightarrow d$, which, for example, one encounters in the $K^0 - \bar{K}^0$

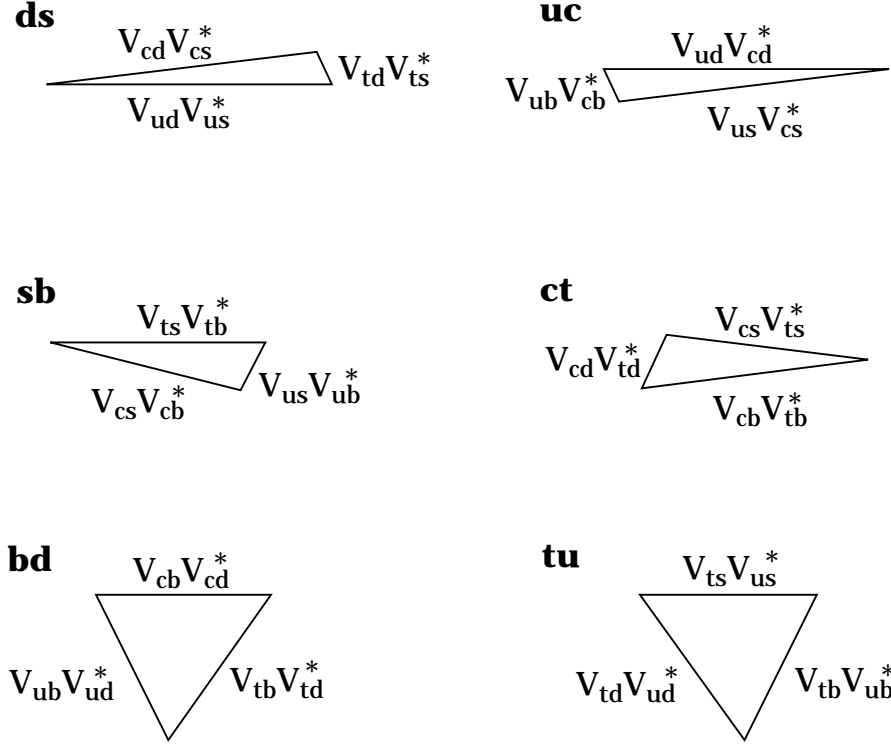


Figure 3.1: The unitarity triangles of the CKM matrix.

transition. It can be shown, that all six triangles have the same area which is related to the measure of CP violation.

These unitarity triangles are just a geometrical presentation of the equations (3.11) and summarize nicely direct and indirect information on the CKM matrix. The unitarity is simply expressed through $\alpha + \beta + \gamma = 180^\circ$, where α , β and γ are the three angles of a unitarity triangle.

Phenomenologically the most interesting is the triangle resulting from the relation

$$V_{ud}V_{ub}^* + V_{cd}V_{cb}^* + V_{td}V_{tb}^* = 0 \quad (3.12)$$

as it involves the elements V_{ub} and V_{td} which are still rather poorly known at present. The corresponding unitarity triangle is shown in figure 3.2.

In the Wolfenstein parametrization of the CKM matrix $V_{ud} \simeq V_{tb} \simeq 1$ and $V_{cd} \simeq \lambda$, and setting cosines of small angles to unity, the relation (3.12) becomes:

$$A\lambda^3(\rho + i\eta) + A\lambda^2(-\lambda) + A\lambda^3(1 - \rho - i\eta) = 0 \quad (3.13)$$

and can be represented as a triangle in the $\rho - \eta$ complex plane, with the three angles α, β, γ . The three angles are all related to the complex phase δ in the CKM matrix.

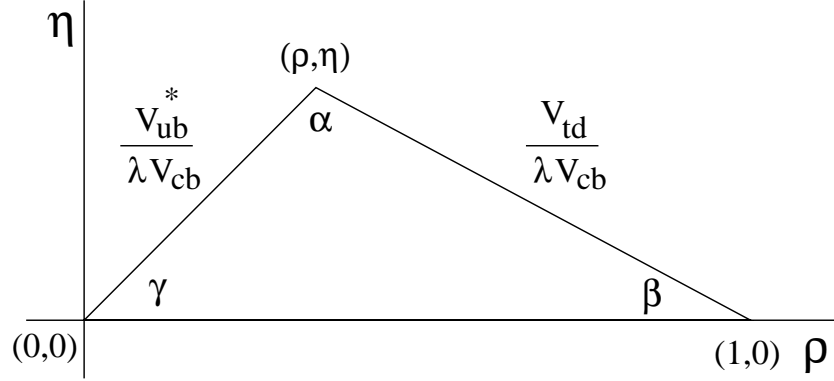


Figure 3.2: *The unitarity triangle.*

Before discussing how to measure the parameters in equation (3.15), let us discuss a few properties of the CKM matrix.

One can show [71] that all CP-violating amplitudes in the Standard Model are proportional to

$$J = |\text{Im}[V_{ij}V_{kl}V_{il}^*V_{kj}^*]| \quad \text{with} \quad i \neq k, j \neq l \quad (3.14)$$

where J is independent of the parametrization used for the CKM matrix and of phase conventions. In the parametrization of (3.6) and in the Wolfenstein parametrization² it can be written as:

$$J = 2s_1^2 s_2 s_3 c_1 c_2 c_3 \sin \delta = \eta A^2 \lambda^6 \quad (3.15)$$

J must be very small since CP is a relatively well preserved symmetry. Since J is a product of several small factors it is indeed a very small quantity implying that CP violation is naturally small. One can easily show that the parameter J in equation (3.15) has the geometrical interpretation of $2 \times (\text{area of the unitarity triangle})$; therefore all six triangles defined by equations (3.11a) – (3.11f) have the same area. If the CKM matrix elements are all real, the triangles will collapse into straight lines in the complex plane.

Whereas all the unitarity triangles have the same area, their shapes can differ significantly. Indeed from equations (3.11a,f) one can see that in the corresponding triangles all the sides are of the same order ($\sim \lambda^3$); on the contrary, in the triangles described by (3.11b,d) one side is very small ($|V_{td}V_{ts}^*| \sim \lambda^5$) and the other ones are of the order of λ .

²One has to be careful when calculating this in the Wolfenstein parametrization, as this is of order λ^6 and thus beyond the accuracy of the approximation.

Let us now discuss equation (3.12) in more detail: We can choose to orient the triangle so that $V_{cd}V_{cb}^*$ lies along the real axis in the complex (ρ, η) plane. Now we can scale all sides of the triangle by $|V_{cd}V_{cb}^*|$. This makes the base of the triangle real and of unit length and the apex of the triangle is (ρ, η) . The relation (3.12) becomes now:

$$\frac{V_{ub}^*}{\lambda V_{cb}} + \frac{V_{td}}{\lambda V_{cb}} = 1 \quad (3.16)$$

In the Wolfenstein parametrization the three vertices of the scaled triangle have coordinates:

$$A = (\rho, \eta) \quad B = (1, 0) \quad C = (0, 0)$$

and the corresponding angles α , β , and γ . Figure 3.2 shows the unitarity triangle, as it is usually drawn.

It is clear that CP violation in B decays within the Standard Model is only possible if all three angles of the unitarity triangle shown in figure 3.2 are different from 0. The angles can be related to the elements of the CKM matrix by the following relations:

$$\sin 2\alpha = \frac{2\eta(\eta^2 + \rho^2 - \rho)}{(\rho^2 + \eta^2)((1 - \rho)^2 + \eta^2)} \quad (3.17a)$$

$$\sin 2\beta = \frac{2\eta(1 - \rho)}{(1 - \rho)^2 + \eta^2} \quad (3.17b)$$

$$\sin 2\gamma = \frac{2\eta\rho}{\rho^2 + \eta^2} \quad (3.17c)$$

One advantage of using the B system compared to the neutral K system to study CP violation effects is simply illustrated in figure 3.1, which compares the unitarity triangles of the two cases. For B_d^0 all three sides of the triangle have comparable lengths ($\mathcal{O}(\lambda^3)$), while in the K meson triangle, which essentially collapses to a line, two sides are much longer ($\mathcal{O}(\lambda)$) and the third one is extremely tiny ($\mathcal{O}(\lambda^5)$).

3.4 Mixing of Neutral B Mesons

Mixing and CP violation in the neutral B system can be described in much the same way as in the neutral kaon system. By mixing or oscillation one means transitions of the type $B^0 \leftrightarrow \bar{B}^0$. These transitions result from flavour non-conservation in weak interactions. The neutral B mesons are degenerate eigenstates of the strong interaction that are distinguished by their quark flavour. The weak interaction connects the two states and, assuming conservation of CP, the eigenstates of the complete Hamiltonian are linear combinations of these flavour eigenstates. The flavour oscillation in the B^0 – \bar{B}^0 system proceed via a second-order weak interaction described by the Feynman box

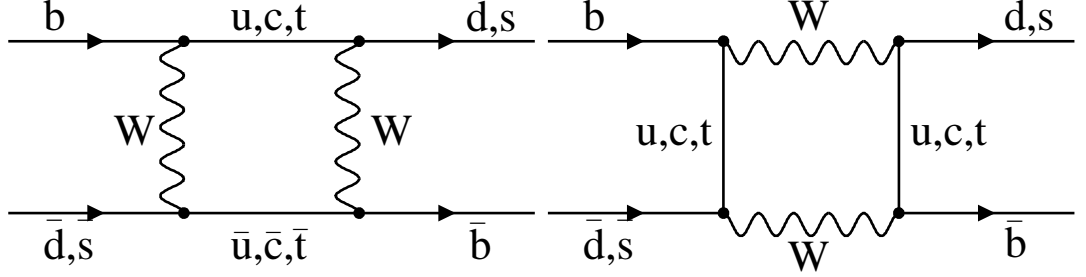


Figure 3.3: Box diagrams responsible for $B_d^0 \leftrightarrow \bar{B}_d^0$ mixing.

diagrams in figure 3.3. From an evaluation of these box diagrams it follows that the dominant contribution comes from diagrams with top quark exchange and the rate of mixing depends on the top mass and the CKM matrix elements V_{tq} .

The mass difference between the two eigenstates, ΔM , introduces a time-dependent phase difference between their wave functions which, in turn, results in an oscillation between them with a period given by $2\pi/\Delta M$. This case is a complete analogy to the well known phenomenon of oscillations in the neutral kaon system, which was observed experimentally for the first time in the 1950's [72].

The two CP-conjugate states $|B^0\rangle$ and $|\bar{B}^0\rangle$ are eigenstates of the strong and electromagnetic, but not of the weak interactions, which are responsible for their decay. Thus they are not the eigenvectors of the Hamiltonian H considered to be made from a strong and a weak interaction part. Taking into account CPT invariance, one can write the 2×2 Hamiltonian in the $|B^0\rangle$, $|\bar{B}^0\rangle$ basis:

$$H = M - \frac{i}{2}\Gamma = \begin{pmatrix} M_{11} - \frac{i}{2}\Gamma_{11} & M_{12} - \frac{i}{2}\Gamma_{12} \\ M_{12}^* - \frac{i}{2}\Gamma_{12}^* & M_{11} - \frac{i}{2}\Gamma_{11} \end{pmatrix} \quad (3.18)$$

where the mass matrix M and the decay matrix Γ are hermitian. If also CP conservation is assumed, then $M_{12} = M_{12}^*$ and $\Gamma_{12} = \Gamma_{12}^*$. The fact that H contains nonvanishing off-diagonal matrix elements is due to weak interactions. In contrast to M and Γ , which are associated with measurable quantities, H is not hermitian and therefore the eigenvalues are not real and the eigenvectors do not need to be orthogonal. The physical mass eigenstates $|B_1\rangle$ and $|B_2\rangle$ are:

$$|B_1\rangle = p|B^0\rangle + q|\bar{B}^0\rangle \quad (3.19a)$$

$$|B_2\rangle = p|B^0\rangle - q|\bar{B}^0\rangle \quad (3.19b)$$

where p and q are obtained by diagonalizing H :

$$\frac{p}{q} \equiv \eta = \sqrt{\frac{M_{12} - \frac{i}{2}\Gamma_{12}}{M_{12}^* - \frac{i}{2}\Gamma_{12}^*}} = \frac{V_{ti}V_{tb}^*}{V_{ti}^*V_{tb}} \quad , \quad i = d, s \quad (3.20)$$

Whereas in the kaon case the lifetimes of the two eigenstates are significantly different and the difference in masses between them is small, in the B system it is the mass differences that dominate the physics, and the two states have nearly equal predicted widths (and thus lifetimes).

$$\Gamma = (\Gamma_1 + \Gamma_2)/2 \quad \Delta\Gamma = \Gamma_1 - \Gamma_2 \quad (3.21a)$$

$$M = (M_1 + M_2)/2 \quad \Delta M = M_1 - M_2 \quad (3.21b)$$

The mass splitting ΔM for the B_d^0 system can be written as:

$$\Delta M = \frac{G_F^2}{6\pi^2} |V_{td}|^2 |V_{tb}|^2 m_W^2 m_B f_B^2 B_B \eta_B S(m_t^2/M_W^2) \quad (3.22)$$

where f_B is the B meson decay constant, B_B is a parameter describing the degree to which the graphs of figure 3.3 dominate the mixing, η_B is a QCD correction, and $S(x) = \frac{x}{4} [1 + \frac{3-9x}{(x-1)^2} + \frac{6x^2 \ln x}{(x-1)^3}]$.

The proper time evolution of an initially ($t = 0$) pure B^0 or \bar{B}^0 is given by

$$|B_{\text{phys}}^0(t)\rangle = e^{-\frac{\Gamma t}{2}} e^{-iMt} \left\{ \cos(\frac{\Delta Mt}{2}) |B^0\rangle + i \frac{q}{p} \sin(\frac{\Delta Mt}{2}) |\bar{B}^0\rangle \right\} \quad (3.23a)$$

$$|\bar{B}_{\text{phys}}^0(t)\rangle = e^{-\frac{\Gamma t}{2}} e^{-iMt} \left\{ i \frac{p}{q} \sin(\frac{\Delta Mt}{2}) |B^0\rangle + \cos(\frac{\Delta Mt}{2}) |\bar{B}^0\rangle \right\} \quad (3.23b)$$

and the probability that an initial B^0 (\bar{B}^0) decays as a \bar{B}^0 (B^0) is thus

$$P(t) = \frac{1}{2} e^{-\Gamma t} (1 - \cos(\Delta Mt)) \quad (3.24)$$

where $|p/q|$ was set to 1, which is true when effects of $\Delta\Gamma$ are neglected.

One can either perform a time-dependent mixing measurement or measure the time-integrated mixing, which is parametrized by a parameter χ . The quantity χ measures the total probability that a created B^0 decays as a \bar{B}^0 ; it is given by

$$\chi_q = \int_0^\infty P_q(t) dt = \frac{x_q^2}{2(1 + x_q^2)} \quad (3.25)$$

where $q = d, s$ and $x_q = \frac{\Delta M}{\Gamma_q}$.

First experimental evidence for B^0 - \bar{B}^0 mixing was reported in 1987 by the UA1 collaboration at the CERN $\bar{p}p$ collider [15] and the ARGUS collaboration at the DESY e^+e^- collider [73].

3.5 CP Violation in B Decays

In the Standard Model 14 conditions must be satisfied in order to get CP violation:

1) The quarks with the same charge are not allowed to be degenerate:

$$m_u \neq m_c, m_c \neq m_t, m_t \neq m_u, m_d \neq m_s, m_s \neq m_b, m_b \neq m_d$$

2) The angles must satisfy:

$$\theta_1, \theta_2, \theta_3 \neq 0, \pi/2 \quad \text{and} \quad \delta \neq 0, \pi$$

where the angles are those of the Kobayashi-Maskawa parametrization [63] of the quark mixing matrix (see equation (3.6)). These 14 conditions are unified [71] in a single relation: CP is violated if

$$\det C \neq 0 \tag{3.26}$$

where C is the commutator of the square of the quark mass matrices:

$$[M_U M_U^\dagger, M_D M_D^\dagger] = iC \tag{3.27}$$

$$\begin{aligned} \det C = & - 2(m_u^2 - m_c^2)(m_c^2 - m_t^2)(m_t^2 - m_u^2) \\ & \times (m_d^2 - m_s^2)(m_s^2 - m_b^2)(m_b^2 - m_d^2) \\ & \times s_1^2 s_2 s_3 c_1 c_2 c_3 \sin \delta \end{aligned} \tag{3.28}$$

It is important to notice, that none of the elements of the quark mixing matrix is allowed to be zero, if CP is to be violated.

In the framework of the Standard Model, CP violation will arise because of the complex CKM matrix elements. Therefore, any process where only $|V_{ij}|$ terms enter in the decay mechanism cannot be sensitive to these effects, in contrast to processes containing products of CKM matrix elements with at least one complex element. As described by equation (3.14) the product will be of the form $V_{ai} V_{ak}^* V_{bj} V_{bk}^*$, which could lead to a difference between $B \rightarrow f$ and $\bar{B} \rightarrow \bar{f}$ as V_{ij} changes to V_{ij}^* when the amplitude is transformed to describe the charge conjugated process.

Therefore in the Standard Model, CP violation in B decays may occur whenever there are at least two weak decay amplitudes with different CKM factors which lead to a given final state. This can proceed through one or both of the following methods:

- (i) $\Delta B = 2$ transitions: via $B^0 - \bar{B}^0$ mixing (box diagrams)
- (ii) $\Delta B = 1$ transitions: via interference of direct quark decays and penguin diagrams

When comparing the amplitude for a decay into a CP eigenstate to that for the related CP-conjugate process, the weak phase ϕ_k of each contribution changes sign, while the strong phase δ_k is unchanged:

$$\mathcal{A} = \langle f | B \rangle = \sum_k \mathcal{A}_k e^{i\delta_k} e^{i\phi_k} \quad , \quad \overline{\mathcal{A}} = \langle \bar{f} | \bar{B} \rangle = \sum_k \mathcal{A}_k e^{i\delta_k} e^{-i\phi_k} \quad (3.29)$$

where \mathcal{A}_k are real, ϕ_k are CKM phases, and δ_k are strong phases.

Direct CP violation :

Direct CP violation is a difference in the direct decay rate between $B \rightarrow f$ and $\bar{B} \rightarrow \bar{f}$ without any contribution from mixing effects. This requires $|\mathcal{A}| \neq |\overline{\mathcal{A}}|$, which occurs only if there is more than one term in the sum of equation (3.29), and only if the two terms have both different weak phases and different strong phases. Direct CP violation can occur both in charged and neutral channels.

In the Standard Model direct CP violation occurs when there are two sets of diagrams with different weak phases that contribute to the same decay. There are two major classes of diagrams that contribute to weak decays, tree diagrams and penguin diagrams. There may be several different tree diagrams for a given process but they will contribute with the same CKM phase. Thus in the Standard Model direct CP violation occurs because of interference between tree and penguin diagrams when these have different weak phases, or, in channels where there are no tree contributions it can also arise because of different weak phases of different penguin contributions. The necessary condition for CP violation is then the presence of at least two $\Delta B = 1$ decay mechanisms with different CKM matrix elements and final state strong interaction phases leading to the same final state.

CP violation due to interference between decay and mixing :

In neutral B decays there are additional effects which can produce CP violation. If the B^0 and \bar{B}^0 mesons are able to decay into the same final state f (and hence necessarily into \bar{f}), CP violation could be observed as a result of the interplay between mixing and decay amplitudes. There are two possible ways for a neutral meson B^0 and its antiparticle \bar{B}^0 to decay into a final state f : $B \rightarrow f$ or $B \rightarrow \bar{B} \rightarrow f$. The interference between the two contributions can produce rate differences between the decay and its CP conjugate. These effects are of particular interest because they do not depend upon strong phases and hence the measured asymmetries can be directly related to the CKM phases.

Indirect CP violation:

Indirect CP violation or CP violation in mixing would arise from any difference in

the widths $\Delta\Gamma$ of the two mass eigenstates, or more precisely from complex mixing effects that would also give a nonvanishing lifetime difference for the two B states. Such effects are expected to be tiny in the B_d^0 system. For the B_s^0 a small difference in the widths is possible, due to the fact that a number of the simplest two-body channel contribute only to a single CP state.

To summarize, *direct* CP violation occurs when $|\mathcal{A}/\overline{\mathcal{A}}| \neq 1$, *indirect* CP violation requires $|p/q| \neq 1$, and CP violation due to interference between direct decay and decay after mixing can occur when both quantities have unit absolute value; it requires only that their product have a non-zero weak phase [62].

The B decays which promise to provide the cleanest information on phases in the CKM matrix are those of the neutral B mesons. For CP-violating asymmetries of neutral B mesons decaying to CP eigenstates, there is a direct relationship between the magnitude of the asymmetry in a given decay and $\sin 2\phi$, where $\phi = \alpha, \beta, \gamma$ is an appropriate angle of the unitarity triangle in figure 3.2.

3.6 How to Measure CP Violation

The Standard Model predictions for the CP asymmetries in neutral B decays into certain CP eigenstates are fully determined by the values of the three angles of the unitary triangle, α , β , and γ . Their measurement will test these Standard Model predictions and consequently provide a probe for physics beyond the Standard Model.

Our present knowledge of the shape of the unitarity triangle is summarized in figure 3.4. The top of the triangle must lie in the shaded area. One can easily see that none of the three angles is particularly small; the corresponding CP asymmetries are then predicted to fall in the range of a few times 10%. The preferred values obtained from this fit are [74]:

$$(\rho, \eta) = (-0.05, 0.37) \quad (\text{with } \chi^2 = 0.1)$$

In principle all three angles of the unitarity triangle (see figure 3.2) are accessible to direct experimental measurements, for instance from the neutral B decays $B_d^0 \rightarrow \pi^+\pi^-$, $B_d^0 \rightarrow J/\psi K_S^0$ and $B_s^0 \rightarrow \rho K_S^0$.

The most promising method to measure CP violation in B decays is to consider a final state f which is a CP eigenstate to which both B_d^0 and \overline{B}_d^0 can decay and to look for an asymmetry between $\Gamma(B_d^0 \rightarrow f)$ and $\Gamma(\overline{B}_d^0 \rightarrow f)$. In order to interpret the measurement and to extract the CKM parameter one needs channels with small uncertainties due to final state interactions (strong phase).

The time dependent rates for initially pure B_d^0 or \overline{B}_d^0 states to decay into a final CP

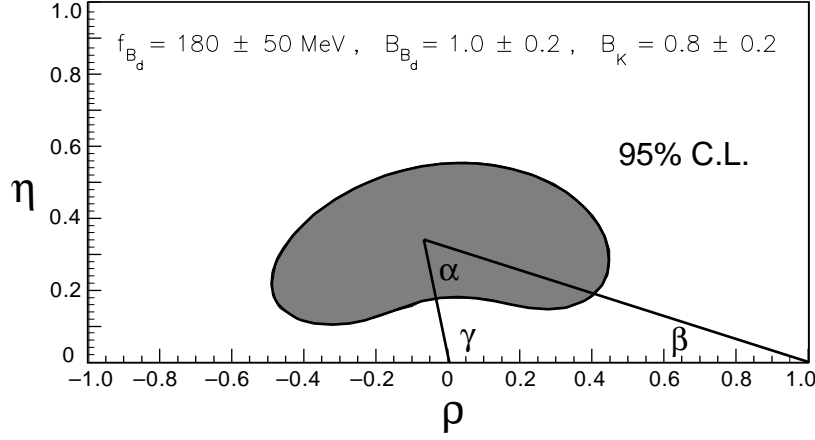


Figure 3.4: The unitarity triangle with present experimental constraints. Allowed region in $\rho - \eta$ space.

eigenstate at time t are given by:

$$\Gamma(B_d^0(t) \rightarrow f) = |\mathcal{A}|^2 e^{-\Gamma t} \left[\frac{1+|\lambda|^2}{2} + \frac{1-|\lambda|^2}{2} \cos(\Delta Mt) - \text{Im}\lambda \sin(\Delta Mt) \right] \quad (3.30a)$$

$$\Gamma(\bar{B}_d^0(t) \rightarrow f) = |\mathcal{A}|^2 e^{-\Gamma t} \left[\frac{1+|\lambda|^2}{2} - \frac{1-|\lambda|^2}{2} \cos(\Delta Mt) + \text{Im}\lambda \sin(\Delta Mt) \right] \quad (3.30b)$$

where

$$\lambda = \frac{q}{p} \frac{\bar{\mathcal{A}}}{\mathcal{A}} \quad (3.31)$$

CP violation is manifested in a non-zero value of the time-dependent asymmetry:

$$A(t) = \frac{\Gamma(B_d^0(t) \rightarrow f) - \Gamma(\bar{B}_d^0(t) \rightarrow f)}{\Gamma(B_d^0(t) \rightarrow f) + \Gamma(\bar{B}_d^0(t) \rightarrow f)} = -\text{Im}\lambda \sin(\Delta Mt) = \sin 2\phi \sin(\Delta Mt) \quad (3.32)$$

where $\text{Im}\lambda$ is related to an angle of $\phi = \alpha, \beta, \gamma$ of the unitarity triangle. For a time-integrated measurement the asymmetry is $x_q/(1+x_q^2) \sin 2\phi$. Table 3.2 gives the CKM factors and the corresponding angles of the unitarity triangle for various B decay modes.

The simplest of the three angles to measure is β . The “gold plated channel” for this measurement is $B_d^0 \rightarrow J/\psi K_S^0$ which determines $\sin 2\beta$. This channel has a very clear signal, low background and is theoretically well understood. The penguin diagrams do not cause any problem, since the weak phase of the penguin diagram is the same as that of the tree contribution.

To measure the angle α the most appropriate channel is $B_d^0 \rightarrow \pi^+ \pi^-$. The contributing penguin diagrams for this channel are expected to be small with respect

<i>Quark subprocess</i>	<i>Tree CKM factor</i>	<i>Leading-penguin CKM factor</i>	<i>Angle</i>	<i>Sample mode</i>
$b \rightarrow c\bar{c}s$	$V_{cb}V_{cs}^* = A\lambda^2$	$V_{cb}V_{cs}^* = A\lambda^2$	β	$B_d^0 \rightarrow J/\psi K_S^0$
$b \rightarrow s\bar{s}s$	0	$V_{cb}V_{cs}^* = A\lambda^2$	β	$B_d^0 \rightarrow \phi K_S^0$
$b \rightarrow c\bar{u}s$	$V_{cb}V_{us}^* = A\lambda^3$	0	γ	$B_d^0 \rightarrow D^0 K^*$
$b \rightarrow c\bar{c}d$	$V_{cb}V_{cd}^* = -A\lambda^3$	$V_{tb}V_{td}^* = A\lambda^3(1 - \rho + i\eta)$	β	$B_d^0 \rightarrow D^+ D^-$
$b \rightarrow u\bar{u}d$	$V_{ub}V_{ud}^* = A\lambda^3(\rho - i\eta)$	$V_{tb}V_{td}^* = A\lambda^3(1 - \rho + i\eta)$	α	$B_d^0 \rightarrow \pi^+ \pi^-$

Table 3.2: *B decay modes for CP violation studies.*

to the tree diagram. Experimentally this channel is more challenging to study since the background from other two-body B decays is not easy to separate which makes it necessary to have a detector with particle identification.

The most difficult angle to measure is γ . A possible channel for such a measurement could be $B_s^0 \rightarrow \rho K_S^0$. However, it is not easy to extract $\sin 2\gamma$ from such a measurement, since the penguin contribution for this channel is probably larger than the tree contribution. A second possibility would be to measure the angle γ by charged B decays e.g. $B^\pm \rightarrow DK^\pm$.

The final goal of CP violation studies must be to perform enough independent measurements to demonstrate either that the unitarity triangle is closed and therefore to prove that CP violation is due to the CKM matrix or to show that the triangle is not closed which would be a strong indication for new physics.

Chapter 4

The DELPHI Experiment

Man is a tool-using animal ...

Without tools he is nothing, with tools he is all.

— THOMAS CARLYLE, Sartor Resartus

The data for the analysis presented in this thesis was collected with the DELPHI detector at the LEP (Large Electron Positron) collider. This chapter briefly describes the LEP collider and the components of the DELPHI detector. This is followed by an outline of the triggers and the data acquisition. Lastly, there is a brief description of the DELPHI particle identification.

4.1 The LEP Collider

The Large Electron Positron collider LEP at CERN is situated in a circular tunnel of 27 km circumference on both sides of the border between France and Switzerland. The tunnel is between 50 and 150 m below the surface and its diameter is 3.8 m, except for the four large experimental halls having diameters of 23 m and 80 m lengths.

The collider consists of eight bending sections, each 2840 m long, with a radius of curvature of 3300 m. To guide the beam 3304 dipole magnets are installed. The bending field of these dipoles has been made unusually low (0.065 T) to increase the bending radius and thereby reduce the amount of synchrotron radiation. There are eight 500 m long straight sections, four of which house the four experiments – ALEPH [75], DELPHI [76], L3 [77] and OPAL [78] – and the other four are intended for the RF accelerating cavities and beam dump.

The LEP collider has been operational since the summer of 1989 when the first Z^0 event was recorded in August. It currently operates at a center-of-mass energy of about 91 GeV, i.e. at the resonance peak of the Z^0 .

Before injection into the LEP ring, four accelerators are employed to accumulate and preaccelerate the positron and electron bunches. The LEP Injector Linacs (LIL) create the electrons and positrons in pulses of 12 ns and accelerate them up to 600 MeV. These are then accumulated in the Electron Positron Accumulator (EPA) into bunches. The Proton Synchrotron (PS) then accelerates these bunches up to 3.5 GeV followed by the Super Proton Synchrotron (SPS) which further accelerates them to 20 GeV and injects them into the LEP ring. In LEP, the beams are further accelerated to 45 GeV, ‘squeezed’ until the luminosity is optimized and then brought into collision.

The lifetime of the beams in colliding mode is typically 12 hours, which is not limited by rest gas in the vacuum tube but by beam-beam bremsstrahlung. The single beam lifetime is limited by electron-scattering on background thermal photons (the machine components are heated up by synchrotron radiation). The rest gas density alone would allow 200 hours lifetime due to the very low static pressure in the range of 10^{-11} Torr.

The radiation loss per revolution of an electron of energy E circulating in LEP is:

$$\Delta E = \frac{4\pi}{3} \frac{r_e}{E_0^3} \frac{E^4}{\rho} = 0.0885 \frac{E^4(\text{GeV})}{\rho(\text{m})}$$

with r_e (the classical electron radius) $= 2.8 \times 10^{-15}$ m, E_0 (the rest energy of the electron) 0.511 MeV and ρ the radius of curvature. This energy loss is 130 MeV at the Z^0 increasing up to 2.3 GeV at LEP200.

The number of bunches in each beam was four from the start of LEP operations. Since 1992 LEP is operating with eight bunches per beam in ‘pretzel’ orbits which increases the luminosity by a factor of two. The pretzel-scheme in principle allows up to 36 bunches but more than 18 bunches would require a considerable upgrade of the detectors. Each bunch contains about 10^{11} particles, corresponding to a current of 3 mA per circulating beam. At the interaction points the bunches have strongly elliptical cross-sectional areas. The beam dimensions depend on the equilibrium between the damping of the oscillations and the noise excitation from quantum emission due to synchrotron radiation. The current beam dimensions at collision are: $\sigma_x \simeq 200 \mu\text{m}$, $\sigma_y \simeq 10 \mu\text{m}$ and $\sigma_z \simeq 20$ mm. The maximum LEP luminosity¹ is $1.9 \times 10^{31} \text{ cm}^{-2}\text{s}^{-1}$, but normal luminosities seldom exceeded $1 \times 10^{31} \text{ cm}^{-2}\text{s}^{-1}$.

A detailed description of the LEP accelerator and injection chains can be found in the LEP design reports [79,80].

¹The luminosity is defined as

$$\mathcal{L} = f_{\text{rev}} k \frac{N_+^{\text{bunch}} N_-^{\text{bunch}}}{4\pi\sigma_x\sigma_y}$$

where f_{rev} is the LEP revolution frequency of the order of 11 KHz, k is the number of bunches in each beam, σ_x and σ_y are the beam dimensions and N_-^{bunch} and N_+^{bunch} are the numbers of electrons and positrons in a bunch. For a process of cross-section σ , the number of events per second is $\mathcal{L} \cdot \sigma$.

4.2 The DELPHI Detector

DELPHI, a DEtector with Lepton, Photon and Hadron Identification, is one of the four detectors at LEP. Since 1989 it has collected about 4 million Z^0 decays [81]. The apparatus was designed, built and is run by an international collaboration of 52 institutes including the Institute for High Energy Physics of the Austrian Academy of Sciences, Vienna.

It was designed as a general purpose detector with special emphasis on good particle identification and very accurate vertex reconstruction [82]. Some of the special features of the DELPHI detector are the high resolution vertex detector and the Ring Imaging Cherenkov detectors for particle identification up to high momenta.

In the following, the main features of the apparatus, in particular those relevant for the present analysis, are reviewed. The geometric setup and the relevant performances of these detectors are briefly discussed. A more detailed description of the DELPHI detector can be found in [76].

4.2.1 General Layout

DELPHI is installed in a cavern about 100 m below ground level. The detector consists of a cylindrical barrel section and two end-caps. The two end-caps can be moved sideways, to allow access to the different sub-detectors. Figure 4.1 shows the schematic layout of the barrel and of one end-cap. One sub-detector (the Very Small Angle Tagger, VSAT) is located inside the LEP tunnel.

The ensemble of sub-detectors are grouped according to their primary function into tracking detectors, calorimeters, scintillation counters and detectors for particle identification.

Close to the beam-pipe, inside a 1.2 T magnetic field, are a set of detectors for charged particle track reconstruction. Two calorimeters, an electromagnetic calorimeter for the detection of photons and electrons, and a hadron calorimeter, surround the tracking detectors. The whole detector is enveloped by muon chambers. In addition DELPHI is equipped with Ring Imaging Cherenkov (RICH) detectors for particle identification, a set of scintillation counters used for time-of-flight measurements, and luminosity monitors.

The arrangement of some of the most important sub-detectors is shown in Figure 4.2 in a longitudinal view along the beam axis.

The coordinate system is given by the magnetic field of the superconducting solenoid. The z -axis is parallel to the beam axis, pointing in the direction of the electron beam. The x -axis is the horizontal and the y -axis the vertical coordinate. The polar angle will be called θ and the azimuthal angle φ ; the coordinate R will be defined as $R = \sqrt{x^2 + y^2}$.

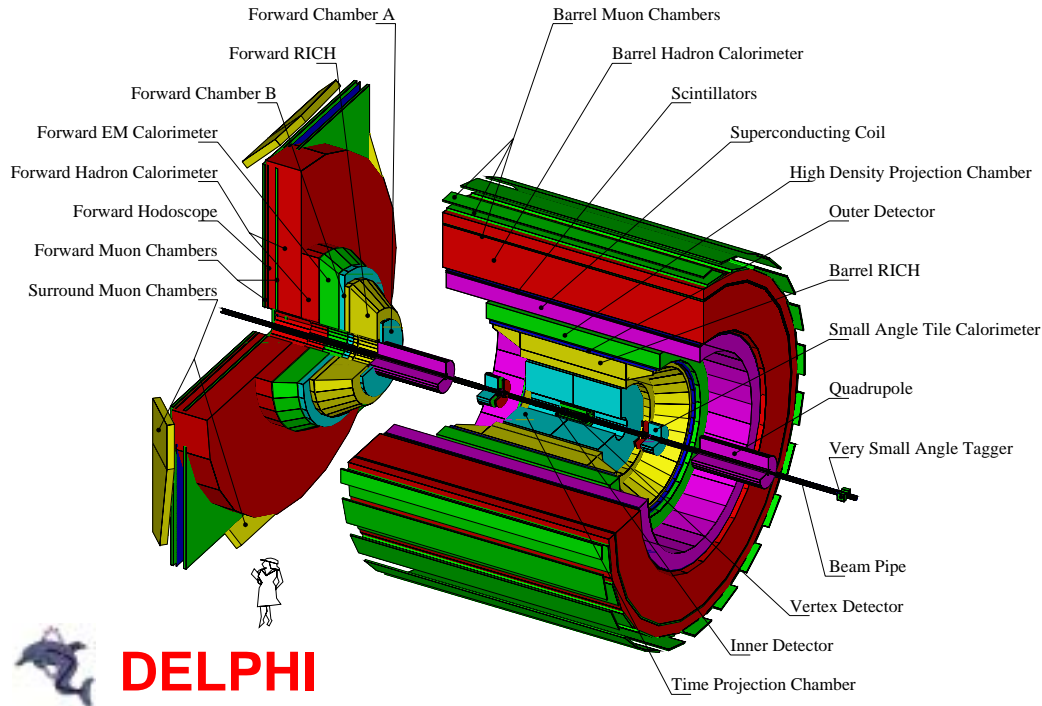


Figure 4.1: *A three dimensional view of the DELPHI detector.*

4.2.2 Tracking

The reconstruction of the trajectory of a charged particle is achieved with a combination of several independent tracking detectors. The barrel contains four cylindrical detectors, one of which is specially designed for precise tracking near the interaction point. The tracking capability is extended to the end-cap region with a combination of planar tracking detectors. Each of the tracking devices measures track segments which are combined at a later stage in order to reconstruct the full particle trajectory.

Charged particles move along a helix within the homogeneous magnetic field given by the superconducting solenoid. The tracking detectors measure the curvature of tracks from which the momentum and the charge of the particle can be determined.

The magnetic field of 1.2 T is produced by a superconducting coil with a radial dimension of 2.75 m and a length of 7.4 m. This makes it one of the worlds largest coils ever built. The conductor consists of a single layer of NbTi which carries a current of 5000 A. It is cooled from the outside by forced flow of liquid helium to a temperature

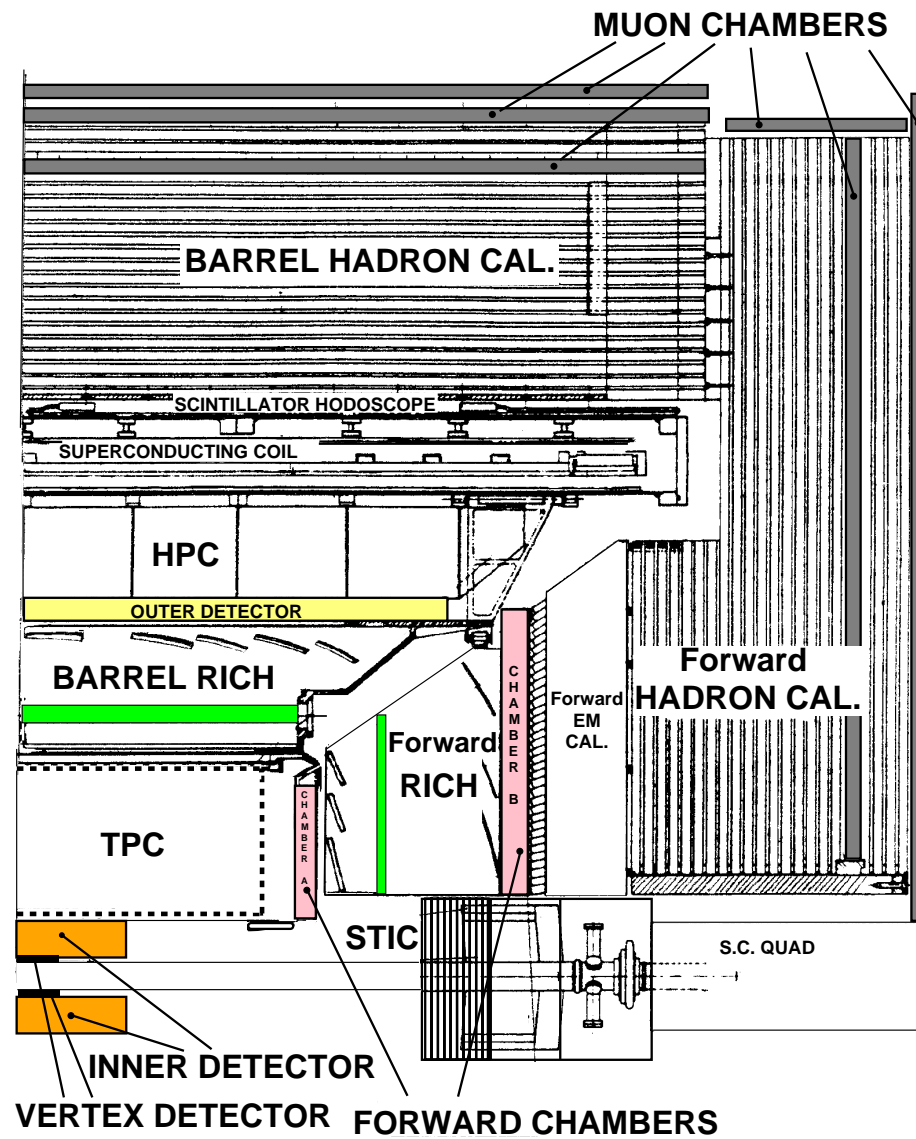


Figure 4.2: *Longitudinal view of the DELPHI detector.*

of 4.5° K. Essential for the homogeneity of the field are two compensating coils at the end flanges of the main coil.

4.2.2.1 The Time Projection Chamber

The Time Projection Chamber (TPC) [83] is the main tracking detector of DELPHI. The detector provides three-dimensional space points in a volume with a radius of 120 cm and a length of 2×150 cm. For polar angles θ between 21° and 39° and between 141° and 159°, track reconstruction is based on at least four space points. For polar angles between 39° and 141° up to 16 points can be used.

The detector consists of two field cages, filled with a mixture of about 80% Argon and 20% CH₄ at atmospheric pressure. The chamber is split into two halves along the $z = 0$ plane and both halves have a uniform and homogeneous electric field of 150 V/cm, which is pointing inwards from the end planes and parallel to the magnetic field. The end-caps are divided azimuthally into 6 sectors where each sector has 192 anode wires and 16 circular cathode pad rows concentric with the beam-pipe.

When a charged particle traverses the TPC it creates, through ionization, electron-ion pairs at a rate of approximately 70 primary pairs per cm. Under the influence of the electric field the free electrons drift with a velocity of 6.7 cm/ μ s parallel to the magnetic field until they reach either of the two end-planes. Due to the intense magnetic field, the drift electrons are bent to a helical trajectory around the field lines attenuating any transverse diffusion. The longitudinal diffusion is not affected by the presence of the magnetic field. The final detection of the drift electrons is carried out by anode sense wires operating in proportional mode. Both ends of the TPC, the end-planes, are equipped with 6 sectors consisting of wire arrays and cathode pads, where each sector covers 60° in the azimuth with the first sector boundary being at $\varphi = 30^\circ$. The drifting electrons avalanche near the anode sense wires and hence induce a pulse on the cathode pads, which are about 7.5 mm long and 8 mm wide. The center-of-gravity of the charges is used to determine the azimuth, φ . The radial coordinate, R , is determined from the wire number hit and the time-of-arrival of the drifted electrons is used to determine the z coordinate.

In addition the measured energy deposited by the charges (dE/dX) provides information on the specific ionization of the traversing particles (see section 4.3.1.1).

The single point resolution for tracks from hadronic Z^0 decays is about 250 μ m in the $R\varphi$ plane and 880 μ m in z . The two-point separation is about 1 cm.

4.2.2.2 The Inner Detector

The Inner Detector (ID) [84] provides high redundancy information for vertex reconstruction. It has an inner radius of 12 cm and an outer radius of 28 cm, covering polar angles between 29° and 151°. It consists of two concentric parts. An inner drift chamber

with jet-chamber geometry provides 24 $R\varphi$ -points per track. Around this inner part there are 5 cylindrical multi-wire proportional chambers (MWPC), each with 192 wires and 192 circular cathode strips with about 5 mm pitch, proportional to R . The wires provide additional information to resolve left-right ambiguities from the jet-chambers and fast trigger information. In addition the cathode strips provide z -information. A precision of about 90 μm in $R\varphi$ and about 1 mm in z has been obtained.

4.2.2.3 The Outer Detector

The Outer Detector (OD) [85] consists of 5 layers of drift tubes, operated in limited streamer mode, located between radii of 197 and 206 cm. It is composed of 24 modules, each consisting of 145 drift tubes with 4.7 m length along z . Successive layers are staggered and adjacent modules are designed to overlap, giving full azimuthal coverage. Additional z information is provided by relative timing of signals from both ends of the anode wires with a precision of 4.4 cm.

The OD covers polar angles from 42° to 138° and provides $R\varphi$ coordinates with a precision of 110 μm . The resolution in the z coordinate is $\sigma(z) = 3.5$ cm. Besides improving the momentum resolution it is an important part of the fast trigger.

4.2.2.4 The Vertex Detector

The Vertex Detector (VD) [86] is inserted between the LEP beam-pipe and the ID. The aim of this detector is to provide high precision measurements of the position of particles close to the primary collision point, allowing accurate track reconstruction and precise extrapolations to the interaction region.

The DELPHI Vertex Detector was installed during the 1990 run period. The design was constrained by the small amount of space between the beam-pipe and the Inner Detector. The beam-pipe in 1990 was made of aluminium with an inner radius of 7.8 cm and a thickness of 1.2 mm, which contributed 1.3% of a radiation length. Two layers of single-sided microstrip detectors, referred to as Inner and Outer layer, were installed at radii of 9 and 11 cm. The detector had 192 plaquettes and 49152 read-out strips in all.

For the 1991 running, a new beam-pipe made of beryllium was installed with an inner radius of 5.3 cm and thickness 1.45 mm, which contributed 0.4% of a radiation length. This allowed an additional third layer (the Closer layer) to be added at an average radius of 6.3 cm. The upgraded detector had now 288 plaquettes and 73728 read-out strips and improved the overall performance of the detector substantially. The higher redundancy of hits along a track allowed to improve the association of VD hits to tracks from the outside. In addition the smaller extrapolation distance together with the thinner Beryllium beam-pipe resulted in a considerably improved extrapolation accuracy to the interaction region.

In 1994 the detector has been upgraded from two to three coordinate readout. The Closer and Outer layers have been equipped with double-sided silicon detectors, having strips orthogonal to each other on opposite sides of the detector wafer [87]. These detectors provide high precision $R\varphi$ and z coordinates.

The present detector consists of three concentric layers of silicon microstrip detectors at average radii of 6.3, 9.0 and 10.9 cm within the central region of the DELPHI detector surrounding the beam-pipe. The two layers at average radii 6.3 and 10.9 cm, consist of double-sided silicon strip detectors, while the Inner layer, at 9.0 cm, consists of single-sided detectors. The Outer layer covers the angular region between 44° and 136° . The Inner layer spans from 37° to 143° , the Closer has been extended to cover the region between 25° and 155° . A schematic view of the detector is presented in Figure 4.3. As for the previous VD versions, each layer consists of 24 modules, each of them built with 4 silicon detectors.

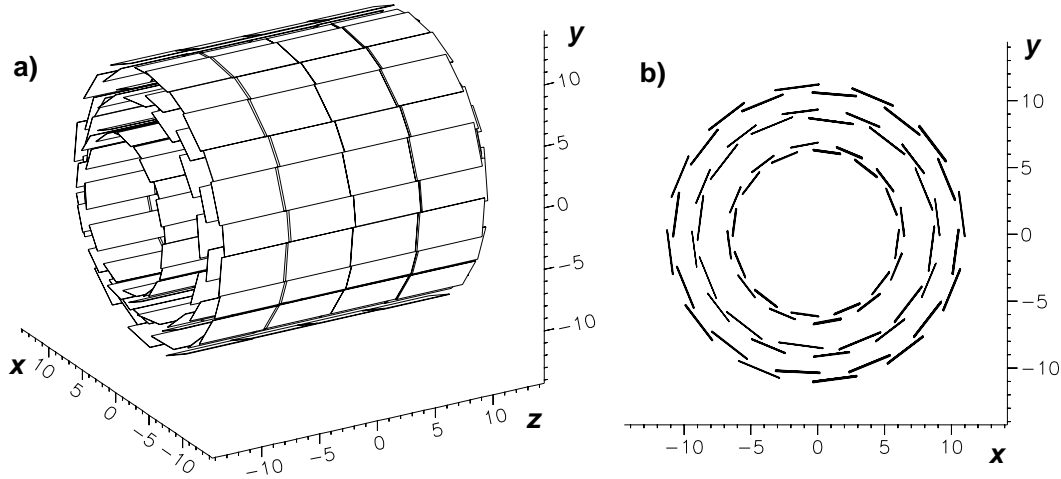


Figure 4.3: Schematic view of the DELPHI Vertex Detector in the 1994 configuration (in cm). a) Perspective view. b) Projection on the plane transverse to the beam.

The basic unit of the Vertex Detector is a plaquette of n-doped silicon crystal $300\ \mu\text{m}$ thick. Diode strips, $7\ \mu\text{m}$ wide, are implanted along the plaquettes with a pitch of $25\ \mu\text{m}$. A layer of silicon dioxide insulates them from a series of aluminium readout strips having a pitch of $50\ \mu\text{m}$, coincident with every second diode strip. A bias voltage is applied between the front and back surfaces of the plaquette in order to deplete the silicon. Reconstruction of hits is based on the ionization charge of particles traversing the depletion zone. In contrast to gaseous detectors, there is no charge amplification inside the detector. Therefore low noise read-out electronics is of crucial importance.

For the reconstruction of charged particle trajectories the intrinsic precision of the

hits is important as well as residual effects from the alignment and the stability of the detector during the running period. Since a 1° C change of temperature corresponds to a movement of the detector of $5 \mu\text{m}$, the detector must be maintained at a constant temperature. Integrated over all effects, the single point resolution in $R\varphi$ of the detector in 1990 was $11 \mu\text{m}$ and improved to $8 \mu\text{m}$ in 1991. After the alignment the remaining systematic uncertainties were less than $7 \mu\text{m}$ and $4 \mu\text{m}$ respectively.

For the present configuration the intrinsic resolution is $7.6 \mu\text{m}$ in $R\varphi$ and $9 \mu\text{m}$ in z (for perpendicular tracks). The impact parameter uncertainty (see section 4.2.2.7) is $20 \mu\text{m}$ in $R\varphi$ and $34 \mu\text{m}$ in Rz (for perpendicular tracks).

4.2.2.5 Forward Chamber A

The Forward Chamber A (FCA) [88,89] consists of two identical sub-detectors, one on either end of the TPC. One sub-detector consists of three circular chambers, each with two staggered layers and split into half-discs with an outer radius of 103 cm. The chambers are rotated with respect to each other by 120° , thus providing 2×3 coordinates. Each layer consists of 128 square drift tubes, constructed from extruded conductive plastic [90], with a $100 \mu\text{m}$ anode wire in the center.

In addition there are 32 cathode strips on each outer side of a module, rotated by 60 degrees with respect to the corresponding anode wires, to improve local pattern recognition.

The chamber is operated in limited streamer mode and is designed to measure the impact points of charged tracks at a distance of about 1.6 m from the interaction point, providing tracking and triggering information in the angular region of about $12^\circ \leq \theta \leq 30^\circ$.

After calibration a space resolution of $\sim 260 \mu\text{m}$ per layer has been obtained [91].

4.2.2.6 Forward Chamber B

Forward Chamber B (FCB) provides precise track elements using 4×3 coordinates. It is inserted at a distance of 2 m in z from the interaction point between the FRICH and the FEMC and improves therefore substantially the momentum resolution in the forward direction. It has six double wire planes which together give a high efficiency for track finding. The 12 sense wire planes are rotated in pairs by 120° with respect to each other. A complete disc covers radii from 48 cm to 211 cm. The typical point resolution per layer is $\sigma \approx 250 \mu\text{m}$ which results in a space resolution $\sigma_x = \sigma_y$ of approximately $130 \mu\text{m}$.

4.2.2.7 Overall Tracking Performance

To study the performance of the DELPHI tracking system, muons from the decay $Z^0 \rightarrow \mu^+ \mu^-$ can be used [81]. These tracks have a well defined momentum of approximately

45 GeV/c. Figure 4.4a shows the measured momentum of muons in the barrel region, where tracks contain information from all barrel detectors (VD,ID,TPC,OD) and rise from $Z^0 \rightarrow \mu^+\mu^-$ events in which the acollinearity of the two muons is $< 0.15^\circ$ to remove radiative decays. A resolution of

$$\sigma(1/p) = 0.57 \times 10^{-3}(\text{GeV}/c)^{-1} \quad (4.1)$$

is obtained. A similar plot for muons in the forward region seen in at least the Closer layer of the VD and in the FCB is shown in Figure 4.4b where a precision of

$$\sigma(1/p) = 1.31 \times 10^{-3}(\text{GeV}/c)^{-1} \quad (4.2)$$

is measured. Table 4.1 summarizes the momentum resolution for 45 GeV/c muons in different polar angle regions and with different combinations of tracking detectors included in the track fit.

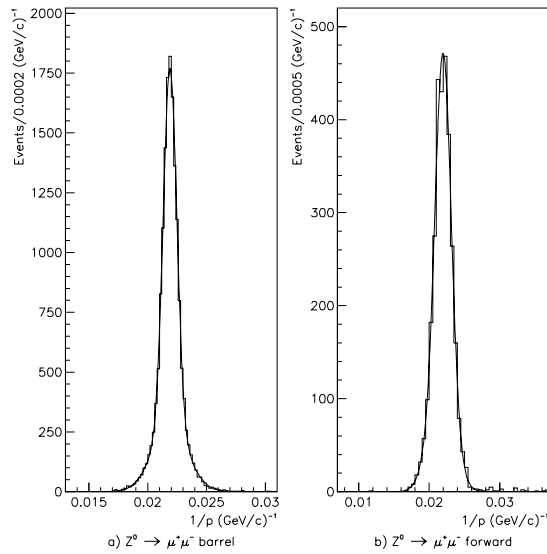


Figure 4.4: *Inverse momentum distributions for muons from $Z^0 \rightarrow \mu^+\mu^-$ decays. a) Tracks containing VD,ID,TPC and OD. b) forward tracks containing at least VD and FCB.*

For the study of short lived particles the impact parameter resolution, which is dominated by the performance of the VD, is of crucial importance. The impact parameter is defined as the distance of closest approach of a given track to the reconstructed primary vertex. For tracks coming from the primary vertex it should be exactly zero, but resolution effects smear this value. There are two types of smearing effects: the purely

$\theta(^{\circ})$	<i>Detectors</i>	$\sigma(1/p)(\text{GeV}/c)^{-1}$
≥ 42	VD+ID+TPC+OD	0.6×10^{-3}
≥ 42	ID+TPC+OD	1.1×10^{-3}
≥ 42	VD+ID+TPC	1.7×10^{-3}
≤ 36	VD + FCB included	1.3×10^{-3}
25-30	FCB included	1.5×10^{-3}
< 25	FCB included	2.7×10^{-3}

Table 4.1: *Momentum resolution for 45 GeV/c muons.*

geometric extrapolation uncertainty due to the point measurement error in the Vertex Detector (σ_{asympt}) and the multiple scattering effects due to the material in front of the measured points (σ_{ms}). The impact parameter resolution can be parametrized as the quadratic sum of these two terms:

$$\sigma_{\text{IP}}^2 = \left(\frac{\sigma_{\text{ms}}}{p_t} \right)^2 + \sigma_{\text{asympt}}^2 \quad (4.3)$$

where p_t is the transverse particle momentum in GeV/c.

The asymptotic value of the impact parameter resolution can be estimated from the apparent distance between the tracks from $Z^0 \rightarrow \mu^+ \mu^-$ decays (dimuon miss distance), where multiple scattering and vertex contributions are negligible. For the 1994 VD configuration the distribution of the distance is shown in figure 4.5. It is well described by a Gaussian, centered around zero. The 28 μm width of this distribution indicates a single track impact parameter resolution of $\sigma_{\text{IP}} = 20 \mu\text{m}$ in the $R\varphi$ plane. In the Rz plane, the dimuon miss distance varies as a function of θ . For tracks at normal incidence the impact parameter resolution in z is $\sigma_{\text{IP}} = 20 \mu\text{m}$. The extrapolation resolution for high momentum tracks, unfolding the uncertainty on the reconstructed primary vertex, was 65 μm for the 1990 VD configuration and improved to 21 μm in 1991 when the Closer layer was added to the VD.

After subtracting the resolution on the vertex position, the impact parameter uncertainties in the $R\varphi$ and Rz planes can be parametrized as:

$$\sigma_{\text{IP}_{R\varphi}}^2 = \left(\frac{\alpha_{\text{ms}}}{p \sin^{3/2} \theta} \right)^2 + (\sigma_{\text{asympt}, R\varphi})^2 \quad \sigma_{\text{IP}_z}^2 = \left(\frac{\alpha_{\text{ms}}}{p \sin^{5/2} \theta} \right)^2 + (\sigma_{\text{asympt}, Rz})^2 \quad (4.4)$$

where α_{ms} is a multiple scattering coefficient [$\text{GeV} \cdot \mu\text{m}/c$] and p is the track momentum [GeV/c]. In both expressions, the first term is the multiple scattering contribution and the second one is the track extrapolation uncertainty. Figure 4.6a shows the measured error on the impact parameter in the $R\varphi$ plane as a function of $p \sin^{3/2} \theta$. The vertex position uncertainty, shown by the bottom curve, has been quadratically subtracted.

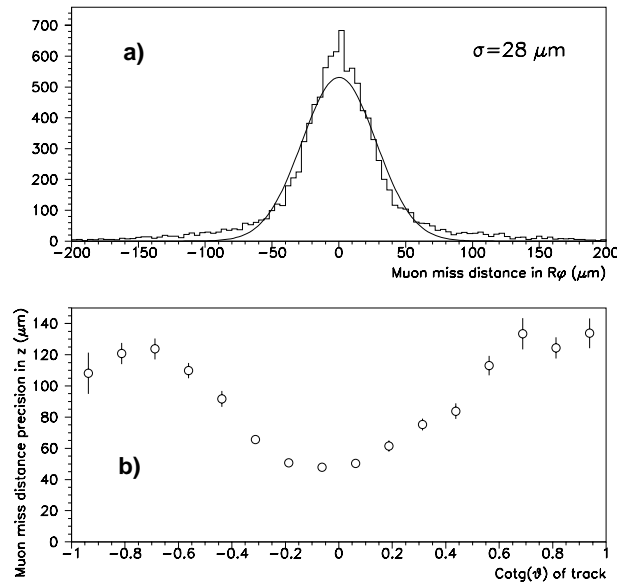


Figure 4.5: a) Miss distance between the two muons in $Z^0 \rightarrow \mu^+\mu^-$ in the $R\phi$ plane. The fitted Gaussian has a width $\sigma = 28 \mu\text{m}$, corresponding to a track extrapolation accuracy of $20 \mu\text{m}$. b) Miss distance precision between the two muons in $Z^0 \rightarrow \mu^+\mu^-$ in the Rz plane as a function of the track polar angle.

Parametrizing the impact parameter uncertainty as above gives $\alpha_{\text{ms}} = 65 \text{ GeV}\cdot\mu\text{m}/c$ and $\sigma_{\text{asympt}, R\phi} = 20 \mu\text{m}$.

The impact parameter resolution in the Rz plane depends strongly on the polar angle of the particle track. There are two effects, both contributing to degrade the impact parameter uncertainty for non-perpendicular tracks. The first is the varying point precision in z which affects the track extrapolation uncertainty; the second is the larger path in the material which contributes to increase the multiple scattering uncertainty. In Figure 4.6b, the impact parameter uncertainty is displayed as a function of momentum p for $45^\circ < \theta < 55^\circ$ and $80^\circ < \theta < 90^\circ$, after the vertex reconstruction uncertainty has been subtracted. The multiple scattering coefficient α_{ms} is $71 \text{ GeV}\cdot\mu\text{m}/c$. The effect of adding the z information, provided by the VD since 1994, can be seen in Figure 4.7, where the impact parameter in the Rz plane is shown both with and without the VD z hits, for nearly perpendicular tracks above $6 \text{ GeV}/c$. There is nearly a factor 20 improvement in the Rz impact parameter precision.

4.2.3 Calorimetry

Calorimeter detectors are used to determine the particle energy and to identify neutral hadrons and photons, which are not detected in the gaseous tracking detectors. For

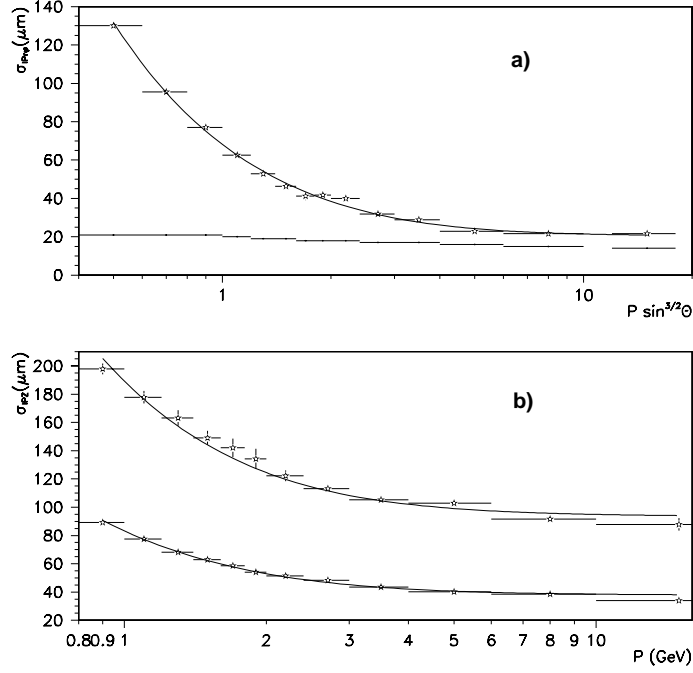


Figure 4.6: a) $R\phi$ impact parameter uncertainty measured as a function of $p \sin^{3/2} \theta$. The full line is a fit to $(65/p \sin^{3/2} \theta \oplus 20) \mu\text{m}$. b) Impact parameter uncertainty in Rz plane, measured as a function of the particle momentum. The two curves correspond to tracks with $80^\circ < \theta < 90^\circ$ (bottom) and with $45^\circ < \theta < 55^\circ$ (top), respectively. The full lines are fits of $(71/p \oplus 39) \mu\text{m}$ and $(151/p \oplus 96) \mu\text{m}$ respectively.

charged particles the information from the calorimetry is complementary to the momentum reconstruction and can be used to identify the particle type, in particular for electrons.

DELPHI is equipped with both electromagnetic and hadronic calorimeters. The electromagnetic calorimeter consists of two separate sub-detectors based on different techniques.

4.2.3.1 The High Density Projection Chamber

The High Density Projection Chamber (HPC) [92] is the barrel electromagnetic calorimeter. It is a combined sampling calorimeter and drift chamber, using the time-projection principle to measure the three-dimensional charge distribution induced by electromagnetic showers with very high granularity.

The detector has 144 modules, 24 in azimuth and 6 along the z -axis, mounted inside the magnetic field, covering the polar angles $43^\circ \leq \theta \leq 137^\circ$. Each module has

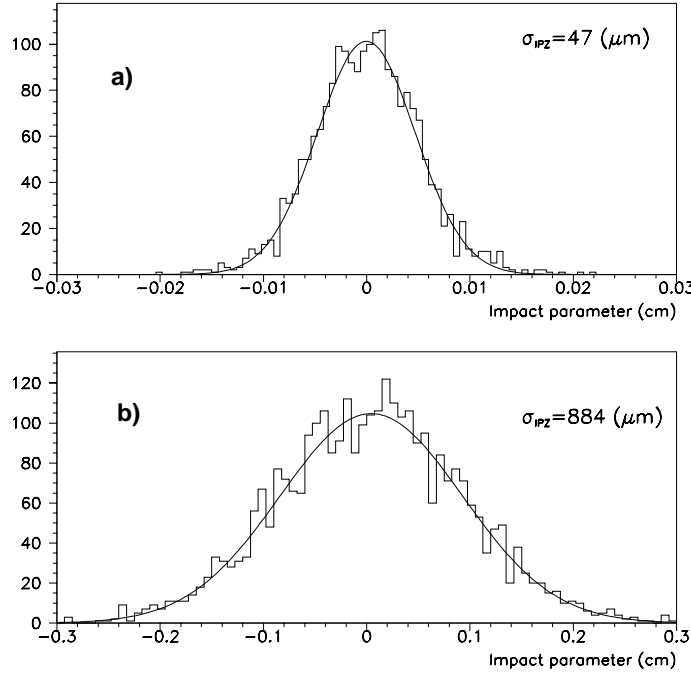


Figure 4.7: *Impact parameter in the Rz plane for tracks with $p > 6 \text{ GeV}/c$ ($70^\circ < \theta < 90^\circ$) a) using the Vertex detector z coordinate and b) taking it out of the fit.*

41 planes of lead converters separated by 8 mm gas gaps, which act as time projection chambers. The lead converters are used as electric field cage establishing an electric field along z . A total of 18 radiation lengths is distributed over 9 radial layers. The ionization charge of tracks in electromagnetic showers drift onto a single multi-wire plane at the end of each module. For fast triggering a scintillator layer has been inserted after five radiation lengths. The gaps between the modules are covered by scintillator-lead sandwich blocks to increase the hermiticity.

The linearity of the HPC energy response is monitored using neutral pions reconstructed with high precision from one photon converted before the TPC and one photon reconstructed in the HPC. The HPC has a read-out precision of 4 mm along z , 1 mrad in azimuth and 1.7 mrad in the polar angle θ . The energy resolution is:

$$\frac{\Delta E}{E} \approx \frac{32.0\%}{\sqrt{E}} \oplus \frac{20\%}{E} \oplus 4.3\% \quad [E \text{ in GeV}] \quad (4.5)$$

The resolution has been measured using electron showers from Bhabha and Compton events [81], as shown in figure 4.8.

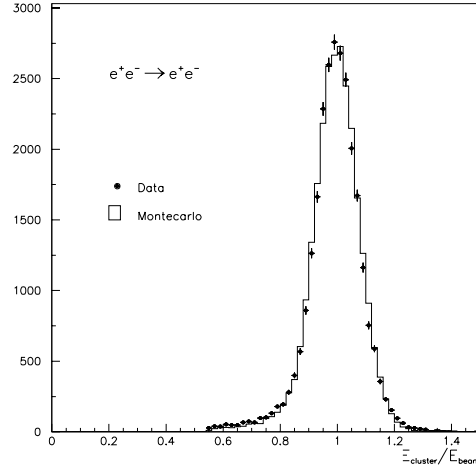


Figure 4.8: *Energy Distribution of Bhabha electrons hitting the HPC in real and simulated data.*

4.2.3.2 The Forward Electromagnetic Calorimeter

The Forward Electromagnetic Calorimeter (FEMC) complements the electromagnetic calorimetry in the forward direction. It consists of two arrays of 4532 lead-glass blocks, each placed at 284 cm from the interaction point. The scintillator blocks, shaped like truncated pyramids, have a depths of 40 cm, corresponding to 20 radiation lengths. They are arranged to point to the interaction region. Each block covers an area of $5 \times 5 \text{ cm}^2$ which results in a granularity of $1^\circ \times 1^\circ$. The detector covers polar angles from $10^\circ < \theta < 36.5^\circ$ and $143.5^\circ < \theta < 170^\circ$. The energy resolution is [81]:

$$\frac{\Delta E}{E} \approx \frac{12.0\%}{\sqrt{E}} \oplus \frac{11\%}{E} \oplus 3.0\% \quad [E \text{ in GeV}] \quad (4.6)$$

4.2.3.3 The Hadron Calorimeter

The hadron calorimeter (HCAL) is a sampling gas calorimeter which uses the iron return yoke of the magnet as absorber. The barrel part has an angular coverage of $43^\circ < \theta < 137^\circ$ and consists of 20 layers of limited streamer mode tubes inserted into 2 cm wide gaps between 5 cm thick layers of iron. Similarly, the end-caps have a sampling depth of 19 layers and covers polar angles from 11° to 48° and from 131° to 168° . The streamer charges are read out with wire chambers. The chambers operate with Ar/CO₂/Isobutane in a 1/6/3 ratio. The detector is segmented radially into four towers pointing towards the interaction point. The energy resolution was measured to

be [81]:

$$\frac{\Delta E}{E} \approx \frac{112\%}{\sqrt{E}} \oplus 21\% \quad [E \text{ in GeV}] \quad (4.7)$$

The resolution achieved in z is approximately 10 cm.

In addition to the reconstruction of neutral hadrons, the detector is used to study muons inside hadronic events. The difference in the shower shape between a particle with hadronic interactions and a muon can be used to measure the hadron contamination in a muon sample tagged by the muon chambers.

4.2.4 The Scintillation Counters

Two detectors, consisting of scintillators, cover the barrel and end-cap regions. Their main functions are to participate in fast trigger decisions, to measure the time of flight of particles (barrel scintillators) and to provide information about cosmic particles.

4.2.4.1 The Time of Flight Detector

The Time of Flight Detector (TOF) consists of scintillator counters surrounding the superconducting coil. It covers polar angles from 41° to 139° . Each of the 172 scintillators is equipped with a photomultiplier at both ends. It is used in the first level trigger of DELPHI and for elimination of cosmic events. The z -coordinate is measured with a precision of about 20 cm.

4.2.4.2 The Forward Hodoscope

The Forward Hodoscope (HOF) consists of scintillator detectors and is installed between the end-cap yoke and the second layer of the muon chambers. It is subdivided into 4 quadrants with 28 counters each. It is used as a muon trigger in the forward region.

4.2.5 The Luminosity Detectors

The luminosity is measured by counting the number of $e^+e^- \rightarrow e^+e^-$ Bhabha events at small angles with high statistics. The cross-section for this process, which proceeds almost entirely through the exchange of a photon in the t -channel, can be calculated theoretically with very high precision. Until 1994, the luminosity at the Z^0 peak was measured by using the SAT detector and the VSAT detector was used to measure the relative luminosity at different energies. In 1994 the SAT has been replaced by a new calorimeter, the STIC [93].

4.2.5.1 The Small Angle Tagger

The Small Angle Tagger (SAT) covering polar angles from 43 to 135 mrad, consists of alternating layers of lead sheets and plastic scintillating fibres, aligned parallel to the beam. The fibres and the lead layers provide a total thickness of 28 radiation lengths. Behind the calorimeters the fibres are collected in bundles and coupled via conical light-guides to circular photodiodes.

4.2.5.2 The Small Angle Tile Calorimeter

The Small angle Tile Calorimeter (STIC) is a sampling calorimeter with 49 sandwiches of 3.4 mm steel laminated lead plates and 3 mm thick scintillator tiles for a total of 27 radiation lengths. It provides hermiticity in the angular region between 29 and 185 mrad. Two planes of silicon microstrips, extending radially between 70 and 170 mm, are inserted to provide a precise measurement of the θ position of the shower. The full calorimeter is formed by two cylinders with projective geometry and a front radius between 65 and 420 mm. It is placed on both sides of the interaction point at a distance of 2200 mm.

This calorimeter is used to define the normalization, by measuring the luminosity at the per mil level. At 45.6 GeV the energy resolution is $\sigma_E/E = 2.7\%$.

4.2.5.3 The Very Small Angle Tagger

The Very Small Angle Tagger (VSAT) is used to measure the relative luminosity at the off-peak energy points. It covers the very forward region from 0.29 to 0.40°. The monitor is 7.7 m away from the interaction point and consists of a 24 radiation length deep W/Si calorimeter with a relative resolution of about 5% for 45 GeV/ c particles. The VSAT provides also fast beam background information and tagging information for two-photon physics.

4.2.6 The Muon Chambers

The Muon Chambers identify muons, which penetrate the iron yoke of the magnet. The DELPHI muon detector consists of the Barrel Muon Chambers and the Forward Muon Chambers. For the 1994 data taking period the so-called Surround Muon Chambers were added to bridge the small gap between the barrel and the forward region.

4.2.6.1 The Barrel Muon Chambers

The Barrel Muon Chambers (MUB) cover polar angles between 53° and 127°. It consists of six active planes of drift chambers. Two of them, the inner layers, are within the magnet return yoke after 90 cm of iron. The remaining four layers, the

outer and the peripheral layers, are installed after a further 20 cm of iron. The inner and the outer layer have the same azimuthal coverage. The dead space between these detectors is covered by the peripheral layer with a small overlap. Typically, therefore, a muon traverses either two inner layer chambers and two outer layer chambers, or just two peripheral layer chambers.

Each chamber measures the $R\varphi$ coordinate to ± 6 mm. Measuring $R\varphi$ in both the inner and the outer layer determines the azimuthal angle φ of muon candidates leaving the HCAL within about 1° . These errors are much smaller than the effect of multiple scattering on muons traversing the calorimeter.

4.2.6.2 The Forward Muon Chambers

The forward region is covered by two planes of drift chambers, the MUF. One of them is inside the magnet return yoke after about 85 cm of iron and the second after a further 20 cm of iron. Each plane is subdivided into four quadrants, consisting of two layers of drift cells which are rotated by 90° relative to each other. The MUF covers polar angles from 9° to 43° . The spatial resolution has been measured to be about 3 mm.

4.2.7 The Ring Imaging Cherenkov Detectors

The Ring Imaging Cherenkov detectors are special to the DELPHI detector and provide superior hadron identification by Cherenkov angle reconstruction. The full solid angle coverage is provided by two independent detectors, the Barrel Ring Imaging Cherenkov Detector (BRICH) in the barrel region and the Forward Ring Imaging Cherenkov Detector (FRICH) in the forward region. The detectors combine liquid and gaseous radiator media to identify stable particles over most of the momentum range.

During the data taking in 1990 and 1991 the RICH detectors were partially installed and covered a restricted angular interval. The BRICH was fully installed and operational by the end of 1991, whereas the FRICH came fully into operation in 1993.

4.2.7.1 The Barrel Ring Imaging Cherenkov Detector

The Barrel Ring Imaging Cherenkov Detector (BRICH) is a 3.5 m long cylinder located between radii of 246 and 394 cm [94]. Liquid radiator boxes, filled with C_6F_{14} , are mounted near the inner radius. The photo electrons are detected by drift-tubes, which act as a TPC with read out chambers at the outer end. Photo electrons produced in the gas volume, which is filled with C_5F_{12} , are reflected by parabolic mirrors on the same drift tubes. The detector is split in two halves by a central support wall. Each half contains 24 drift-tubes and liquid radiators in azimuth.

4.2.7.2 The Forward Ring Imaging Cherenkov Detector

The Forward Ring Imaging Cherenkov Detector (FRICH) [95,96] covers both end-cap regions in the polar angle $15^\circ < \theta < 35^\circ$ and $145^\circ < \theta < 165^\circ$. The principle of operation is similar to the BRICH. The design is different because of the geometry and the crossed E - B field in the photon detector. The photo electrons, produced by the ionization of TMAE, drift in the crossed E and B fields with a Lorentz angle of 52° . The detector combines a layer of liquid C_6F_{14} and a volume of gaseous C_4F_{10} into a single assembly. Each of the two end-caps of the FRICH detector consists of two 180° segments joined together in the vertical plane. These are assembled out of two parts: a main vessel, that houses the photon detector and which serves as gas radiator volume, and a shallower vessel, flanged onto the main vessel, which carries the liquid radiator containers. Inside the vessels the components are arranged in sectors spanning 30° in azimuth. Each sector contains three liquid radiator boxes, a photon detector and five spherical mirrors. The detector operates at about 30°C temperature, and all the fluids are individually referred to atmospheric pressure.

4.2.8 The Trigger System

In order to cope with high luminosities and large background rates, the DELPHI trigger system is composed of four successive levels (T1, T2, T3 and T4) of increasing selectivity. The first two trigger levels (T1 and T2 respectively) are synchronous with respect to the Beam Cross Over signal (BCO) while the third and fourth (T3 and T4 respectively) are software filters performed asynchronously with respect to the BCO. With eight bunches of electrons and positrons circulating at equal distances in the machine, the LEP bunch-crossing interval is $11\ \mu\text{s}$. The T1 and T2 trigger decisions are taken $3.5\ \mu\text{s}$ and $39\ \mu\text{s}$ after the BCO respectively. T3 halves the background passing T2 by applying the same logic as T2 but using more detailed information.

Each sub-detector contributes to the trigger decision with data generated by the respective sub-trigger processors. The decision of both T1 and T2 is taken by OR-ing a number of “in time” combinations of the sub-detector data. The overlapping geometrical acceptance of the different detectors provides a good amount of redundancy between the different trigger conditions:

- Track elements give trigger signals in the Time Projection Chamber (TPC), Forward Chambers A and B (FCA/FCB), Inner Detector (ID), Outer Detector (OD), Time Of Flight detector (TOF). A transverse momentum cut $p_t \geq 1\ \text{GeV}/c$ for $29^\circ \leq \theta \leq 151^\circ$ and $p_t \geq 1.6\ \text{GeV}/c$ in the forward region $11^\circ \leq \theta \leq 33^\circ$ and $147^\circ \leq \theta \leq 169^\circ$ is applied.
- Muons are triggered in the barrel region, $50^\circ \leq \theta \leq 130^\circ$ with a 1° hole at 90° by the Barrel Muon detector (MUB) and in the forward regions, $15^\circ \leq \theta \leq 41^\circ$

and $139^\circ \leq \theta \leq 165^\circ$, by the Forward Muon sub-detector (MUF).

- Electromagnetic energy deposition gives trigger signals in the barrel region by the High density Projection Chamber (HPC) and in the forward regions by the Forward Electromagnetic Calorimeter (FEMC), demanding energy depositions above 2 GeV and 2.5 GeV respectively. A lower threshold for the FEMC (1.2 GeV) is used when correlated with other detectors.
- Hadronic energy deposition is triggered by the Hadron Calorimeter barrel (HAB) and forward (HAF). Energy deposition thresholds of 0.5, 2 and 5 GeV are used.

The interplay of the different trigger components produces an efficiency very close to 1.0 over nearly the full solid angle. Global inefficiencies of the order of 10^{-4} to 10^{-5} are obtained for $\mu^+\mu^-$ and e^+e^- . Due to a higher final state multiplicity, hadronic events ($e^+e^- \rightarrow Z^0 \rightarrow \text{hadrons}$) are easily detected and triggered with an efficiency close to 100% over the full solid angle.

4.2.9 The Data Acquisition System

The DELPHI Data Acquisition System (DAS) [97] was designed to provide a high degree of independence for the individual sub-detectors. The readout multiplicity of the DELPHI detector corresponds to a total of about 200,000 channels. In view of this complexity the DAS was designed to meet a number of demands typical for high-energy physics experiments: low dead time at trigger rates up to 20 Hz, possibility of independent running and monitoring of each sub-detector, standardization of hardware and software. The DELPHI Data Acquisition System (DAS) has been divided into 19 individual partitions, including two partitions for the trigger system and the central readout. The organization of these partitions has been standardized up to a high level.

The hardware of the readout system, placed in huts beside the detector, is based on the FASTBUS standard. Data accepted by the first- and second-level trigger is accumulated in the Front End Buffers (FEB) of the FASTBUS modules for third-level trigger processing. In a number of intermediary steps the data is then filtered, merged and temporarily stored in higher-level buffers, before being collected in the Global Event Buffer (GEB). The condensed data is transferred from the GEB to the central DAS computer at ground level by an optical link. In parallel to the main data stream, ending with storage on IBM 3480 cartridges, a secondary stream of specially selected events, e.g. hadronic Z^0 events, is stored for later use by the sub-detectors for calibration and monitoring.

4.3 Particle Identification

The identification of charged particles in DELPHI relies on the specific ionization energy loss dE/dx in the TPC, on the RICH detectors, and on the electron and muon identification provided by the calorimeters and the muon chambers.

4.3.1 Hadron Identification

4.3.1.1 Specific Ionization in the TPC

The energy loss of a charged particle is described by the *Bethe-Bloch* formula as a function of the momentum:

$$-\frac{dE}{dx} = 4\pi N_A r_e^2 m_e c^2 q^2 \frac{Z}{A} \frac{1}{\beta^2} \left\{ \ln \left(\frac{2m_e c^2 \gamma^2 \beta^2}{I} \right) - \beta^2 - \frac{\delta}{2} \right\} \quad (4.8)$$

where N_A is Avogadro's number, m_e , r_e and e are mass, charge and the classical radius of the electron, Z and A are the atomic number and the atomic weight of the absorbing material and I is the mean excitation potential of the element. The additional factor δ takes into account density effects which become significant only for very energetic particles.

The deposited energy per unit trail length (dE/dx) is a function of the particle's speed. Measuring dE/dx and momentum simultaneously therefore allows one to deduce a particle's mass, thus identifying the particle. However, the velocity β is not directly measured, but the momentum $p = \beta\gamma m$ is. This implies $\log(p) = \log(\beta\gamma) + \log(m)$, so when dE/dx is plotted as a function of $\log(p)$ for different particle species, the curves for different species are simple translations, with respect to $\log(p)$, of the same curve that traces how dE/dx depends upon $\log(\beta\gamma)$.

The precision of the measurement is increasing with the number of space points measured along the track. The sense wires of the TPC provide up to 192 ionization measurements per track. To be used in the physics analysis, the dE/dx value coming from the truncated mean is required to have at least 30 contributing measurements. Sense wire signals with a width incompatible with a single track are not used. The dependence of dE/dx on the momentum p of the particle is shown in figure 4.9. The value of the Fermi plateau, normalized to the minimum ionizing particle, is found to be 1.52 units and for particles in jets the average precision is about 7.4%.

Thus in the momentum region between 4 and 10 GeV/ c a 1.5σ separation between pion and kaon tracks is reached. In combination with the information of the Ring Imaging Cherenkov detector, this provides a powerful tool for particle identification.

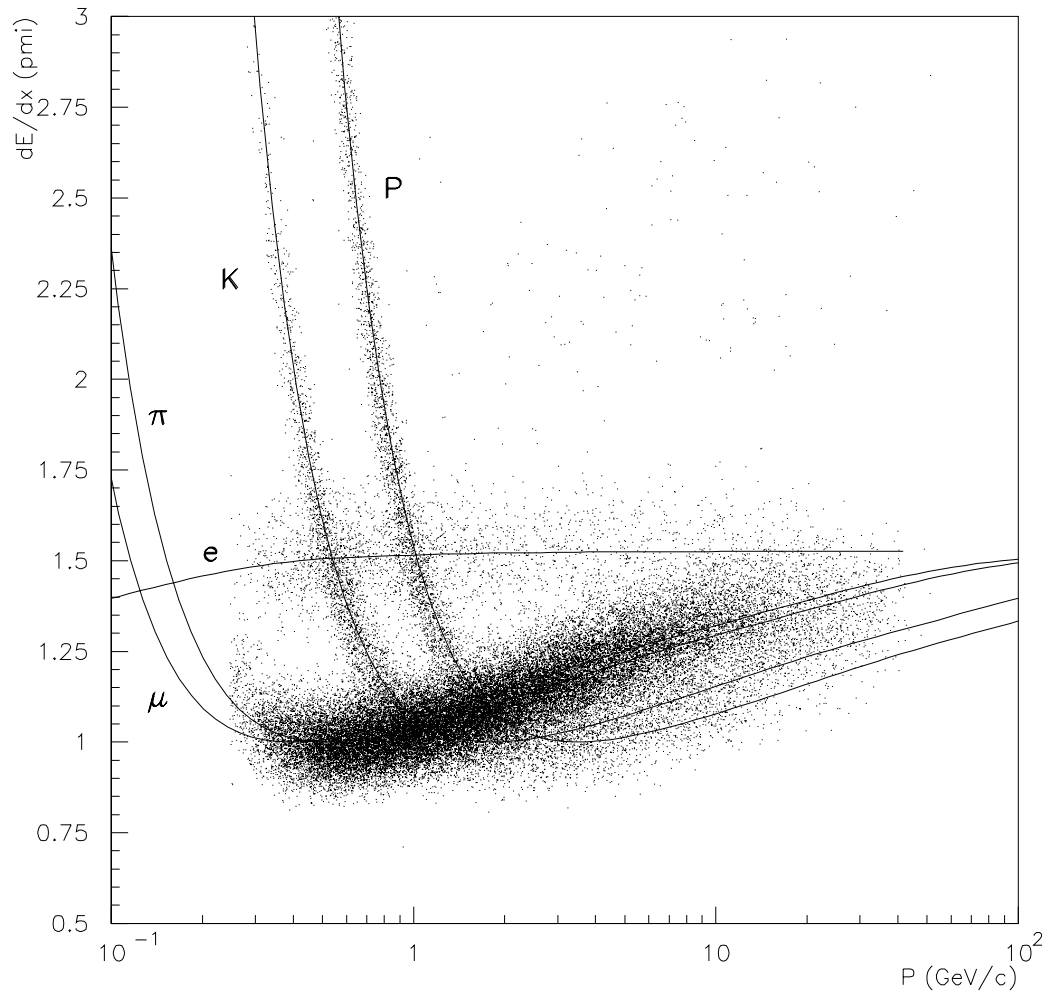


Figure 4.9: *Specific energy loss in the TPC as a function of momentum.*

4.3.1.2 Ring Imaging Cherenkov Detectors

Charged particles traversing a dielectric medium with a velocity larger than the speed of light in that medium produce a cone of Cherenkov light. The emission angle θ_C depends on the mass M and the momentum p via the relation $\cos \theta_C = 1/n \times \sqrt{1 + M^2/p^2}$, where n is the refractive index of the radiator medium. The number of photons emitted per unit length is proportional to $\sin^2 \theta_C$. The number of photons associated to a particle track and their Cherenkov angles are the input information used for identifying its mass. In the momentum range where kaons and protons are below the Cherenkov threshold no light is emitted by these particles. This property is used to separate kaons and protons in this momentum range from lighter particles, which emit photons.

The DELPHI RICH contains two radiators of different refractive indices. A particle first crosses the liquid radiator, which is used to identify particles with momenta lower than 10 GeV/ c . The gas radiator is used to identify particles between 2.5 GeV/ c and 25 GeV/ c . Both the emission angles of individual UV photons in the liquid and gas radiators and the total number of detected photons provide information about the mass of a charged particle. The total momentum range is divided into intervals, which depend on the refractive indices of the two radiators. The liquid radiator is used for $\pi/K/p$ separation up to ≈ 4.5 GeV/ c and for K/p separation up to ≈ 6 GeV/ c . The gas radiator serves for veto identification of heavy particles below the K threshold. At higher momenta it provides $\pi/K/p$ separation up to ≈ 20 GeV/ c . The particle identification is based on the comparison between the measured Cherenkov angle and the expected angle for each mass hypothesis at the measured momentum. In the region between 4 GeV/ c and 20 GeV/ c a 2.5σ separation of kaons and pions has been obtained.

In a hadronic event, the main difficulty is to deal with the background under the Cherenkov signal, whose shape and level is different for each track and a priori unknown. The algorithm used fits a flat background and no attempt is made to separate it from the signal. For each mass hypothesis, the expected signal is known. A flat background is adjusted in order to build and maximize a likelihood probability. The probabilities corresponding to the known particle types are then used for tagging. For statistical analysis, the likelihood probability is computed as a function of the Cherenkov angle, and the best one retained. In figure 4.10 the average Cherenkov angle of tracks in hadronic events is shown for the liquid and the gas radiator as a function of the momentum.

The RICH information together with the dE/dx data allow charged particle identification over most of the momentum range. They can be combined, providing three levels of proton and kaon tags (*loose*, *standard* and *tight*) corresponding to different purities. The efficiency for the identification of a K^\pm using a standard tag, averaged over the momentum spectrum above 0.7 GeV/ c , is about 70% with a contamination of 30% [81].

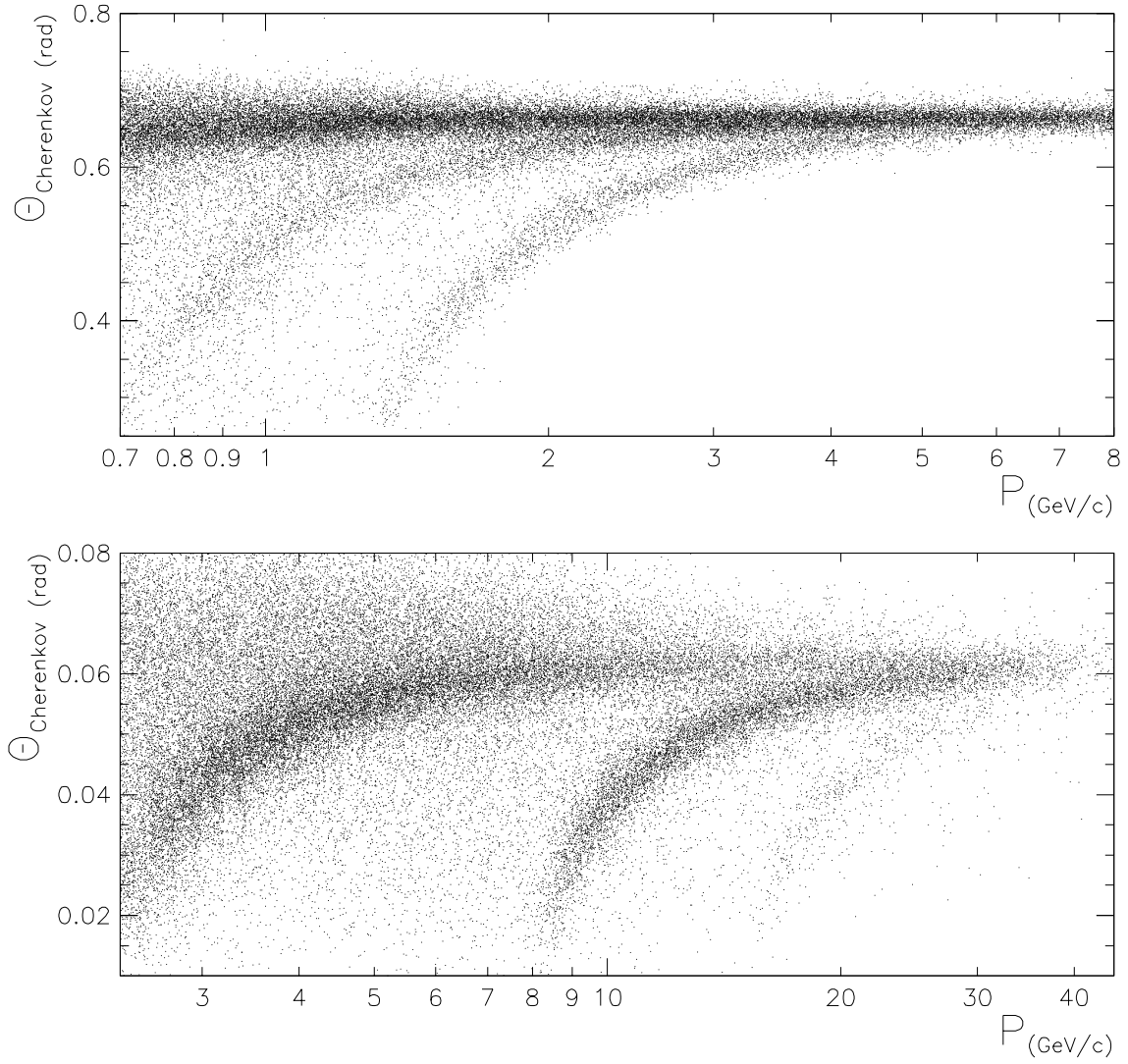


Figure 4.10: Average Cherenkov angle per track as a function of momentum in hadronic events in the Barrel RICH, for the liquid (top) and gas (bottom) radiators. The three bands on both plots correspond to pions (uppermost band), kaons (middle band) and protons (lowest band).

4.3.2 Lepton Identification

4.3.2.1 Muon Identification

The identification of muons is based on tracking information from the muon chambers which is combined with track extrapolations from the central tracking detectors. The identification strategy relies on the ability of muons to travel through large depths of matter before being absorbed. The iron of the hadron calorimeter provides a filter which enables a first level of separation between muons and hadrons. The bulk of hadrons are stopped by this material, whereas all muons of momentum above 2 GeV/ c are expected to penetrate to the muon chambers.

Charged particle tracks, reconstructed in the central tracking detectors, are extrapolated through the solenoid and the iron of the HCAL, to the muon chambers. During this extrapolation the tracking errors are propagated and the errors from multiple scattering and from chamber resolutions are added. For each extrapolated track, the muon chamber hits in the event are searched through. A χ^2 comparison is then made between a hit and the extrapolated track coordinates in that layer. In this way a set of hits is selected and a χ^2 fit is made at the innermost reference surface. If the fit does not converge the worst hit is removed and the fit is repeated. The actual identification of a particle as being a muon is made with the routine MUFLAG. A description of the algorithm may be found in reference [98]. In MUFLAG four tag levels are defined, which correspond to different sets of refit criteria and cuts on χ^2 quantities constructed after the refit:

- The **very loose** tag gives high efficiencies but has also a high misidentification probability
- The **loose** tag is designed to give muon samples with high efficiency, but still with acceptably low levels of background.
- The **standard** tag provides samples with well understood efficiencies and purities. The standard tag is a subset of the loose tag.
- The **tight** tag gives high-purity muon samples.

Table 4.2 shows the efficiencies and misidentification probabilities for the four tags averaged over the barrel and end-cap regions using $Z^0 \rightarrow \mu^+\mu^-$ events.

The identification of muons created within jets in hadronic events is more complicated. In this case the muons are surrounded by a large number of hadrons of which some occasionally penetrate the iron. Due to the lower momentum of muons in jets, multiple-scattering effects become significant. Therefore the muon identification efficiencies will be somewhat lower in hadronic events.

<i>Tag</i>	<i>Efficiency (%)</i>	<i>Misid. Probability (%)</i>
Very loose	95.94 ± 0.08	5.40 ± 0.19
Loose	94.81 ± 0.09	1.46 ± 0.10
Standard	86.14 ± 0.15	0.69 ± 0.07
Tight	76.01 ± 0.19	0.44 ± 0.06

Table 4.2: *Efficiencies and misidentification probabilities for muons [81].*

4.3.2.2 Electron Identification

Electron identification is performed using two independent and complementary measurements: the dE/dx measurement of the TPC and the energy deposition in the HPC.

Charged particle tracks are extrapolated from the TPC to the calorimeter and their crossing point with the calorimeter as well as their directions are calculated. The comparison of the energy E in the calorimeter with the independently measured momentum p from the tracking detectors provides a powerful tool for electron identification. After correction for radiation effects in front of the calorimeter, the ratio E/p should be close to unity independent of the electron energy. In addition the longitudinal shower profile is parametrized as a function of the shower depths. In order to quantify the electromagnetic character of the measured showers, the shower profiles are fitted and a cut on the χ^2 is used to select electron candidates.

The second completely independent piece of information for electron identification is the measurement of the specific energy loss in the TPC. The value of the Fermi plateau, normalized to the minimum ionizing particle, is found to be 1.52 units (see section 4.3.1.1). The separation between e and π in jets is above 3σ for momenta below 4.5 GeV/ c and above 2σ for momenta up to 20 GeV/ c .

Three different levels of electron tagging are provided; they can classify electrons with a momentum above 2 GeV/ c . Their typical efficiencies and misidentification probabilities are shown in table 4.3.

<i>Tag</i>	<i>Efficiency (%)</i>	<i>Misid. Probability (%)</i>
Loose	85	≈ 1.6
Standard	55	≈ 0.4
Tight	45	≈ 0.2

Table 4.3: *Efficiencies and misidentification probabilities for electrons [81].*

Chapter 5

Analysis

Measurements are not to provide numbers but insight.

— INGRID BUCHER

5.1 Introduction

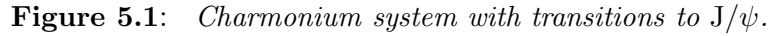
The J/ψ meson was discovered in 1974 and interpreted as a $c\bar{c}$ bound state [64,65]. In the spectrum of charmonium states, the J/ψ and ψ' are the only states which decay into two leptons with non negligible branching fractions. The ψ' meson is also referred to as $\psi(2S)$ or $\psi(3685)$. Figure 5.1 shows the transitions between the different charmonium states and their decay chain to J/ψ . Some properties of the J/ψ and ψ' mesons are listed in table 5.1.

	J/ψ	ψ'
Mass	$3096.88 \pm 0.04 \text{ MeV}/c^2$	$3686.00 \pm 0.09 \text{ MeV}/c^2$
Width	$88 \pm 5 \text{ keV}/c^2$	$277 \pm 31 \text{ keV}/c^2$
$Br(\mu^+\mu^-)$	$(5.97 \pm 0.25)\%$	$(7.7 \pm 1.7) \times 10^{-3}$
$Br(e^+e^-)$	$(5.99 \pm 0.25)\%$	$(8.8 \pm 1.3) \times 10^{-3}$

Table 5.1: *The properties of the J/ψ and ψ' mesons [27].*

According to theoretical calculations [99], charmonium states are produced in b hadron decays on average in the following proportions:

$$\eta_c : J/\psi : \chi_{c1} : \psi' = 0.57 : 1 : 0.27 : 0.31$$



In Z^0 decays J/ψ mesons are predominantly produced via b hadron decays through a *colour suppressed* spectator diagram (see section 2.3.6). Other production mechanisms at LEP energies are:

1. Decays of higher charmonium states; $Br \approx 0.8 \times 10^{-3}$;
2. $Z^0 \rightarrow q\bar{q}g^*$, $g^* \rightarrow J/\psi + X$; $Br \approx 1.7 \times 10^{-4}$;
3. $Z^0 \rightarrow c\bar{c}J/\psi$; $Br \approx 2.7 \times 10^{-5}$;
4. $Z^0 \rightarrow J/\psi gg$; $Br \approx 5.0 \times 10^{-7}$;
5. $Z^0 \rightarrow J/\psi \gamma$; $Br \approx 10^{-8}$

$$Br(Z^0 \rightarrow \text{direct } J/\psi) = 3.3 \times 10^{-4}$$

Since the *direct* J/ψ production gives only a small contribution, J/ψ events can be used to tag b events. J/ψ decays represent a clear signature for individual b hadrons. Since the J/ψ has no significant lifetime, the J/ψ decay vertex corresponds also to the B decay vertex. This makes the identification of other decay particles of the B meson easier and allows the full reconstruction of exclusive B meson decays. If a sufficient number of b hadrons can be fully reconstructed, these decays provide clean mass measurements. The measurement of the two body decay branching ratios is also a good test of the factorization model of beauty mesons (see section 2.3.5).

Low multiplicity modes like $B_d^0 \rightarrow J/\psi K_S^0$, $B_d^0 \rightarrow J/\psi K^{*0}$ and $B^\pm \rightarrow J/\psi K^\pm$ have been observed with significant statistics in $p\bar{p}$ collisions [101,102] and in $\Upsilon(4S)$ decays [103–105], and with marginal statistics in Z^0 decays [106–109].

The aim of this study is to reconstruct B mesons, through their decay into charmonium states using the full data sample DELPHI recorded from 1991 to 1994. In this analysis the J/ψ and ψ' mesons are both tagged via their decays into lepton pairs, i.e. $J/\psi \rightarrow \ell^+\ell^-$ and $\psi' \rightarrow \ell^+\ell^-$ where $\ell = \mu$ or e. First a sample of J/ψ and ψ' events was selected and the inclusive branching fraction was measured. The resulting candidate sample was used to perform a search for exclusive B meson decays.

5.2 Event Selection

The data used in this analysis correspond to about 3.2 million hadronic Z^0 decays recorded by the DELPHI experiment in 1991 – 1994. A detailed description of the data sample is given in table 5.2. In the first step of the analysis hadronic Z^0 events are

<i>Year</i>	<i>Number of hadronic Z^0 recorded by DELPHI</i>	<i>Integrated Luminosity</i>	<i>Number of events after hadronic event selection</i>
1991	275 K	$\sim 16 \text{ pb}^{-1}$	255154
1992	751 K	$\sim 23 \text{ pb}^{-1}$	704145
1993	755 K	$\sim 35 \text{ pb}^{-1}$	710044
1994	1484 K	$\sim 46 \text{ pb}^{-1}$	1392879
total	3265 K	$\sim 120 \text{ pb}^{-1}$	3062222

Table 5.2: *Data sample used in this analysis.*

selected. In order to reduce the background contamination, only charged and neutral particles that fulfilled a set of quality criteria were selected. For charged particles to be used in this analysis, the reconstructed track had to meet the following requirements:

- Momentum in the range $0.4 \text{ GeV}/c < p < \sqrt{s}/2$
- Error on measured momentum $\Delta p/p < 100\%$

- Track length $L > 30$ cm.
- Track impact parameter in the $r\phi$ plane < 5 cm
- Track distance in z to the interaction point < 10 cm
- Polar angle of the track in the range $20^\circ < \theta < 160^\circ$

Neutral particles were selected with the electromagnetic calorimeters. For neutrals to be used in the analysis they must have

- Electromagnetic shower energy $E_{\text{HPC}} > 0.8$ GeV or $E_{\text{FEMC}} > 0.4$ GeV
- Polar angle in the range $20^\circ < \theta < 160^\circ$

Hadronic Z^0 events used for this analysis were selected by requiring

- at least 4 charged particles with a momentum above 400 MeV/ c
- the total energy of the selected charged tracks amounted to at least 12% of the available center-of-mass energy
- the thrust axis is well separated from the beam-pipe, $|\cos \theta_{\text{thrust}}| < 0.95$, where θ_{thrust} is the polar angle of the event thrust axis.

The resulting data sample has a small contamination from $\tau^+\tau^-$ events (about 0.1%), and negligible contamination from beam-gas scattering and $\gamma\gamma$ interactions. The efficiency for this hadronic event selection was estimated with the Monte Carlo sample to be $(95.3 \pm 0.1)\%$.

Charged and neutral particles were clustered into jets using the LUCCLUS algorithm with default parameters [110]. Each event was divided into two hemispheres by the plane perpendicular to the thrust axis, which was computed using all the charged and neutral particles.

The primary vertex was reconstructed for every hadronic event using the beamspot position as a constraint. The beamspot is defined as the interaction region of the electron and positron beams. The x and y positions are known with typical uncertainties of about 9 μm and 4 μm respectively. Only tracks with at least 2 VD hits were used in the primary vertex fit. The resolution of the reconstructed primary vertex was found to be: $\sigma(x) \approx 22$ μm , $\sigma(y) \approx 10$ μm and $\sigma(z) \approx 430$ μm . Since 1994 the VD provides the measurement of the z coordinate which improved the vertex resolution. Therefore the vertex resolution in 1994 was measured to be: $\sigma(x) \approx 20$ μm , $\sigma(y) \approx 9.6$ μm and $\sigma(z) \approx 23$ μm . This resolution is worse in $b\bar{b}$ events where a high fraction of tracks comes from secondary vertices.

A sample of about 5 million $Z^0 \rightarrow q\bar{q}$ events has been simulated using the Lund Parton Shower Monte Carlo JETSET 7.3 [45,110]. The generated events were followed

through the detailed detector simulation DELSIM [111] and then processed through the same analysis chain as the real data. In addition dedicated samples of $Z^0 \rightarrow b\bar{b}$ and $Z^0 \rightarrow b\bar{b} \rightarrow J/\psi X$ have been generated.

5.3 Kinematical Study

A sample of 20 000 $Z^0 \rightarrow b\bar{b} \rightarrow J/\psi X$ events has been generated with the Lund Parton Shower Monte Carlo JETSET 7.3 in order to study the kinematical properties of J/ψ events and to find the optimal selection criteria. The J/ψ was forced to decay into either a muon or an electron pair.

The momentum distribution of B mesons produced in Z^0 decays is shown in figure 5.2a. The mean value is about 31 GeV/c and approximately 94% of the B mesons have momentum greater than 15 GeV/c. The mass of the J/ψ meson is 60% of the B meson mass and the momentum spectrum is in principle determined by the fragmentation function of the b quark (see section 2.2.2). The momentum spectrum of the J/ψ meson is shown in figure 5.2b. It has a mean value of about 19 GeV/c and shows an almost symmetric distribution. About 98% of the J/ψ mesons have a momentum larger than 5 GeV/c.

In the laboratory system, the J/ψ tends to decay asymmetrically – one of the leptons carries off most of the momentum. Therefore the decay $J/\psi \rightarrow \ell^+\ell^-$ typically results in one high and one low momentum lepton. Figure 5.2d shows the momentum spectrum of muons from J/ψ decays. The mean value is about 10 GeV/c. For electrons the average momentum is somewhat smaller. This is due to the *final state radiation* which affects about 45% of electron pairs but only 15% of the muon pairs. In order to reconstruct J/ψ mesons with high efficiency, the cut on the lepton momentum should be as low as possible. However, leptons with momentum less than 2 GeV/c cannot be reconstructed and the reconstruction efficiency increases with momentum.

In the J/ψ rest frame the leptons are always back to back but due to the boost of the J/ψ the mean opening angle becomes about 30°. The opening angle of the leptons coming from J/ψ decays is shown in figure 5.2e. The long tail of the distribution comes from slow J/ψ 's. For J/ψ 's with a momentum larger than 5 GeV/c the opening angle of the two leptons is almost always below 1.6 rad (see figure 5.2f).

5.4 J/ψ Reconstruction

After having studied the kinematical properties of J/ψ decays, the next step is to reconstruct J/ψ candidates from their decays into muon and electron pairs. The data sample used consists of the full statistics recorded by the DELPHI experiment in 1991 – 1994, corresponding to an integrated luminosity of about 120 pb⁻¹. After applying

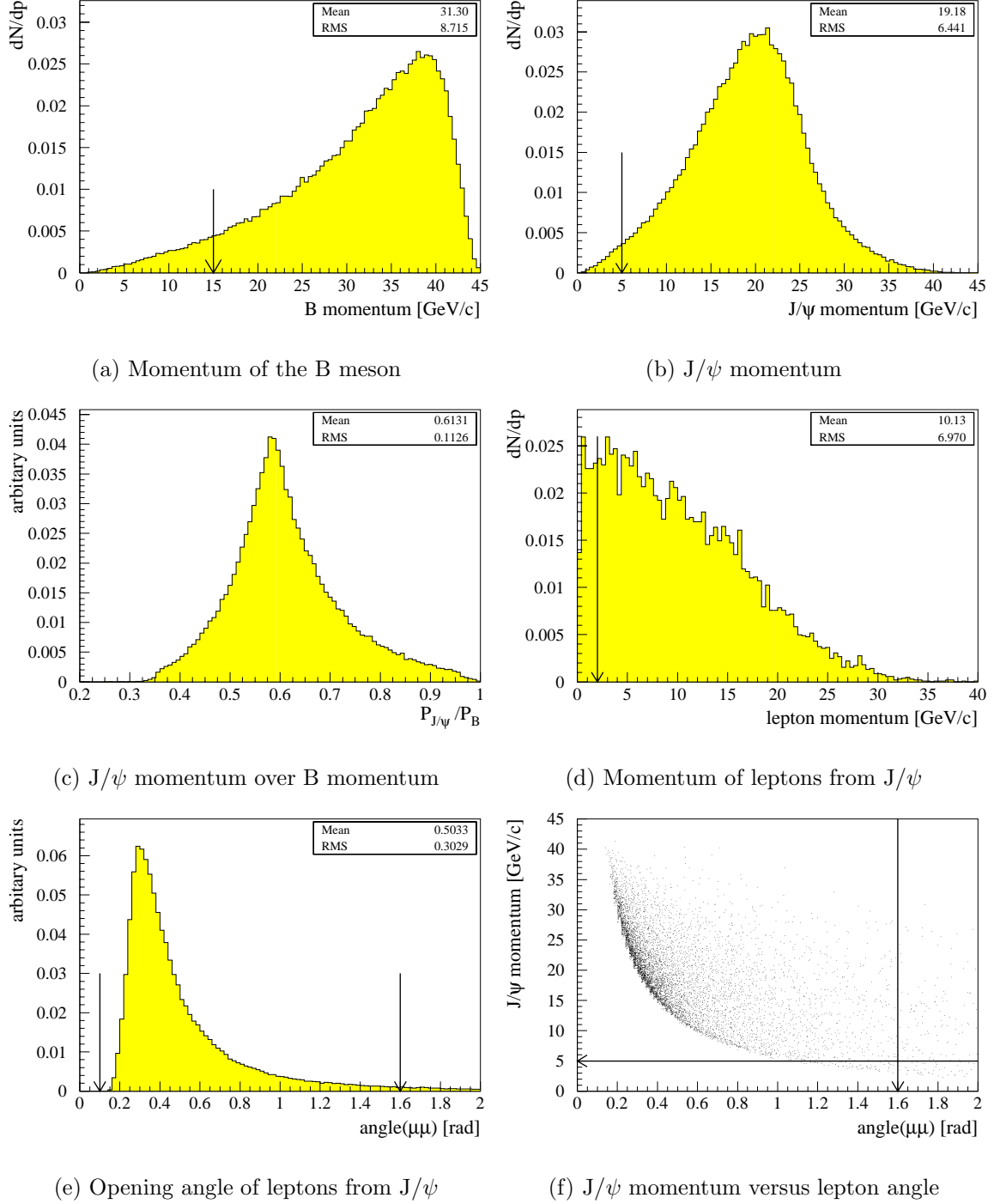


Figure 5.2: Kinematical distributions from the Monte Carlo study. The arrows indicate the cuts applied in the analysis.

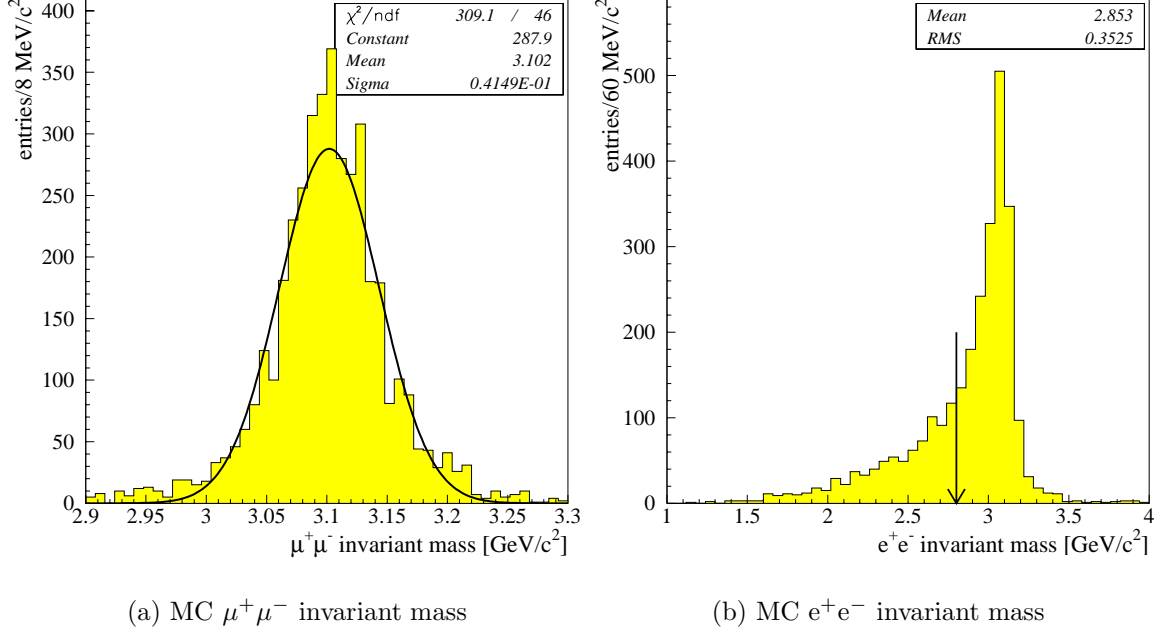


Figure 5.3: Invariant mass spectrum of simulated $Z^0 \rightarrow J/\psi + X$ events.

the hadronic event selection described in section 5.2 about 3 million hadronic events were selected.

Since the selection of J/ψ mesons is only the starting point of the analysis, the emphasis was put on the maximization of the efficiency. For both decay channels the first requirement has been to have at least one precisely tagged lepton in the event. For the second track somehow looser identification criteria have been assumed to keep the tagging efficiency high.

5.4.1 Muon Selection

Two muon candidates with momentum above 2 GeV/ c were selected. Both muon candidates had to be identified by the MUFLAG algorithm described in section 4.3.2.1.

To recover lost muons, mainly those outside the geometrical acceptance of the Muon Chambers, information from the HCAL was used, requiring a muon-like energy deposition in at least 3 of its 4 layers. These additional muons improve the efficiency with a slightly increased background.

At least one of the muon candidates has been required to be identified by MUFLAG as a *tight*, *standard* or *loose* tagged muon. The second muon candidate could have a looser identification. It has been also accepted if it was tagged in the HCAL or as a *very loose* muon according to MUFLAG.

The invariant mass spectrum of $\mu^+\mu^-$ pairs from $Z^0 \rightarrow b\bar{b} \rightarrow J/\psi X$ Monte Carlo events is shown in figure 5.3a. A Gaussian fit to the distribution gives a width of 41 MeV/ c^2 .

5.4.2 Electron Selection

Electrons have been selected using the electron identification algorithm based on the longitudinal shower profile in the HPC and the dE/dx information from the TPC, described in section 4.3.2.2. This electron tagging gives a lower efficiency than the tagging for muons. Both tracks have been required to have momentum greater than 2.0 GeV/ c and to be identified with a *tight*, *standard* or *loose* tag. Combinations with *very loose* electron candidates were rejected. Since muons have a certain probability to be misidentified as *loose* electrons, it has been cross-checked, that there is no double-counting due to electron, and muon identification at the same time.

Due to the energy loss by bremsstrahlung and final state radiation the measured electron momenta will be reduced and the e^+e^- mass spectrum has a significant low mass tail. Figure 5.3b shows the invariant mass spectrum of electron pairs from simulated Monte Carlo events. About 30% of the $J/\psi \rightarrow e^+e^-$ events are below 2.8 GeV/ c^2 . Therefore the reconstruction efficiency for $J/\psi \rightarrow e^+e^-$ events is lower than for $J/\psi \rightarrow \mu^+\mu^-$ events.

5.4.3 Secondary vertex fit

With this procedure two leptons with opposite charge were selected. Both lepton tracks have been required to be contained in the same hemisphere defined by the event thrust axis. For each J/ψ candidate, with tracks having an opening angle larger than 0.1 rad, a three-dimensional secondary vertex fit was performed. A cut has been put on the vertex fit probability rejecting pairs giving a probability of forming a common vertex below 1%. Figure 5.5 shows the distribution of the secondary vertex probability for Monte Carlo $\mu^+\mu^-$ events in the J/ψ mass region. The cut on $Prob(\chi^2) > 1\%$ removes contributions from the combinatorial background quite efficiently.

For J/ψ candidates passing these cuts, the difference between the generated and the reconstructed J/ψ vertex position for x , y and z coordinate is shown in figure 5.4. The distributions were fitted with two Gaussians. The first Gaussian describes the contribution from tracks associated with hits in the vertex detector, while the second Gaussian takes into account contributions from tracks with no associated VD hits or badly measured momentum. Table 5.3 shows the obtained resolution of the reconstructed secondary vertex. It can be seen that the resolution in z improved significantly since 1994, when double-sided layers were added to the VD. Reconstructed J/ψ candidates have been required to have a momentum larger than 5 GeV/ c to select J/ψ 's produced in B decays.

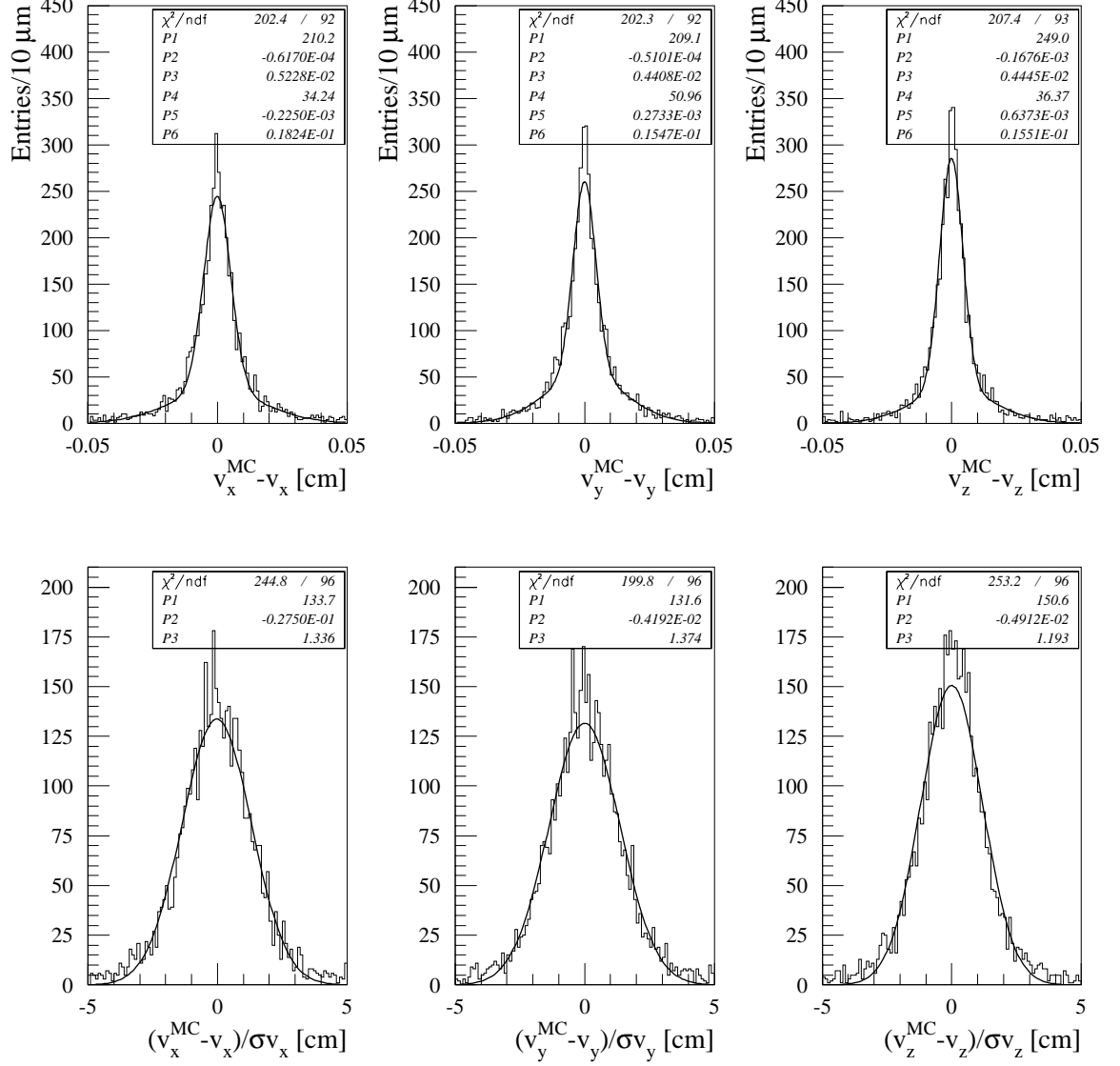


Figure 5.4: The upper plots show the difference between the reconstructed and generated J/ψ vertex position for x , y and z coordinate. The full line is a fit to the data with a sum of two Gaussians. The lower plots show the corresponding pull quantities.

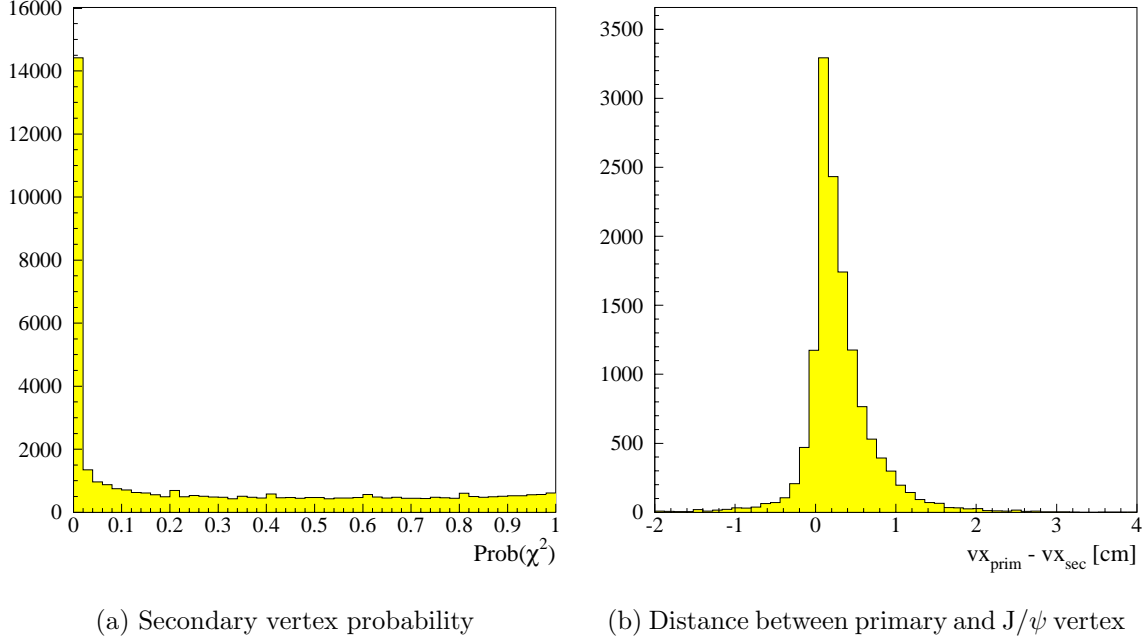


Figure 5.5: *Secondary vertex probability.*

In summary the following cuts have been applied to J/ψ candidates:

- the two leptons have to be in the same hemisphere, defined by the thrust axis, and must have a momentum greater than 2 GeV/c;
- angle between leptons must be between 0.1 and 1.6 rad;
- total reconstructed momentum $p_{J/\psi}$ greater 5 GeV/c;
- secondary vertex probability $Prob(\chi^2) > 1\%$

The resulting invariant mass distributions for muon and electron pairs are shown in figure 5.6. J/ψ candidates have been defined as unlike sign lepton pairs passing all the above cuts and having an invariant mass $2.95 < m_{\mu\mu} < 3.25$ GeV/ c^2 and $2.80 < m_{ee} < 3.25$ GeV/ c^2 . For electron pairs a wider and asymmetric mass window was allowed to take radiation effects into account. The total number of J/ψ candidates in the muon sample is $N_{cand} = 627$ and $N_{cand} = 279$ in the electron sample.

Decays of ψ' mesons have been searched for in the channel $\psi' \rightarrow \ell^+\ell^-$ applying the same procedure as for the J/ψ . Taking into account the reduced leptonic branching ratio of this channel, the ψ' yield is expected to be approximately 20 times smaller than the J/ψ yield. The number of ψ' 's obtained from the fit to the dimuon sample

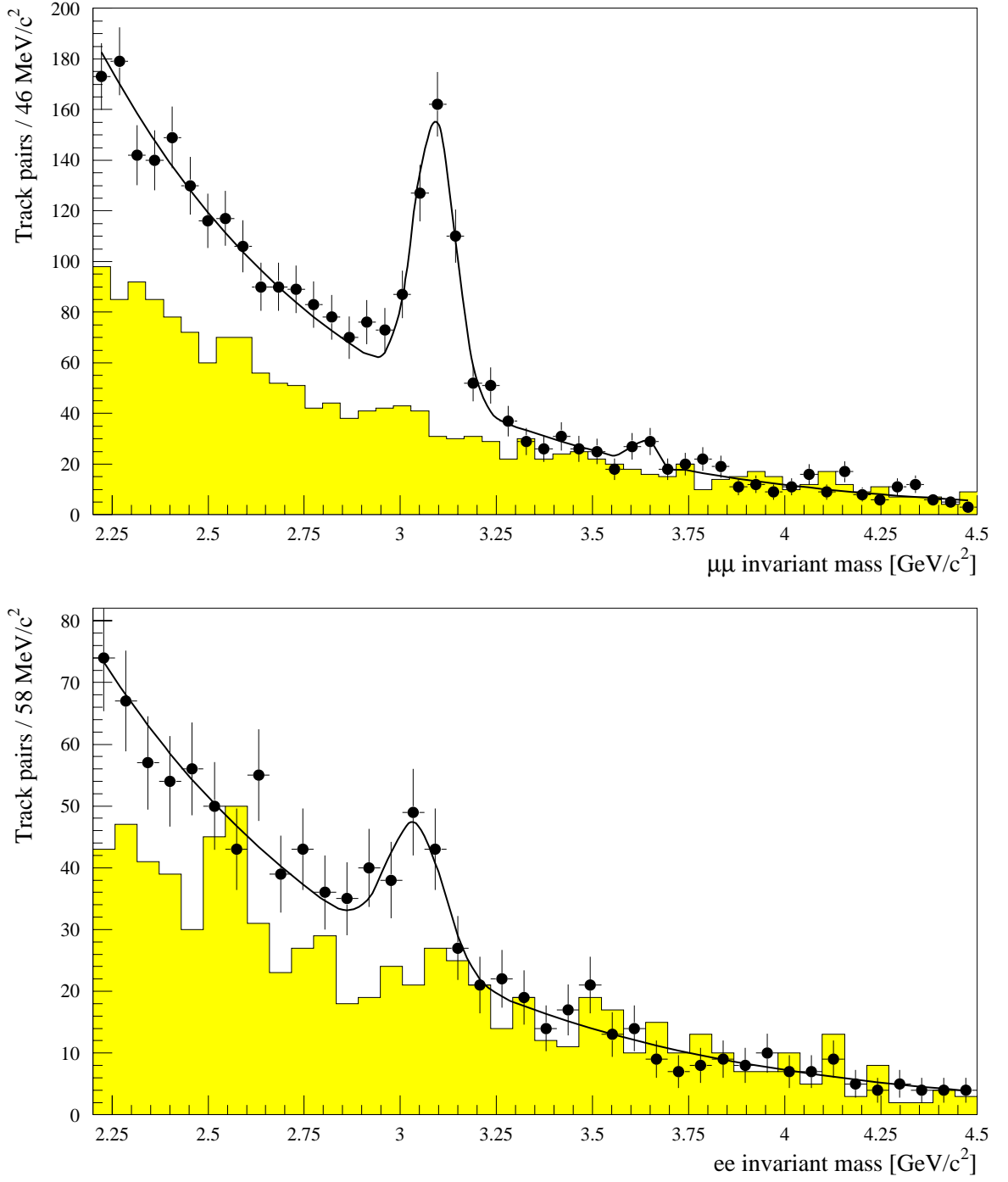
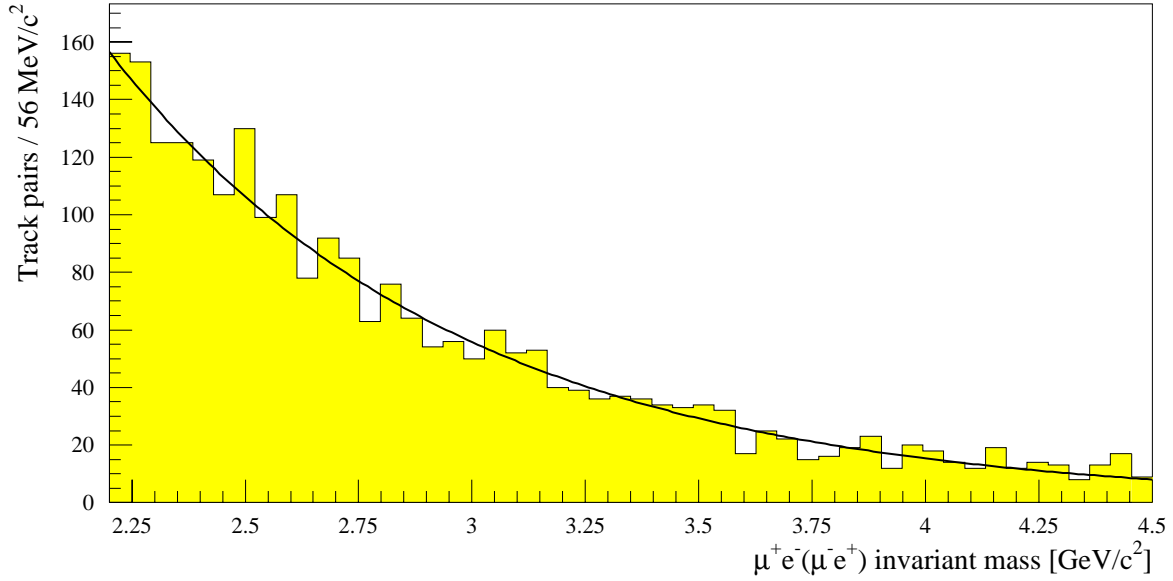


Figure 5.6: Invariant mass distributions for $\mu\mu$ and ee pairs. The points represent unlike-sign lepton combinations, while the shaded histogram shows like-sign lepton combinations. The full line shows the fit to the data.

<i>Data sample</i>	<i>First Gaussian</i>			<i>Second Gaussian</i>		
	x (μm)	y (μm)	z (μm)	x (μm)	y (μm)	z (μm)
1991 – 1993	51 ± 2	56 ± 2	686 ± 15	228 ± 8	227 ± 9	2025 ± 80
1994	52 ± 2	44 ± 4	44 ± 2	182 ± 10	155 ± 9	156 ± 17

Table 5.3: *Secondary vertex resolution.***Figure 5.7:** $\mu^\pm e^\mp$ invariant mass distribution.

is compatible with the expected number. An excess of 14 ± 3 events has been found in the ψ' mass region in the dimuon sample, whereas no excess was found in the e^+e^- sample.

5.5 Background and Efficiency

In order to obtain the number of signal events, the invariant mass distributions of unlike-sign muon and electron pairs have been separately fitted by a Gaussian superimposed to an exponential background. An exponential was found suitable to describe the shape of the background whereas the signal shape was modelled with a Gaussian. The mean and the width of the Gaussian and the background shape were left free in the fit. From the fit to the muon sample, the J/ψ mass and width were found to be 3.091 ± 0.005 GeV/c^2 and 51 ± 5 MeV/c^2 , respectively. The resulting values from the

<i>Sample</i>	<i>Channel</i>	<i>Mass</i> (GeV/ c^2)	<i>Width</i> (MeV/ c^2)	<i>Number of</i> J/ ψ	<i>Number of</i> <i>background events</i>
Data	$\mu^+\mu^-$	3.091 ± 0.005	51 ± 5	335 ± 27	291
MC	$\mu^+\mu^-$	3.102 ± 0.003	46 ± 4		
Data	e^+e^-	3.031 ± 0.027	75 ± 23	76 ± 12	203
MC	e^+e^-	3.017 ± 0.015	77 ± 14		

Table 5.4: J/ ψ reconstruction results for data and Monte Carlo.

fits on data and Monte Carlo for the $J/\psi \rightarrow \mu^+\mu^-$ and the $J/\psi \rightarrow e^+e^-$ sample are listed in table 5.4. It can be seen that the measured masses and widths are in agreement with Monte Carlo. The invariant mass spectra for muon and electron candidate pairs are shown in figure 5.6. The number of signal events has been derived from the result of the fit and are given separately for the two samples in table 5.4.

An alternative method to determine the background of the J/ψ sample is to use *wrong lepton combinations*. These are combinations of opposite charge track pairs formed by an electron and a muon, but passing otherwise the same selection criteria as J/ψ candidates. The invariant mass spectrum of wrong lepton combinations is shown in figure 5.7. The slope parameter in the exponential term of the background obtained by the fit to the $\mu^+\mu^-$ and e^+e^- distributions has been checked on the $e^\pm\mu^\mp$ pair sample and was found to be consistent. As can be seen from figure 5.6 (shaded histograms) the like-sign lepton distribution can not be used to model the shape of the background.

The background under the J/ψ peak has been studied on a sample of about 5 million inclusive $Z^0 \rightarrow q\bar{q}$ Monte Carlo events. These events were subjected to the same selection cuts as used for the data sample and the same analysis procedure was applied. The dominant background comes from cascade decays. These are semileptonic decays of a b quark ($b \rightarrow c\ell\bar{\nu}$) followed by the semileptonic decay of the c quark ($c \rightarrow s\bar{\ell}\nu$) and results in events with two unlike-sign leptons. Furthermore there is a contribution from combinations of one real lepton with a misidentified hadron or combinations of two misidentified hadrons. In the muon sample also combinations with muons from a K or π decay can contribute.

Since the process $Z^0 \rightarrow J/\psi + X$ has a small branching ratio, the efficiency of the J/ψ selection has been calculated using a dedicated Monte Carlo event sample containing about 10000 J/ψ mesons produced in b hadron decays. The events were passed through the full detector simulation. About half of the events were forced to decay into muon pairs and the other half into electron pairs. After having applied the same selection cuts, the selection efficiencies for $J/\psi \rightarrow \mu^+\mu^-$ and $J/\psi \rightarrow e^+e^-$ have been calculated. The reconstruction efficiency $\epsilon_{J/\psi}$ for the muon channel was found to be of $(33.4 \pm 1.7)\%$ and $(8.2 \pm 0.9)\%$ for the electron channel. The $J/\psi \rightarrow e^+e^-$

reconstruction efficiency is significantly lower, due to the low mass tail of the dilepton spectrum and reduced efficiency and acceptance of the electron tagging.

5.6 Inclusive Branching Ratios

The number of signal events can be turned into an evaluation of the branching ratio $Br(Z^0 \rightarrow J/\psi + X)$ as:

$$Br(Z^0 \rightarrow J/\psi + X) = \frac{N_{J/\psi}}{\epsilon_{J/\psi}} \cdot \frac{\epsilon_{\text{had}}}{N_{\text{had}}} \cdot \frac{\Gamma_{\text{had}}}{\Gamma_{Z^0}} \cdot \frac{1}{Br(J/\psi \rightarrow \ell^+ \ell^-)} \quad (5.1)$$

where

- $N_{J/\psi}$ is the number of J/ψ candidates (corrected for background);
- $\epsilon_{J/\psi}$ is the J/ψ reconstruction efficiency;
- N_{had} is the number of multihadronic events;
- Γ_{Z^0} and Γ_{had} are the total and hadronic Z^0 decay widths; $R_{\text{had}} = \Gamma_{\text{had}}/\Gamma_{Z^0} = 0.699 \pm 0.002$ [27];
- $Br(J/\psi \rightarrow \ell^+ \ell^-) = (5.91 \pm 0.23)\%$ [112] (where ℓ can be either an electron or a muon).

In order to minimize the total error on the measurement, only the $\mu^+ \mu^-$ sample has been used to calculate the inclusive branching ratio. The final result is:

$$Br(Z^0 \rightarrow J/\psi + X) = (3.7 \pm 0.3 \pm 0.3) \times 10^{-3}$$

The various contributions to the systematic error are listed in table 5.5. All percentage errors are relative to the central value.

The result obtained is in good agreement with a previous measurement made by DELPHI [106] and measurements of other LEP experiments. Table 5.6 summarizes the current LEP measurements.

The inclusive branching ratio of b quarks to J/ψ mesons is calculated as follows:

$$Br(b \rightarrow J/\psi + X) = \frac{N_{J/\psi}^b}{\epsilon_{J/\psi}} \cdot \frac{\epsilon_{\text{had}}}{2N_{\text{had}}} \cdot \frac{\Gamma_{\text{had}}}{\Gamma_{b\bar{b}}} \cdot \frac{1}{Br(J/\psi \rightarrow \ell^+ \ell^-)} \quad (5.2)$$

where $N_{J/\psi}^b$ is the number of J/ψ mesons produced in b quark decays. In order to calculate this number the component coming from direct J/ψ production has to be subtracted from $N_{J/\psi}$. According to the colour-octet model [100], $Br(Z^0 \rightarrow \text{direct } J/\psi) = 3.3 \times 10^{-4}$, which gives a 8.9% contribution from direct J/ψ production.

Error source	$\Delta(Z^0 \rightarrow J/\psi(\mu^+\mu^-)X)$
Selection cuts	3.6%
$\epsilon_{J/\psi}$	5.1%
$N_{\text{background}}$	3.3%
ϵ_{had}	0.1%
R_{had}	0.3%
$Br(J/\psi \rightarrow \ell^+\ell^-)$	3.9%
Total systematic error	8.1%

Table 5.5: Systematic errors in the measurement of the inclusive branching ratio.

Measurement	Ref.	$Br(Z^0 \rightarrow J/\psi X)$
DELPHI	[106]	$(3.7 \pm 0.4 \pm 0.4) \times 10^{-3}$
OPAL	[108]	$(3.9 \pm 0.2 \pm 0.3) \times 10^{-3}$
ALEPH	[107]	$(3.8 \pm 0.4 \pm 0.3) \times 10^{-3}$
L3	[113]	$(3.6 \pm 0.5 \pm 0.4) \times 10^{-3}$
my analysis		$(3.7 \pm 0.3 \pm 0.3) \times 10^{-3}$

Table 5.6: LEP measurements of the J/ψ production in Z^0 decays.

From the muon samples, by using $R_b = \Gamma_{b\bar{b}}/\Gamma_{\text{had}} = 0.221 \pm 0.003$ [27] and after subtracting the component from $N_{J/\psi}$ coming from direct J/ψ production, one obtains:

$$Br(b \rightarrow J/\psi + X) = (1.15 \pm 0.09 \pm 0.14) \times 10^{-2}$$

The result obtained is in good agreement with the measurement by CLEO performed in $\Upsilon(4S)$ decays of $Br(b \rightarrow J/\psi + X) = (1.12 \pm 0.07)\%$ [114]. The different b hadron composition in Z^0 and $\Upsilon(4S)$ ¹ decays is not expected to produce any substantial difference between the two measurements.

5.7 Exclusive B Meson Reconstruction

Since the direct J/ψ production in Z^0 decays is very small, the presence of a J/ψ in an event almost certainly indicates a B hadron decay. After the selection of J/ψ candidates through their decays into muon and electron pairs, as described in the previous sections, an analysis of exclusive B meson decays has been performed. As a result of this J/ψ selection 627 candidates have been found in the $J/\psi \rightarrow \mu^+\mu^-$ channel and 279 in the

¹At the $\Upsilon(4S)$ resonance only B^\pm and B_d^0 mesons can be produced.

$J/\psi \rightarrow e^+e^-$ channel. This sample was used as a starting point for the reconstruction of exclusive B meson decays. B meson candidates can be reconstructed by combining further tracks with the two leptons of the J/ψ . The following decay channels have been investigated²:

- $B^\pm \rightarrow J/\psi K^\pm$; $B^\pm \rightarrow \psi' K^\pm$
- $B_d^0 \rightarrow J/\psi K_S^0$; $B_d^0 \rightarrow \psi' K_S^0$
- $B_d^0 \rightarrow J/\psi K^{*0}$; $B_d^0 \rightarrow \psi' K^{*0}$ where $K^{*0} \rightarrow K^+\pi^-$
- $B_d^0 \rightarrow J/\psi K^+\pi^-$; $B_d^0 \rightarrow \psi' K^+\pi^-$ (non resonant)
- $B^\pm \rightarrow J/\psi K^\pm \pi^+\pi^-$; $B^\pm \rightarrow \psi' K^\pm \pi^+\pi^-$
- $B^\pm \rightarrow J/\psi K^{*\pm}$; $B^\pm \rightarrow \psi' K^{*\pm}$ where $K^{*\pm} \rightarrow K_S^0 \pi^\pm$ (non resonant)
- $B^\pm \rightarrow J/\psi K_S^0 \pi^\pm$; $B^\pm \rightarrow \psi' K_S^0 \pi^\pm$ (non resonant)

In the following J/ψ denotes also ψ' , except otherwise mentioned. For the reconstruction of the K_S^0 only the decay channel $K_S^0 \rightarrow \pi^+\pi^-$ has been considered. K^{*0} mesons were reconstructed in the channel $K^+\pi^-$ and $K^{*\pm}$ mesons in the channel $K^{*\pm} \rightarrow K_S^0 \pi^\pm$.

In table 5.7 the expected number of signal events per 10^6 Z^0 events are given for the individual decay channels. For the B decay branching ratios recent experimental measurements [27] have been used. In order to get the real number of reconstructed events, the numbers in table 5.7 have to be multiplied by the corresponding reconstruction efficiencies.

<i>Channel</i>	<i>Br</i>	<i>Br tot</i>	<i>Number of events</i>
$B^\pm \rightarrow J/\psi K^\pm$	1.02×10^{-3}	6.03×10^{-5}	8
$B_d^0 \rightarrow J/\psi K_S^0$	3.75×10^{-4}	1.52×10^{-5}	2
$B_d^0 \rightarrow J/\psi K^{*0}$	1.58×10^{-3}	6.23×10^{-5}	8
$B^\pm \rightarrow J/\psi K^{*\pm}$	1.70×10^{-3}	6.70×10^{-5}	8
$B_d^0 \rightarrow J/\psi K^+\pi^-$	1.20×10^{-3}	7.09×10^{-5}	9
$B^\pm \rightarrow J/\psi K_S^0 \pi^\pm$	1.70×10^{-3}	6.89×10^{-5}	9
$B^\pm \rightarrow J/\psi K^\pm \pi^+\pi^-$	1.40×10^{-3}	8.27×10^{-5}	10

Table 5.7: Expected number of B mesons per 10^6 Z^0 .

²Charge conjugated states are also considered.

5.7.1 Monte Carlo Study

Before reconstructing B meson decays in data, a study on a dedicated sample of Monte Carlo events has been performed in order to find the optimal selection criteria.

The produced B mesons have a mean momentum of 31 GeV/c and a mean flight distance of about $d = \beta\gamma c\tau = 2.5$ mm (see figure 5.8). The decay vertex of the B meson corresponds also to the J/ψ vertex and is well separated from the primary vertex. Therefore a cut on the distance d between the primary and the secondary vertex of $d/\sigma_d > 1.5$ was applied. Figure 5.8a shows the momentum distributions of kaons from the decays $B \rightarrow J/\psi K$, $B \rightarrow J/\psi K\pi$ and $B \rightarrow J/\psi K\pi\pi$. It can be seen that for the decay channel $B \rightarrow J/\psi K$ the kaon has a mean momentum of about 5 GeV/c and the mean kaon momentum decreases for decay modes with larger decay multiplicity. Figure 5.8b shows the angle between the J/ψ and the K from B decays. As the distribution peaks at about 0.2 rad and has a long tail, only tracks within a cone of 0.8 rad around the J/ψ direction were considered in the analysis. Decays with a K_S^0 in the final states are particularly difficult to reconstruct. A cut on the K_S^0 flight distance in the transverse plane (see figure 5.8f) at 0.5 cm was found to reduce the combinatorial background under the K_S^0 peak sufficiently.

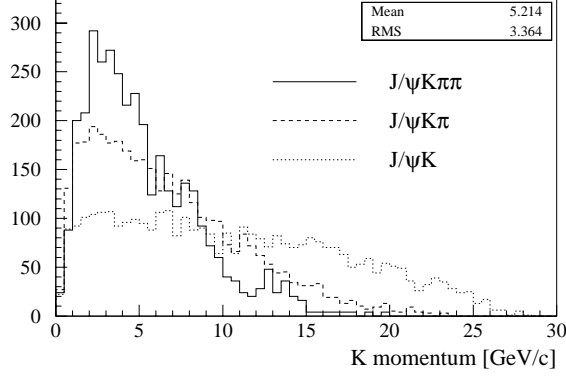
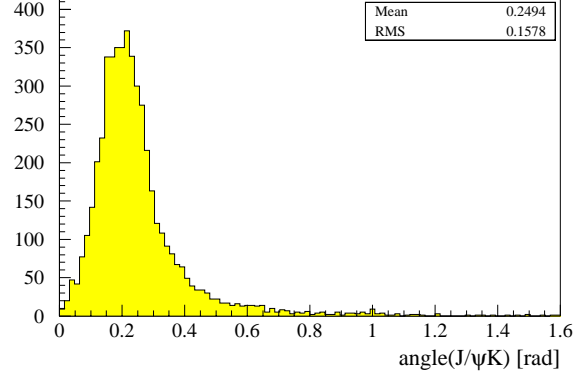
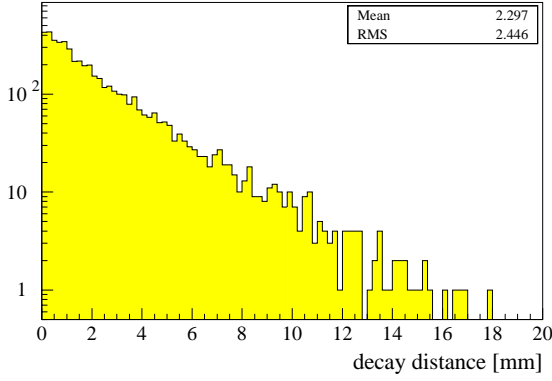
5.7.2 Reconstruction of the Individual Decay Channels

To reconstruct B mesons, charged tracks within a cone of 0.80 rad around the J/ψ flight direction have been selected, requiring at least one track to have $p > 2$ GeV/c and at least $p > 0.5$ GeV/c for the others. A common vertex has been tested with these tracks and the two leptons from the J/ψ candidate. Vertices with probabilities below 1% have been rejected. Proper cuts on the opening angle between the hadrons and the J/ψ direction and particle identification have been used to reduce the combinatorial background. Finally a minimum momentum of 15 GeV/c has been required for the reconstructed B mesons.

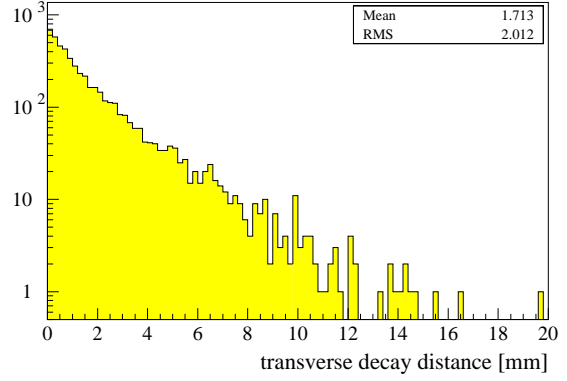
For tracks passing this cuts the particle momentum vectors have been recomputed at the fitted vertex. B meson candidates have been selected in an invariant mass range of $5.2 < m_B < 5.35$ GeV/c².

In summary the following selection criteria have been applied for all channels:

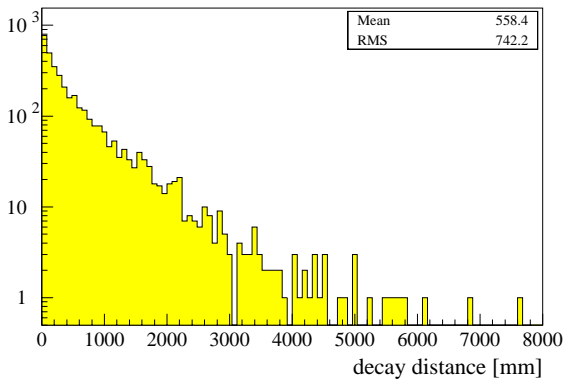
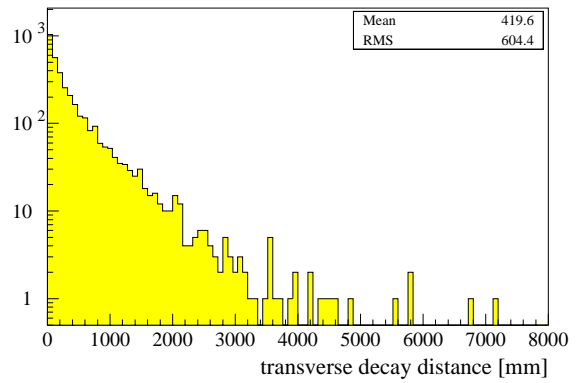
- J/ψ momentum greater 5 GeV/c;
- all added tracks were required to lie in the same thrust hemisphere as the J/ψ ;
- the momentum of the reconstructed B meson was required to exceed 15 GeV/c;
- at least one hadron with a momentum greater than 2 GeV/c;

(a) K momentum in $B \rightarrow J/\psi K + n\pi$ decays(b) Angle between J/ψ and K

(c) B decay distance



(d) B transverse decay distance

(e) K_S^0 decay distance(f) K_S^0 transverse decay distance**Figure 5.8:** *Kinematical distributions from the Monte Carlo study.*

- all tracks, except those from K_S^0 decays, were required to have an impact parameter with respect to the J/ψ vertex, t , satisfying $|t| < 2$ mm and $|t|/\sigma_t < 3$;
- the distance d between the primary and the secondary vertex must be greater than $1.5\sigma_d$;
- the secondary vertex probability was required to be $Prob(\chi^2) > 1\%$

Kinematic fitting was employed for all channels to improve the mass resolution of the reconstructed B mesons. In these fits the J/ψ , the K_S^0 , K^{*0} and $K^{*\pm}$ were kinematically constrained to their nominal masses. The χ^2 probability for the overall kinematic fit, including all particles involved in the B meson decay, was required to exceed 1%. In this way, the mass resolution was improved significantly. For instance in the channel $B^\pm \rightarrow J/\psi K^{*0}$ the mass resolution was improved from $45 \text{ MeV}/c^2$ without kinematical fitting to $26 \text{ MeV}/c^2$ with kinematical fitting, according to the Monte Carlo.

5.7.2.1 $B^\pm \rightarrow J/\psi K^\pm$

This channel is the easiest to reconstruct. Charged tracks with momentum above $2 \text{ GeV}/c$ in a cone of 0.6 rad around the J/ψ direction have been selected and attributed the K mass. For these tracks the information of the specific ionization in the TPC and the RICH information have been checked (see section 4.3.1). For tracks with reliable TPC dE/dx or/and RICH information, the K candidate has been required to be identified either in the RICH or in the TPC.

5.7.2.2 $B_d^0 \rightarrow J/\psi K_S^0$

K_S^0 candidates were selected in a cone of 0.8 rad around the J/ψ direction. K_S^0 's have been reconstructed through their decays into $\pi^+\pi^-$ pairs. All unlike sign tracks with momentum $p > 0.5 \text{ GeV}/c$ in the same hemisphere of the J/ψ and having a crossing point in the $r\phi$ plane and an impact parameter w.r.t. the primary vertex larger than 0.05 cm have been paired and a common vertex has been fitted. A mass window of $\pm 40 \text{ MeV}/c^2$ around the nominal K_S^0 mass was chosen to select K_S^0 candidates. This method was checked with a dedicated V^0 finding algorithm and the results were found to be in good agreement. Figure 5.9 shows the invariant mass distributions of the selected K_S^0 for both data and Monte Carlo. From the Monte Carlo study the K_S^0 mass resolution was found to be $5.5 \text{ MeV}/c^2$. The selected K_S^0 candidates were required to have a momentum $p_K > 2 \text{ GeV}/c$ and a minimum projected K_S^0 decay length of 0.5 cm.

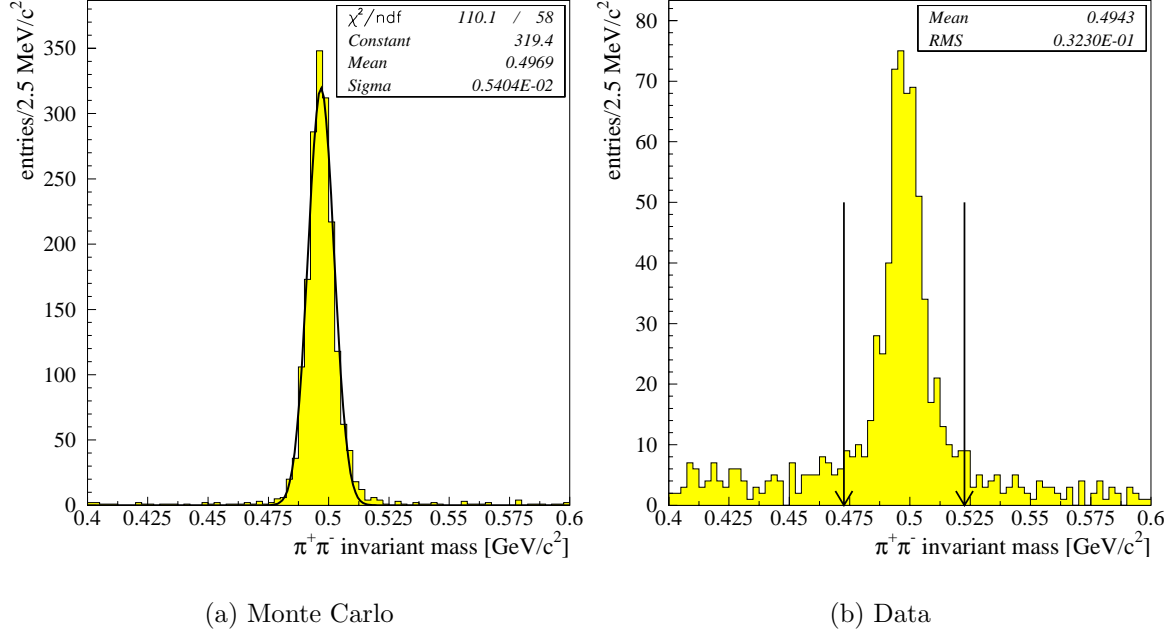


Figure 5.9: Reconstructed K_S^0 in $Z^0 \rightarrow J/\psi X$ events.

5.7.2.3 $B_d^0 \rightarrow J/\psi K^{*0}$

This decay channel was reconstructed by looking for a 4 prong secondary vertex with two leptons coming from a J/ψ and two further charged tracks, which were selected in a cone of 0.6 rad around the reconstructed J/ψ direction. Each selected track was required to have a momentum above 1 GeV/c. Both possible combinations of mass assignments, $m_{K_1\pi_2}$ and $m_{\pi_1K_2}$, have been tried for the two tracks. In addition one track was required to be identified as a K by the RICH or the TPC dE/dx. Unlike sign $K\pi$ pairs within 70 MeV/c² from the nominal $K^*(892)^0$ mass have been taken as K^{*0} candidates. Only the decay channel $K^{*0} \rightarrow K^+\pi^-$ with a branching ratio of 0.667 has been taken into account.

5.7.2.4 $B^\pm \rightarrow J/\psi K^{*\pm}$

The K_S^0 from the decay $K^{*\pm} \rightarrow K_S^0\pi^\pm$ was reconstructed as described in section 5.7.2.2, requiring $p_{K_S^0} > 1$ GeV/c. An additional pion was attached to the J/ψ vertex. The momentum of the pion was required to exceed 0.5 GeV/c. $K^{*\pm}$ candidates were selected by requiring the invariant mass of the $K_S^0\pi$ combination to lie within 70 MeV/c² from the nominal $K^{*\pm}$ mass. The momentum of the reconstructed K_S^0 was required to be above 2 GeV/c.

5.7.2.5 $B_d^0 \rightarrow J/\psi K^+ \pi^-$

The same procedure as for the channel $B_d^0 \rightarrow J/\psi K^{*0}$ was used, but all $K_S^0 \pi$ combinations with an invariant mass compatible with an K^{*0} were rejected.

5.7.2.6 $B^\pm \rightarrow J/\psi K_S^0 \pi^\pm$

The K_S^0 was reconstructed as described in section 5.7.2.2. An additional pion was attached to the J/ψ vertex. The momentum of the pion was required to exceed $0.5 \text{ GeV}/c$ and the momentum of the reconstructed K_S^0 must be above $1 \text{ GeV}/c$. All $K_S^0 \pi$ combinations with an invariant mass compatible with an $K^{*\pm}$ were rejected.

5.7.2.7 $B^\pm \rightarrow J/\psi K^\pm \pi^- \pi^+$

Charged particles with momenta greater $0.5 \text{ GeV}/c$ have been selected in a cone of 0.6 rad around the reconstructed J/ψ direction and combinations of three particles have been formed. All possible mass assignments of the three tracks were applied. One particle was required to be tagged as a kaon by the hadron identification algorithm described in section 4.3.1. The selected kaon was required to have a momentum $p_K > 1 \text{ GeV}/c$. B meson candidates were selected in a mass window $5.2 - 5.35 \text{ GeV}/c^2$.

5.7.3 Background and Efficiency

A sample of Monte Carlo events containing decays of B hadrons into a J/ψ has been used to study the background and to calculate the efficiencies of the selection cuts. The obtained efficiencies for the individual decay channels (excluding the efficiency of the J/ψ selection) are listed in table 5.8.

<i>Channel</i>	<i>Mass</i> (GeV/c^2)	<i>Width</i> (MeV/c^2)	<i>Number of</i> <i>candidates</i>	<i>Number of</i> <i>background events</i>	<i>Selection</i> <i>efficiency</i>
$J/\psi K^\pm$	5.278 ± 0.004	26 ± 2	14	4.2 ± 0.3	$59 \pm 5\%$
$J/\psi K_S^0$	5.279 ± 0.007	33 ± 6	4	1.1 ± 0.2	$32 \pm 8\%$
$J/\psi K^{*0}$	5.281 ± 0.005	24 ± 5	8	1.2 ± 0.3	$43 \pm 4\%$
$J/\psi K^{*\pm}$	5.277 ± 0.003	31 ± 5	3	0.5 ± 0.5	$15 \pm 7\%$
$J/\psi K^+ \pi^-$	5.278 ± 0.006	22 ± 4	24	13.1 ± 0.5	$48 \pm 4\%$
$J/\psi K_S^0 \pi^\pm$	5.275 ± 0.003	32 ± 2	8	5.6 ± 0.8	$14 \pm 3\%$
$J/\psi K^\pm \pi^+ \pi^-$	5.272 ± 0.009	39 ± 7	6	1.1 ± 0.4	$24 \pm 4\%$

Table 5.8: *Summary of efficiencies for the B meson reconstruction.*

The invariant mass distributions for all decay channels have been fitted in the range $4.5 - 6.0 \text{ GeV}/c^2$ with a Gaussian, for the signal, plus and exponential, which seems

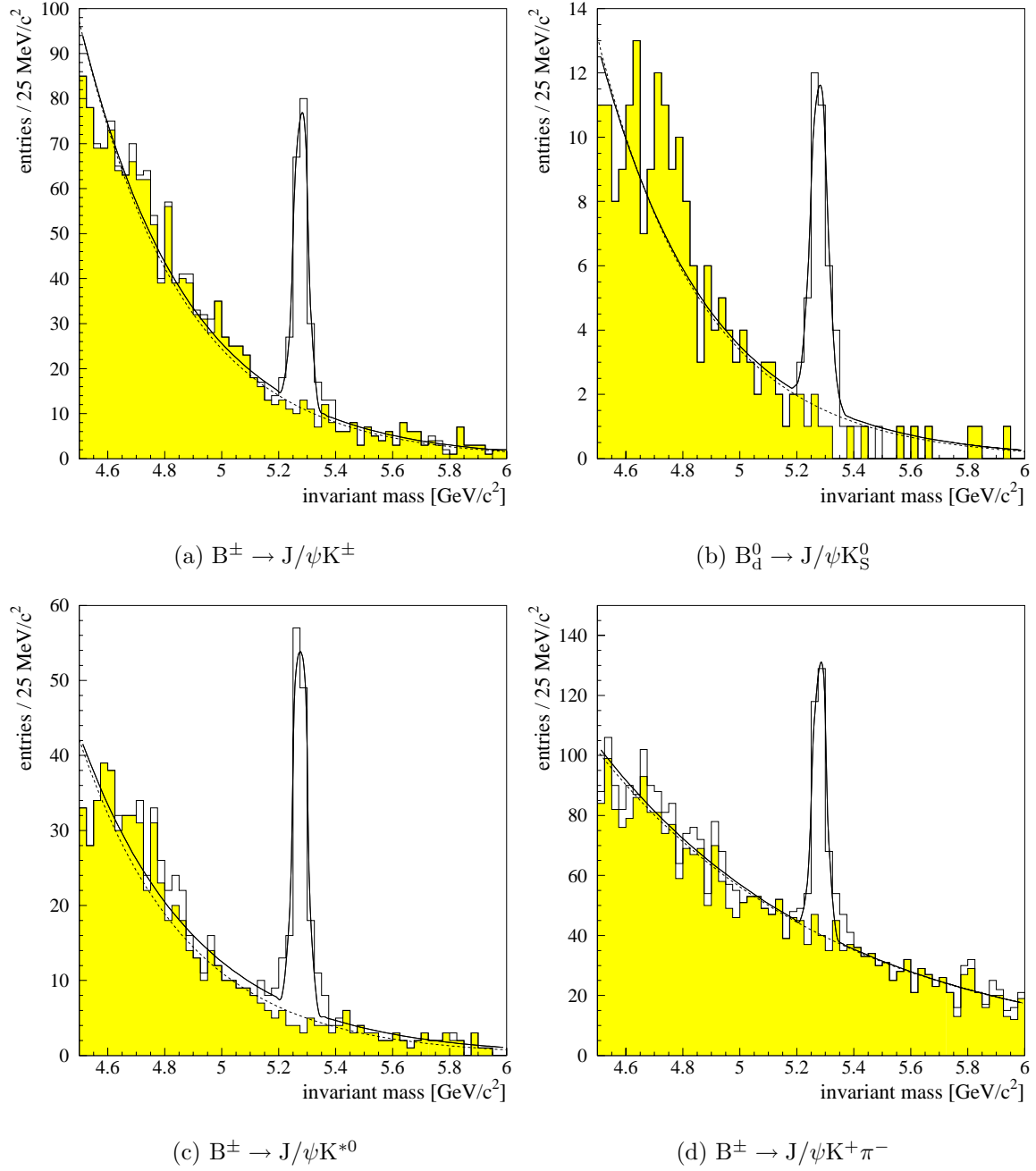


Figure 5.10: Monte Carlo: The shaded area indicates the background obtained from the inclusive $B \rightarrow J/\psi X$ Monte Carlo.

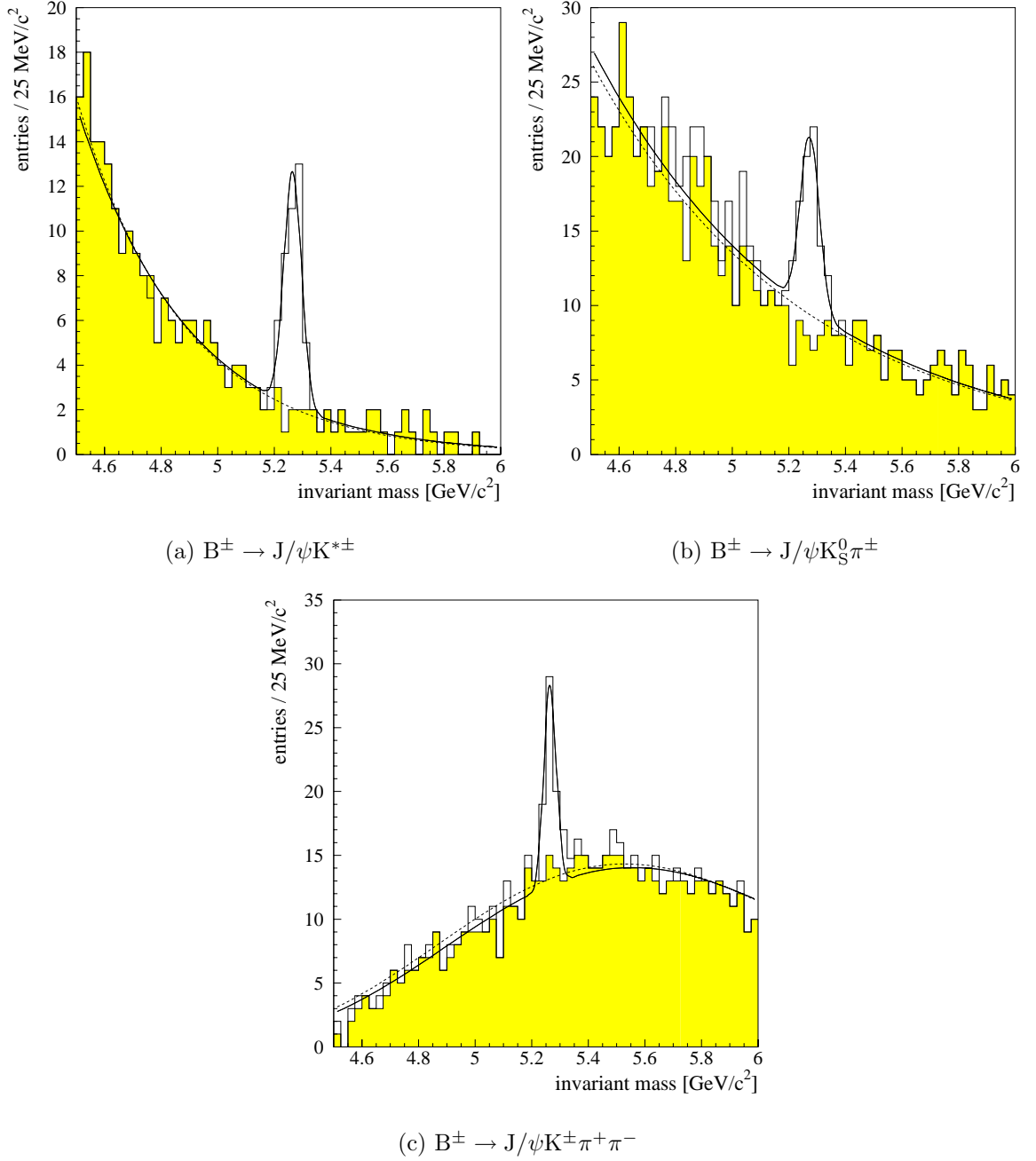


Figure 5.11: Monte Carlo: The shaded area indicates the background obtained from the inclusive $B \rightarrow J/\psi X$ Monte Carlo.

to describe the background quite good. Only for the channel $B^\pm \rightarrow J/\psi K^\pm \pi^+ \pi^-$ the shape of the background can not be described by an exponential has been modelled with the following function: $a \cdot (x - b)^c \cdot e^{dx}$. For this decay channel the shape of the background is determined by the available phase-space.

Figures 5.10 and 5.11 show the invariant distributions obtained from the Monte Carlo study for the individual decay channels. It can be seen that the combinatorial background increases with larger decay multiplicity.

The background can be divided into two components:

- *Combinatorial background*
- *Partially reconstructed B mesons and reflection effects*

The combinatorial background is due to accidental combinations of one or more tracks from the hadronization process with either a real J/ψ or a fake J/ψ candidate. The shape is similar for all decay channels except for $B^\pm \rightarrow J/\psi K^\pm \pi^+ \pi^-$, and can be parametrized by an decreasing exponential, reflecting the momentum spectrum of the tracks from the hadronization. The background from fake J/ψ events was found to be negligible.

Physics background can come either from reflections, where one particle is misidentified as another, or from satellites, where one or more particles are missed. The reflection effect can lead to a peak in the signal region or gives a double counting or a shift from a resonant to a non resonant channel. The selection cuts for those channels were chosen to reduce such backgrounds. The effect of misidentified particles is higher for non resonant decays, i.e. $B \rightarrow J/\psi K \pi$, because there is no K^{*0} invariant mass constraint. Partially reconstructed B mesons typically produce structure located below the signal region. Since there was no such structure found in either data or Monte Carlo this effect is taken to be subsumed in the exponential.

Reflections are most important in channels with two hadronic particles and affect mainly $K^+ \pi^-$ vs. K^{*0} . In order to reduce the contribution from wrong K mass assignment, particle identification has been used. For track pairs with reliable TPC dE/dx or/and RICH information, the K candidate has been required to be identified either in the RICH or in the TPC.

The invariant mass distributions for the individual decay channels are shown in figures 5.12 and 5.13. B_d^0 and B^\pm meson candidates have been accepted if they were consistent with the invariant mass requirement $5.2 < m_B < 5.35 \text{ GeV}/c^2$. The exponential resulting from the fits (see figures 5.10 and 5.11) was used to calculate the expected background inside the invariant mass window. The number of background subtracted candidates is obtained in each individual mode by subtracting this background from the total number of candidates. The results are listed in table 5.8.

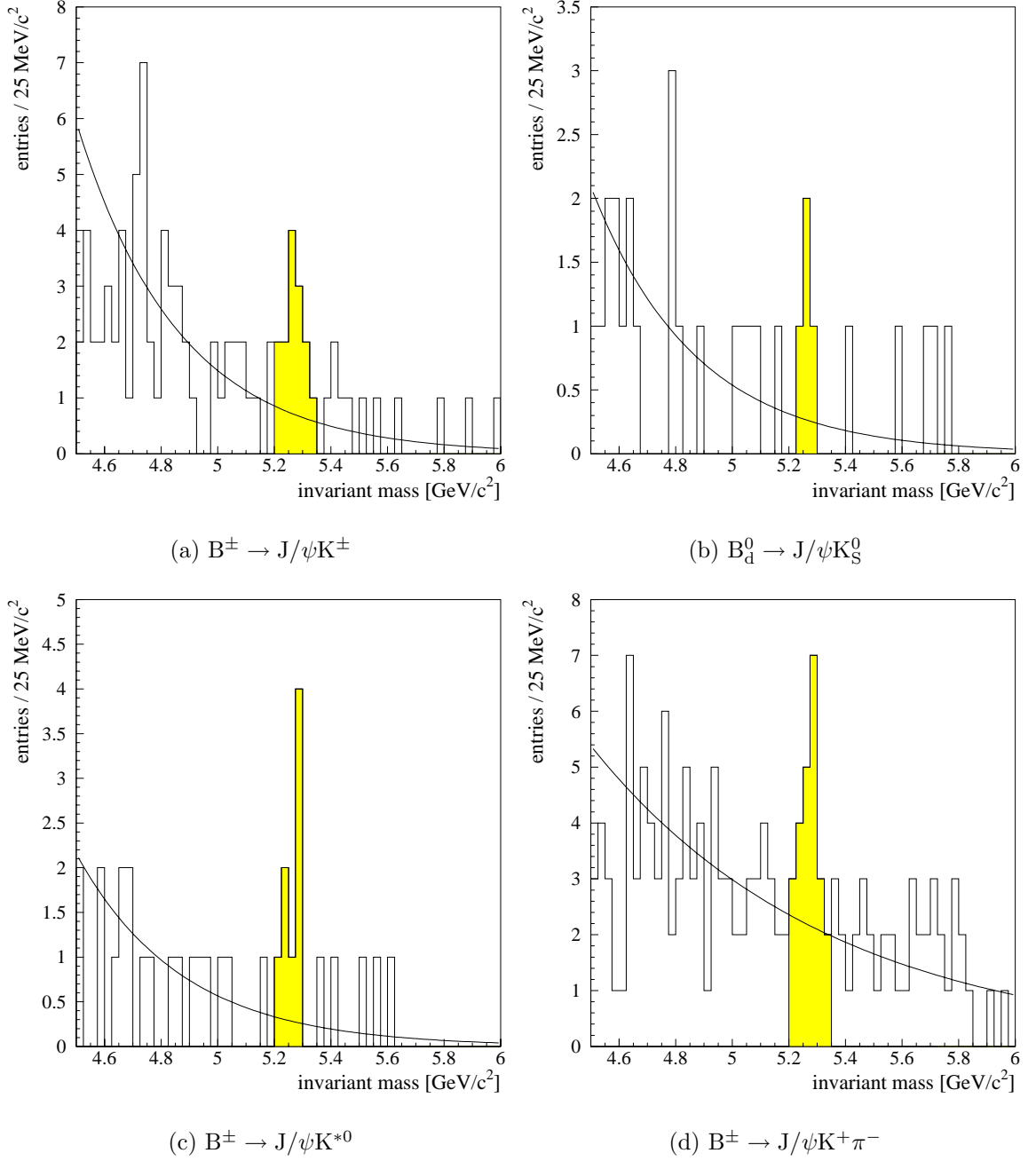


Figure 5.12: Data: B invariant mass distributions for the individual decay modes.

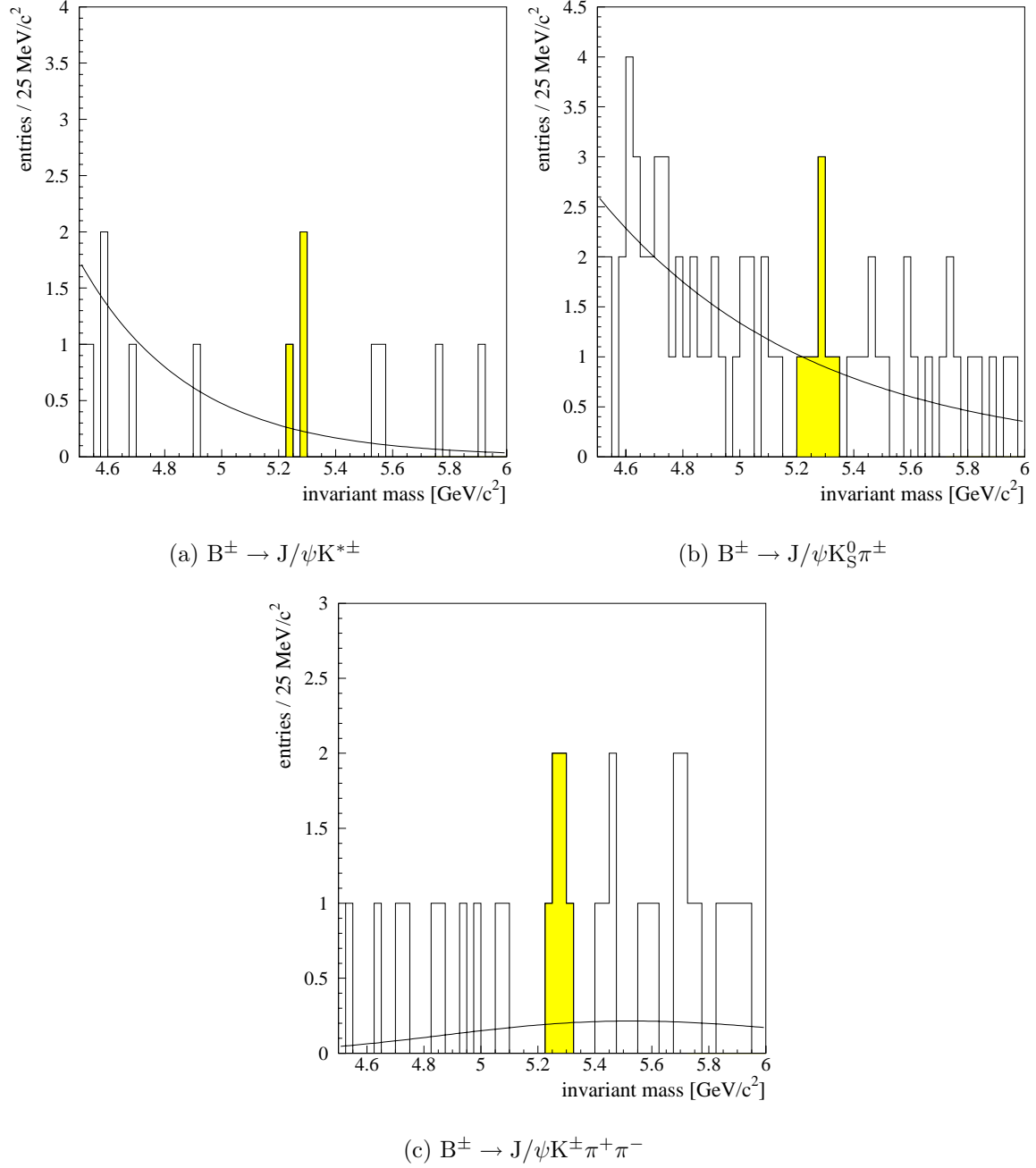


Figure 5.13: Data: B invariant mass distributions for the individual decay modes.

<i>Meson</i>	<i>Mass</i> (GeV/ c^2)	<i>Width</i> (MeV/ c^2)	<i>Number of</i> <i>candidates</i>	<i>Number of</i> <i>signal events</i>	<i>Number of</i> <i>background events</i>
B^0	5.271 ± 0.009	25 ± 6	36	20.6 ± 6	15.4 ± 6
B^\pm	5.274 ± 0.008	24 ± 7	31	19.6 ± 8	11.4 ± 8
B	5.273 ± 0.009	25 ± 7	67	40.2 ± 7	26.8 ± 7

Table 5.9: *Summary of the reconstructed B decays.*

5.8 Results and Discussion

The reconstruction of exclusive decays of B mesons into J/ψ has been studied using data collected with the DELPHI detector from 1991–1994. Starting with a selection of J/ψ candidates in the decay channels $J/\psi \rightarrow \mu^+\mu^-$ and $J/\psi \rightarrow e^+e^-$, the inclusive branching ratios $Br(Z^0 \rightarrow J/\psi + X) = (3.7 \pm 0.3 \pm 0.3) \times 10^{-3}$ and $Br(b \rightarrow J/\psi + X) = (1.15 \pm 0.09 \pm 0.14) \times 10^{-2}$ have been measured. The sample of selected J/ψ candidates was used to reconstruct B meson decays.

67 B meson candidates have been selected: 14 $B^\pm \rightarrow J/\psi K^\pm$, 4 $B^0 \rightarrow J/\psi K_S^0$, 8 $B^0 \rightarrow J/\psi K^{*0}$, 3 $B^\pm \rightarrow J/\psi K^{*\pm}$, 24 $B^0 \rightarrow J/\psi K^+\pi^-$, 8 $B^0 \rightarrow J/\psi K_S^0\pi^\pm$ and 6 $B^\pm \rightarrow J/\psi K^\pm\pi^+\pi^-$.

After background subtraction 40.2 ± 7 signal events were obtained. Figure 5.14 shows the invariant mass distributions for B^\pm and B_d^0 mesons, where several decay modes were added. The shape of the background for the individual channels has been extracted from a Monte Carlo study and was normalized to the real number of events. The number of candidates obtained in each channel has been compared with the expectations normalized to the number of reconstructed J/ψ events. The results summarized in table 5.9, are consistent with the expectations within errors.

The averaged masses of all B_d^0 and B^\pm meson candidates were found to be 5.271 ± 0.009 GeV/ c^2 and 5.274 ± 0.008 GeV/ c^2 , respectively, which can be compared with the measured masses of $m_{B^0} = 5.279 \pm 0.002$ GeV/ c^2 and $m_{B^\pm} = 5.278 \pm 0.002$ GeV/ c^2 [27].

Typical candidates for the different decay modes are shown in figures 5.15–5.18. The lower figures show a view close to the interaction point, where the reconstructed vertices can be seen. The ellipses indicate the error on the reconstructed vertices.

The main limitation for the reconstruction of exclusive B decays at LEP appears to be the small statistics, which precludes to study CP violation in the B system.

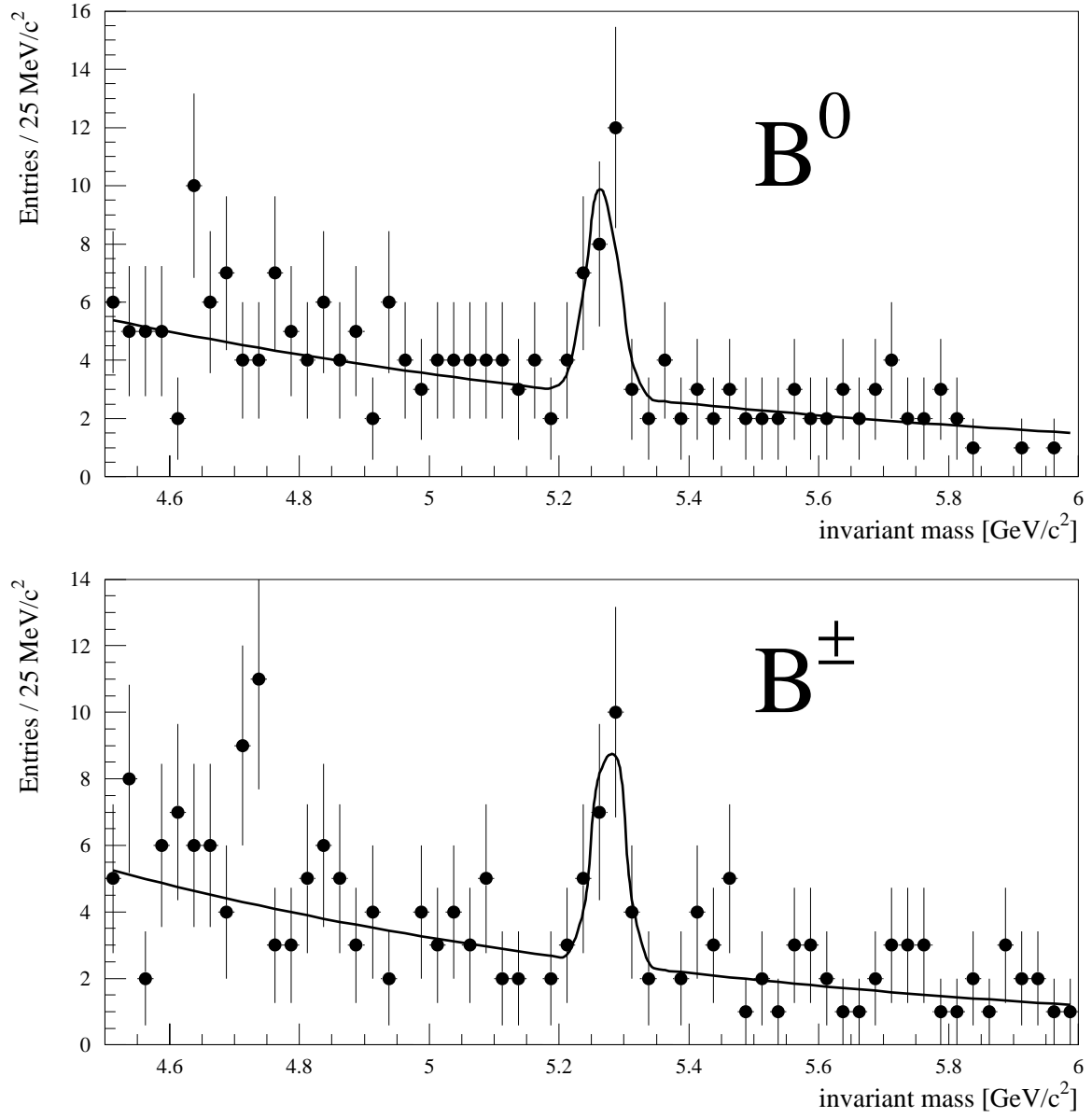


Figure 5.14: B mass distribution.

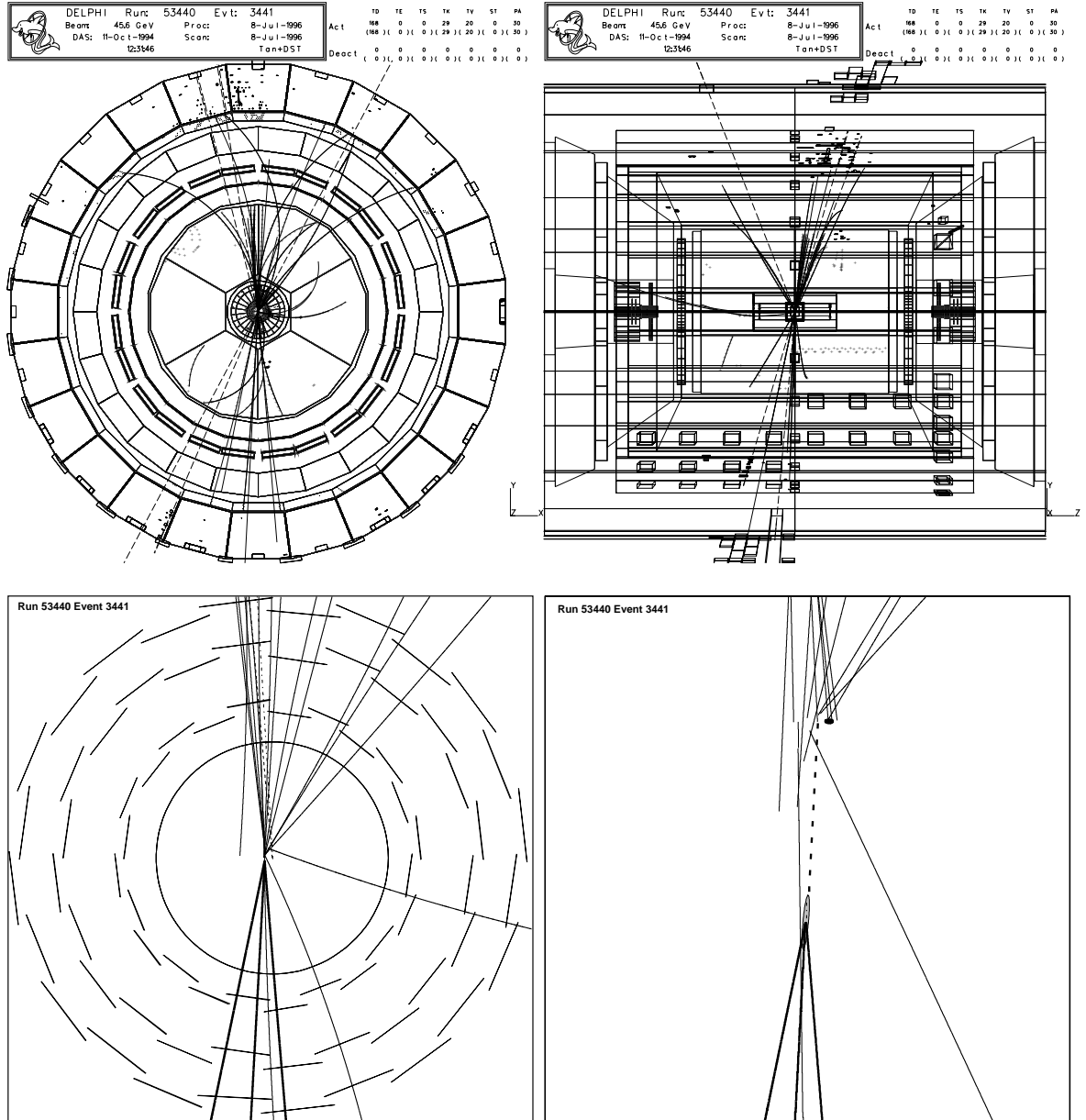


Figure 5.15: Event display: $B^+ \rightarrow J/\psi K^+ \rightarrow \mu^+ \mu^- K^+$.

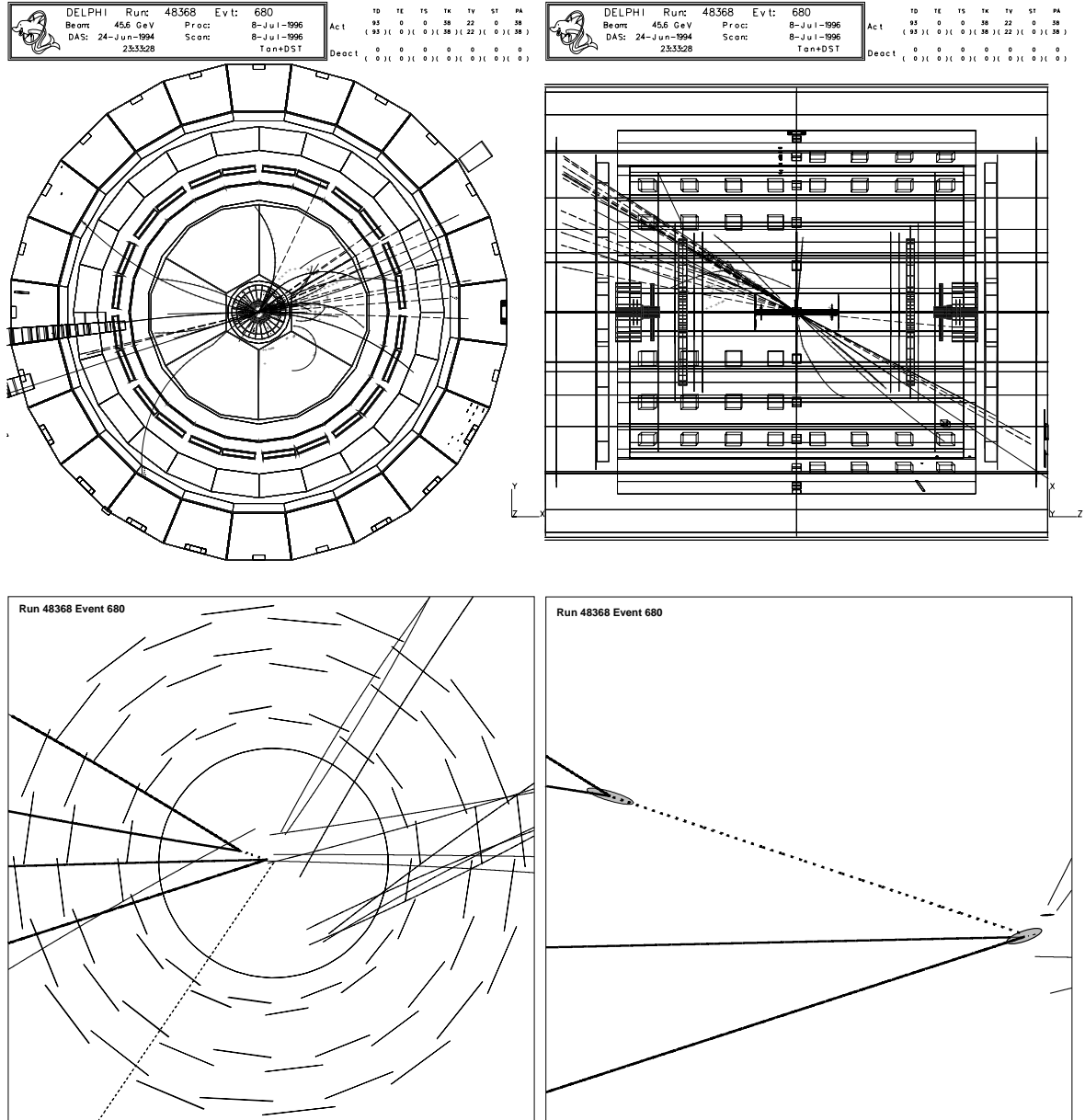


Figure 5.16: *Event display:* $B_d^0 \rightarrow J/\psi K_S^0 \rightarrow \mu^+ \mu^- \pi^+ \pi^-$.

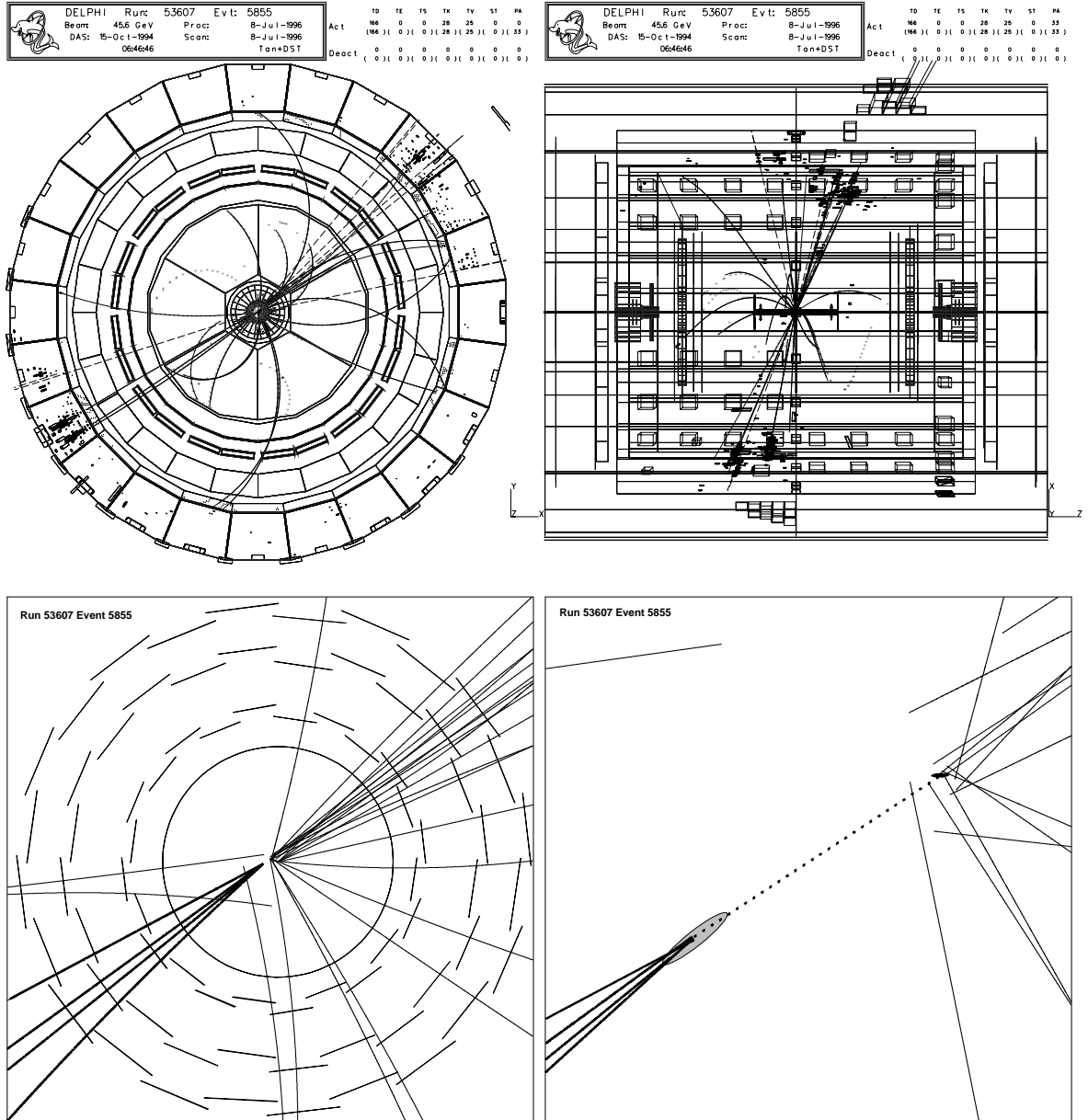


Figure 5.17: Event display: $B_d^0 \rightarrow J/\psi K^{*0} \rightarrow e^+e^-K^+\pi^-$.

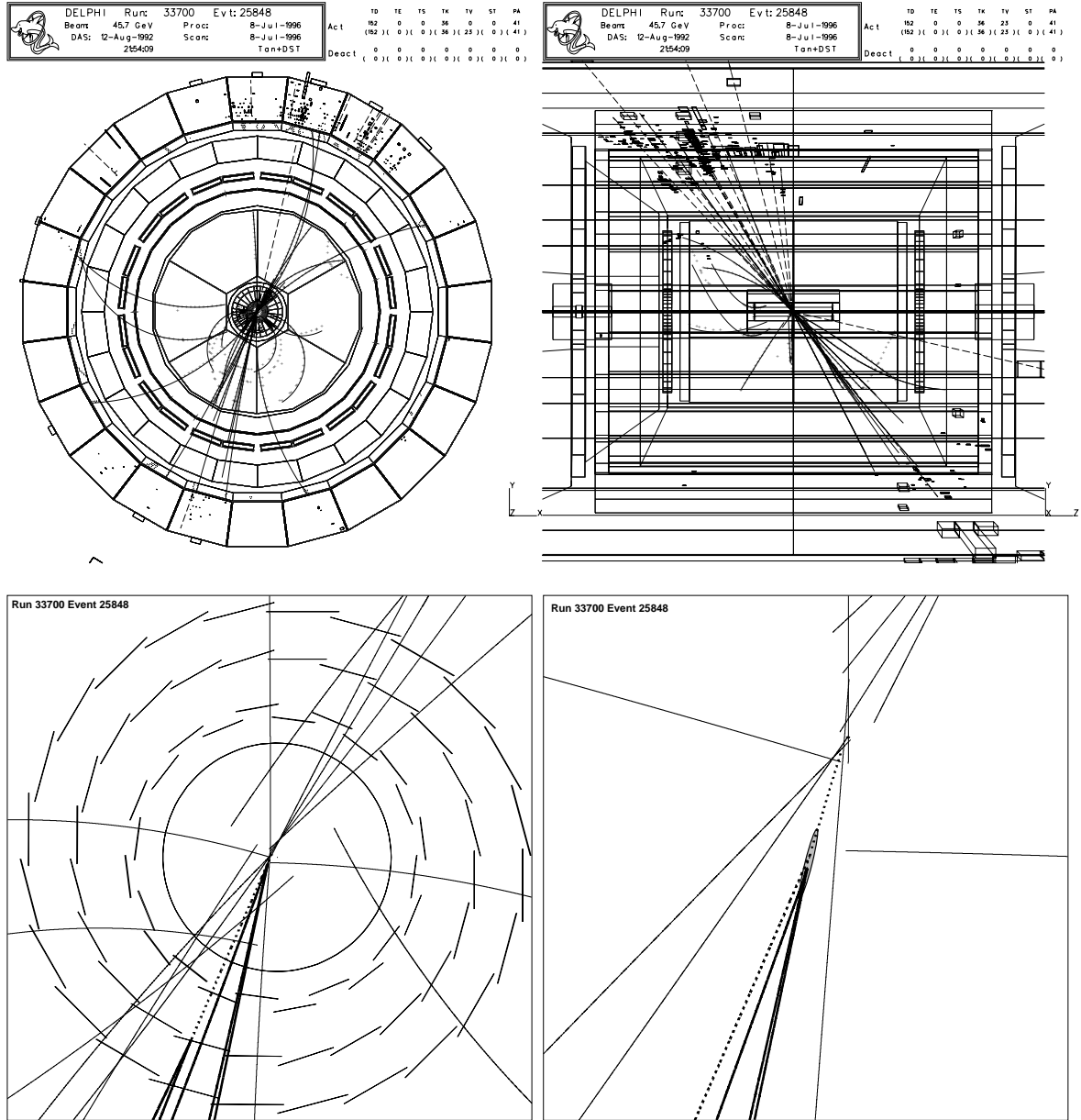


Figure 5.18: *Event display:* $B^+ \rightarrow J/\psi K_S^0 \pi^+ \rightarrow \mu^+ \mu^- \pi^+ \pi^- \pi^+$.

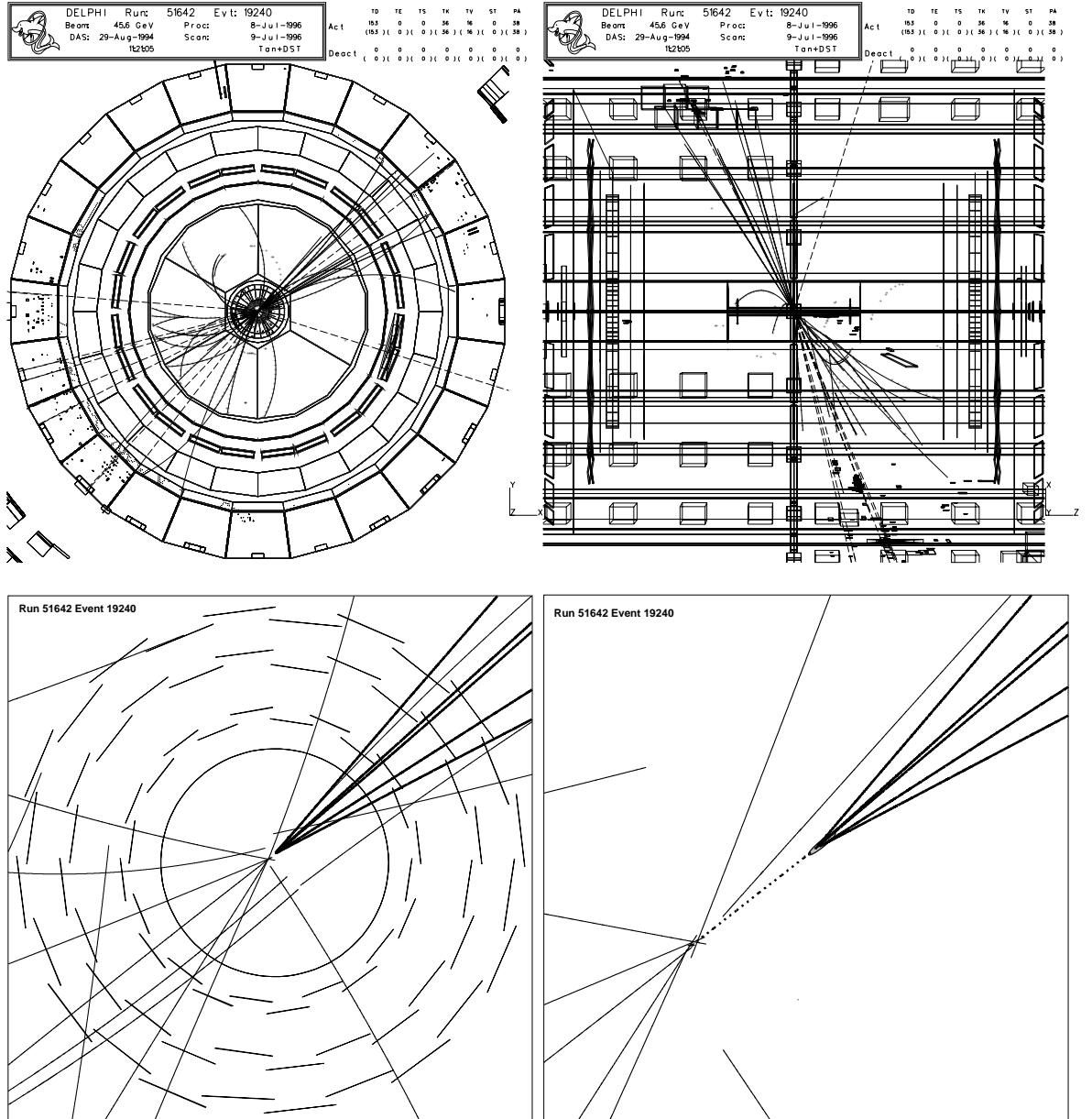


Figure 5.19: *Event display:* $B^+ \rightarrow J/\psi K^+ \pi^- \pi^+ \rightarrow \mu^+ \mu^- K^+ \pi^- \pi^+$.

Chapter 6

Future Search for CP Violation

Pure logical thinking cannot yield us any knowledge of the empirical world. All knowledge of reality starts from experiments and ends in it.

— ALBERT EINSTEIN

6.1 Introduction

One of the most interesting observations in particle physics is the violation of CP symmetry in decays of neutral kaons. Despite more than thirty years of impressive experimental effort, we still have little insight into the origin of CP violation. Neutral B mesons provide one of the few other systems in nature, where CP violation might be observable, and where stringent tests of the Standard Model description of the mechanism of CP violation can be made. Unlike in the kaon system, some B decay modes are predicted to show large CP asymmetries, whose related strength is directly related to the parameters of the CKM matrix, without involving poorly known hadronic matrix elements. The most promising channels to measure CP asymmetries have been discussed in chapter 3. While the measurable asymmetries are expected to be sizable ($\mathcal{O}(10^{-1})$), the relevant branching fractions into observable final states are small ($\mathcal{O}(10^{-5})$). Therefore copious B meson production is needed to measure CP violation. In order to measure the asymmetries with errors better than the 10% level in excess of 10^7 $B^0\bar{B}^0$ pairs need to be produced.

The current generation of B experiments, LEP, SLD, CLEO, and CDF, are already making important measurements and placing constraints on the parameters of the CKM matrix.

Each of the four LEP experiments has recorded about four million hadronic Z^0 decays during 1989–1995. This corresponds to roughly two million produced B hadrons,

with about 1600K B_d^0 and B^\pm , 200K B_s^0 and 200K B baryons. While these numbers are large, the number of fully reconstructed B hadrons is quite small. At most 30 B_d^0 and B^\pm are reconstructed per 10^6 hadronic Z^0 decays. Clearly, with this statistics LEP experiments are not sensitive to CP violation in the B system.

A considerably larger number of B mesons has been produced at CDF, but only decays with a J/ψ or a $\psi(2S)$ in the final state have been fully reconstructed. CDF has already collected a few hundred fully reconstructed B hadrons. In order to observe CP violation in B decays one needs of the order of 1000 fully reconstructed $B_d^0 \rightarrow J/\psi K_S^0$ events.

The CLEO experiment running at the CESR in Cornell produced $\sim 4 \times 10^6$ $B^0 \bar{B}^0$ pairs. At CLEO, nearly enough B^0 mesons have been produced to observe CP asymmetry, in principle. However, the B mesons are produced almost at rest and it is impossible to observe the proper-time distribution of the decays, even using state-of-the-art vertex detectors. At LEP on the other hand, the time distributions of B meson decays have been already measured, but as shown in the previous chapter, the small number of fully reconstructed exclusive events in the various channels precludes a measurement of the CP asymmetries.

It can be concluded, that none of the existing facilities can provide such a large number of B mesons to search for CP violation in the B system. New experimental approaches now being attempted may lead to substantially improved understanding of CP violation in the next five to ten years.

In order to be sensitive to CP-violating asymmetries in an experiment, two different tasks have to be performed on the same event:

- the CP eigenstate, such as $J/\psi K_S^0$ has to be fully reconstructed;
- the flavour of the other B hadron has to be tagged

To produce the large number of B mesons necessary to observe CP violation a collider with copious B production is needed. In principle there are two kinds of colliders which can achieve this requirement: e^+e^- B factories running at the $\Upsilon(4S)$ or hadron colliders.

The main advantages of an experiment at an e^+e^- collider are:

- high signal-to-background ratio;
- clean events with low multiplicity;
- low interaction rates;
- the straightforward extrapolation from existing experiments;
- years of experience

The disadvantages are the low $b\bar{b}$ cross-section and the fact that only B^\pm and B_d^0 mesons can be produced in $\Upsilon(4S)$ decays. Hadron colliders on the other hand have the following advantages:

- large $b\bar{b}$ cross-section and therefore good sensitivity to rare decays;
- all species of B hadrons are produced (B_s^0);
- the produced B mesons will have enough momentum to obtain a good proper time resolution

But the disadvantage of experiments at hadron colliders is that $\sigma_{b\bar{b}}/\sigma_{\text{tot}}$ is much smaller than at e^+e^- experiments. This makes it necessary to use dedicated trigger systems to select the interesting events.

Several new B-physics experiments which hope to achieve enough sensitivity to observe and study CP violation are being constructed using different experimental approaches: the experiments BABAR and BELLE at the new e^+e^- B factories PEP-II and KEKB; HERA-B, a fixed target experiment using the proton beam halo at HERA; an upgraded version of the CDF detector using the existing Tevatron at Fermilab; and the proposed detectors ATLAS, CMS and LHC-B at the planned Large Hadron Collider (LHC) at CERN. Table 6.1 gives a summary of these proposed B-physics experiments.

<i>Experiment</i>	<i>Collider</i>	<i>Type</i>	\sqrt{s} [GeV]	<i>Luminosity</i>	$\frac{10^{32}}{\text{cm}^2\text{s}}$	$\sigma_{b\bar{b}}$ [μb]
CDF II	Tevatron	$p\bar{p}$ collider	1800	0.2 – 0.5		50
HERA-B	HERA	p-wire	40	10–30		0.01
BABAR	PEP-II	e^+e^- asym	10.6	~ 30		0.001
BELLE	KEKB	e^+e^- asym	10.6	20 – 100		0.001
LHC-B	LHC	pp collider	14000	0.5 – 8		500
CMS	LHC	pp collider	14000	10 – 200		500
ATLAS	LHC	pp collider	14000	10 – 200		500

Table 6.1: *Future B physics experiments*

6.2 e^+e^- B Factories

The term B factory is used for a high luminosity e^+e^- collider running at the energy of the $\Upsilon(4S)$ resonance. The $\Upsilon(4S)$ decays almost exclusively into $B^0\bar{B}^0$ and B^+B^- pairs. The two proposed projects at SLAC in the US and KEK in Japan are based on an *asymmetric* collider, with two rings at different energies. The purpose of this asymmetry in the energies of the e^+ and e^- storage rings is to produce a $B^0\bar{B}^0$ system that is moving with a significant relativistic γ factor in the laboratory. This will cause the two B mesons to decay far enough apart in space that the separation between their decay

vertices can be measured¹. This then allows a reconstruction of the time difference between the two decays and enables a time-dependent CP asymmetry measurement.

The challenge is thus to design an asymmetric collider with sufficient luminosity ($3 \times 10^{33} \text{ cm}^{-2}\text{s}^{-1}$) at the $\Upsilon(4S)$ to allow these interesting measurements to be made. It should be noted that with such a collider no B_s^0 decay modes can be studied. In order to investigate B_s^0 decay modes, the machine could be operated at the $\Upsilon(5S)$ resonance, but the small cross-section, $\sigma(e^+e^- \rightarrow \Upsilon(5S)) = 0.16 \text{ nb}$, and the small branching ratio, $Br(\Upsilon(5S) \rightarrow B_s^0 \bar{B}_s^0) \leq 0.1$, make it difficult to achieve a sufficient sample for CP asymmetry measurements.

The PEP-II collider at SLAC consists of two independent storage rings, one located atop the other in the PEP tunnel. The high-energy ring, which stores a 9 GeV electron beam, is an upgrade of the existing PEP collider. The low-energy ring, which stores 3.1 GeV positrons, will be newly constructed. The KEK B factory in Japan will use a 8 GeV electron storage ring and a 3.5 GeV positron storage ring. The most significant and important difference between PEP-II and KEK B is the beam crossing arrangement at the interaction point. At PEP-II the two beams collide at zero crossing angle (i.e. head-on), while at KEK B the beams cross at an angle of 11 mrad. Both colliders will be completed in 1999.

The BABAR experiment [115] at SLAC and the the BELLE experiment [116] at KEK will both make use of the large number of slightly boosted B mesons produced at the asymmetric electron-positron collisions, to measure time-dependent CP asymmetries. In this clean environment it is possible to do many studies of inclusive and exclusive final states. However, the numbers of events in specific rare decay channels is not sufficiently large for more accurate measurements and a study of the strange B mesons will, possibly, only be done at a later stage. The basic design concepts of the BABAR and the BELLE detectors are very similar. Both detectors will have a silicon vertex detector, central tracking, a CsI calorimeter and detectors for particle identification (RICH, DIRC).

6.3 Fixed Target Experiments

The HERA-B experiment [117] at DESY is an attempt to be the first at finding and measuring CP violation in the B system. This experiment is a dedicated B-physics experiment which will use the protons from the 820 GeV HERA ring and collide them with an internal fixed target. The target will consist of a set of movable wires which act like collimators in the halo of the proton beam.

The main goal of the experiment is to measure CP violation in the decay channel $B_d^0 \rightarrow J/\psi K_S^0$, with subsequent decays of the J/ψ into two leptons and K_S^0 into two

¹In contrast, an $\Upsilon(4S)$ decay at rest would produce B mesons almost at rest, and their decay vertices could not be resolved experimentally.

charged pions. The proton energy at HERA is 820 GeV which gives a center-of-mass energy of $\sqrt{s} = 40$ GeV. The predicted $b\bar{b}$ cross-section at this energy is about 12 nb. In one year of running about 3.7×10^8 $b\bar{b}$ pairs will be produced. The topology of an event produced in a proton-nucleus interaction in fixed target mode at 820 GeV is the following: a pair of b quarks is produced together with about 10 other tracks and low-momentum nuclear fragments. Due to the Lorentz boost the decay products are confined to a small cone in the forward hemisphere. Almost all decay products will lie within a range of $10 \text{ mrad} < \theta_{\text{Lab}} < 210 \text{ mrad}$. Due to the low b production cross-section, a large geometrical acceptance is needed. Therefore the detector will cover an angular range between 10 mrad and 200 mrad.

The most important detector requirements are: i) the ability to reconstruct multiple events per bunch crossing, ii) a good B decay vertex reconstruction and resolution, iii) lepton and kaon identification, iv) a fast and selective J/ψ trigger and v) a radiation hard implementation.

The HERA-B detector will consist of a 2 m long vertex detector with several layers of double-sided silicon detectors, followed by tracking chambers inside the spectrometer magnet which provides a field integral of 2.2 Tm. Electron identification is provided by a TRD and a fine grained electromagnetic calorimeter. Kaons are identified in a RICH which uses a C_4F_{10} -radiator. The hadron absorber is interleaved with fast drift chambers for muon identification. An essential detector component is the trigger system which selects lepton pairs with an invariant mass above $2.5 \text{ GeV}/c^2$.

The detector should be ready in 1998. With the assumption of a 40 MHz interaction rate, and a $b\bar{b}$ cross-section of 12 nb, the statistical error on $\sin 2\beta$ for one year (10^7 s) of running will be about 0.13.

6.4 Hadron Colliders

High energy hadron machines are a copious source of B hadrons, because of the large cross-section and high luminosity. The usual argument against the use of hadron machines for B studies is the “dirty” environment that makes event reconstruction and triggering difficult. However, the recent observation by the CDF [118] collaboration at the Tevatron collider of a number of fully reconstructed exclusive B decay modes such as $B_d^0 \rightarrow J/\psi K_S^0$, $J/\psi K^\pm$ and $J/\psi K^{*0}$ shows that at least some exclusive channels can be extracted with a good signal-to-noise ratio. About 240 $J/\psi K_S^0$ events with a signal-to-background ratio better than 1 : 1 have been observed. This is currently the world’s largest sample of $B_d^0 \rightarrow J/\psi K_S^0$ events and proves that CP violation can be studied in a hadron collider environment.

In a collider mode the main difficulty is the extraction of the signal from the large backgrounds. An advantage is that unlike the $\Upsilon(4S)$ machines, in hadron colliders there is no coherent $B\bar{B}$ production, so time-integrated measurements of CP asymmetries can

be made.

A useful signature for B hadrons is the lepton pair coming from the subsequent decay $J/\psi \rightarrow \ell^+ \ell^-$. The large b quark cross-section compensates for the low branching ratio $Br(B \rightarrow J/\psi X) \sim 1\%$, which has to be combined with the leptonic branching ratio of the J/ψ meson, which is about 6%.

The CDF experiment [119] is an already existing experiment that took plenty of data in Run I during 1992–1996. Run II will start in 1999 when the Tevatron together with the new Main Injector is supposed to deliver 2 fb^{-1} in two years. By then the CDF detector will be upgraded with a new silicon vertex detector which doubles the fiducial volume of the current vertex detector and provides 3-dimensional tracking. A new central tracking system with dE/dx capabilities will be in place as well as a new end-cap calorimeter. With an upgraded trigger and data acquisition system, which will allow to lower the muon trigger threshold to $p_t > 1.5 \text{ GeV}/c$, CDF plans to collect enough fully reconstructed events to measure CP violation in the B system. CDF proposes to measure $\sin 2\beta$ with a precision of $\delta(\sin 2\beta) = 0.09$ in Run II.

6.5 LHC

The CERN Large Hadron Collider (LHC) [120] will be a proton-proton collider installed in the 27 km long LEP tunnel with beam energies up to 7 TeV, giving a center-of-mass energy of 14 TeV at the points of collision. The maximum luminosity will be $10^{34} \text{ cm}^{-2} \text{ s}^{-1}$ with a bunch crossing every 25 ns. This unprecedented high collision center-of-mass energy and the high luminosity are required in order to create massive particles which have a small production cross-section relative to their background processes. The LHC is supposed to start running in the year 2005.

Two high luminosity proton-proton experiments ATLAS [121] and CMS [122] will be located at diametrically opposite straight sections. In addition one heavy ion experiment and one dedicated B-physics experiment LHC-B will be installed. The design parameters of the LHC are given in table 6.2.

At the LHC proton-proton collider a very large number of B hadrons will be produced. The $b\bar{b}$ cross-section at $\sqrt{s} = 14 \text{ TeV}$ is expected to be $500 \mu\text{b}$. Figure 6.1 shows the typical cross-sections expected at the LHC. It can be seen that $\sigma_{b\bar{b}}/\sigma_{\text{tot}} \approx 0.5\%$ which makes the extraction of B decays a challenge. However there will be an initial low luminosity phase with $\mathcal{L} \simeq 10^{33} \text{ cm}^{-2} \text{ s}^{-1}$ where CP violation studies will be possible. At that luminosity about 5×10^{12} $b\bar{b}$ events will be produced per year (10^7 s). Most of the b-particles will be produced in forward direction close to the beam line. The two general purpose detectors, ATLAS and CMS, will use the centrally produced b's while LHC-B, a dedicated B-physics experiment, will use forward b's to study CP violation.

<i>Parameter</i>	<i>Unit</i>	<i>Value</i>
Energy	(TeV)	7.0
Dipole field	(T)	8.36
Coil aperture	(mm)	56
Distance between apertures	(mm)	180
Number of dipoles		1232
Luminosity	$\text{cm}^{-2}\text{s}^{-1}$	10^{34}
Beam-beam parameter		0.0032
Injection energy	(GeV)	450
Circulation current/beam	(A)	0.53
Bunch spacing	(ns)	25
Particles per bunch		1×10^{11}
Stored beam energy	(MJ)	332
Normalized transverse emittance	(μm)	3.75
R.m.s bunch length	(m)	0.075
Beta values at I.P.	(m)	0.5
Full crossing angle	(μrad)	200
Beam lifetime	(h)	22
Luminosity lifetime	(h)	10
Energy loss per turn	(keV)	6.9
Critical photon energy	(eV)	45.6
Total radiated power per beam	(kW)	3.7

Table 6.2: *LHC machine parameters*

6.5.1 LHC Experiments

Although the goals of the two general purpose detectors, ATLAS and CMS, are very much the same, the experimental techniques are different and complementary, in particular in the B -field configuration, the muon system and the calorimeter choices. Both detectors will have a sophisticated tracking system, many planes of silicon detectors, good muon and electron identification and a large bandwidth data acquisition system with a flexible multi-level trigger.

The central feature of the ATLAS (A Toroidal LHC ApparatuS) is a large air-core toroidal magnet muon spectrometer consisting of a 26 m long barrel toroid with 0.8 T average field, and two end-cap toroids. This system would allow precise muon measurements at highest luminosities using the external muon system alone. The measurements are done in the air behind calorimeters that have absorbed all the hadrons. The electromagnetic calorimeter is a liquid argon one with a particular “accordion”

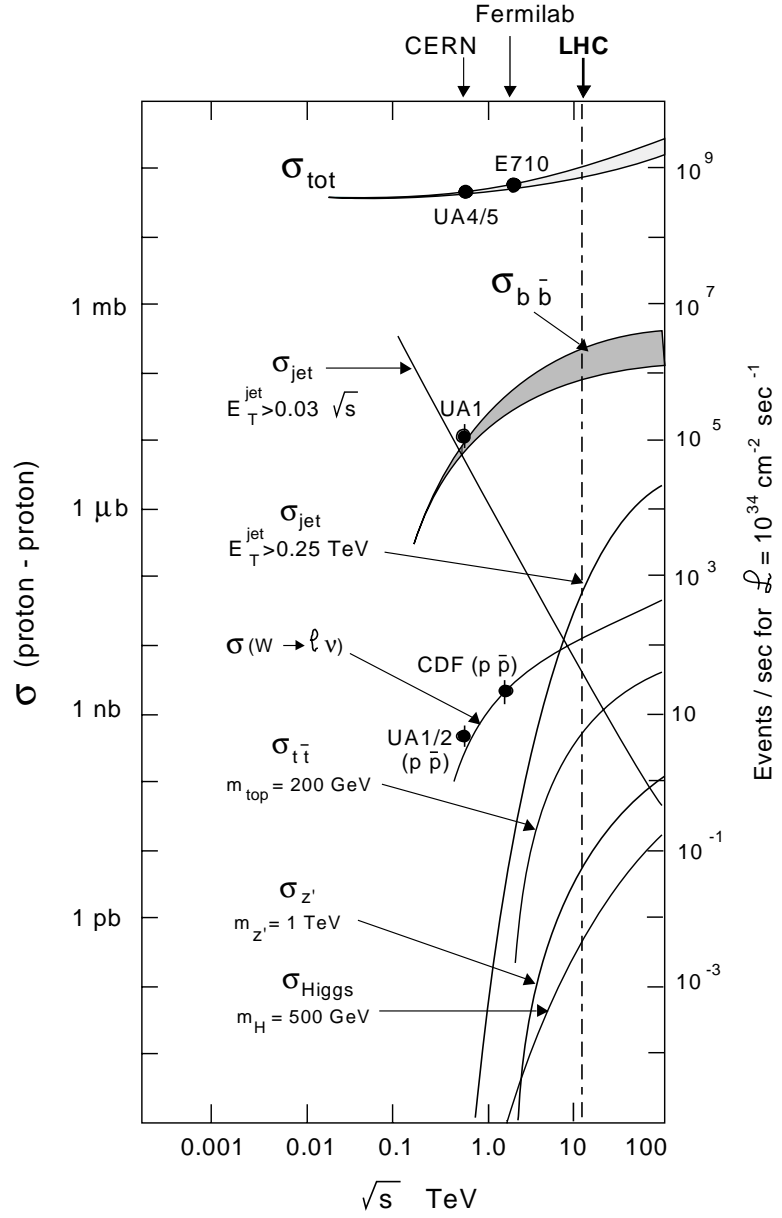


Figure 6.1: Energy dependence of some characteristic cross-sections, from present colliders to the LHC [123].

geometry. A thin 2 T solenoid is placed in front of the electromagnetic calorimeter to allow momentum measurements in the inner tracker.

The basis of the CMS (Compact Muon Solenoid) detector is a long (13 m) superconducting solenoid with a 6 m bore and a uniform 4 T field. A brief description of the CMS detector is given in section 7.3.

ATLAS and CMS are designed to take full benefit of the lower luminosity phase of LHC and will do their best to unravel the mysteries of CP violation using mainly centrally produced B mesons. Both detectors have foreseen high-resolution vertex detectors for B-physics.

While ATLAS and CMS were optimized for searching the Higgs particle and various other kinds of new physics, with event signatures concentrated in the central region, the LHC-B detector [124] is dedicated to recording as many of the interesting B decays as possible, making use of the large cross-section and the high event rate. LHC-B is a forward spectrometer with a dipole magnet optimized for the study of CP violation and other rare phenomena in the decays of beauty particles at the LHC. The trigger of this detector must not only reject minimum bias events and many charm events, but it should also try to enrich the sample that contains the specific final states. Although the experiment is in collider mode, it looks very much like a fixed target experiment. This is because the largest part of all b-particles are produced at a very small angle w.r.t. the beam pipe, and with momenta of roughly 80-100 GeV/c on average. A large dipole magnet with a field perpendicular to the beam direction can provide a very good momentum resolution for the many B decays that go in this direction. The dedicated geometry eases the optimization of the detector for this angular region, while there is space for additional measurements which are not possible at ATLAS and CMS. A vertex detector will be mounted inside the vacuum system very close to the interaction point. Particle identification by RICH detectors is essential for a clean measurement of certain final states.

It is not clear if CP violation will be measured before the start-up of the LHC. But even if the CP violating parameters by that time are already known to some extent the LHC will offer the possibility for a measurement with ultimate precision.

Chapter 7

Simulation

*No amount of experimentation can ever prove me right;
a single experiment can prove me wrong.*

— ALBERT EINSTEIN

7.1 Introduction

The large number of $b\bar{b}$ events at the Large Hadron Collider (LHC) will offer the possibility to search for CP violation in the $B_d^0\text{--}\bar{B}_d^0$ system, which may still be an open question at the start-up of the LHC. The unitarity of the 3×3 CKM matrix implies a relation between the elements: $V_{ub}^* + V_{td} \simeq \lambda V_{cb}$, which can be visualized as a triangle in the complex plane (see figure 3.4). In principle all three angles of this unitarity triangle are accessible to direct experimental measurements, for instance from the neutral B decays $B_d^0 \rightarrow \pi^+\pi^-$, $B_d^0 \rightarrow J/\psi K_S^0$ and $B_s^0 \rightarrow D_s^+K^-$, respectively.

In the initial phase of LHC operation, it is likely that the luminosity will be of the order of $10^{33} \text{ cm}^{-2}\text{s}^{-1}$. B-physics studies will be easiest at this initial luminosity, where pile-up effects are small and vertex detectors close to the beam pipe are expected to survive for several years. At a luminosity of $10^{33} \text{ cm}^{-2}\text{s}^{-1}$ the number of $b\bar{b}$ pairs produced at LHC is of the order of 5×10^{12} per year (10^7 s). In comparison, an e^+e^- B factory running at a high luminosity of $10^{33} \text{ cm}^{-2}\text{s}^{-1}$ produces a few times 10^7 $b\bar{b}$ pairs/year. CDF and HERA-B could produce up to 10^9 $b\bar{b}$ pairs/year.

The problem lies in how to exploit this rate. The experimental difficulties are the high rates and the large associated multiplicities. What is needed is a powerful trigger system to select the interesting modes, detectors with high granularity, high-resolution vertex detectors, efficient track reconstruction and good momentum resolution [123].

A simulation has been performed in order to investigate whether a CP violation

measurement is possible with a general purpose detector at the LHC. In this study we explored the possibility to determine the angle β of the unitarity triangle by measuring the time-integrated decay-asymmetry in the channel $B_d^0 \rightarrow J/\psi K_S^0$. The CMS detector was used as an example for a general purpose detector at the LHC. A Monte Carlo event generator was used to simulate $b\bar{b}$ events including the decay $B_d^0 \rightarrow J/\psi K_S^0$. The detector response was studied with a full detector simulation and the obtained efficiencies were parametrized and applied to the sample of generated events.

First I will discuss the production of $b\bar{b}$ events at the LHC and explain the uncertainties in the estimate of $\sigma_{b\bar{b}}$. Then I briefly describe the components of the CMS detector relevant for a CP violation measurement. The different methods for measuring the angle β are discussed in section 7.4 followed by a description of the trigger and event selection cuts. In order to measure a CP asymmetry in the channel $B_d^0 \rightarrow J/\psi K_S^0$, the nature of the B_d^0 meson at production has to be determined in order to know whether it was produced as a B_d^0 or a \bar{B}_d^0 . In section 7.6 various tagging techniques are described and the different sources of mistagging, which will dilute the measured decay-asymmetry, are discussed. The backgrounds to the decay channel $B_d^0 \rightarrow J/\psi K_S^0$ are discussed in section 7.7. Finally the expected error on the measurement of the angle β is calculated and the obtained results are summarized.

7.2 B Production at the LHC

The principle mechanism of $b\bar{b}$ production at hadron colliders is shown in figure 7.1. The high energy colliding hadrons can be viewed as a broad band of partons (quarks

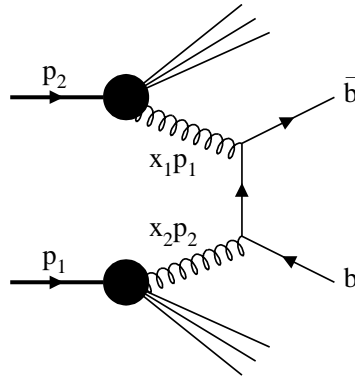


Figure 7.1: $b\bar{b}$ production at the LHC.

and gluons), which collide and fuse to produce the $b\bar{b}$ pair. Thus the $b\bar{b}$ cross-section

for pp collisions is given by the formula:

$$\sigma_{b\bar{b}} = \int dx_1 dx_2 f_i^p(x_1, \mu) f_j^p(x_2, \mu) \hat{\sigma}_{ij}(x_1 p_1, x_2 p_2, m_b, \alpha_s) \quad (7.1)$$

where f_i^p is the parton density function of the proton and $\hat{\sigma}$ is the hard-scattering cross-section, which is calculable in perturbative QCD as a series in $\alpha_s(\mu^2)$. The coupling constant α_s is evaluated at a scale μ which is of the order of the mass of the b quark, thus it is roughly 0.2.

In figure 7.1 only one lowest order diagram is represented. At lowest order ($\mathcal{O}(\alpha_s^2)$) there are contributions to $\hat{\sigma}$ due to gluon-gluon fusion ($g + g \rightarrow b + \bar{b}$) and quark-antiquark annihilation ($q + \bar{q} \rightarrow b + \bar{b}$). The diagrams contributing to the lowest order cross-section are shown in figure 7.2.

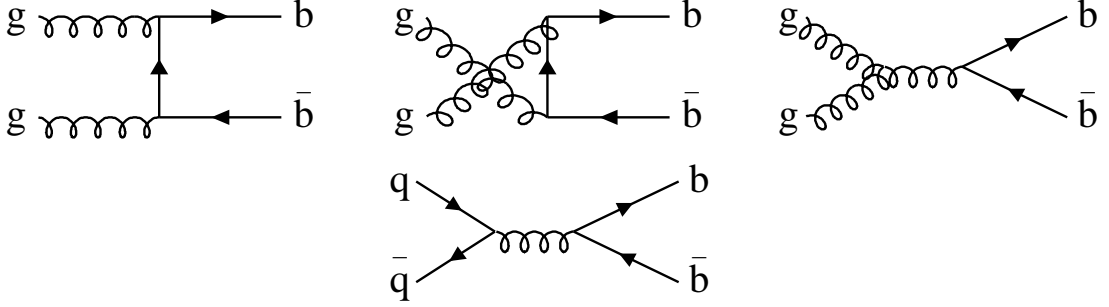


Figure 7.2: Lowest order Feynman diagrams for $b\bar{b}$ production $gg \rightarrow b\bar{b}$ and $q\bar{q} \rightarrow b\bar{b}$.

Thus, the leading process is of order α_s^2 , and the next-to-leading one is α_s^3 . In fact, next-to-leading order corrections are $\sim 100\%$ for $\sigma_{b\bar{b}}$. This can be seen in the fragmentation process $gg \rightarrow gg$ where one gluon goes to $b\bar{b}$ ($g \rightarrow b\bar{b}$, gluon splitting). Although formally of order α_s^3 this process can be as important as the leading order $\mathcal{O}(\alpha_s^2)$ process. This happens because the lowest order cross-section for the process $gg \rightarrow q\bar{q}$ is about hundred times smaller than the cross-section for $gg \rightarrow gg$ and a gluon jet will fragment into a $b\bar{b}$ pair a fraction $\alpha_s(m_b^2)/2\pi$ of the time. Because of the large cross-section for the production of gluons, the gluon splitting production is competitive with the leading order production.

The calculation of $\sigma_{b\bar{b}}$ is sensitive to a number of parameters, including the b quark mass, Λ_{QCD} , the gluon structure function, and the contribution of higher order terms, and there are large uncertainties in the estimate of $\sigma_{b\bar{b}}$ at the LHC. This is in part due to the limited knowledge of the gluon structure function at low x . At LHC energies the bottom quark production is predominantly due to gluons with small values of x ($x \sim 10^{-4}$ is probed here). In this small x region the form of the gluon

structure function is unmeasured although the most recent HERA results remedy this in part [125,126].

In addition there are uncertainties in the estimate of $\sigma_{b\bar{b}}$ due to the questionable applicability of perturbative QCD calculations (of order $\mathcal{O}(\alpha_s^3)$) in the regime, where $m_b/\sqrt{s} \ll 1$ (s is the center-of-mass energy squared). This is due to the appearance of large logarithms of s/m_b^2 in the perturbative expansion. At very large s the expansion parameter $\alpha_s \log(s/m_b^2)$ becomes of the order 1, thereby spoiling the convergence of the perturbative expansion.

Therefore one can expect deviations from theoretical predictions due to higher order and non-perturbative effects.

The next-to-leading order calculation of Nason *et al.* [127,128] for $\sqrt{s} = 14$ TeV gives a $b\bar{b}$ cross-section in the range 0.1 to 0.7 mb. An independent estimate by Berger *et al.* [129] gives $\sigma_{b\bar{b}} \approx 0.5 - 0.9$ mb.

For this study we assume a $b\bar{b}$ cross-section of $500 \mu\text{b}$. The fraction of $b\bar{b}$ events at the LHC is thus $\sigma_{b\bar{b}}/\sigma_{\text{tot}} \sim 0.5\%$. At a luminosity of $\mathcal{L} \approx 10^{33} \text{ cm}^{-2}\text{s}^{-1}$ such a cross-section implies production of $\sim 5 \times 10^{12}$ $b\bar{b}$ events per year (10^7 s).

The distributions of the transverse momentum p_t and the pseudorapidity η of the produced b quarks are very sensitive to the choice of structure functions. As can be seen from fig. 7.3, most of the B hadrons are produced with low p_t and in forward direction. Therefore, for the simulation of $b\bar{b}$ events the selection of the structure functions is very important.

Figure 7.3 shows the structure function dependents of the p_t and η spectra of B hadrons generated with the Monte Carlo program PYTHIA [130,110]. The two sets of structure functions favoured by recent HERA data [126,125] are CTEQ2L [131] and EHLQ1 [132]. For this study we used the leading order structure functions CTEQ2L.

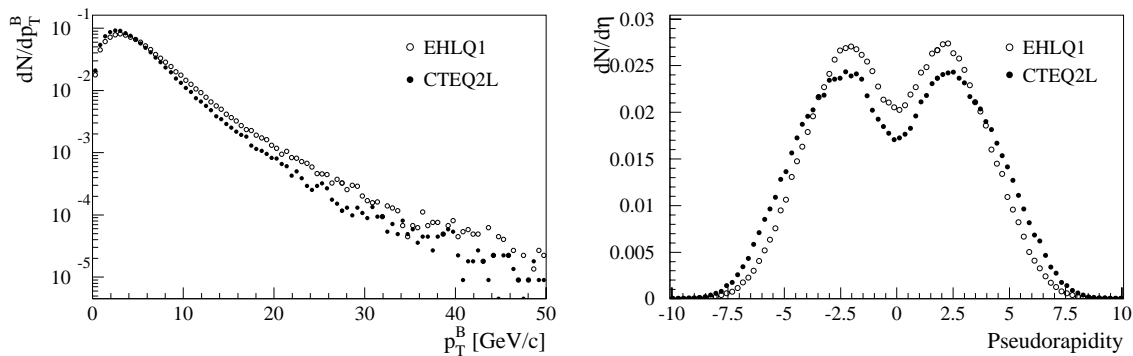


Figure 7.3: p_t and η spectra of B hadrons for two different sets of structure functions.

7.3 The CMS Detector

The CMS (Compact Muon Solenoid) is designed as a general purpose detector for discoveries at the highest luminosity in proton-proton collisions at the LHC. However, during the initial period of LHC operation, it is expected that there will be an opportunity to carry out heavy flavour studies, such as CP violation, at lower luminosity.

Here I will just concentrate on the detector parts most important for measuring CP violation, i.e. the muon system, the tracker and the trigger system. A detailed description of the CMS detector can be found in ref. [133,122].

Emphasis is put on the identification and precise measurement of muons, photons and electrons, in order to detect signatures of new physics efficiently. The goal is to measure these particles with an energy resolution of about 1% over a large momentum range. To achieve this goal the design priorities of CMS have been set to have a very good and redundant muon system, the best possible electromagnetic calorimeter and a high quality central tracker.

The basis of the CMS detector is a long (13 m) superconducting solenoid with an inner radius of 2.95 m generating a uniform magnetic field of 4 T. The magnetic flux is returned through a 1.8 m thick saturated iron yoke (1.8 T) instrumented with muon chambers. The 4 T central field together with a powerful tracking leads to a good momentum resolution.

The innermost part of the detector is occupied by a 6 m long central tracker with a radius of 1.3 m. The electromagnetic calorimeter and the hadronic calorimeter are built around it, all inside of the superconducting coil. Behind the coil there are four muon stations in the barrel and in the end-cap. The muon stations are embedded in the iron return yoke of the solenoid. The very forward calorimeter is located behind the end-cap muon chambers. The overall dimensions of the detector are about 22 m in length, with a diameter of 14.6 m and a total weight of 14500 tons.

7.3.1 Muon System

The muon momentum is measured three times almost independently, which makes the muon identification very robust. Starting from the primary vertex, centrally produced muons are first measured in the inner tracker inside the uniform 4 T magnetic field. They then traverse the calorimeters (7λ at 90°), still inside the 4 T magnetic field, the coil (1.1λ) and a non-magnetic “tail catcher” (2λ). They are then identified and measured in four identical muon stations inserted in the return yoke in the barrel and end-cap regions. Each muon station consists of several planes of drift chambers designed to give a muon vector in space, with $100\ \mu\text{m}$ precision in position and better than 1 mrad in direction. The four muon stations also include triggering planes which identify the bunch crossing and enable a cut on the muon transverse momentum at the first trigger level.

The four muon stations provide redundancy and optimize geometrical acceptance. Special care has been taken to avoid pointing cracks and to maximize the acceptance. The region $|\eta| < 1.3$ is covered by the barrel detector, whereas the end-cap detector covers the region $0.9 < |\eta| < 2.4$.

7.3.2 Tracker

The design goal of the central tracking system of CMS is to reconstruct isolated high p_t muons and electrons in $|\eta| < 2.5$ with a momentum resolution of $\Delta p_t/p_t \approx 0.15 p_t \oplus 0.5\%$ (p_t in TeV/ c), as well as hadrons down to low transverse momenta (≥ 1 GeV/ c). Isolated high p_t tracks should be reconstructed with an efficiency of better than 95%, and high p_t tracks within jets with an efficiency of better than 90%.

The main problem in tracking will be pattern recognition. At a luminosity of 10^{34} cm $^{-2}$ s $^{-1}$, interesting events will be superimposed on a background of about 500 soft charged tracks within the rapidity range from ~ 15 minimum bias events occurring in the same bunch crossing. Their vertices are distributed along the beam direction (z -axis) with an r.m.s of 5.3 cm. To solve the pattern recognition problem detectors with small cell sizes are required. Silicon pixel and microstrip detectors as well as microstrip gas chambers (MSGC) were chosen, as they can provide the necessary granularity and precision. Strip lengths of the order of 10 cm are needed to maintain cell occupancy below 1%. This leads to a large number of detection channels ($\approx 10^7$).

Many physics studies may depend on the ability of the tracking system to perform efficient b-tagging and secondary vertex reconstruction. Microvertex b-tagging also played a key role in the recent discovery of the top quark. Therefore the design goal is to achieve an impact parameter resolution for high p_t tracks of order 20 μm in the transverse plane and 100 μm in z -direction.

To fulfill these high requirements the innermost layers of the central tracker have been chosen to be silicon pixel detectors. There will be two barrel layers at a radial distance of 7.5 and 11 cm from the beam line and three end-cap layers placed close to the interaction vertex. These detectors provide three dimensional space points suitable for the high track density close to the interaction point and guarantee high precision for secondary vertex reconstruction and flavour tagging. The effective $r\varphi$ -resolution is assumed to be 15 μm .

The pixel detector will be followed by three layers of silicon microstrip detectors in the radial region between $20.5 \text{ cm} < r < 40 \text{ cm}$. High spatial precision (resolution of $\sim 15 \mu\text{m}$) and time resolution combined with adequate radiation hardness make silicon strip detectors ideal for the intermediate tracking region.

The outer tracking consists of seven layers of microstrip gas chambers (MSGC). The fast charge collection from the thin gas volume ensures good time resolution. Good

spatial resolution in the less congested outer region is provided by the MSGC's having a coarser pitch ($200\ \mu\text{m}$) than that of the silicon detectors ($50\ \mu\text{m}$). The strip length is chosen to limit the average occupancy to $\approx 4\%$ everywhere. The $r\varphi$ -resolution will be around $50\ \mu\text{m}$.

With the distributed tracking of CMS it should be possible to reconstruct $K_S^0 \rightarrow \pi^+\pi^-$ with sufficient efficiency (see section 7.5.3).

7.3.3 Trigger

The task of the trigger system is to reduce the input rate of $\sim 10^9$ events/s at high luminosity to < 100 Hz, the maximum rate at which events can be written on a permanent storage device. The average event size is ~ 1 MByte, most of the information being provided by the tracker. The needed data reduction is done in two steps. The level-1 trigger system, using only information from the muon system and the calorimeter, is implemented in hardware processors. It reduces the input rate of 40 MHz to a rate of less than 100 kHz. For the higher-level triggers, a high bandwidth (~ 500 Gbits/s) readout network treating the ~ 1000 front-end readout units with ~ 1000 Bytes/event and a high processing power event filter is needed. The event filter is implemented in an on-line farm (about 1000 units) where full event reconstruction is performed, reducing the event rate by a factor ~ 1000 for writing on mass storage. The total data production will be of the order of 1 TByte/day.

Here I will just concentrate on the level-1 muon trigger, because it is the crucial trigger component for the study of CP violation. A detailed description can be found in ref. [134]. The level-1 muon trigger should be very flexible and for luminosities of the order of $10^{33}\ \text{cm}^{-2}\text{s}^{-1}$ the following two trigger options are considered:

- inclusive single muon trigger that requires at least one muon with a p_t threshold of $5 - 100\ \text{GeV}/c$ (dependent on luminosity) in the rapidity range $|\eta^\mu| < 2.4$;
- inclusive dimuon trigger that requires at least two muons with a p_t threshold of $2.5 - 5\ \text{GeV}/c$ in the rapidity range $|\eta^\mu| < 2.4$.

The inclusive single muon trigger, whose threshold must be 4.5, 10 and 25 GeV/c at luminosities of 10^{32} , 10^{33} , and $10^{34}\ \text{cm}^{-2}\text{s}^{-1}$, respectively to cope with an acceptable level-1 trigger rate (≤ 100 kHz), is well suited for the study of the channel $B_d^0 \rightarrow \pi^+\pi^-$ [135] at low luminosity.

The dimuon trigger, whose threshold can be lower because of a lesser rate, is limited by the range of muons in the material that must be traversed to reach at least the first two layers of muon chambers out of the four possible ones. This trigger is well suited to accept a large fraction of the events containing J/ψ 's and is used for the CP violation measurement in the channel $B_d^0 \rightarrow J/\psi K_S^0$. The lowest values of the dimuon thresholds

(determined by muon penetration through the calorimeters) for 90% trigger efficiency for various rapidity ranges are:

$$\begin{aligned} p_t(\mu) &> 4.3 \text{ GeV}/c \text{ for } 0.0 < |\eta| \leq 1.5 \\ p_t(\mu) &> 3.4 \text{ GeV}/c \text{ for } 1.5 < |\eta| \leq 2.0 \\ p_t(\mu) &> 2.4 \text{ GeV}/c \text{ for } 2.0 < |\eta| \leq 2.5 \end{aligned}$$

These low thresholds are very useful for multi-muon final states in the low luminosity phase ($\sim 10^{33} \text{ cm}^{-2}\text{s}^{-1}$) because muons from $b\bar{b}$ events have relatively low p_t and a large number of triggered events is necessary to study CP violation.

7.4 Measuring $\sin 2\beta$

To determine the angle β of the unitarity triangle (see figure 3.4) the most appropriate decay-channel is $B_d^0 \rightarrow J/\psi K_S^0$ followed by $J/\psi \rightarrow \ell^+\ell^-$ ($\ell = \mu, e$) and $K_S^0 \rightarrow \pi^+\pi^-$, because it has the clearest signature and the most tractable background [136]. Moreover a nonvanishing asymmetry is guaranteed for this decay-channel in the Standard Model and a lower bound of the CP violation parameter can be predicted. Also penguin contributions to $b \rightarrow c\bar{c}s$ do not cause any problems, since the weak phase of the penguin contribution is the same as that of the tree level contribution. Hence, only a single weak phase contributes to the decay. The currently allowed range of $\sin 2\beta$ is $0.21 < \sin 2\beta < 1$ [74] and a fit of Standard Model parameters gives: $\sin 2\beta = 0.65 \pm 0.12$ [137]. Further advantages are the relatively high branching ratio and the fact that triggering on $J/\psi \rightarrow \ell^+\ell^-$ is relatively easy. Recent CDF results are most encouraging in this respect [118].

The time-dependent decay rates for B_d^0 and \bar{B}_d^0 to the final state $J/\psi K_S^0$ are:

$$\Gamma[B_d^0(t) \rightarrow J/\psi K_S^0] \propto e^{-\frac{t}{\tau}} (1 - \sin 2\beta \sin \Delta m t) \quad (7.2a)$$

$$\Gamma[\bar{B}_d^0(t) \rightarrow J/\psi K_S^0] \propto e^{-\frac{t}{\tau}} (1 + \sin 2\beta \sin \Delta m t) \quad (7.2b)$$

where $\Gamma = 1/\tau$ is the average of the widths Γ_1 and Γ_2 of the B_d^0 meson mass eigenstates, and Δm is the mass difference between the two eigenstates.

The experimentally measurable **time-dependent** decay asymmetry for this decay-channel is related to the CP violation parameter $\sin 2\beta$:

$$A(t) = \frac{\Gamma(B_d^0(t) \rightarrow J/\psi K_S^0) - \Gamma(\bar{B}_d^0(t) \rightarrow J/\psi K_S^0)}{\Gamma(B_d^0(t) \rightarrow J/\psi K_S^0) + \Gamma(\bar{B}_d^0(t) \rightarrow J/\psi K_S^0)} = \sin 2\beta \quad (7.3)$$

A measurement of this time-dependent decay rate asymmetry can be performed by reconstructing the decay vertex of the B_d^0 meson and measuring the decay distance.

Integrating the asymmetry (7.3) over all decay times $[0, \infty]$, one obtains the **time-integrated** decay asymmetry:

$$A = \frac{\Gamma(B_d^0 \rightarrow J/\psi K_S^0) - \Gamma(\bar{B}_d^0 \rightarrow J/\psi K_S^0)}{\Gamma(B_d^0 \rightarrow J/\psi K_S^0) + \Gamma(\bar{B}_d^0 \rightarrow J/\psi K_S^0)} = \sin 2\beta \cdot \frac{x_d}{1 + x_d^2} \quad (7.4)$$

where $x_d/(1 + x_d^2)$ is a factor due to time-integration and $x_d = \Delta m/\Gamma$ has been measured to be 0.71 [27]. In our study we just concentrate on the measurement of this time-integrated asymmetry, because it is easier to perform than a time-dependent measurement and less demanding on the performance of the vertex detector.

In order to measure this asymmetry, it is necessary to tag the flavour of the B_d^0 (\bar{B}_d^0) at production ($t = 0$). This can be done by using the techniques described in section 7.6. Here we assume that the flavour is tagged by the charge of the muon from the semileptonic decay of the associated B hadron. However, the flavour tagging will not be fully efficient and the measured asymmetry is affected by dilution effects. The really observed time-independent asymmetry takes the form:

$$A^{\text{obs}} \approx D \cdot (\sin 2\beta + A^{\text{fake}}) \quad (7.5)$$

where D is the dilution factor discussed in section 7.6 and A^{fake} is a fake asymmetry, which can arise from instrumental asymmetries and from unequal B_d^0 and \bar{B}_d^0 production in hadron collisions. Monte Carlo investigations [136,138] show that differences in B_d^0 and \bar{B}_d^0 production are minor in the p_t and η range of interest. Fake asymmetries are expected to be of the order of 1% compared to an expected CP asymmetry in this channel of the order of 30%. In any case they can be measured directly from the difference between B^+ and B^- or B_d^0 and \bar{B}_d^0 decaying to non-CP-violating final states.

7.5 Simulation of the $B_d^0 \rightarrow J/\psi K_S^0$ Channel

Events were generated using the Monte Carlo event generator PYTHIA [130,110] with gluon-gluon fusion, quark-antiquark annihilation and gluon splitting (next-to-leading order) contributions included. The leading order structure function set CTEQ2L [131] has been used. For fragmentation we used the Peterson fragmentation function with $\varepsilon_b = 0.006$ (see section 2.2.2). The default branching ratios of PYTHIA for all B hadron decay-channels have been updated in accordance with the 1994 Review of Particle Properties [27]. The B hadron lifetimes were set as follows: $\tau(B_d^0) = 1.63$ ps, $\tau(B^\pm) = 1.59$ ps, $\tau(B_s^0) = 1.56$ ps and $\tau(\Lambda_b^0) = 1.36$ ps.

We simulated $pp \rightarrow b\bar{b}$ events, where one b quark was forced to go to $B_d^0 \rightarrow J/\psi K_S^0 \rightarrow \mu^+ \mu^- \pi^+ \pi^-$. The muon with the highest p_t in the event, additional to the muons from the J/ψ decay, was taken to be the tagging muon. Figure 7.4 shows the typical topology of an event with $B_d^0 \rightarrow J/\psi K_S^0 \rightarrow \mu^+ \mu^- \pi^+ \pi^- + \text{tagging muon}$.

<i>Channel</i>	<i>Branching Ratio</i>
$b \rightarrow B_d^0$	0.4
$B_d^0 \rightarrow J/\psi K_S^0$	3.75×10^{-4}
$J/\psi \rightarrow \mu^+ \mu^-$	0.0597
$K_S^0 \rightarrow \pi^+ \pi^-$	0.6861
$b \rightarrow \mu X$	0.103

Table 7.1: *Branching ratios used for the simulation of the $B_d^0 \rightarrow J/\psi K_S^0$ channel [27].*

We assumed a center-of-mass energy of $\sqrt{s} = 14$ TeV and a total $b\bar{b}$ cross-section of $\sigma_{b\bar{b}} = 500 \mu\text{b}$. To avoid problems due to multiple events per bunch-crossing we assumed a luminosity of $\mathcal{L} = 10^{33} \text{ cm}^{-2}\text{s}^{-1}$ (corresponding to an integrated luminosity of 10^4 pb^{-1}), which might be realistic for the first years of LHC operation. In this regime we expect from 1.5 to 2 underlying events per bunch crossing. With this integrated luminosity we anticipate about 5×10^{12} $b\bar{b}$ events per year (10^7 s), out of which approximately one third is produced with both B hadrons in the central region of the detector ($|\eta| \leq 2.4$).

The branching ratios used for this analysis are listed in table 7.1. The total branching fraction for the decay-channel $B_d^0 \rightarrow J/\psi K_S^0 \rightarrow \mu^+ \mu^- \pi^+ \pi^-$ including the semileptonic branching ratio of the associated b (tagging) is 1.58×10^{-6} . Before any trigger and selection cut, the number of expected $B_d^0 \rightarrow J/\psi K_S^0$ events (including a muon for tagging) is 6.3×10^6 per year (10^7 s).

A simple detector simulation was performed to estimate the detector effects. The kinematical parameters ($1/p, \lambda, \varphi$) of all charged particles have been smeared according to a parametrization obtained by a full detector simulation [138,139] as a function of pseudorapidity and transverse momentum.

7.5.1 Kinematics

As can be seen from figure 7.3, most of the B hadrons are produced with low p_t in the forward region. This results from the boost, due to the unequal energies of the interacting partons at high energy pp collisions. A trigger on one or two high- p_t leptons will select a sample of central B hadrons. The average momentum of B mesons before any selection cuts is $\langle p^B \rangle = 140 \text{ GeV}/c$ and the average transverse momentum (with respect to the beam direction) is $\langle p_t^B \rangle = 4.8 \text{ GeV}/c$. After applying the trigger cuts and requiring a third muon to reach the first muon station, the values are: $\langle p^B \rangle = 37 \text{ GeV}/c$ and $\langle p_t^B \rangle = 14 \text{ GeV}/c$. Figure 7.5 shows the p and p_t distributions of B hadrons before and after applying trigger cuts. The average decay distance of B hadrons in space before any cuts is $\langle d^B \rangle = 26 \text{ mm}$ and the decay

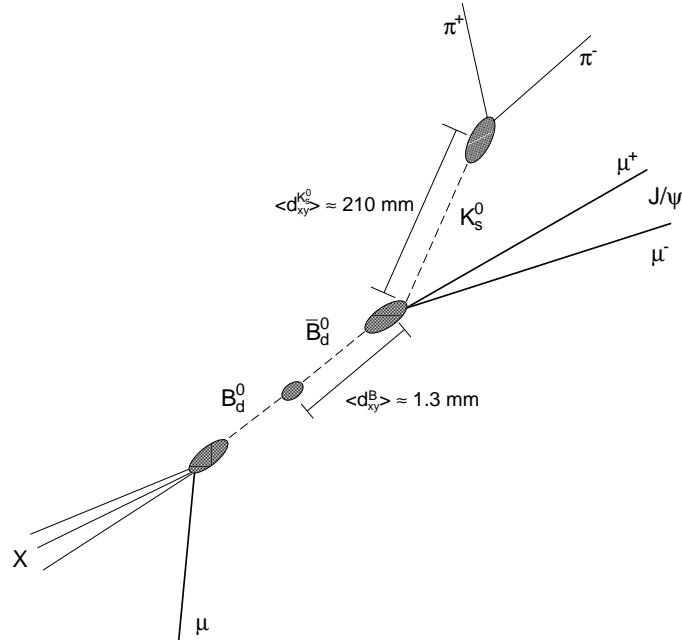


Figure 7.4: Topology of an $B_d^0 \rightarrow J/\psi K_S^0$ event in the transverse plane.

distance in the transverse plane is $\langle d_{xy}^B \rangle = 0.51 \text{ mm}$. After applying the trigger cuts the transverse decay distance becomes $\langle d_{xy}^B \rangle = 1.3 \text{ mm}$ (see fig. 7.6). Selecting central $B\bar{B}$ events with a high- p_t lepton trigger, the kinematic of the decay $B_d^0 \rightarrow J/\psi K_S^0$ is very similar to that of a typical B decay at LEP. Figure 7.7 shows the p_t and η distributions of the tagging muon. The arrow indicates the cuts applied in the analysis.

7.5.2 Trigger and Event Selection

In order to cope with the high rates and to select the interesting events ($\sigma_{b\bar{b}}/\sigma_{\text{tot}} \sim 0.5\%$) one has to trigger either on one high p_t muon or on two muons. In principle there are 3 possibilities to select $B_d^0 \rightarrow J/\psi K_S^0$ events including one additional lepton (muon or electron) for tagging:

- (i) muon-tag with $J/\psi \rightarrow \mu^+ \mu^-$
- (ii) muon-tag with $J/\psi \rightarrow e^+ e^-$
- (iii) electron-tag with $J/\psi \rightarrow \mu^+ \mu^-$

For our simulation we consider only muons since electrons are much more difficult to identify [140], therefore only case (1) is studied here.

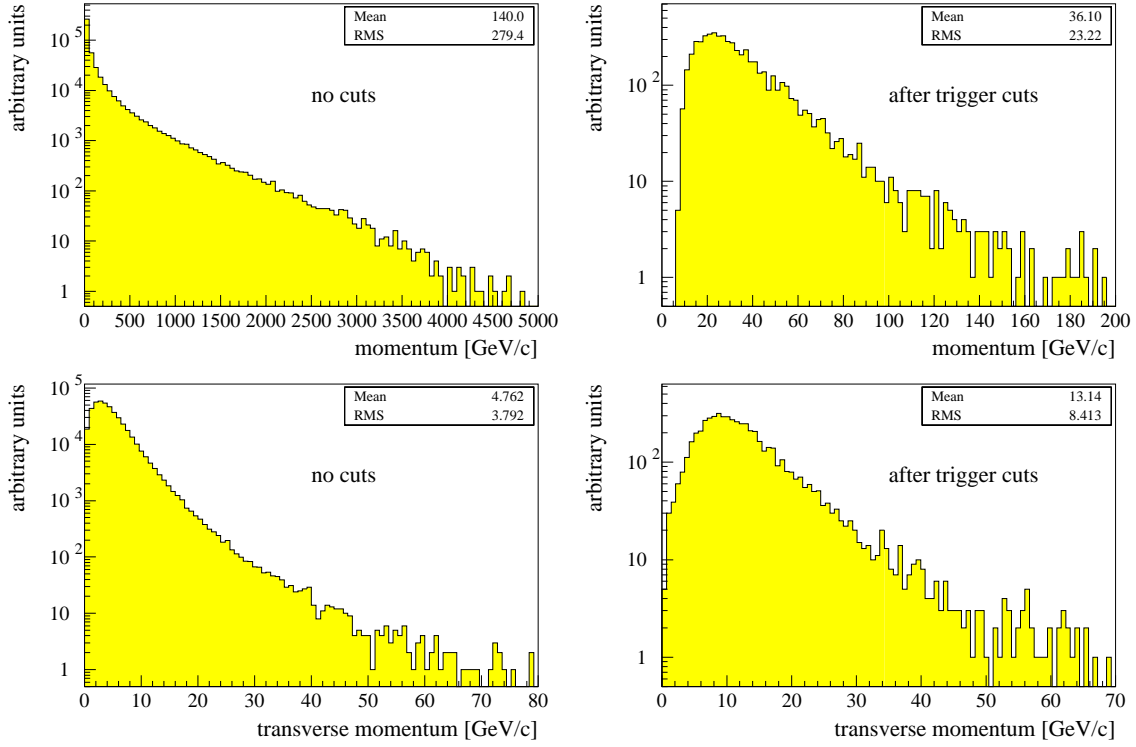


Figure 7.5: Momentum and transverse momentum distribution of B hadrons before and after trigger cuts.

The trigger is provided by two low- p_t muons with rapidity-dependent trigger thresholds:

$$\begin{aligned}
 p_t^\mu &> 4.3 \text{ GeV}/c & \text{for } 0.0 < |\eta| \leq 1.5 \\
 p_t^\mu &> 3.4 \text{ GeV}/c & \text{for } 1.5 < |\eta| \leq 2.0 \\
 p_t^\mu &> 2.4 \text{ GeV}/c & \text{for } 2.0 < |\eta| \leq 2.5
 \end{aligned}$$

The trigger efficiencies were calculated with a full detector simulation [134] and parametrized as a function of p_t and η .

In addition to the two triggered muons, a third muon is required to be within the geometrical acceptance of $|\eta| \leq 2.4$ and reach at least the first muon station.

The following further cuts were applied to all events:

- two charged π 's from K_S^0 within $|\eta^\pi| \leq 2.4$ and $p_t^\pi \geq 0.7 \text{ GeV}/c$,
- K_S^0 decay length in the transverse plane between 2 and 40 cm, to avoid problems due to pattern recognition,

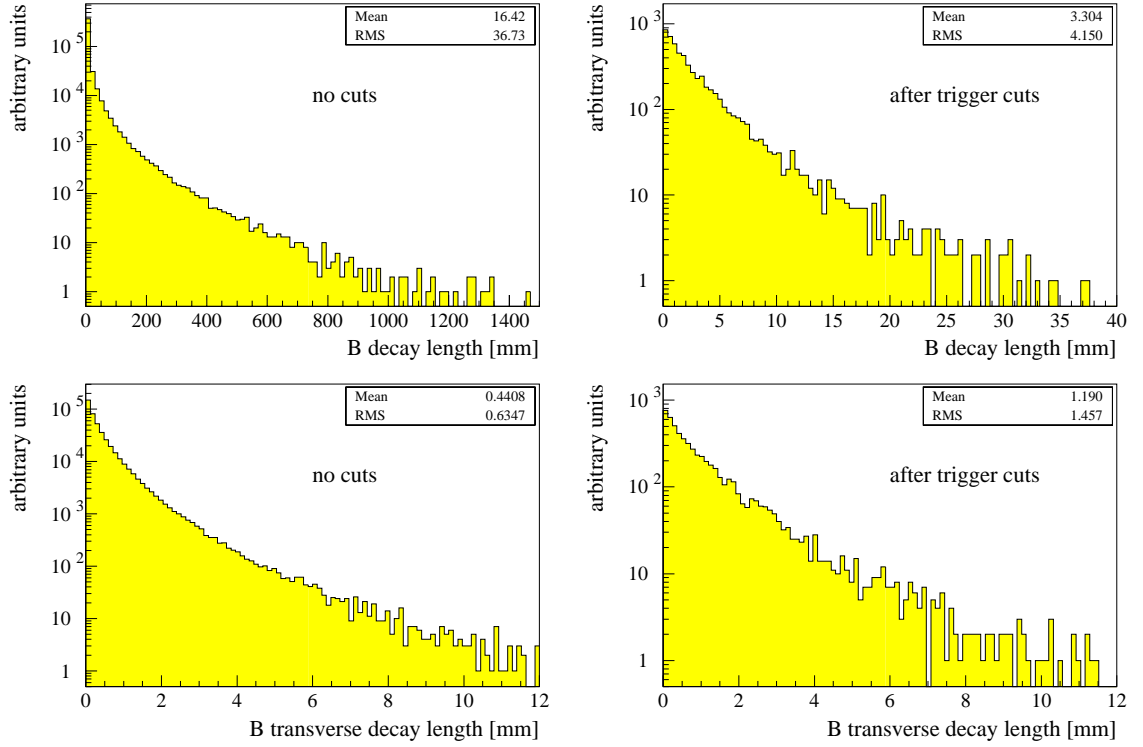


Figure 7.6: *Decay length and transverse decay length of the B_d^0 before and after trigger cuts.*

- the reconstructed invariant masses of J/ψ , K_S^0 and B_d^0 must lie within $\pm 2\sigma$ of their known masses,
- tag muon with $p_t > 5 \text{ GeV}/c$

All combinations of the three muons were taken to reconstruct the J/ψ . If more than one combination of tracks satisfied the J/ψ selection requirements, only the pair with invariant mass closest to the J/ψ mass was retained for further analysis. Table 7.2 lists the selection efficiencies for the individual cuts. The number in the first line includes also the trigger efficiency. The cut on the transverse decay length of the K_S^0 is included in the K_S^0 reconstruction efficiency.

The reconstructed invariant mass distributions for $J/\psi \rightarrow \mu^+\mu^-$ and for $B_d^0 \rightarrow J/\psi K_S^0 \rightarrow \mu^+\mu^-\pi^+\pi^-$ according to our detector simulation are shown in figure 7.8. The fitted values for the mass resolutions are: $\sigma(K_S^0) = 8.6 \text{ MeV}/c^2$, $\sigma(J/\psi) = 16 \text{ MeV}/c^2$, $\sigma(B_d^0) = 22 \text{ MeV}/c^2$. Using the known values of the J/ψ and K_S^0 masses as constraints, we obtain $\sigma(B_d^0) = 12 \text{ MeV}/c^2$ [135].

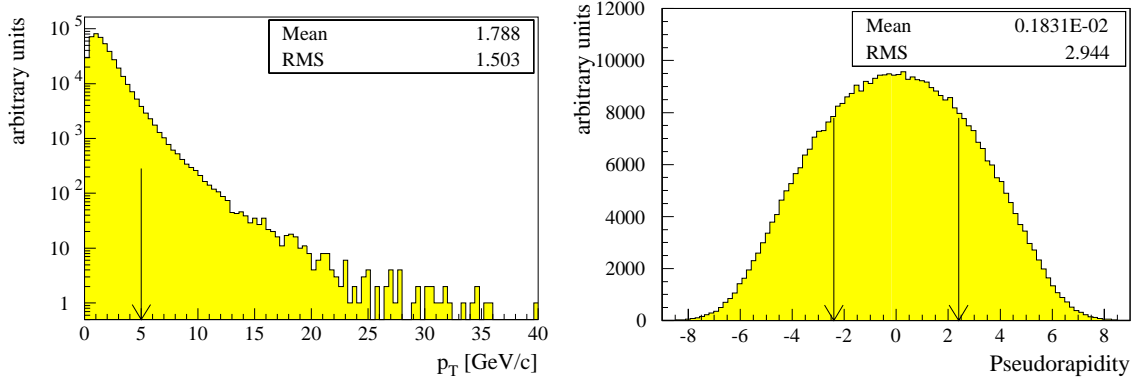


Figure 7.7: *Transverse momentum and pseudorapidity of the tagging muon. The arrows indicate the cuts applied in the analysis.*

<i>Cut</i>	<i>Efficiency</i>
2μ triggered + 1μ accepted $ \eta < 2.4$	$\varepsilon = 1.32 \times 10^{-2}$
μ^{tag} : $p_t > 5$ GeV/c and $ \eta < 2.4$	$\varepsilon = 0.34$
π 's from K_S^0 : $p_t > 0.7$ GeV/c and $ \eta < 2.4$	$\varepsilon = 0.55$
invariant mass cut ($\pm 2\sigma$) for J/ψ , K_S^0 and B_d^0	$\varepsilon = 0.86$

Table 7.2: *Event selection efficiency.*

To obtain the expected number of events, in addition to the trigger and selection cut efficiencies a track reconstruction efficiency of 95% for triggered muons and 90% for the third (not triggered) muon is considered.

7.5.3 K_S^0 Reconstruction

A dedicated track finder optimized for low p_t tracks that attempts to find all tracks above a transverse momentum of 350 MeV/c was developed for CMS [141]. To estimate the efficiency for K_S^0 reconstruction, B events with K_S^0 decays were fully simulated. For low momentum tracks bent in the strong magnetic field, the performance of the MSGC's degrades and the measured behaviour of the MSGC's as a function of the angle of incidence was implemented. Pairs of tracks consistent with a secondary vertex separated from the primary vertex by more than 2 cm are formed. Figure 7.9 shows the reconstructed invariant mass for all candidate pairs including the combinatorial background coming from the same event. The K_S^0 mass resolution is 8.6 MeV/c and the average signal to background ratio (background from the combinatorics of all candidate pairs) is $\approx 2 : 1$. Because of the p_t cut imposed in our analysis ($p_t^\pi > 700$ MeV/c),

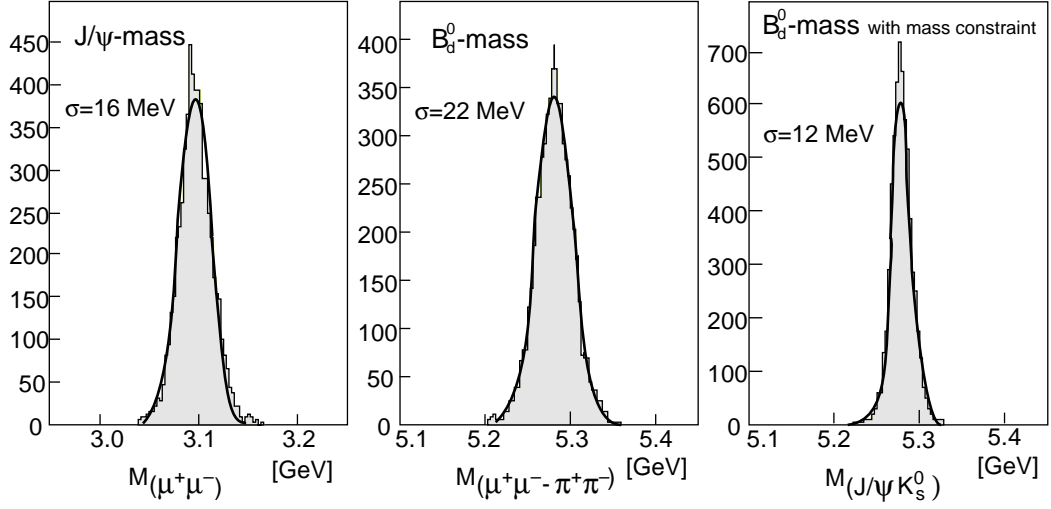


Figure 7.8: *Invariant mass resolution of $J/\psi \rightarrow \mu^+\mu^-$, $B_d^0 \rightarrow \mu^+\mu^-\pi^+\pi^-$ and $B_d^0 \rightarrow J/\psi K_S^0$.*

the minimum p_t considered for the K_S^0 is ≈ 1.4 GeV/ c . For our rapidity coverage the average K_S^0 reconstruction efficiency is about 35% [141]. This reconstruction efficiency can be compared, for example, with the values of 21% in UA1 (for $p_t^\pi > 200$ MeV/ c) and 32% in CDF for $p_t^\pi > 400$ MeV/ c . The results discussed above correspond to events in which there are about 200 tracks per bunch crossing.

7.6 Tagging and Dilution

To measure the CP asymmetry it is necessary to tag the flavour of the decaying B_d^0 meson at production time ($t = 0$) to know whether it was produced as a B_d^0 or a \bar{B}_d^0 . However, the flavour tagging will not be fully efficient and the measured decay asymmetry will be affected by dilution effects (see equation 7.5).

Several flavour tagging techniques have been proposed in literature:

- charge of the lepton from the semileptonic decay $b \rightarrow \ell^- \nu X$ (ℓ = muon, electron),
- jet charge,
- charge of the pion from $B^{**} \rightarrow B\pi^\pm$ decays,
- charge of the associated B^\pm , through a complete B^\pm reconstruction,
- charge of the kaons from the decay $b \rightarrow c \rightarrow s$

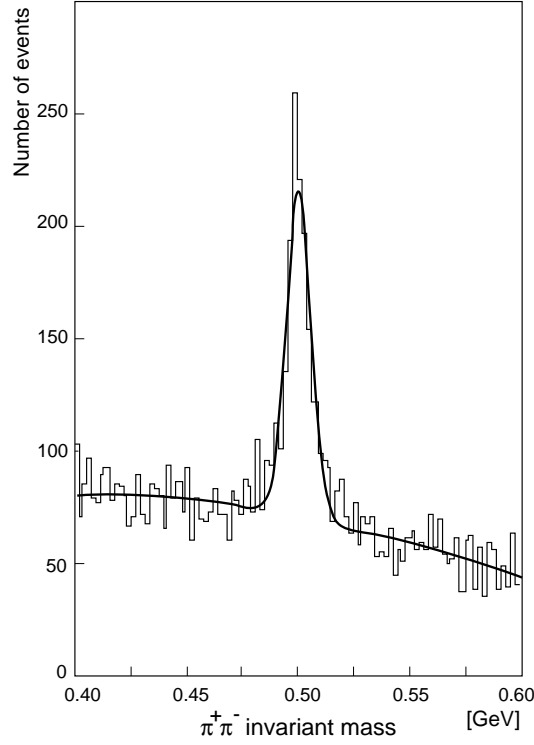


Figure 7.9: K_S^0 invariant mass, with the combinatorial background coming from the same event.

Each of these flavour tagging methods will have a certain efficiency ε and dilution D . It is a trade-off between efficiency and purity to optimize the “effective flavour tagging efficiency” (εD^2)¹.

For this study we consider only the first method where the flavour of the produced B_d^0 is tagged by the charge of the lepton from the semileptonic decay of the associated b quark in the event. Practically the flavour is misidentified part of the time which will introduce a tagging dilution factor D_{tag} .

The muon mistagging can be due to:

1. oscillating of B_d^0 or B_s^0 before decaying into muons
2. cascade-decays $b \rightarrow c \rightarrow \mu^+ X$
3. μ 's from hadron decays (K's and π 's)

¹For a flavour tagging method with efficiency ε and dilution D , the uncertainty on the CP asymmetry is given by $\delta A_{\text{CP}}^2 \approx 1/(\varepsilon D^2 N)$, where N is the total number of signal events prior to flavour tagging (see section 7.8).

4. extra c and b quark pairs produced in the event
5. punch-through in the detector.

The dominant contribution to mistagging is from oscillations of B_d^0 or B_s^0 before decaying into muons and from cascade decays.

The tagging dilution factor D_{tag} is defined as:

$$D_{\text{tag}} = \frac{N(\text{good tags}) - N(\text{bad tags})}{N(\text{good tags}) + N(\text{bad tags})} = 1 - 2 \times w \quad (7.6)$$

where w is the fraction of wrong sign muons.

The contribution to the tagging dilution factor due to mixing (source 1.) can be written as:

$$D_{\text{mix}} = \sum_i p_i \frac{1}{1 + x_i^2} \quad (7.7)$$

where p_i are the production rates for B^\pm , B_d^0 , B_s^0 and Λ_b^0 . With $p^\pm : p_d : p_s : p_\Lambda = 0.40 : 0.40 : 0.12 : 0.08$, $x_d = 0.71$ [27] and $x_s = 20.0$, the dilution factor due to mixing is $D_{\text{mix}} = 0.75$.

Figure 7.10 shows the fraction of wrong sign muons plotted as a function of the p_t cut of the muon for various sources of mistags. The tagging-quality increases with higher p_t -cuts on the muon [142].

The major contribution to w (except from mixing) is from cascade decays. These are processes in which the muon does not come directly from a b or \bar{b} decay but from a decay $b \rightarrow c \rightarrow \mu^+ X$ where the μ has a charge opposite to that of a muon from the direct decay $b \rightarrow \mu$. Because of the hard fragmentation and the large mass of the b quark, muons from semileptonic B decays have larger transverse momentum than muons from cascade decays.

We considered muons coming from K^\pm and π^\pm decays with a production vertex inside a cylindrical volume of $r = 1.3$ m and $l = 7$ m as possible sources of mistags.

Mistags due to additional $b\bar{b}$ and $c\bar{c}$ pairs in the event are also considered. This contribution is of the order of 1%.

The punch-through has not been included, but the fraction of punch-through muons is expected to be lower than the fraction of muons from hadron decays.

With a muon p_t^μ -threshold of 5.0 GeV/ c , the fraction of wrong sign muons (excluding mixing) was found to be 13%. Including mixing we obtain a tagging dilution factor of $D_{\text{tag}} = 0.56$.

The presence of background (see section 7.7) introduces a second dilution factor:

$$D_{\text{back}} = \frac{N_S}{N_S + N_B} \quad (7.8)$$

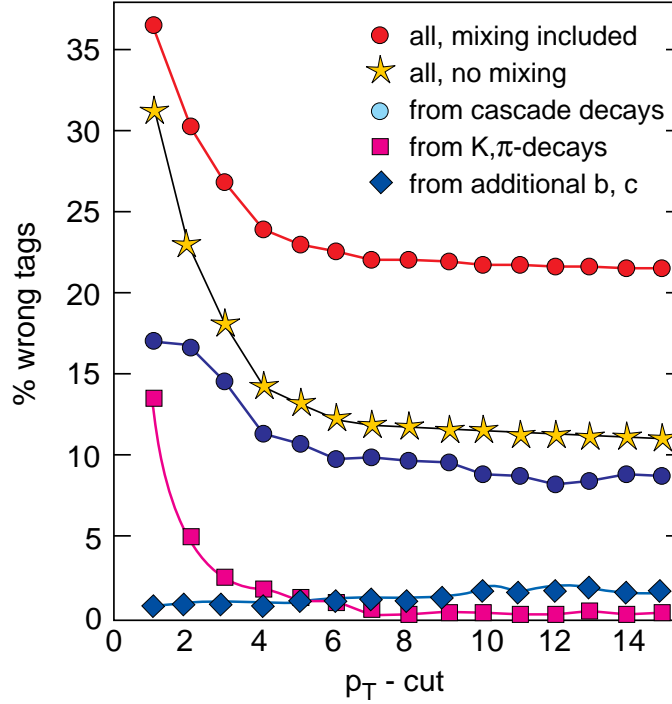


Figure 7.10: Number of wrong tags as a function of p_t^μ

where N_S and N_B are the numbers of signal and background events.

In the case of a time-integrated measurement there is an additional dilution factor D_{int} from time-integration:

$$D_{\text{int}} = \frac{\sin \Delta m t_0 + x_d \cos \Delta m t_0}{1 + x_d^2} \quad (7.9)$$

where t_0 is the start time of the integration, $x_d = \Delta m / \Gamma$ is the B_d^0 mixing parameter, Δm is the mass difference between the B_d^0 meson mass-eigenstates, and Γ is the average width of the eigenstates. Starting the time-integration from $t_0 = 0$ D_{int} is exactly $x_d / (1 + x_d^2) = 0.472$ in equation 7.4.

The total dilution factor D in equation 7.5 can be written as:

$$D = D_{\text{int}} \cdot D_{\text{tag}} \cdot D_{\text{back}} \quad (7.10)$$

In order to measure the dilution factor, one must identify simultaneously the charge (or flavour) of one B hadron via its decay products and of the other one via the charge of the tagging muon. The following channels can be considered to measure the dilution factor: $B^\pm \rightarrow J/\psi K^\pm$ and $B_d^0 \rightarrow J/\psi K^{*0}$. After applying all kinematical cuts and efficiencies we estimate to obtain approximately ten times more reconstructed events for these control channels than for the signal channel [143].

7.7 Background

The background for this channel can come from (i) inclusive J/ψ production in b-decays, (ii) direct J/ψ production, and (iii) combinatorial background. The combinatorial background comes from events where the invariant mass of two muons falls accidentally in the allowed J/ψ mass window and two charged hadrons pass the K_S^0 selection criteria. The K_S^0 can be either from a b-decay, from jet fragmentation, from an underlying event or from accidental coincidences of two tracks. Fake K_S^0 are highly suppressed by demanding a transverse decay length of the K_S^0 greater than 2 cm.

The dominant background comes from accidental coincidences between a real J/ψ and a K_S^0 from fragmentation ((i) and (ii)). For the simulation of the background an inclusive cross-section for the process $pp \rightarrow b\bar{b} \rightarrow J/\psi + X$ of $16\mu\text{b}$ was assumed, which corresponds to our total $b\bar{b}$ cross-section with branching ratios $Br(b \rightarrow J/\psi + X) = 1.1\%$ and $Br(b \rightarrow \psi' + X) = 0.5\%$.

The direct J/ψ production ($gg \rightarrow J/\psi$) gives much softer J/ψ 's than those from beauty hadron decays and is highly suppressed by applying the p_t -cuts on the muons from a J/ψ and requiring a third muon in the event. A cut on the proper decay time of the J/ψ will further remove events in which the J/ψ is produced at the primary vertex.

In beauty hadron decays to $J/\psi + X$ there is a special class of decays, where K_S^0 is a decay product in the B decay chain:

$$\begin{aligned} B^\pm &\rightarrow J/\psi K^{*\pm} \rightarrow J/\psi K_S^0 \pi^\pm \\ B_d^0 &\rightarrow J/\psi K^{*0} \rightarrow J/\psi K_S^0 \pi^0 \\ B &\rightarrow \psi'(K/K^*) \rightarrow J/\psi K_S^0 + n\pi^\pm \end{aligned}$$

The background from these events has been specially studied. In all the above channels at least one additional particle is produced. This causes the invariant mass of $\mu^+\mu^-\pi^+\pi^-$ to be shifted to a value lower than $m_{B_d^0}$. Because of the very good mass resolution, all channels that contain additional pions in the decay chain peak below the accepted signal mass peak and are highly rejected.

The reconstructed invariant mass $m_{\mu\mu\pi\pi}$ after all selection cuts for signal and background is shown in fig. 7.11. The signal to background ratio is about 10 : 1.

7.8 Expected Sensitivity

The expected number of signal events for an integrated luminosity \mathcal{L}_{int} is:

$$\begin{aligned} N_{\text{sig}} = & 2 \cdot \mathcal{L}_{\text{int}} \cdot \sigma_{b\bar{b}} \cdot Br[\bar{b} \rightarrow B_d^0] \cdot Br[B_d^0 \rightarrow J/\psi K_S^0] \cdot Br[J/\psi \rightarrow \mu^+\mu^-] \cdot \\ & \cdot Br[K_S^0 \rightarrow \pi^+\pi^-] \cdot Br[b \rightarrow \mu X] \cdot \varepsilon^{\text{trig}} \cdot \varepsilon^{\text{cut}} \cdot \varepsilon^{\text{rec}} \end{aligned} \quad (7.11)$$

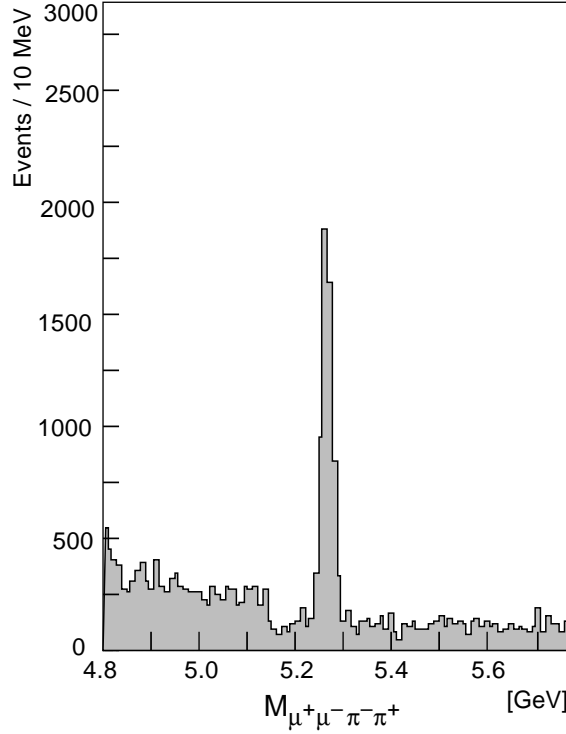


Figure 7.11: *Invariant mass spectrum of $\mu^+\mu^-\pi^+\pi^-$ for $p_t(\mu^{\text{tag}}) \geq 5 \text{ GeV}/c$.*

where $\varepsilon^{\text{trig}}$ is the trigger efficiency, ε^{cut} is the efficiency of the selection cuts and ε^{rec} is the reconstruction efficiency, which includes a track reconstruction efficiency of $(0.95)^2 \cdot 0.9$ and a K_S^0 reconstruction efficiency of 0.35.

The total numbers of fully reconstructed and μ -tagged events for 10^4 pb^{-1} are given in table 7.3 as a function of the tagging muon p_t . These numbers include the kinematical acceptance, trigger efficiencies, efficiencies for a tracking and identification and K_S^0 reconstruction efficiency.

The statistical error on the measurement of $\sin 2\beta$ is given by:

$$\delta(\sin 2\beta) \simeq \frac{\sqrt{1 - (D \cdot \sin 2\beta)^2}}{D \cdot \sqrt{N_{\text{tot}}}} \simeq \frac{1}{D \cdot \sqrt{N_{\text{tot}}}} \quad (7.12)$$

where $D = D_{\text{int}} \cdot D_{\text{tag}} \cdot D_{\text{back}}$ is the dilution factor and N_{tot} is the total number of reconstructed events. The expected statistical error on $\sin 2\beta$ for different cuts on the tagging muon is given in table 7.3. For a p_t cut of $5 \text{ GeV}/c$ and with 10^4 pb^{-1} the error on $\sin 2\beta$ is 0.064.

Fig. 7.12 shows the number of reconstructed events necessary to measure $\sin 2\beta$ with 3 and 5 standard deviations. The present expected theoretical lower limit on

$p_t^{\mu, \text{tag}}$ [GeV/c]	3.0	3.5	4.0	4.5	5.0
N_{sig}	7740	6840	5830	4590	3810
N_{back}	750	670	580	480	350
N_{tot}	8490	7510	6410	5070	4160
D_{int}	0.47	0.47	0.47	0.47	0.47
D_{tag}	0.48	0.51	0.53	0.54	0.56
D_{back}	0.91	0.91	0.91	0.91	0.92
D	0.21	0.22	0.23	0.23	0.24
$\delta(\sin 2\beta)$	0.052	0.053	0.054	0.061	0.064

Table 7.3: The expected sensitivity to $\sin 2\beta$ as a function of the p_t cut of the tagging-muon.

$\sin 2\beta$ is 0.21 [74]. The statistical significance of the measurement of $\sin 2\beta$ is given by:

$$S = \frac{\sin 2\beta}{\delta(\sin 2\beta)} = \sqrt{N} \cdot \frac{D \cdot \sin 2\beta}{\sqrt{1 - (D \cdot \sin 2\beta)^2}} \quad (7.13)$$

Systematic uncertainties in the measurement of $\sin 2\beta$ can originate from the production asymmetry of B_d^0 and \bar{B}_d^0 at LHC. This asymmetry has been estimated to be at the per cent level, and it can be measured from data using CP-conserving B decay modes. Estimation of the dilution factor could be another source of possible systematic uncertainty, which should be measured from data using semileptonic B decays or exclusive decay-channels like: $B^\pm \rightarrow J/\psi K^\pm$ or $B_d^0 \rightarrow J/\psi K^{*0}$. The B_d^0 and B_s^0 mixing strength will be known at the time of the LHC start-up with quite high accuracy.

The theoretical uncertainties in the measurement of $\sin 2\beta$ are expected to be less than 1%. and the experimental sources of systematic uncertainties can be controlled with comparable accuracy.

7.9 Results and Discussion

A simulation of a time-integrated measurement of the CP violation parameter $\sin 2\beta$ has been performed. The CMS detector was taken as an example for a general purpose detector at the LHC. Including all possible dilution effects and taking into account detector efficiencies, the potential of such a general purpose detector in measuring CP violation was studied. It is shown, that with an integrated luminosity of 10^4 pb^{-1} , which is expected to be delivered after one year of LHC running, a 3σ measurement of $\sin 2\beta$ in the presently allowed range will be possible.

Even if $\sin 2\beta$ is already measured at the time of LHC start-up, the copious production of beauty hadrons at the LHC will allow a precision measurement of CP violation with unmatched statistics.

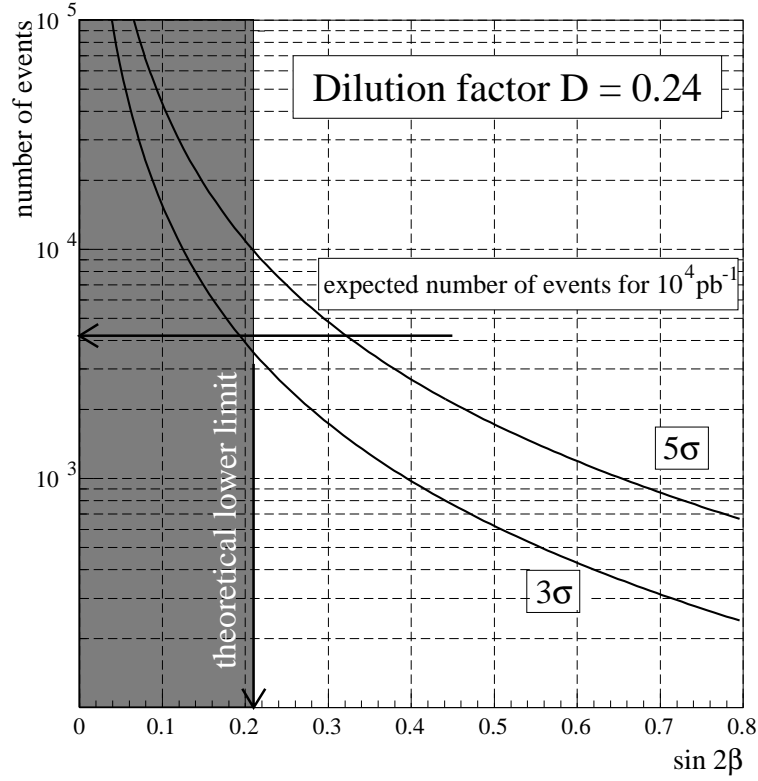


Figure 7.12: Number of reconstructed events required for measuring 3σ and 5σ effects as a function of the CP violation parameter $\sin 2\beta$. The arrow represents the total number of reconstructed events with a p_t cut of 5 GeV/c on the tagging muon for 10^4 pb^{-1} .

The obtained results show, that a general purpose LHC detector, like CMS, is well suited to study CP violation in the $B_d^0 \rightarrow J/\psi K_S^0$ channel and will be quite competitive with dedicated B-physics experiments in the measurement of the angle β .

Chapter 8

Summary and Conclusions

Anyone who keeps the ability to see beauty never grows old.

— FRANZ KAFKA

This thesis describes an analysis of exclusive B meson decays into final states including a J/ψ , using data recorded by the DELPHI experiment at LEP. The selection of J/ψ events was used as a starting point for the analysis of colour suppressed B meson decays into charmonium. J/ψ mesons have been reconstructed from their decays into muon and electron pairs. Using the sample of reconstructed J/ψ candidates, the inclusive branching ratios $Br(Z^0 \rightarrow J/\psi X)$ and $Br(b \rightarrow J/\psi X)$ have been calculated. The obtained results of $Br(Z^0 \rightarrow J/\psi X) = (3.7 \pm 0.3 \pm 0.3) \times 10^{-3}$ and $Br(b \rightarrow J/\psi X) = (1.15 \pm 0.09 \pm 0.14) \times 10^{-2}$ are in good agreement with measurements of the other LEP experiments and show an improvement compared to the published DELPHI results.

Starting from the inclusive J/ψ sample a search for exclusive B meson decays into final states including a J/ψ has been performed. The following channels have been searched for: $B^\pm \rightarrow J/\psi K^\pm$, $B_d^0 \rightarrow J/\psi K_S^0$, $B_d^0 \rightarrow J/\psi K^{*0}$, $B_d^0 \rightarrow J/\psi K^+ \pi^-$, $B^\pm \rightarrow J/\psi K^\pm \pi^+ \pi^-$, $B^\pm \rightarrow J/\psi K^{*\pm}$ and $B^\pm \rightarrow J/\psi K_S^0 \pi^\pm$.

After background subtraction 40.2 ± 7 signal events were obtained. Due to the limited statistics available, it can be concluded, that a measurement of CP violation in the B system is not possible at LEP.

Therefore, in the second part of this thesis, the possibilities of future experiments in the search for CP violation, with special emphasis on the planned experiments at the LHC, have been studied. The CMS detector has been used as an example to demonstrate the capacity of a general purpose LHC detector in measuring CP violation in the decay channel $B_d^0 \rightarrow J/\psi K_S^0$. A simulation of a time-integrated measurement of the CP asymmetry has been performed in order to extract the angle β of the CKM unitarity triangle. Including all possible dilution effects and taking into account detector

efficiencies, the potential of the CMS detector in measuring the angle β was studied.

It could be shown, that with an integrated luminosity of 10^4 pb^{-1} , which is expected to be delivered after one year of LHC running, a 3σ measurement of $\sin 2\beta$ in the presently allowed range will be possible.

List of Figures

2.1	Feynman diagrams for electron positron annihilation	18
2.2	Total e^+e^- cross-section	20
2.3	Evolution of a hadronic e^+e^- event	22
2.4	Fragmentation function	24
2.5	Lowest order Feynman diagrams for weak decays of B mesons	28
2.6	J/ψ production through the decay of a B meson	32
3.1	The unitarity triangles of the CKM matrix	42
3.2	Unitarity triangle	43
3.3	Box diagrams responsible for $B^0-\bar{B}^0$ mixing	45
3.4	The unitarity triangle with present experimental constraints	50
4.1	A 3-dimensional view of the DELPHI detector	56
4.2	Longitudinal view of the DELPHI detector	57
4.3	Schematic view of the VD in the 1994 configuration	60
4.4	Inverse momentum distributions for muons from $Z^0 \rightarrow \mu^+\mu^-$	62
4.5	Dimuon miss distance distribution	64
4.6	Impact parameter resolution	65
4.7	Impact parameter in the Rz plane	66
4.8	Resolution of the HPC	67
4.9	Specific energy loss in the TPC as a function of momentum	74
4.10	Average Cherenkov angle distribution <i>vs</i> momentum	76
5.1	Charmonium system	80
5.2	Kinematical distributions of the J/ψ meson	84
5.3	Invariant mass spectrum of simulated J/ψ events	85
5.4	Reconstructed secondary vertex resolution	87
5.5	Secondary vertex probability	88
5.6	Dilepton invariant mass distribution	89
5.7	Invariant mass distribution of $\mu^\pm e^\mp$ pairs	90
5.8	Kinematical distributions of the B meson	96
5.9	K_S^0 reconstruction in J/ψ events	98

5.10	Monte Carlo: B reconstruction	100
5.11	Monte Carlo: B reconstruction	101
5.12	Data: B reconstruction	103
5.13	Data: B reconstruction	104
5.14	B mass distribution	106
5.15	Event display: $B^+ \rightarrow J/\psi K^+ \rightarrow \mu^+ \mu^- K^+$	107
5.16	Event display: $B_d^0 \rightarrow J/\psi K_S^0 \rightarrow \mu^+ \mu^- \pi^+ \pi^-$	108
5.17	Event display: $B_d^0 \rightarrow J/\psi K^{*0} \rightarrow e^+ e^- K^+ \pi^-$	109
5.18	Event display: $B^+ \rightarrow J/\psi K_S^0 \pi^+ \rightarrow \mu^+ \mu^- \pi^+ \pi^- \pi^+$	110
5.19	Event display: $B^+ \rightarrow J/\psi K^+ \pi^- \pi^+ \rightarrow \mu^+ \mu^- K^+ \pi^- \pi^+$	111
6.1	LHC cross-sections	120
7.1	$b\bar{b}$ production at the LHC	124
7.2	Lowest order Feynman diagrams for $b\bar{b}$ production	125
7.3	p_t and η spectra of B hadrons for different structure functions	126
7.4	Topology of an $B_d^0 \rightarrow J/\psi K_S^0$ event	133
7.5	Momentum and transverse momentum distribution	134
7.6	Decay length of the B_d^0	135
7.7	Transverse momentum and pseudorapidity of the tagging muon	136
7.8	Invariant mass resolution of J/ψ and B_d^0	137
7.9	K_S^0 invariant mass	138
7.10	Number of wrong tags as a function of p_t^μ	140
7.11	Invariant mass spectrum of $\mu^+ \mu^- \pi^+ \pi^-$	142
7.12	Sensitivity to $\sin 2\beta$	144

List of Tables

2.1	The properties of quarks	10
2.2	Electroweak quantum numbers of the fundamental fermions	12
2.3	Electroweak quantum numbers of the Standard Model bosons.	13
2.4	Standard Model parameters	18
2.5	Branching ratios for exclusive B decays	33
3.1	Experimental values of the elements of the CKM matrix	41
3.2	B decay modes for CP violation studies	51
4.1	Momentum resolution for 45 GeV/c muons	63
4.2	Muon identification efficiency	78
4.3	Electron identification efficiency	78
5.1	Properties of the J/ψ and ψ' mesons	79
5.2	Data sample used in this analysis	81
5.3	Secondary vertex resolution	90
5.4	J/ψ reconstruction results for data and Monte Carlo	91
5.5	Systematic errors in the measurement	93
5.6	LEP measurements of the J/ψ production in Z^0 decays	93
5.7	Expected number of B mesons	94
5.8	Summary of efficiencies for the B reconstruction	99
5.9	Summary of reconstructed B decays	105
6.1	Future B physics experiments	115
6.2	LHC machine parameters	119
7.1	Branching ratios used for the simulation	132
7.2	Event selection efficiency	136
7.3	Expected sensitivity to $\sin 2\beta$	143

Bibliography

- [1] G. Arnison *et al.* (UA1 Collaboration), *Experimental Observation of Isolated Large Transverse Energy Electrons with Associated Missing Energy at $\sqrt{s} = 540$ GeV*, Phys. Lett. **B 122** (1983) 103.
- [2] M. Banner *et al.* (UA2 Collaboration), *Observation of Single Isolated Electrons of High Transverse Momentum in Events with Missing Transverse Energy at the CERN $\bar{p}p$ Collider*, Phys. Lett. **B 122** (1983) 476.
- [3] G. Arnison *et al.* (UA1 Collaboration), *Experimental Observation of Lepton Pairs of Invariant Mass Around 95 GeV/c² at the CERN SPS Collider*, Phys. Lett. **B 126** (1983) 398.
- [4] P. Bagnaia *et al.* (UA2 Collaboration), *Evidence for $Z^0 \rightarrow e^+e^-$ at the CERN $\bar{p}p$ Collider*, Phys. Lett. **B 129** (1983) 130.
- [5] F. Abe *et al.* (CDF Collaboration), *Observation of Top Quark Production in $\bar{p}p$ Collisions with the Collider Detector at Fermilab*, Phys. Rev. Lett. **74** (1995) 2626–2631.
- [6] S. Abachi *et al.* (D0 Collaboration), *Observation of the Top Quark*, Phys. Rev. Lett. **74** (1995) 2632–2637.
- [7] M. Lindner, *Implications of Triviality for the Standard Model*, Z. Phys. **C 31** (1986) 295.
- [8] S.W. Herb *et al.* (CFS Collaboration), *Observation of a Dimuon Resonance at 9.5 GeV in 400 GeV Proton Nucleus Collisions*, Phys. Rev. Lett. **39** (1977) 252.
- [9] Ch. Berger *et al.* (PLUTO Collaboration), *Observation of a Narrow Resonance formed in e^+e^- Annihilation at 9.46 GeV*, Phys. Lett. **B 76** (1978) 246.
- [10] C.W. Darden *et al.* (DASP Collaboration), *Observation of a Narrow Resonance at 9.46 GeV in Electron-Positron Annihilation*, Phys. Lett. **B 76** (1978) 246.

- [11] D. Andrews *et al.*, *Observation of Three Upsilon States*, Phys. Rev. Lett. **44** (1980) 1108.
- [12] T. Böhringer *et al.*, *Observation of Υ, Υ' , and Υ'' at the Cornell Electron Storage Ring*, Phys. Rev. Lett. **44** (1980) 1111.
- [13] M. Artuso, *Experimental Facilities for b-Quark Physics*, In: B Decays, revised 2nd edition, ed. S. Stone, World Scientific (1994) 80–131.
- [14] J.H. Kühn and P.M. Zerwas, *Heavy Flavors*, In: Z Physics at LEP 1, Volume 1: Standard Physics (1989) 267–372, CERN 89-08.
- [15] C. Albajar *et al.* (UA1 Collaboration), *Search for $B^0-\bar{B}^0$ Oscillations at the CERN Proton-Antiproton Collider*, Phys. Lett. **B 186** (1987) 247.
- [16] C. Albajar *et al.* (UA1 Collaboration), *First observation of the beauty baryon Λ_b in the decay channel $\Lambda_b \rightarrow J/\psi \Lambda$ at the CERN proton-antiproton collider*, Phys. Lett. **B 273** (1991) 540–548.
- [17] S. Behrends *et al.* (CLEO Collaboration), *Observation of Exclusive Decay Modes of b Flavored Mesons*, Phys. Rev. Lett. **50** (1983) 881.
- [18] S.L. Glashow, *Partial-Symmetries of Weak Interactions*, Nucl. Phys. **22** (1961) 579–588.
- [19] S. Weinberg, *A Model of Leptons*, Phys. Rev. Lett. **19** (1967) 1264–1270.
- [20] A. Salam and J.C. Ward, *Electromagnetic and Weak Interactions*, Phys. Lett. **13** (1964) 168–171.
- [21] A. Salam, *Elementary Particle Theory*, ed. N. Svartholm, p. 367, Almquist & Wiksell, Stockholm, 1968.
- [22] M. Gell-Mann, *Quarks*, Acta Physica Austriaca **Suppl. IX** (1972) 733.
- [23] M. Gell-Mann, *A Schematic Model of Baryons and Mesons*, Phys. Lett. **8** (1964) 214.
- [24] G. Zweig, *An $SU(3)$ Model for Strong Interaction Symmetry and its Breaking*, CERN-TH-412/1964 (1964).
- [25] O. W. Greenberg, *Spin and Unitarity-Spin Independence in a Paraquark Model of Baryons and Mesons*, Phys. Rev. Lett. **13** (1964) 598.
- [26] H. Fritzsch, M. Gell-Mann, and H. Leutwyler, *Advantages of the Color Octet Gluon Picture*, Phys. Lett. **B 47** (1973) 365–368.

- [27] L. Montanet *et al.* (Particle Data Group), *Review of Particle Properties*, Phys. Rev. **D 50** (1994).
- [28] G. 't Hooft and M. Veltman, *Regularization and Renormalization of Gauge Fields*, Nucl. Phys. **B 44** (1972) 189–213.
- [29] P.W. Higgs, *Broken Symmetries, Massless Particles and Gauge Fields*, Phys. Lett. **12** (1964) 132–133.
- [30] P.W. Higgs, *Broken Symmetries and the Masses of Gauge Bosons*, Phys. Rev. Lett. **13** (1964) 508.
- [31] P.W. Higgs, *Spontaneous Symmetry Breakdown without Massless Bosons*, Phys. Rev. **145** (1966) 1156.
- [32] W.A. Bardeen, A.J. Buras, W.D. Duke, and T. Muta, *Deep Inelastic Scattering Beyond the Leading Order in Asymptotically Free Gauge Theories*, Phys. Rev. **D 18** (1978) 3998.
- [33] S. Bethke, *Summary of α_s Measurements*, Nucl. Phys. Proc. Suppl. **BC 39** (1995) 198.
- [34] D.A. Ross and J.C. Taylor, *Renormalization of a Unified Theory of Weak and Electromagnetic Interactions*, Nucl. Phys. **B 51** (1973) 125.
- [35] A. Sirlin, *Radiative Corrections in the $SU(2) \otimes U(1)$ Theory: A Simple Renormalization Framework*, Phys. Rev. **D 22** (1980) 971.
- [36] P. Antilogus *et al.* (LEP Electroweak Working Group), *A Combination of Preliminary LEP Electroweak Measurements and Constraints on the Standard Model*, CERN-PPE/95-172, 1995.
- [37] M. Consoli and W. Hollik, *Electroweak Radiative Corrections for Z Physics*, In: Z Physics at LEP 1, Volume 1: Standard Physics (1989) 7–54, CERN 89-08.
- [38] G. Hanson *et al.* (SPEAR Collaboration), *Evidence for Jet Structure in Hadron Production by e^+e^- Annihilation*, Phys. Rev. Lett. **35** (1975) 1609.
- [39] R. Brandelik *et al.* (TASSO Collaboration), *Evidence for Planar Events in e^+e^- Annihilation at High Energy*, Phys. Lett. **B 86** (1979) 243.
- [40] Ch. Berger *et al.* (PLUTO Collaboration), *Evidence for Gluon Bremsstrahlung in e^+e^- Annihilation at High Energy*, Phys. Lett. **B 86** (1979) 418.
- [41] D.P. Barber *et al.* (MARK J Collaboration), *Discovery of Three-Jet Events and a Test of Quantum Chromodynamics at PETRA*, Phys. Rev. Lett. **43** (1979) 830.

- [42] W. Bartel *et al.* (JADE Collaboration), *Observation of Planar Three-jet Events in e^+e^- Annihilation and Evidence for Gluon Bremsstrahlung*, Phys. Lett. **B 91** (1980) 142.
- [43] R.P. Feynman and R.D. Field, *A Parametrization of the Properties of Quark Jets*, Nucl. Phys. **B 136** (1978) 1.
- [44] B. Andersson, G. Gustafson, and T. Sjöstrand, *Parton Fragmentation and String Dynamics*, Phys. Rept. **97** (1983) 31–145.
- [45] T. Sjöstrand and M. Bengtsson, *The Lund Monte Carlo for Jet Fragmentation and e^+e^- Physics - JETSET Version 6.3*, Compt. Phys. Comm. **43** (1987) 367.
- [46] G. Marchesini and B.R. Webber, *Monte Carlo Simulation of General Hard Processes with Coherent QCD Radiation*, Nucl. Phys. **B 310** (1988) 461.
- [47] P. Abreu *et al.* (DELPHI Collaboration), *Production of Strange B Baryons Decaying into $\Xi^\mp - \ell^\mp$ Pairs at LEP*, Z. Phys. **C 68** (1995) 541–554.
- [48] G. Altarelli, N. Cabibbo, G. Carbone, L. Maiani, and G. Martinelli, *Leptonic Decays of Heavy Flavours: A Theoretical Update*, Nucl. Phys **B 208** (1982) 365.
- [49] N. Isgur, B. Grinstein, D. Scora, and M.B. Wise, *Semileptonic B and D Decays in the Quark Model*, Phys. Rev. **D 39** (1989) 799.
- [50] M. Wirbel, B. Stech, and M. Bauer, *Exclusive Semileptonic Decays of Heavy Mesons*, Z. Phys. **C 29** (1985) 637.
- [51] M. Bauer, B. Stech, and M. Wirbel, *Exclusive Nonleptonic Decays of D , D_s , and B Mesons*, Z. Phys. **C 34** (1987) 103.
- [52] J. Körner and G. Schuler, *Exclusive Semileptonic Decays of Bottom Mesons in the Spectator Quark Model*, Z. Phys. **C 38** (1988) 511.
- [53] N. Isgur and M.B. Wise, *Weak Decays of Heavy Mesons in the Static Quark Approximation*, Phys. Lett. **B 232** (1989) 113.
- [54] A. Chen *et al.* (CLEO Collaboration), *Limits on the $b \rightarrow u$ Coupling from Semileptonic B Decay*, Phys. Rev. Lett. **52** (1984) 1084–1087.
- [55] C. Klopfenstein *et al.* (CUSB Collaboration), *Semileptonic B Decay of the B Meson*, Phys. Lett. **B 130** (1983) 444–448.
- [56] I. Bigi *et al.*, *Non-Leptonic Decays of Beauty Hadrons – From Phenomenology to Theory*, In: *B Decays*, revised 2nd edition, ed. S. Stone, World Scientific (1994) 132–157.

- [57] M. Neubert, V. Rieckert, B. Stech, and Q.P. Xu, *Exclusive Weak Decays of B-Mesons*, In: Heavy Flavours, ed. A. Buras and M. Lindner, World Scientific (1992) 286–333.
- [58] A. Deandrea, N. Di Bartolomeo, R. Gatto, and G. Nardulli, *Two Body Nonleptonic Decays of B and B_s Mesons*, Phys. Lett. **B 318** (1993) 549.
- [59] J.H. Christenson, J.W. Cronin, V.L. Fitch, and R. Turlay, *Evidence for the 2 π Decay of the K₂⁰ Meson*, Phys. Rev. Lett. **13** (1964) 138.
- [60] A.D. Sakharov, *Violation of CP Invariance, C Asymmetry, and Baryon Asymmetry in the Universe*, JETP Lett. **5** (1967) 24.
- [61] L. Wolfenstein, *Violation of CP Invariance and the Possibility of Very Weak Interactions*, Phys. Rev. Lett. **13** (1964) 562.
- [62] Y. Nir and H. Quinn, *CP Violation in B Physics*, Annu. Rev. Nucl. Part. Sci. **42** (1992) 211.
- [63] M. Kobayashi and T. Maskawa, *CP-Violation in the Renormalisable Theory of Weak Interactions*, Prog. Theor. Phys. **49** (1973) 652–657.
- [64] J.J. Aubert *et al.*, *Experimental Observation of a Heavy Particle J*, Phys. Rev. Lett **33** (1974) 1404.
- [65] J.E. Augustin *et al.*, *Discovery of a Narrow Resonance in e⁺e⁻ Annihilation*, Phys. Rev. Lett **33** (1974) 1406.
- [66] M.L. Perl *et al.* (MARK I Collaboration), *Evidence for Anomalous Lepton Production in e⁺e⁻ Annihilation*, Phys. Rev. Lett. **35** (1975) 1489–1492.
- [67] N. Cabibbo, *Unitary Symmetry and Leptonic Decay*, Phys. Rev. Lett. **10** (1963) 531–533.
- [68] S.L. Glashow, J. Iliopoulos, and L. Maiani, *Weak Interactions with Lepton-Hadron Symmetry*, Phys. Rev. **D 2** (1970) 1285–1292.
- [69] L. Wolfenstein, *Parametrization of the Kobayashi-Maskawa Matrix*, Phys. Rev. Lett. **51** (1983) 1945.
- [70] J.L. Rosner, *The Cabibbo-Kobayashi-Maskawa Matrix*, In: B Decays, revised 2nd edition, ed. S. Stone, World Scientific (1994) 470–519.
- [71] C. Jarlskog, *Commutator of the Quark Mass Matrices in the Standard Electroweak Model and a Measure of Maximal CP Violation*, Phys. Rev. Lett. **55** (1985) 1039.

-
- [72] K. Lande *et al.*, *Observation of Long-Lived neutral V Particles*, Phys. Rev. **103** (1956) 1901.
- [73] H. Albrecht *et al.* (ARGUS Collaboration), *Observation of B^0 – \bar{B}^0 Mixing*, Phys. Lett. **B 192** (1987) 245.
- [74] A. Ali and D. London, *CP Violation and Flavor Mixing in the Standard Model*, DESY-95-148, Jun 1995.
- [75] D. Decamp *et al.* (ALEPH Collaboration), *ALEPH: A Detector for Electron-Positron Annihilations at LEP*, Nucl. Instr. and Meth. **A 294** (1990) 121.
- [76] P. Aarnio *et al.* (DELPHI Collaboration), *The DELPHI Detector at LEP*, Nucl. Instr. and Meth. **A 303** (1991) 233–276.
- [77] B. Adeva *et al.* (L3 Collaboration), *The Construction of the L3 Detector at LEP*, Nucl. Instr. and Meth. **A 289** (1990) 35.
- [78] K. Ahmet *et al.* (OPAL Collaboration), *The OPAL Detector at LEP*, Nucl. Instr. and Meth. **A 305** (1991) 275.
- [79] LEP design report, *The LEP injector chain*, CERN-LEP/TH/83–29, vol. I, 1983.
- [80] LEP design report, *The LEP main ring*, CERN-LEP/TH/84–01, vol. II, 1984.
- [81] P. Abreu *et al.* (DELPHI Collaboration), *Performance of the DELPHI Detector*, Nucl. Instr. and Meth. **A 378** (1996) 57–100.
- [82] *DELPHI Technical Proposal*, CERN/LEPC 83–3, 1983.
- [83] C. Brand *et al.*, *The DELPHI Time Projection Chamber*, Nucl. Instr. and Meth. **A 283** (1989) 567–572.
- [84] F. Hartjes *et al.*, *A Drift Chamber with Variable Drift Velocity*, Nucl. Instr. and Meth. **A 256** (1987) 55–64.
- [85] A. Amery *et al.*, *The DELPHI Outer Detector*, Nucl. Instr. and Meth. **A 283** (1989) 502.
- [86] N. Bingfors *et al.*, *The DELPHI Microvertex Detector*, Nucl. Instr. and Meth. **A 328** (1993) 447.
- [87] V. Chabaud *et al.*, *The DELPHI Silicon Strip Microvertex Detector with Double Sided Readout*, Nucl. Instr. and Meth. **A 368** (1996) 314–332.

-
- [88] W. Bartl, G. Leder, and M. Pernicka, *Design principles for the forward chamber FCA in the DELPHI experiment*, DELPHI Note/83–49.
- [89] M. Pernicka, *Electronics for short drifttime measurements for the Forward Chamber FCA in the DELPHI experiment*, DELPHI Note/83–51 ELEC.
- [90] W. Bartl, *Conductive PVC for drift tubes*, Nucl. Instr. and Meth. **A 305** (1991) 82–90.
- [91] R. Frühwirth and N. Neumeister, *Automatic Analysis of FCA Drift Time Spectra*, DELPHI Note/95–43 TRACK 80.
- [92] H.G. Fisher *et al.*, *The DELPHI High Density Projection Chamber*, Nucl. Instr. and Meth. **A 265** (1988) 218.
- [93] DELPHI Collaboration, *Proposal for the Replacement of the Small Angle Calorimeter of DELPHI*, CERN/LEPC 92–6, 1992.
- [94] E.G. Anassontzis *et al.*, *The Barrel Ring Imaging Cherenkov Counter of DELPHI*, Nucl. Instr. and Meth. **A 323** (1992) 351–362.
- [95] W. Adam *et al.*, *The Forward Ring Imaging Cherenkov Detector of DELPHI*, Nucl. Instr. and Meth. **A 338** (1994) 284–309.
- [96] W. Adam *et al.*, *Recent Results of the Forward Ring Imaging Cherenkov Detector of the DELPHI Experiment at LEP*, IEEE Trans. Nucl. Sci. **41** (1994) 856.
- [97] Ph. Charpentier *et al.*, *The DELPHI Fastbus Data Acquisition System*, DELPHI NOTE/91–92 DAS 112.
- [98] H. De Boeck and G. Wilkinson, *MUFLAG: A Framework for Muon Identification*, DELPHI NOTE/93–14 PHYS 263.
- [99] J.H. Kühn, S. Nussinov, and R. Rückl, *Charmonium Production in B Decays*, Z. Phys. **C 5** (1980) 117.
- [100] P. Cho, *Prompt Upsilon and Psi Production at LEP*, Phys. Lett **B 368** (1996) 171.
- [101] F. Abe *et al.* (CDF Collaboration), *Inclusive J/ψ , $\psi(2S)$ and b Quark Production in $\bar{p}p$ Collisions at $\sqrt{s} = 1.8$ TeV*, Phys. Rev. Lett. **69** (1992) 3704–3708.
- [102] F. Abe *et al.* (CDF Collaboration), *Measurement of the B^+ and B^0 Meson Lifetimes*, Phys. Rev. Lett. **72** (1994) 3456.

-
- [103] D. Bortoletto *et al.* (CLEO Collaboration), *Inclusive and Exclusive Decays of B Mesons to Final States Including Charm and Charmonium Mesons*, Phys. Rev. **D 45** (1992) 21–35.
- [104] M.S. Alam *et al.* (CLEO Collaboration), *Exclusive Hadronic B Decays to Charm and Charmonium Final States*, Phys. Rev. **D 50** (1994) 43–68.
- [105] H. Albrecht *et al.* (ARGUS Collaboration), *Exclusive Hadronic Decays of B Mesons*, Z. Phys. **C 48** (1990) 543–552.
- [106] P. Abreu *et al.* (DELPHI Collaboration), *J/ ψ Production in the Hadronic Decays of the Z^0* , Phys. Lett. **B 341** (1994) 109.
- [107] D. Buskulic *et al.* (ALEPH Collaboration), *Measurements of Mean Lifetime and Branching Fractions of B Hadrons Decaying to J/ ψ* , Phys. Lett. **B 295** (1992) 396.
- [108] G. Alexander *et al.* (OPAL Collaboration), *J/ ψ and ψ' Production in Hadronic Z^0 Decays*, Z. Phys. **C 70** (1996) 197.
- [109] M. Battaglia and D. Liko, *Reconstruction of Exclusive Decays of B Mesons into Charmonium States with the DELPHI Detector at LEP*, DELPHI Note/92–122 PHYS 230.
- [110] T. Sjöstrand, *PYTHIA 5.7 and JETSET 7.4: Physics and Manual*, Computer Phys. Comm. **82** (1994) 74.
- [111] DELSIM Reference Manual, DELPHI Note/87–98 PROG 100, 1989.
- [112] D. Coffman *et al.* (MARK III Collaboration), *A Direct Measurement of the J/ ψ Leptonic Branching Fractions*, Phys. Rev. Lett **68** (1992) 282–285.
- [113] O. Adriani *et al.* (L3 Collaboration), *χ_c Production in Hadronic Z Decays*, Phys. Lett. **B 317** (1993) 467.
- [114] R. Balest *et al.* (CLEO Collaboration), *Inclusive Decays of B Mesons to Charmonium*, Phys. Rev. **D 52** (1995) 2661–2672.
- [115] BABAR Collaboration, *BABAR Technical Design Report*, SLAC-R-95-457, (1995).
- [116] BELLE Collaboration, *BELLE Technical Design Report*, KEK-REPORT 95-1, (1995).

- [117] HERA-B Collaboration, *HERA-B: An Experiment to Study CP Violation in the B System Using an Internal Target at the Hera Proton Ring – Design Report*, DESY-PRC 95/01, (1995).
- [118] J.C. Yun, *B Physics Results at CDF*, FERMILAB-CONF-95-346-E (1995).
- [119] CDF Collaboration, *Physics with CDF in Run II*, CDF Note 3172, (1995).
- [120] LHC Study Group, *The Large Hadron Collider: Conceptual Design*, CERN-AC 95-05 (1995).
- [121] ATLAS Collaboration, *Technical Proposal for a General-Purpose pp Experiment at the Large Hadron Collider at CERN*, CERN-LHCC 94-43, LHCC/P 2, 1994.
- [122] CMS Collaboration, *Compact Muon Solenoid, Technical Proposal*, CERN-LHCC 94-38, LHCC/P 1, 1994.
- [123] D. Denegri, *Standard Model Physics at the LHC*, In: Proceedings of the LHC Workshop, Aachen 1990, CERN 90-10 vol. I (1990) 56.
- [124] LHC-B Collaboration, *LHC-B: Letter of Intent*, CERN/LHCC 95-5, (1995).
- [125] I. Abt *et al.* (H1 Collaboration), *Measurement of the Proton Structure Function $F_2(x, Q^2)$ in the Low x Region at HERA*, Nucl. Phys. **B 407** (1993) 515–538.
- [126] M. Derrick *et al.* (ZEUS Collaboration), *Measurement of the Proton Structure Function F_2 in ep Scattering at HERA*, Phys. Lett. **B 316** (1993) 412–426.
- [127] J.P. Guillet, P. Nason, and H. Plochow-Besch, *Heavy Quark Production at the LHC*, In: Proceedings of the LHC Workshop, Aachen 1990, CERN 90-10 vol. II (1990) 116.
- [128] P. Nason, S. Dawson, and R.K. Ellis, *The Total Cross Section for the Production of Heavy Quarks in Hadronic Collisions*, Nucl. Phys. **B 303** (1988) 607–633.
- [129] E.L. Berger and R. Meng, *Bottom Quark Cross Sections at Collider and Fixed-Target Energies at the SSC and LHC*, In: Proceedings of the Workshop on B Physics at Hadron Accelerators, Snowmass, Colorado, June 21 – July 2 (1993) 339–342.
- [130] H.-U. Bengtsson and T. Sjöstrand, *The Lund Monte Carlo for Hadronic Processes: PYTHIA Version 4.8*, Computer Phys. Comm. **46** (1987) 43.
- [131] J. Botts, J.G. Morfin, J.F. Owens, Jianwei Qiu, Wu-Ki Tung, and H. Weerts, *CTEQ Parton Distributions and Flavor Dependence of Sea Quarks*, Phys. Lett. **B 304** (1993) 159–166.

-
- [132] E.J. Eichten, I. Hinchliffe, C. Quigg, and K.D. Lane, *Super Collider Physics*, Rev. Mod. Phys. **56** (1984) 579–707.
- [133] CMS Collaboration, *Compact Muon Solenoid, Letter of Intent*, CERN-LHCC 92–3, LHCC/I 1, 1992.
- [134] H. Czyrkowski *et al.*, CMS TN/93-111 (1993).
- [135] D. Denegri, A. Fridman, N. Neumeister, *et al.*, *B Physics and CP Violation Studies with the CMS Detector at the LHC*, Int. Journal of Modern Physics **A9 24** (1994) 4211–4255.
- [136] M. Botlo *et al.*, *Further Comments about B-Physics in pp-Interactions*, SSCL-538 (1992).
- [137] M. Ciuchini *et al.*, *An Upgraded Analysis of ε'/ε at the next-to-leading Order*, Z. Phys. **C 68** (1995) 239–256.
- [138] N. Neumeister, *Measurement of CP-Violation in B-Decays with the CMS Detector*, Nucl. Instr. and Meth. **A333** (1993) 239.
- [139] N. Neumeister, *Measurement of $\sin(2\beta)$ with the CMS Detector at LHC*, In: Proceedings of the Workshop on B Physics at Hadron Accelerators, Snowmass, Colorado, June 21 – July 2 (1993) 275.
- [140] N. Neumeister, *CP Violation Studies in ATLAS and CMS*, In: Proceedings of the Four Seas Conference held at SISSA, Trieste, June 25 – July 1 (1995).
- [141] J.F. Hassard and S. Margetides, *K_s^0 Finding Efficiencies in Increasing Luminosities*, In: Proceedings of the Workshop on B Physics at Hadron Accelerators, Snowmass, Colorado, June 21 – July 2 (1993) 279.
- [142] M. Cannalire and A. Fridman, *Dilution Effects for CP Violation Measurement in B Decays*, SSCL-566 (1992).
- [143] D. Denegri, M. Konecki, A. Rubbia, and A. Starodumov, *B Physics and CP Violation Studies with the CMS Detector*, Nucl. Instr. and Meth. **A 351** (1994) 95.

Curriculum Vitae

Name: Norbert Neumeister

[REDACTED] [REDACTED]

[REDACTED] [REDACTED]

[REDACTED] [REDACTED]

[REDACTED] [REDACTED]

[REDACTED] [REDACTED]

[REDACTED] [REDACTED]

[REDACTED]

[REDACTED]

Studium: 1986 : Technische Physik und Informatik an der Technischen Universität Wien
1990–1991 : Diplomarbeit am Institut für Hochenergiephysik der OeAW,
Thema : *Der Bose-Einstein Effekt und sein Einfluß auf Intermittency*;
Zweite Diplomprüfung in Technischer Physik am 17.1.1992 mit Auszeichnung;
Sponsion zum Dipl.-Ing. am 30.1.1992
1993–1996 : Dissertation am Institut für Hochenergiephysik der OeAW,
Thema : *Reconstruction of Exclusive B Decays into J/ψ Using Data from the DELPHI Experiment and Implications to Future CP Violation Measurements at the LHC*

Beruf: 1992 Anstellung am Institut für Hochenergiephysik der Österreichischen Akademie der Wissenschaften. Arbeit am Europäischen Laboratorium für Teilchenphysik CERN an den Experimenten DELPHI und CMS.

[REDACTED] [REDACTED]